Spray-flame synthesis of La(Fe, Co, Mn)O_3 perovskite nanoparticles for CO oxidation

Von der Fakultät für Ingenieurwissenschaften,

Abteilung Maschinenbau und Verfahrenstechnik

der Universität Duisburg-Essen

zur Erlangung des akademischen Grades

eines

Doktors der Ingenieurwissenschaften

– Dr.-Ing. –

genehmigte Dissertation

von

Steven Angel

aus

Medellín, Kolumbien

Gutachter: Prof. Dr. Christof Schulz

Prof. Dr. Lutz Mädler

Tag der mündlichen Prüfung: 01.10.2021

Abstract

Perovskite-type nanomaterials are attractive and promising oxides for environmental- (e.g., oxidation of CO) and energy-relevant (e.g., electrochemical water splitting to produce H_2/O_2) catalytic reactions. For these applications, two of the most sought characteristics of perovskite compounds – high specific surface area and phase purity – are hardly attained by conventional synthesis methods. Envisioning the cost-efficient and one-step production of high surface-area perovskite materials, the spray-flame synthesis of three model compounds $LaFeO_3$, $LaCoO_3$ and $LaMnO_3$ for catalytic CO oxidation is investigated in this thesis. Using metal nitrates as low-cost precursors, the effect of two solvents – ethanol and 2-ethylhexanoic acid (2-EHA) – on the chemistry of the precursor solutions and on the particle-size distribution, specific surface area and phase composition of the produced materials is analyzed.

The use of ethanol as solvent for the spray-flame synthesis led to the formation of perovskite ($LaFeO_3$, $LaCoO_3$ and $LaMnO_3$) compounds with multimodal particle-size distributions from which, large particles (> 100 nm) were identified as lanthanum-rich – especially in the $LaCoO_3$ case – and the source of secondary phases as La_2O_3 or La_2CoO_4. ATR-FTIR analyses of the ethanol-based solutions allowed us to identify the formation of species such as HNO_3 at low temperatures, which point to the hydrolysis of the metal ions – especially in the solution containing iron nitrate – and the formation of hydroxide species. The use of ethanol/2-EHA-based solutions was effective to generate perovskite materials with high specific-surface areas, with narrow particle size distributions – only few sub-200 nm particles were identified – and proved also to be effective to reduce the concentration of secondary phases (e.g., La_2O_3) in the final products. Ethanol/2-EHA mixtures have been used before especially for the spray-flame synthesis of single oxides (e.g., Fe_xO_y, Co_xO_y, and Al_2O_3) and they have been related to the generation of droplet micro-explosions or the formation of metal carboxylates. In this thesis, the chemical interaction among ethanol, 2-EHA, and the corresponding metal nitrates is further investigated. Based on ATR-FTIR analyses, esterification between ethanol and 2-EHA to produce ethyl 2-ethylhexanoate and water was identified and in the case of Mn-based solutions, oxidation of Mn^{2+} was induced by the addition of 2-EHA at low temperatures, causing the formation of Mn^{4+}-rich $LaMnO_{3+\delta}$ nanoparticles from spray-flame synthesis. Both esterification and oxidation of manganese are novel aspects related to the use of ethanol/2-EHA-based solutions of metal nitrates for the spray-flame synthesis of perovskites. Furthermore, esterification was identified to be catalyzed by the transition metal ion present in solution with the iron-containing solution presenting a remarkable activity to produce the ester compound and water. Using ethanol/2-EHA-based solutions, the effect of the droplet sizes by modifying the dispersion gas flow rate (5, 6, 7, and 8 slm) and the identified esterification reaction on the particle-size distribution of the three spray-flame synthesized model perovskites are also analyzed in this dissertation.

The spray-flame synthesized $LaFeO_3$, $LaCoO_3$ and $LaMnO_3$ perovskite samples based on different mixtures of ethanol/2-EHA are analyzed for the catalytic oxidation of CO. For this reaction, $LaCoO_3$ samples were identified to present the highest activity followed by $LaMnO_3$ and $LaFeO_3$. The $LaMnO_3$ samples were selected to perform a more detailed catalytic analysis including the selective oxidation (SELOX) of CO and the characterization with *ex situ* techniques as H_2-TPR and O_2-TPD.

This thesis provides relevant information for the spray-flame synthesis of perovskites and by extension, mixed-oxide systems when low-cost metal nitrates are used as precursors. It is shown how chemical/physical effects related to the solutions of precursors play important roles in the spray-flame synthesis of nanomaterials and most importantly, it is presented how these solutions can be modified to improve the quality of the synthesized materials.

Zusammenfassung

Perowskit-Nanomaterialien sind attraktive und vielversprechende Oxide für umwelt- (z. B. Oxidation von CO) und energierelevante (z. B. elektrochemische Wasserspaltung zur Erzeugung von H_2/O_2) katalytische Reaktionen. Für diese Anwendungen sind zwei der am meisten nachgefragten Eigenschaften von Perowskit-Materialien – hohe spezifische Oberfläche und Phasenreinheit – mit herkömmlichen Synthese -Verfahren kaum erreicht. Um eine kostengünstige und einstufige Herstellung von Perowskit-Materialien mit großer Oberfläche zu ermöglichen, ist in dieser Arbeit die Sprayflammensynthese von drei Modellmaterialien – $LaFeO_3$, $LaCoO_3$ und $LaMnO_3$ – für die katalytische CO-Oxidation untersucht. Unter Verwendung von Metallnitraten als kostengünstige Präkursoren ist die Wirkung von zwei Lösungsmitteln – Ethanol und 2-Ethylhexansäure (2-EHA) – auf die Chemie der Lösungen der Präkursoren sowie auf die Partikelgrößenverteilung, die spezifische Oberfläche und die Phasenzusammensetzung der hergestellten Materialien analysiert worden.

Unter Verwendung von Ethanol als Lösungsmittel für die Sprayflammensynthese, Perowskit-Materialien ($LaFeO_3$, $LaCoO_3$ und $LaMnO_3$) mit multimodalen Partikelgrößenverteilungen konnten hergestellt werden, bei denen große Partikel (> 100 nm) als lanthanreich – vor allem in dem $LaCoO_3$-Fall – und die Quelle der Sekundärphasen als La_2O_3 oder La_2CoO_4 identifiziert wurden. ATR-FTIR-Analysen der Lösungen auf Ethanolbasis ermöglichten es, die Bildung von HNO_3 bei niedrigen Temperaturen zu identifizieren, was auf die Hydrolyse der Metallionen – insbesondere in der Lösung mit Eisensalzen – und die Bildung von Hydroxidspezies hinweist. Die Verwendung von Lösungen auf Ethanol/2-EHA-Basis war wirksam, um Perowskitmaterialien mit hochspezifischen Oberflächen mit engen Partikelgrößenverteilungen zu erzeugen – nur wenige Partikel unter 200 nm wurden identifiziert – und erwies sich auch als wirksam zur Verringerung der Konzentration der Sekundärphasen (z.B. La_2O_3) in den Endprodukten. Ethanol/2-EHA-Mischungen wurden zuvor speziell für die Sprayflammensynthese einzelner Oxide (z. B. Fe_xO_y, Co_xO_y und Al_2O_3) verwendet. Sie stehen im Zusammenhang mit der Erzeugung von Mikroexplosionen von Tröpfchen und der Bildung von Metallcarboxylaten. In dieser Dissertation wurde die chemische Wechselwirkung zwischen Ethanol, 2-EHA und den entsprechenden Metallnitraten weiter untersucht. Basierend auf ATR/FTIR-Analysen wurde die Veresterungsreaktion zwischen Ethanol und 2-EHA zur Herstellung von Ethyl-2-ethylhexanoat und Wasser identifiziert und bei Lösungen auf Mn-Basis wurde die Flüssigphasen-Mn^{2+}-Oxidation durch Zugabe von 2-EHA bei niedrigen Temperaturen induziert, wodurch Mn^{4+}-reiche $LaMnO_{3+\delta}$-Nanopartikel aus der Sprayflammensynthese gebildet wurden. Sowohl die Veresterungsreaktion als auch die Oxidation von Mangan sind neu entdeckte Aspekte im Zusammenhang mit der Verwendung von Ethanol/2-EHA-basierten Lösungen von Metallnitraten für die Sprayflammensynthese von Perowskiten. Darüber hinaus wurde festgestellt, dass die Veresterungsreaktion durch das in Lösung vorhandene Übergangsmetallion katalysiert wird, wobei die eisenhaltige Lösung eine bemerkenswerte Aktivität zur Herstellung der Esterverbindung und des Wassers aufweist. Unter Verwendung von Lösungen auf Ethanol/2-EHA-Basis ist die Auswirkung der Tröpfchengrößen durch Modifizieren der Dispersionsgasströmungsrate (5, 6, 7 und 8 slm) und der identifizierten Veresterungsreaktion auf die Partikelgrößenverteilung der drei Sprayflammen-synthetisierte Modellperowskite in dieser Dissertation ebenfalls analysiert worden.

Die synthetisierten $LaFeO_3$-, $LaCoO_3$- und $LaMnO_3$-Perowskitproben unter Verwendung verschiedener Ethanol/2-EHA-Mischungen wurden bzgl. der katalytischen Oxidation von CO analysiert. Für diese Reaktion wurde festgestellt, dass $LaCoO_3$ die höchste Aktivität aufweist, gefolgt von $LaMnO_3$ und $LaFeO_3$. Die $LaMnO_3$-Proben wurden ausgewählt, um eine detailliertere katalytische Analyse durchzuführen, einschließlich der selektiven Oxidation (SELOX) von CO und der Charakterisierung mit Techniken wie H_2-TPR und O_2-TPD.

Diese Dissertation liefert relevante Informationen für die Sprayflammensynthese von Perowskiten und im weiteren Sinne für Mischoxidsysteme, wenn kostengünstige Metallnitrate als Präkursoren verwendet werden. Es ist gezeigt, wie chemische/physikalische Effekte in Bezug auf die Lösungen von Präkursoren eine wichtige Rolle bei der Sprayflammensynthese von Nanomaterialien spielen, und vor allem ist vorgestellt, wie diese Lösungen modifiziert werden können, um die Qualität der synthetisierten Materialien zu verbessern.

Table of Contents

List of symbols

Symbol	Description
δ	Oxygen excess/defect fraction in perovskite structures
A	Large cation in the perovskite structure (e.g., La)
ad	Adsorbed species on surface of catalyst
A_g	Vibrational mode
B	Medium-size cation in the perovskite structure (e.g., Fe, Co, Mn)
B_{2g}	Vibrational mode
D_{10}	Arithmetic mean droplet size
D_{32}	Sauter mean droplet size
d_{32}	Sauter mean particle size
d_{BET}	BET-derived particle size
d_p	Mean particle size
e_g	Twofold degenerate (higher energy) states of the d-levels in octahedral symmetry
g	Gas-phase species
h	Number of water molecules, number of OH species in hydroxylated compounds
k_{H2O}	Water-exchange rate constant
n	Number of cobalt atoms in layered Ruddlesden-Popper structures, oxidation number of transition metal ion, number of water molecules in metal nitrates
N	Number of water molecules in hydrated metal species
P_c	Critical pressure
P_{ME}	Droplet micro-explosion probability
r	Ionic radius, distance from the center of the burner
t_{2g}	Threefold degenerate (lower energy) states of the d-levels in octahedral symmetry
T_{50}	Temperature required for 50 % CO conversion
T_{bp}	Boiling point of solvents
T_d	Decomposition temperature of metal nitrates
T_{mp}	Melting point of precursors
x	Atomic content of an ion in an oxide structure, substitution fraction of A-site element in the perovskite structure
y	Atomic content of an ion in an oxide structure, substitution fraction of B-site element in the perovskite structure

Symbol	Description
z	Valence state of hydrated transition metal species
β	Enantiomer of citronellol
ΔG_{hyd}	Free enthalpy of hydration
α	Physically/chemically adsorbed surface oxygen species
α–O	Measure of weakly chemisorbed/physisorbed oxygen upon oxygen vacancies
β	Reduction of Mn^{4+} ions to Mn^{3+} ions
γ	Mn^{3+} to Mn^{2+} reduction in coordination with unsaturated microenvironments

Abbreviations

Abbreviation	Description
2-EHA	2-ethylhexanoic acid
3DOM	Three-dimensional ordered macroporous
aq	Aqueous species
ARS	Activated reactive synthesis
ATR-FTIR	Attenuated total reflectance – Fourier-transform infrared spectroscopy
BET	Brunauer-Emmett-Teller
cor	Fe_2O_3
DEGBE	Diethylene glycol monobutyl ether
DRIFTS	Diffuse reflectance infrared Fourier transform spectroscopy
EDX	Energy-dispersive X-ray spectroscopy
EPR	Electron paramagnetic resonance
ESI-MS	Electrospray ionization mass spectroscopy
EtOH	Ethanol
GC/MS	Gas chromatography–mass spectrometry
GHSV	Gas hourly space velocity
H_2-TPR	Hydrogen temperature-programmed reduction/reaction
HAB	Height above burner
HEBM	High-energy ball-milling
hex	hexagonal
HS	High-spin
ICSD	Inorganic crystal structure database
J-T	Jahn-Teller
KIT-6	Korea Advanced Institute of Science and Technology-6 (Mesoporous silica)
LS	Low-spin
M	Metal ion
O	Orthorhombically-distorted $LaMnO_{3+\delta}$ phase with high Mn^{4+}-content
O'	Orthorhombically-distorted $LaMnO_{3+\delta}$ phase with low Mn^{4+}-content
O_2-TPD	Oxygen temperature-programmed desorption
OER	Oxygen evolution reaction
o-prv	orthorhombic perovskite
PDA	Phase-Doppler anemometry
PEMFC	Proton exchange membrane fuel cells
PSD	Particle-size distribution

QMS	Quadrupole mass spectrometer
R	Orthorhombically $LaMnO_{3+\delta}$ phase
RP	Ruddlesden–Popper
r-prv	Rhombohedral perovskite
s	Solid
SAED	Selected area electron diffraction
SBA-15	Santa Barbara amorphous-15 (Mesoporous silica)
SD	Standard deviation
SELOX	Selective oxidation
SFS	Spray-flame synthesis
sp	Fe_3O_4
SSA	Specific surface area
TCD	Thermal conductivity detector
TEM	Transmission electron microscopy
TGA	Thermogravimetric analysis
UV-Vis	Ultraviolet–visible spectroscopy
WGSR	Water-gas shift reaction
XPS	X-ray photoelectron spectroscopy
XRD	X-ray diffraction

1 Introduction

Sustainable development in our complex and dynamic world must include a structured short-, middle- and long-term vision with a sense of urgency and adaptability, acknowledging the geographically diverse economic conditions. On a global scale, our society faces pressing challenges related to, e.g., health and climate change. Regarding the latter and in order to reach a climate-neutral circular economy, an energy transition from fossil sources to alternative ones[1] (e.g., photovoltaic and wind energy) is required. This transition is linked with other great challenges including: the electrification of the mobility, industry and building[2] sectors; the development of chemicals[3] and derived products using CO_2 as raw material[4], and the development of affordable and efficient (electro)chemical energy storage systems (e.g., batteries, H_2, NH_3)[5, 6]. The advancements and breakthroughs necessary to overcome these challenges require, to a large extent, the use of nanomaterials as catalysts, enabling to, e.g., increase the power/energy density of batteries, decrease the overpotential[7] required to electrochemically transform water to O_2/H_2 or to induce the formation of a given chemical from CO_2. The identification of nanomaterials as promising candidates for the energy transition obeys approaches that are both empirical and theoretical. One of the nanomaterials systems that is currently being studied for the afore-mentioned applications is the perovskite-like oxide family.

The growing interest in the perovskite (ABO_3) structure[8] comes from its high versatility and structural stability, characteristics that allow to incorporate/substitute different cations in the A- and B-sites of the structure. As the B-site cations are typically transition metal ions with redox capability, the perovskite structure can be tuned to fulfill the requirements of multiple heterogeneous catalytic applications, providing desired features such as, e.g., oxygen vacancies/mobility and active sites. The formation of perovskites on the nano-scale is required to increase the number of such catalytically active sites by profiting from the characteristic high-specific surface areas of nanomaterials. Over the years, diverse perovskite materials as $Ba_{0.5}Sr_{0.5}Co_{0.8}Fe_{0.2}O_{3-\delta}$ and $La_{0.5}Ca_{0.5}CoO_{3-\delta}$ for oxygen evolution reaction in electrochemical water-splitting[9] or $LaB_{0.95}Pd_{0.05}O_3$ (B=Mn, Fe, Co, Ni) for CO oxidation[10] have been proposed and used as promising materials. However, the highly sought characteristics of these structures – phase purity and high specific surface area – have proven difficult to obtain. These challenges come from the synthesis techniques that are typically used for obtaining perovskite nanomaterials (more information in Chapter 2.6). Batch processes[8] as the solid-based (e.g., mechanochemistry) or the liquid-based (e.g., sol-gel, nanocasting) methods require several steps of processing including drying and calcination at high temperatures, obtaining the required phase at expense of the specific surface area. This is, however, not the case for all batch processes. Alternatives as performing a high-energy ball-milling (HEBM) step after calcination or the liquid-phase hard-template[11] methods allow to obtain high surface-area perovskites with a drawback: impurities coming from the milling media or the templates are introduced. In general, batch processes are linked to four further limitations: amorphization of the materials, low yields, long processing times and limited scalability. As an alternative to batch processes, the continuous and scalable spray-flame synthesis[12] method – which enables to synthesize materials in one-step without the use of external agents as templates – has been identified as a suitable candidate to produce pure-phase and high-surface area perovskite materials.

The spray-flame synthesis of nanomaterials is linked to challenges that have been mainly identified from the synthesis of single oxides (Chapter 3.2). One of the challenges is related to the use of metal nitrates as low-cost metal precursors. Through the synthesis of Al-, Co- and Fe-oxides,[13, 14] bimodal particle-size

distributions – containing large particles (> 100 nm) that decrease the specific surface area of the materials – are commonly obtained when ethanol-based solutions of metal nitrates are used. The incorporation of 2-ethylhexanoic acid (2-EHA)[14] to ethanol-based solutions of metal nitrates has led to materials with high specific surface areas which was attributed to multiple effects such as, e.g., micro-explosion of droplets, and formation of metal carboxylates.[13, 15] The beneficial effect of 2-EHA addition is linked, however, with other identified challenges of the method: the understanding of the chemical/physical effects of the metal precursors and solvents both in the liquid-phase (e.g., droplets) and in the gas phase. A detailed discussion regarding these and more aspects is presented in Chapter 3.2.3. Concerning the spray-flame synthesis of perovskites (e.g., $LaCoO_3$) using metal nitrates and other precursors[16, 17], avoiding the formation of secondary phases (e.g., La_2O_3, La_2CoO_4) has proven to be a further challenge.

Even though current promising perovskite materials for catalytic applications contain different A- and B-site substitutions, this thesis is focused on three lanthanum-based perovskite systems ($LaFeO_3$, $LaCoO_3$ and $LaMnO_3$) to clearly identify the conditions that can lead to phase-pure and high surface-area materials from spray-flame synthesis. Acknowledging the need to synthesize nanomaterials from low-cost precursors and the associated challenges, metal-nitrate-based solutions were selected and studied in this thesis and the effect of two solvents – ethanol and 2-ethylhexanoic (2-EHA) – was analyzed. Another goal of this thesis was to link the chemistry of the solution (e.g. esterification reaction between ethanol and 2-EHA) with the spray characteristics (e.g., droplet-size distribution) and the final quality of the materials (e.g., particle-size distribution, phase purity). Furthermore, as a product of fruitful scientific cooperation with local and international research groups, the catalytic activity of the developed materials was analyzed in this thesis, using the low-temperature CO oxidation as a probe reaction and as a way to link the activity with the transition metal ion (Fe, Co, Mn) effect of the perovskite structure.

This thesis is structured in the following way: Chapter 2 and 3 are based on a literature review and in Chapter 4, 5, and 6, the performed experiments, results and discussions are presented. A description of the contents of each chapter is presented as follows:

- In Chapter 2, relevant information regarding the perovskite $LaFeO_3$, $LaCoO_3$ and $LaMnO_3$ materials is presented, involving the corresponding phase diagrams and surface characteristics applied to CO oxidation. Based on literature, low-temperature catalytic CO oxidation using perovskites is reviewed. In the last part of the chapter, challenges involved in the synthesis of perovskites are presented, introducing the spray-flame synthesis as a potential option.
- In Chapter 3, the fundamentals of the spray-flame synthesis technique are presented. The chapter explores some of the history, mechanisms and the facility used for the experiments presented in this thesis. A part of the chapter is used to analyze the use of metal nitrates as precursors, analyzing their chemistry and decomposition characteristics and coupling these factors with the use of ethanol as solvent. As a way to identify the challenges and to learn from previous investigations, the spray-flame synthesis of single oxides using metal nitrates dissolved in ethanol or in mixtures of ethanol and 2-ethylhexanoic acid (2-EHA) is explored, physical and chemical considerations of using the ethanol/2-EHA mixture are included. In the last part of the chapter and based on literature, the spray-flame synthesis of perovskite materials is explored to further understand the associated challenges.
- In Chapter 4, spray-flame synthesis of $LaFeO_3$ and $LaCoO_3$ nano-perovskites from metal nitrates is presented. Using metal-nitrate-based solutions, the effect of the use of three mixtures of solvents – (I) ethanol, (II) a mixture of ethanol (50 Vol.%) and 2-EHA (50 Vol.%) and (III) a mixture of ethanol (35 Vol.%) and 2-EHA (65 Vol.%) – on the phase composition and particle size distribution of the synthesized materials is analyzed. The chemistry of the prepared solutions is analyzed and linked with the

materials' characteristics. Furthermore, the use of the perovskite materials as catalysts for CO oxidation is presented.

- The spray-flame synthesis of $LaMnO_{3+\delta}$ nanoparticles was analyzed separately in Chapter 5 due to the higher complexity of this material in terms of characterization. Using metal-nitrate-based solutions, the effect of the use of two solvents – (I) ethanol, (II) a mixture of ethanol (50 Vol.%) and 2-EHA (50 Vol.%) – on the phase composition and particle-size distribution of the synthesized materials is analyzed. The chemistry of the solutions is also analyzed and the use of the synthesized/heat-treated materials for the catalytic oxidation of CO is analyzed on a deeper level.
- In Chapter 6, using metal-nitrate-based solutions and a mixture of ethanol (35 Vol.%) and 2-EHA (65 Vol.%) as solvent, the effect of spray droplet size and the esterification reaction between ethanol and 2-EHA on the particle size distribution of the spray-flame synthesized $LaMO_3$ (M = Mn, Fe, Co) perovskite nanomaterials is analyzed.

2 $LaBO_3$ (B = Fe, Co, Mn) perovskite-type oxides for CO oxidation

2.1 Background

The history of the perovskite structure is one of exploration and curiosity. It can be traced back to the scientific exploration journey of Russia (1829) by a team of scientists led by Alexander von Humboldt. The German mineralogist Gustav Rose (University of Berlin) was part of the team and as part of his tasks, he visited the private mineral collection of August Alexander Kämmerer in Saint Petersburg. Ten years after the trip, in 1839, A. A. Kämmerer sent a rock collected in the Ural mountains to Gustav Rose to be analyzed. Rose identified the material as a new mineral structure ($CaTiO_3$) (Figure 1a) and named it after Count Lev Alekseevich von Perovskiy, as suggested by Kämmerer. It took more than 70 years to finally confirm the $CaTiO_3$ structure as orthorhombic, it was originally considered as cubic. Since then, the study of perovskite-like structures and their properties has enjoyed prolific scientific periods linked to the discovery of, e.g., ferroelectric $BaTiO_3$ ceramics, ferromagnetic, and magneto-resistant $LaMnO_3$-derived materials and $LaCoO_3$ catalysts. [18-20]

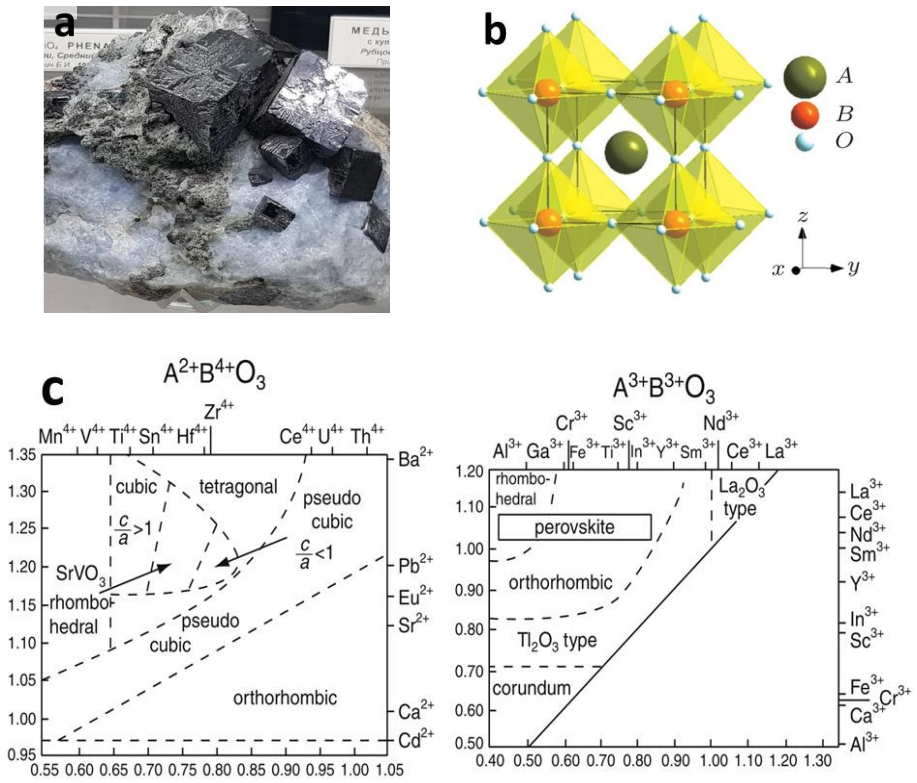

Figure 1. (a) Mineral $CaTiO_3$ perovskite (Photo by E.A. Katz).[20] (b) Ideal cubic ABO_3 perovskite structure.[21] (c) Distortions of the perovskite structure based on the ionic size (A: y-axis, B: x-axis) and the oxidation state of the A and B cations.[22]

The term perovskite has evolved over the years and now it encompasses a more general description of hundreds of materials with a structure of the ABO_3 form (Figure 1b), in which A is a large cation (e.g., La, Ba, Sr) 12-fold coordinated with oxygen atoms and B is a medium-size cation (e.g., Co, Fe, Mn, Ti, Cr, Ni) 6-fold coordinated with oxygen atoms forming BO_6 octahedra.[23] Even though the ideal ABO_3 perovskite structure is cubic, the ion size and oxidation state of the A and B cations influence the symmetry and cause the distortion of the structure leading to, e.g., orthorhombic or rhombohedral structures as presented in

Figure 1c. Distortions of the perovskite structure occur through three main mechanisms: Tilting of the BO_6 octahedra, Jan-Teller (1st order) distortions of the BO_6 octahedra, and Jan-Teller (2nd order) of the A and B polyhedra.[24] Given its ability in tolerating such distortions, the perovskite structure also allows the partial substitution of A and B cations in the $A_{1-x}A_xB_{1-y}B_yO_{3\pm\delta}$ form (double perovskites) and the formation of cationic and/or anionic vacancies (O^{2-}) (e.g., $La_{1-x}Sr_xMnO_{3-\delta}$ and $La_{1-x}Sr_xCoO_{3-\delta}$ materials).[25] Furthermore, as most of the metallic elements (> 90 %) of the periodic table can be stabilized in its structure, the versatile perovskite system can be tuned to target specific applications. Consequently, the field of heterogeneous catalysis started exploring in the early 70s, the use of perovskite-type materials as catalysts in the quest to replace the expensive and scarce noble-metal-based catalysts.[25, 26] In this phase, low-temperature CO oxidation has been identified as a useful probe reaction to elucidate structure–activity correlations when applying lanthanum-based ($LaBO_3$) perovskites as catalysts. The selection of lanthanum (La^{3+}) as an A-site cation – which is considered as catalytically inactive – enables the study of the effect of transition metal ions as B-site cations on the catalytic oxidation of CO.[27] In this regard, three main materials – $LaFeO_3$, $LaCoO_3$ and $LaMnO_3$ – have been identified as the most active single perovskites for CO oxidation.[8] As this thesis is focused on these materials, a more detailed explanation of their chemical and structural properties is presented in Chapter 2.2 to 2.4. The three chapters follow the same structure: Analysis of the structure and phase diagram followed by an introduction to the surface properties of the materials applied to CO oxidation. An overview of their use for CO oxidation is presented in Chapter 2.5.

2.2 $LaFeO_3$

$LaFeO_3$ is an antiferromagnetic perovskite with an orthorhombic distorted structure belonging to the *Pnma* or *Pbnm* space group between 25 and ~1255 K (982 °C)[28] and with a endothermic transition to the rhombohedral structure (*R-3c* space group)[29] occurring at ~1000 °C with an enthalpy change of ~350 J/mol.[30] In the $LaFeO_3$ structure, iron atoms occupy octahedral centers forming 6 covalent bonds with oxygen atoms. The orthorhombic distortion of the structure occurs through the tilting of the Fe-centered octahedra as it can be seen in Figure 2a.

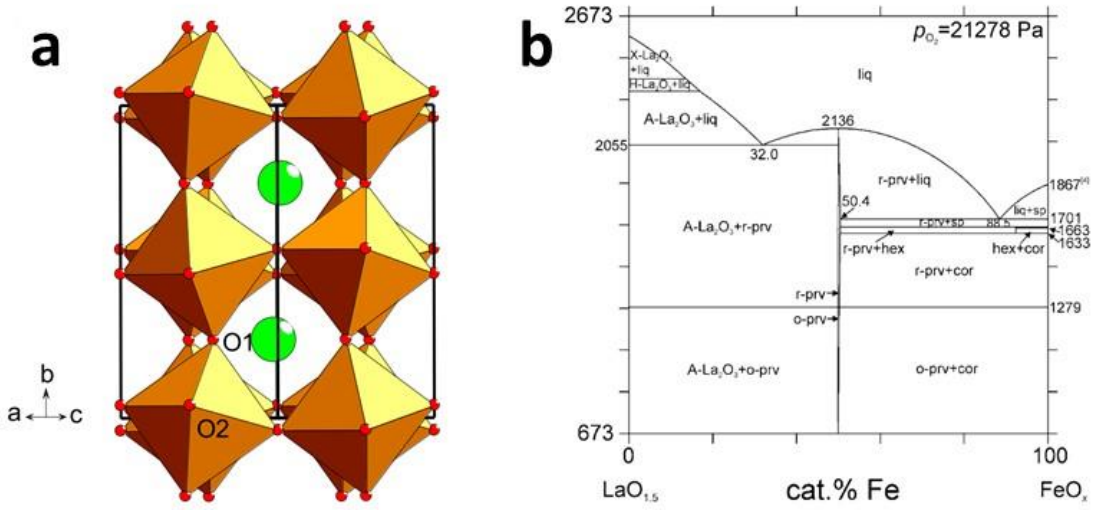

Figure 2. (a) $LaFeO_3$ structure[28] along [101] and (b) temperature-dependent phase diagram of the La-Fe-O system under an atmosphere of air (Temperature in K; symbols: o-prv: orthorhombic perovskite, r-prv: rhombohedral perovskite, cor: Fe_2O_3, sp: Fe_3O_4, hex: hexagonal $LaFe_{12}O_{19}$)[30].

Considering the formation of $LaFeO_3$ from metal oxides – La_2O_3 (i.e., $LaO_{1.5}$) and FeO_x – a temperature-dependent phase diagram is presented in Figure 2b. Based on the diagram, at ~673 K (400 °C), the $LaFeO_3$

phase can already be obtained. Several reports suggest – based on X-ray diffraction (XRD) measurements – the formation of the orthorhombic $LaFeO_3$ phase with high crystallinity at calcination temperatures above ~350 °C.[31, 32] According to Figure 2b, an enrichment of La or Fe in the initial proportions of metal oxides and at temperatures below 1360 °C would lead mainly to the orthorhombic (below ~1000 °C) or rhombohedral $LaFeO_3$ phase plus La_2O_3 or FeO_x phases without the formation of other perovskite-type or perovskite-derived phases (e.g., layered Ruddlesden–Popper (RP) phases). From 1360 °C to 1390 °C and given an iron excess, the formation of the $LaFe_{12}O_{19}$ hexaferrite structure is possible, a phase that can only be stabilized at room temperature after a fast quenching.[33]

In the bulk stoichiometric $LaFeO_3$ phase, both La and Fe cations have an oxidation state of +3, with Fe^{3+} ions forming a high-spin configuration.[34] Similarly, the surface of $LaFeO_3$ nanoparticles is commonly composed of trivalent lanthanum and iron ions as identified by XPS studies.[35] Nevertheless, a reduction of the symmetry and coordination number of surface Fe ions has been previously identified with Mößbauer and EPR spectroscopy measurements.[36] The $LaFeO_3$ surface can be La (LaO)- or Fe (FeO_2)-terminated with non-polar (e.g., (1 2 1), (1 0 0))[37] or polar (0 1 0)[38] surfaces. Regarding the latter surface, density functional theory (DFT) calculations suggest that carbon monoxide is preferentially adsorbed in the Fe–CO mode with the carbon monoxide molecule acting as an electron donor.

2.3 $LaCoO_3$

The $LaCoO_3$ perovskite is a ferroelastic material with a rhombohedrally distorted (*R-3c* space group) structure at room temperature. At ~1337 °C, the perovskite suffers a transition to a cubic structural phase.[39] The temperature-dependent phase diagram of the La–Co–O system,[40] which is presented in Figure 3, suggests a higher number of stable phases than the ones found in the La–Fe–O system (Figure 2b).

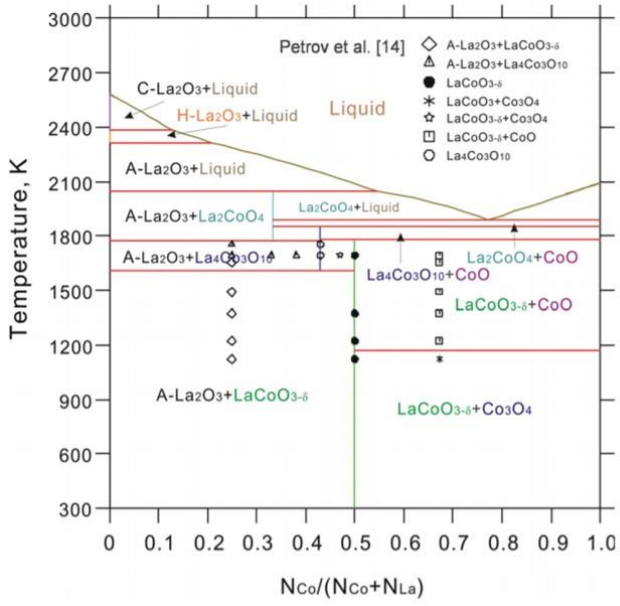

Figure 3. Temperature-dependent phase diagram of the La–Co–O system under an atmosphere of air.[40]

Below 927 °C, it is possible to form oxygen-defect $LaCoO_{3-\delta}$ structures and single oxides (e.g., La_2O_3 or Co_3O_4) if a surplus of La or Co is present in the system. At higher temperatures, layered Ruddlesden–Popper (RP – mixed oxide combining rock-salt and perovskite layers) oxides of the $La_{n+1}Co_nO_{3n+1}$ are formed as the orthorhombic $La_4Co_3O_{10+\delta}$ and $La_2CoO_{4+\delta}$ structures as confirmed by XRD measurements.[41, 42]

The formation of oxygen-deficient $LaCoO_{3-\delta}$ perovskite materials is of special interest for catalytic applications. The simultaneous existence of Co^{2+} and Co^{3+} in the perovskite structure enables the formation of anionic vacancies enabling oxygen-ion mobility in the structure.[43] Furthermore, the electronic structure of the perovskite is influenced by the spin-state of the 3*d* Co^{2+} and Co^{3+} cations: Co^{3+} can have a low-spin (LS) (t_{2g}^6), intermediate-spin (IS) ($t_{2g}^5e_g^1$) or high-spin (HS) ($t_{2g}^4e_g^2$) state, while Co^{2+} is thought to prefer the HS state.[44, 45] For catalytic oxidation of CO, parameters such as the occupancy of 3*d*-orbital together with the Co–O bond covalency in $LaCoO_3$-based perovskites have been used as important descriptors of the CO reaction rate.[46] For other relevant catalytic reactions as the oxygen evolution (OER) in electrochemical water-splitting, the 3*d*-electron occupancy of e_g orbitals has been correlated with the intrinsic activity of Co-based perovskites.[9] For catalytic applications, the Co^{2+}/Co^{3+} atomic ratio on the surface of the $LaCoO_3$ perovskite is also relevant. Co^{2+}/Co^{3+} values between ~0.3 and ~0.6 are normally encountered and depend on several parameters including the synthesis technique and post-treatments used.[47, 48] Given the high content of Co^{2+} on the surface of the non-stoichiometric $LaCoO_3$ perovskite, the formation of vacancies is energetically favorable making (110) O-terminated and (100)-OCoO-terminated surfaces possible.[49]

2.4 $LaMnO_3$

The $LaMnO_3$ perovskite is a material that has attracted attention since the beginning of the 1950s given its colossal magnetoresistance when it is doped with calcium or when pressure is applied.[19, 50] This perovskite is known for its structure polymorphism as several $LaMnO_3$ phases have been identified (e.g., rhombohedral, two orthorhombic, monoclinic and cubic).[51] The occurrence of a given $LaMnO_3$ phase is closely related to the applied temperature, the oxidation state of manganese, and the crystallite size. Considering the formation of the perovskite structure from single La and Mn oxides, La–Mn–O phase diagram[52] is presented in Figure 4a. Besides the perovskite structure, La_2O_3 and Mn_xO_y oxides are expected at temperatures below ~1400 °C when an excess of La or Mn is present. According to the phase-diagram, the perovskite structure is not only stable with stoichiometric La/Mn proportions, some non-stoichiometry of the cations is allowed. Accordingly, the $LaMnO_3$ perovskite structure is usually written as $La_{1-x}Mn_{1-y}O_{3\pm\delta}$. At a La/Mn = 1 ratio, the non-stoichiometry (δ), as in $LaMnO_{3+\delta}$, does not occur through an excess of oxygen in the lattice but through La and Mn cation vacancies. This is possible as the manganese ions can have two oxidation states in the perovskite structure, Mn^{3+} and Mn^{4+}. The content of Mn^{4+} ions in the structure together with the temperature influence the formation of a given polymorph[53] as it is presented in Figure 4b.

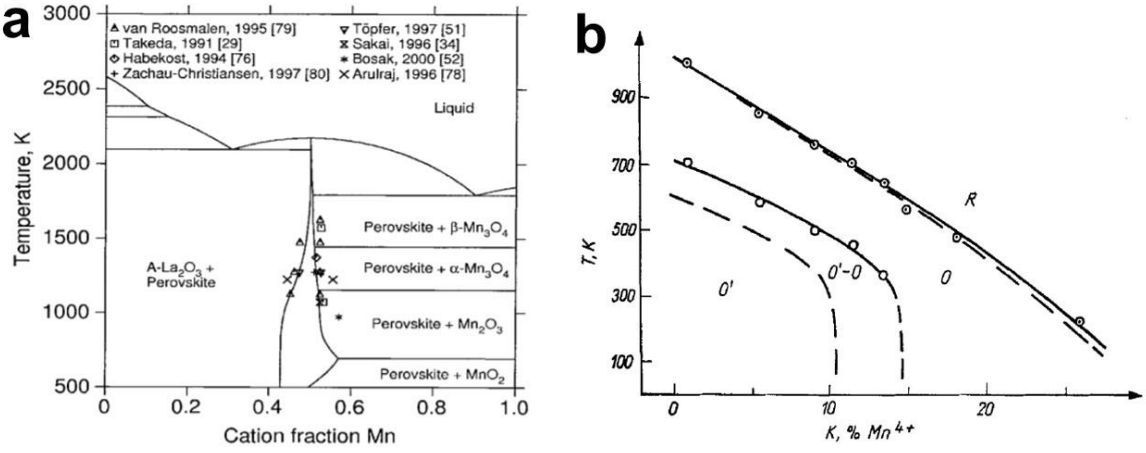

Figure 4. (a) Phase diagram of the La–Mn–O system under an atmosphere of air.[52] (b) Temperature- and Mn^{4+}-content-dependent phase transitions of the $LaMnO_{3+\delta}$ structure.[53]

For bulk crystals, at low temperatures and with a low content of Mn^{4+}, the $LaMnO_{3+\delta}$ structure is orthorhombically-distorted – usually identified as *O*' – counting with the *Pnma* space group. In the *O*' phase, the MnO_6 octahedron presents a Jan–Teller distortion (two shorter and four longer Mn–O bond lengths)[54] due to the presence of one electron in the degenerate e_g orbital of Mn^{3+} (electron-vacant *d*-shell with $t_{2g}^3 e_g^1$ configuration), which content is high in the phase.[53] The increase of temperature and the content of Mn^{+4} (from ~10 to ~15 % at 25 °C) causes the phase transition from the *O*' phase to another orthorhombic phase (identified as *O*) and an important volume contraction of the unit cell leading to its symmetrization. As it can be observed in Figure 4b, further increasing the temperature and the Mn^{4+} content (>23 % at 25 °C) cause the transition of the *O*-phase to the rhombohedral (*R*) phase in which the Jan–Teller distortions are not present.[53]

For nano-crystalline perovskites, it has been reported that the size of the crystallite also affects the stabilization of a given $LaMnO_{3+\delta}$ phase as studied in materials synthesized with the microwave-assisted glycothermal method with subsequent calcination at high temperatures.[55] In this case, the stabilization of the rhombohedral phase occurred for $LaMnO_{3+\delta}$ samples counting with crystallite sizes between ~20 and ~80 nm and a temperature-induced increase of the size led to a phase transition to the orthorhombic system. It is evident that the polymorphism of the $LaMnO_{3+\delta}$ structure is multiparametric and the synthesis techniques and post-treatments applied can play a big role on defining the conditions for a possible phase transition.

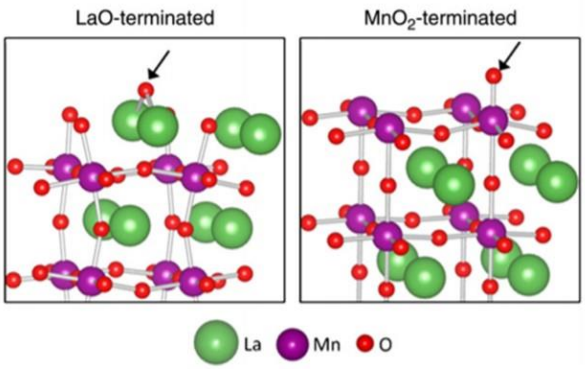

Figure 5. LaO- and MnO_2-terminated (0 0 1) $LaMnO_{3+\delta}$ surface with the arrow indicating an adsorbed oxygen atom.[56]

The formation of a given phase also affects the surface characteristics of this perovskite system. $LaMnO_{3+\delta}$ structures can be LaO- or MnO_2-terminated as presented in Figure 5 for (0 0 1) cubic $LaMnO_{3+\delta}$ facets.[56] Regarding the orthorhombic $LaMnO_{3+\delta}$ structure, the adsorption of CO molecules on the MnO_2-terminated (0 1 0) surface has been previously evaluated identifying the formation of the Mn-CO structure as the most favorable adsorption form of carbon monoxide.[57]

2.5 Catalytic CO oxidation

Based on the previously presented analysis of the structure and surface of the $LaBO_3$ (Fe, Co, Mn) perovskites, the use of these materials on the low-temperature catalytic CO oxidation is discussed in this section. Besides being an important probe reaction, CO oxidation is present in several applications that seek to remove or decrease the content of CO in, e.g., enclosed atmospheres as it is toxic for humans or in proton exchange membrane fuel cells (PEMFC) as CO deactivates the commonly used Pt-based catalysts.[8]

The oxidation of CO using perovskites as catalysts is usually explained with a suprafacial mechanism, i.e., only oxygen species from the surface of the catalyst is participating the oxidation reaction.[26] The oxidation of CO on $LaCoO_3$ has been proposed to proceed according to the following mechanism:

$$O_{2(g)} + 4e^- \rightarrow O^-_{2\,(ad)} + 3e^- \rightarrow 2O^{2-}_{(ad)} \quad (2.1)$$

$$CO_{(g)} \rightarrow CO_{(ad)} \quad (2.2)$$

$$CO_{(ad)} + 2O^-_{(ad)} \rightarrow CO^{2-}_{3\,(ad)} \quad (2.3)$$

$$CO^{2-}_{3\,(ad)} \rightarrow CO_{2\,(ad)} + O^{2-}_{(ad)} \rightarrow CO_{2(g)} + O^{2-}_{(ad)} \quad (2.4)$$

Initially, oxygen from the gas phase ($O_{2(g)}$) is adsorbed on the surface (e.g. on Co^{2+} ions) of the catalyst as molecular $O^-_{2\,(ad)}$ and then as atomic oxygen species ($O^{2-}_{(ad)}$) according to reaction (2.1). CO from the gas phase is also adsorbed on the surface (Reaction (2.2)) and $O^{2-}_{(ad)}$to form carbonates (Reaction (2.3)) which are then desorbed as gaseous $CO_{2(g)}$ leaving atomic oxygen species adsorbed on the surface of the catalyst (Reaction (2.4)). The latter reaction is considered to be the rate-limiting step of the mechanism.[27] A similar mechanism was proposed for the CO oxidation on the $La_{0.8}Ce_{0.2}MnO_3$ perovskite. When analyzing the mechanism, it becomes apparent that many parameters might play an important role in the catalytic CO conversion, e.g., the concentration of active oxygen species on the surface and the partial pressure of oxygen in the gas phase, the oxygen mobility and the reducibility of the cations (B)[58] which participate in the mechanism as a $B^{(n+1)+} \rightleftharpoons B^{n+}$ redox process.[8] Regarding the latter aspect, the reducibility of $LaFeO_3$, $LaCoO_3$ and $LaMnO_3$ perovskites synthesized by reactive grinding (RG) was evaluated[59] with hydrogen temperature-programmed reactions (H_2-TPR) as presented in Figure 6a. The complete reduction of Co^{3+} and Fe^{3+} to its respective metallic states was identified. In contrast, manganese cations were only reduced from Mn^{4+} to Mn^{2+}. Nonetheless, the $LaMnO_3$ perovskite presented the highest reducibility at temperatures lower than 500 °C, followed by $LaCoO_3$ and $LaFeO_3$ materials. Despite the lower reducibility of $LaCoO_3$, the catalytic CO performance of this perovskite is usually the best among the current studied cases ($LaFeO_3$, $LaMnO_3$) as presented in Figure 6b where the CO reaction rate is plotted in function of the number of electrons of the transition metal cations in $LaBO_3$-based perovskites.[60] The high catalytic activity of $LaCoO_3$ perovskites has been related to the preferential adsorption of CO on Co^{3+} sites and of molecular oxygen on Co^{2+} sites.[8]

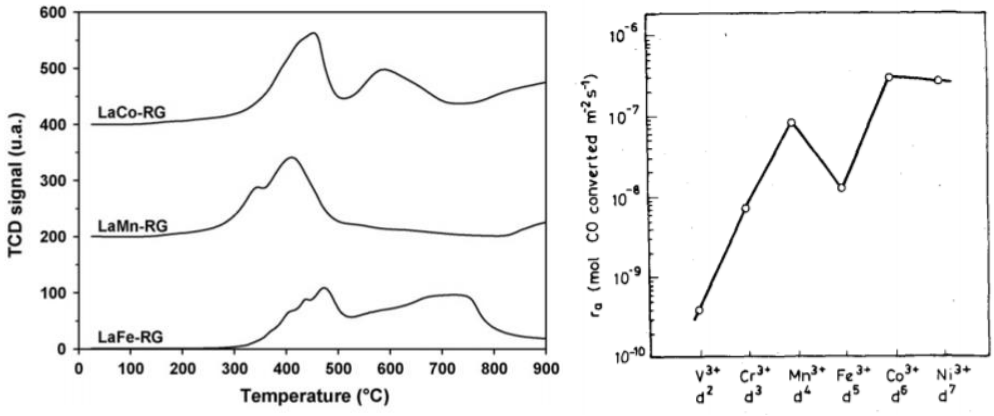

Figure 6. (a) H_2-temperature programmed reaction (TPR) of $LaCoO_3$, $LaMnO_3$ and $LaFeO_3$ perovskites.[59] (b) CO reaction rate in function of the number of electrons of the transition metal cations in $LaBO_3$-based perovskites.[60]

The BET specific surface area (SSA) and the porosity of the materials also influence the catalytic CO oxidation. Xiao et al studied bulk and porous $LaFeO_3$ perovskites counting with a BET of 4.3 and 20.6 m^2/g, respectively.[61] The porous material presented a superior reducibility and a higher amount of oxygen vacancies leading to a better catalytic activity than the bulk material. For a 50 % CO conversion, the porous perovskite required a temperature lower than 300 °C while the bulk perovskite required a temperature of ~425 °C to reach the same conversion.

Perovskite-type oxides have also been used to selectively oxidize CO in H_2-rich gas streams to avoid, e.g., the deactivation of Pt-based catalysts in proton exchange membrane fuel cells (PEMFC).[8, 62] In this case, besides the CO reaction to produce CO_2, additional reactions must be considered:

$$CO + 0.5O_2 \rightarrow CO_2 \quad (2.5)$$

$$H_2 + 0.5O_2 \rightarrow H_2O \quad (2.6)$$

$$CO + H_2O \leftrightarrow H_2 + CO_2 \quad (2.7)$$

$$CO + 3H_2 \rightarrow CH_4 + H_2O \quad (2.8)$$

$$CO_2 + 4H_2 \rightarrow CH_4 + 2H_2O \quad (2.9)$$

In the selective CO oxidation, it is desired to maximize reactions (2.5) and (2.7). Formation of methane from CO and H_2 (2.8) or from the water-gas shift reaction (WGSR) (2.9) should be minimized. $LaCoO_3$-based perovskites (e.g., $La_{1-x}Ce_xCoO_3$) have proven to display high activity for the selective CO oxidation as they present high content of active oxygen species and count with high reducibility. Furthermore, the addition of Ce in low amounts ($La_{0.95}Ce_{0.05}CoO_3$) has been identified as effective to limit methanation reactions (reactions (2.8) and (2.9)) and to increase low-temperature CO conversion when compared with undoped $LaCoO_3$ perovskite.[62]

In conclusion, $LaFeO_3$, $LaCoO_3$, and $LaMnO_3$ perovskites are active and interesting materials for CO oxidation, which is a reaction that helps understanding the requirements of these materials in order to count with high oxidation activities. Such requirements are not only based on phase purity. Perovskite materials with high specific surface areas, defined morphologies and porosities count usually with better activities. Synthesizing these materials with the required phase, size and specific surface area characteristics is not a simple task. In order to give an idea of the associated challenges, an evaluation of different synthesis approaches is presented in the following section.

2.6 Challenges related to the synthesis of perovskite materials

Instead of describing in detail the different synthesis methods available to produce perovskite-type oxides, the purpose of this section is to identify common challenges and most importantly, opportunities to improve the synthesis and the materials characteristics. There are several comprehensive reports regarding the synthesis of perovskite-type oxides.[8, 26, 63, 64] The solid-state synthesis considered as one of the oldest synthesis processes of perovskites. It is based on the mixture of solid metal-ion-containing precursors (e.g., carbonates or oxides) followed by high-temperature treatment and long calcination. The ceramic method is part of the solid–solid category for synthesizing perovskites. Other methods in this category include: microwave, combustion, hydrothermal, and mechanochemistry synthesis. Perovskites synthesized using solid–solid methods count generally with low BET specific surface areas (SSA) (< ~5 m^2/g). One exception is the mechanochemistry-derived method known as activated reactive synthesis (ARS) with BET SSAs up

to ~100 m^2/g.[8] This is a hybrid method with a calcination step of metal-ion-containing precursors until the desired perovskite phase is obtained, followed by high-energy ball-milling (HEBM) lasting typically about 2 h to produce nanocrystalline perovskites. This method has three main challenges: The use of milling media that contaminate the product, the amorphization of the materials, and the difficulty associated with obtaining particles with a defined morphology as it is presented in a SEM picture of a $LaFe_{0.8}Cu_{0.2}O_3$ perovskite[65] in Figure 7a.

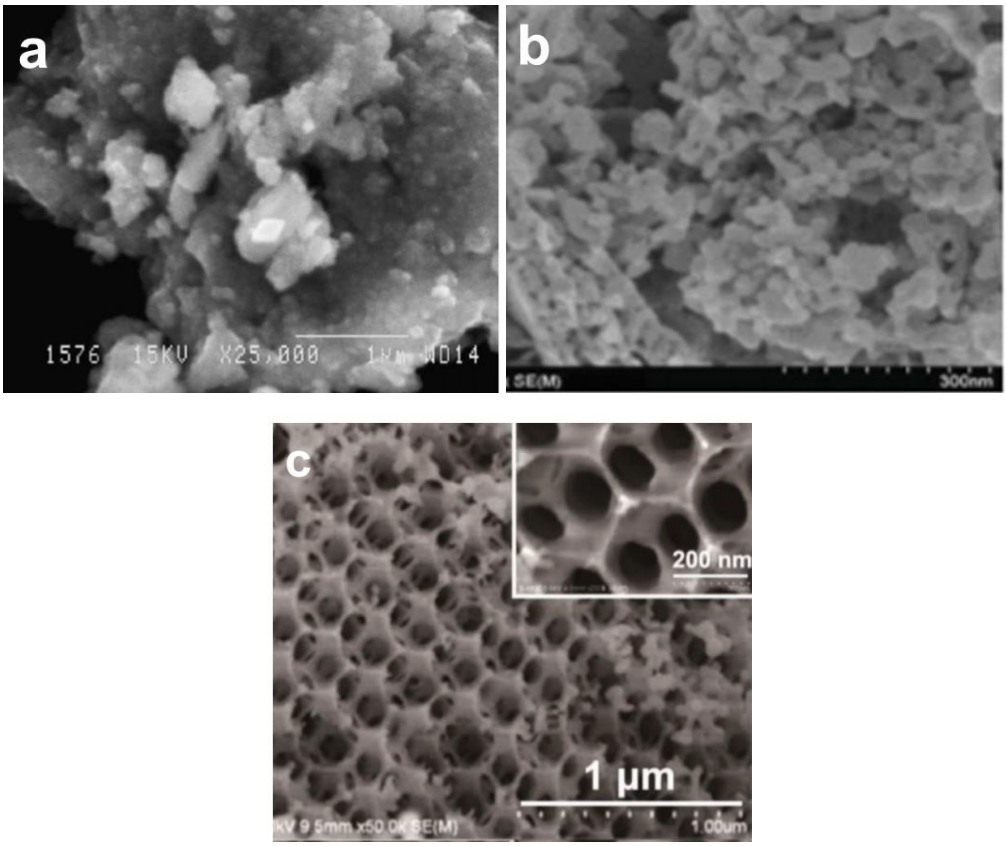

Figure 7. SEM images of $LaFeO_3$-based perovskite-type materials synthesized by the (a) ARS[65], (b) sol-gel[66] or (c) colloidal-crystal template method[67].

Another synthesis category of perovskites is liquid-based or solution-mediated. Some of the typical methods in this category are the well-known sol-gel, Pechini, hydrothermal and nonaqueous solvothermal methods. As an example, the sol-gel method is based on the formation of a colloidal suspension by adding, e.g., citric acid to an aqueous solution of metal precursors in a pH-controlled process in which a La-Fe-citric acid complex precursor gel is formed by concentrating the solution at mild temperatures. A subsequent calcination step at high-temperatures is required for eliminating the organic structures of the complex gel precursor, for forming oxide species and for obtaining crystalline perovskites with a pure-phase, leading to low BET SSAs and non-defined morphologies as it can be seen in Figure 7b taking a $LaFeO_3$ perovskite[66] as example. In the liquid-based synthesis category, the nanocasting methods are recognized for enabling the synthesis of high BET SSA perovskites. These methods – which advantages (features) and disadvantages (challenges) are presented in Figure 8 – include the soft-template, hard-template and colloidal-crystal template processes (e.g., TEM image of 3DOM $LaFeO_3$ perovskite[67] presented in Figure 7c). Mesoporous perovskites can be synthesized with the hard-template method that uses silica-based mesoporous materials (e.g., SBA-15, KIT-6) as templates. The templates are impregnated with a solution-containing metal precursor and chelating agents (e.g., citric acid) and are subsequently calcinated at high temperature.[11] In a final step, the SiO_2-based template is removed using a base solution

(e.g., NaOH). Even though this method also requires high temperature, the final materials usually show high BET SSAs, with a stable mesoporous structure. The problem associated with using template-based methods is that the complete removal of, e.g., silica is difficult. Additional challenges of nanocasting methods are related to low yields of materials and time-consuming steps.[63]

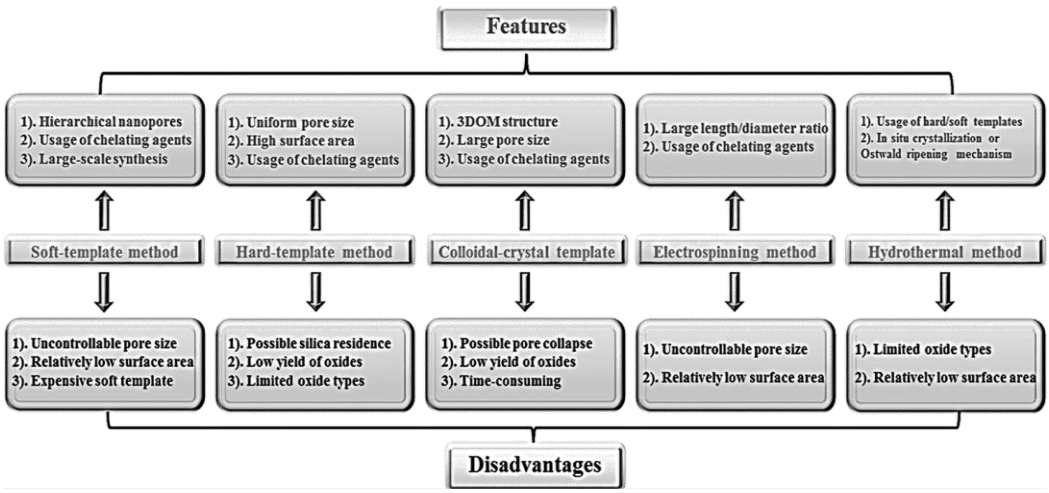

Figure 8. Features and challenges of different synthesis methods of porous perovskite-type oxides. [63]

Some conclusions can be drawn from the analysis of the different synthesis methods to produce perovskite-type oxides. The various perovskite synthesis methods obey specific application needs and these synthesis approaches can be adjusted to deliver materials with the desired characteristics. There are two common goals in the synthesis of perovskites: phase purity and high specific surface areas (SSA), especially for catalytic applications. As most of the methods require high-temperature calcination, phase purity is obtained at the expense of high SSAs. Nevertheless, there are multiple ways to circumvent this problem. The alternatives, which range from using mechanical steps (HEBM) after calcination to using nano-templates, are effective to provide perovskite materials with high SSAs. But as before, the improvement in SSA can be related to contaminations from, e.g., the milling media or the template material. However, these contaminations can be reduced to very low levels with careful optimization of the methods. Additional common challenges are related to low yields, the time required to obtain the perovskite materials and the scalability of the processes. In the process of finding techniques that can simultaneously tackle the identified challenges, the spray-flame synthesis – which was intentionally not discussed in this section – has been identified as a suitable candidate. As it is discussed in Chapter 3, the scalable spray-flame synthesis method has the potential to produce phase–pure, high-SSA perovskites without requiring additional high-temperature calcination and without using templates. This method, which is studied in this thesis for the synthesis of perovskites, has several associated challenges as the other techniques presented in this section. Some of the challenges of the spray-flame synthesis method include: (1) the development of the required technology (e.g., nozzle, burner, particle-collection systems); (2) the selection of precursors (e.g., organic-, inorganic-based) and solvents; (3) the understanding of the multiple reactions involved (e.g., in the liquid-phase, gas-phase, solid-phase and their interfaces/interactions); (4) the modelling/prediction and (5) the measurement of chemical species, molecular clusters, nanoparticle sizes and temperatures in the different phases. In the following chapter, these challenges will be explained with focus on the selection of metal precursors and solvents as possible ways to obtain pure-phase and high-BET $LaFeO_3$, $LaCoO_3$ and $LaMnO_3$ perovskites.

3 Spray-flame synthesis

3.1 Fundamentals

Early scientific reports of flame synthesis of metal oxide particles date back to 1959. For example, fumed alumina (Al_2O_3) particles were produced by supplying $AlCl_3$ vapor to a H_2/O_2 flame.[68] Similarly, Ulrich et al. (1971) synthesized fumed silica (SiO_2) through the combustion of $SiCl_4$ in a premixed flame.[69, 70] Over the years, the flame synthesis of metal oxides using gaseous/vapor metal precursors has been extensively investigated – an early state of the art from 1971 to 1996 was prepared by Pratsinis[71] – and nowadays, this method is used to commercially produce fumed single metal oxides as SiO_2 and Al_2O_3 by multinational chemical companies as Evonik, Cabot and Wacker.[72] Nevertheless, the use of gaseous/vapor precursors has been limited to the flame synthesis of single oxides. For the synthesis of mixed oxides (e.g., perovskites), the use of multiple vapor precursors – with different vapor pressures and reaction kinetics – poses an important limitation in order to obtain phase-pure mixed materials.[12]

In 1963, Nielsen et al.[73] prepared aqueous solutions of $AlCl_3$ and other metal salts and sprayed them in a natural gas/O_2 flame, laying the foundations for the spray-flame synthesis. Many non-volatile and affordable metal precursors (e.g., metal-inorganic, metal-organic or organometallic compounds) can be dissolved with the desired stoichiometry – in case mixed oxides/compounds are required – in combustible liquids (e.g., alcohols or carboxylic acids) to form precursor solutions that can be directly used in the spray-flame synthesis process, allowing to reach the formation of nanocrystalline (mixed) metal oxides and overcoming the challenge posed by the vapor-based flame synthesis. Great reviews have been prepared outlining the main characteristics and findings of the spray-flame process and the related materials that have been synthesized and investigated over the years.[12, 74-79]

The spray-flame synthesis process requires the use of a burner with an integrated nozzle to finely atomize the precursor solutions. The burner design has evolved over the years and currently, the SPP 1980 project (for more information on this DFG-funded priority program, visit: https://www.uni-due.de/spp1980/) is leading an effort to have a standardized burner known as the *SpraySyn* burner – described in detail by Schneider et al.[80] This is being done as a way to foster the scientific cooperation and developments and to have a common ground to link experiments with simulations.[77] In order to describe the spray-flame synthesis experiment, a schematic is presented in Figure 9a. In the spray-flame process, the liquid flow (e.g., solution of metal precursors) is supplied to a stainless-steel capillary – via a syringe pump – which is located at the center of a two-fluid external mixing nozzle. The capillary is surrounded by a low-transversal-area annular aperture through which the dispersion gas (O_2) is supplied at high velocity and put in contact with the solution of precursors, causing the fine atomization of the liquid through shear forces. In order to form the spray-flame – a picture is presented in Figure 9c – the spray flame is supported by a CH_4/O_2 premixed pilot flat flame, which is stabilized on a sintered bronze plate. The flame is shielded against the environment by a surrounding co-axial flow of air. The details about the dimensions of the burner and the parameters (e.g., composition/concentration of solutions of precursors, flow of liquid and gases, pressure) used in the different experiments performed and discussed in this thesis can be found in Chapters 4.2.1, 5.2.1, and 6.2.1.

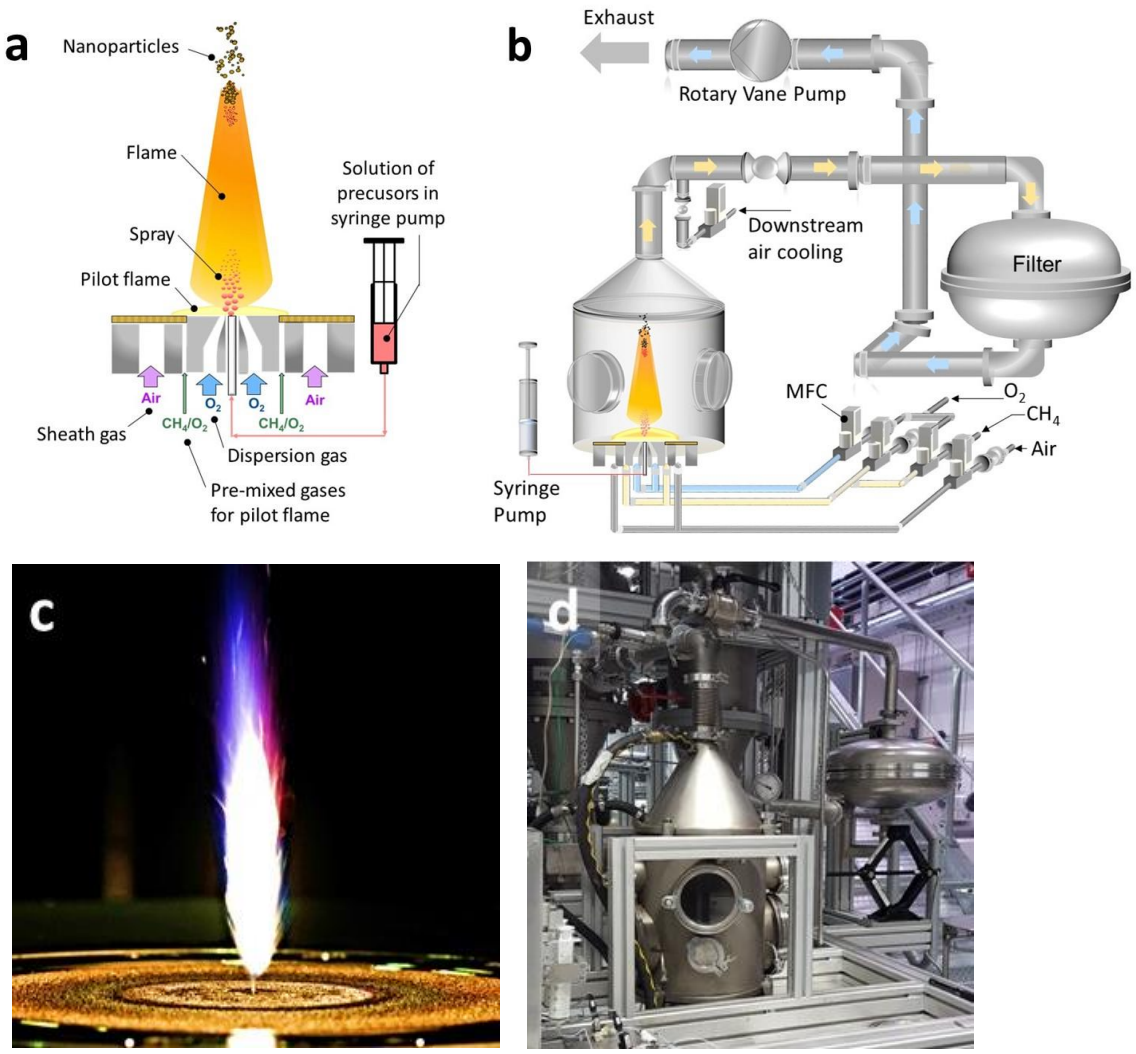

Figure 9. (a) Schematics of the spray-flame synthesis burner. (b) Diagram of the spray-flame reactor. (c) Photo of a spray-flame of a mixture of ethanol and 2-ethylhexanoic acid. (d) Photo of the spray-flame synthesis reactor.

In order to regulate the reactor pressure via a rotary vane pump and to avoid the presence of nanoparticles in the laboratory atmosphere, the spray-flame is enclosed in a reactor chamber as presented in Figure 9b and d. Downstream of the reactor chamber, the temperature of the flow of gases/particles is controlled using an indirect cooling water system – the hollow truncated cone on top of the reactor chamber – and direct mixing with compressed air, which also acts as a quenching gas to reduce the sintering of the particles. The powder is collected in a polymer-coated filter fabric.

The process of particle formation and growth in the spray-flame involves multiple phases of reactive fluids (gas, liquid, solid). The reactions involved in the process are complex and can occur homogeneously or heterogeneously. The understanding of the formation of nanoparticles in the flame has importantly advanced over the last decades with the development of (1) shock-tube studies to understand the reactions kinetics; (2) molecular-beam sampling coupled with particle-mass spectrometers to track the formation of clusters of species and particles and their growth directly in the flame and (3) with laser-based diagnostics (e.g., laser-induced fluorescence or incandescence) to measure temperatures and particle concentrations and sizes.[77, 81-84] Based on the use of simple and volatile precursors[77] as SiH_4 or $Fe(CO)_5$, a series of general steps have been identified in the formation of particles in the flame. First, the precursor is quickly evaporated and decomposed in the high-temperature flame forming radicals, intermediates and

molecules[81]. The first molecular clusters can be formed by collision- or by evaporation-condensation-controlled nucleation of gas-phase species.[85] Based on their stability and given that the clusters reach a critical size, the particle formation process can proceed. The clusters grow by homogeneous or heterogeneous processes (e.g., the addition of monomers to the cluster surface) with a subsequent fast coalescence leading to solid particles that are typically spherical. Further collision, coagulation and coalescence processes cause the formation of soft agglomerates – particles connected by van-der-Waals forces – and hard agglomerates (aggregates). The latter coming from the sintering process of the contacts of the particles.[86] The previously described mechanism is usually known as gas-to-particle conversion and is associated with the flame synthesis of crystalline, small and monomodal nanoparticles.[76, 87] This type of particle formation is also a characteristic result of using gaseous or volatile metal precursors as halides. On the contrary, in the spray-flame synthesis of metal oxides using solutions of non-volatile precursors, an alternative conversion route has been identified and usually named as droplet-to-particle conversion.[76] A scheme of the particle formation processes[88] including this conversion route is presented in Figure 10.

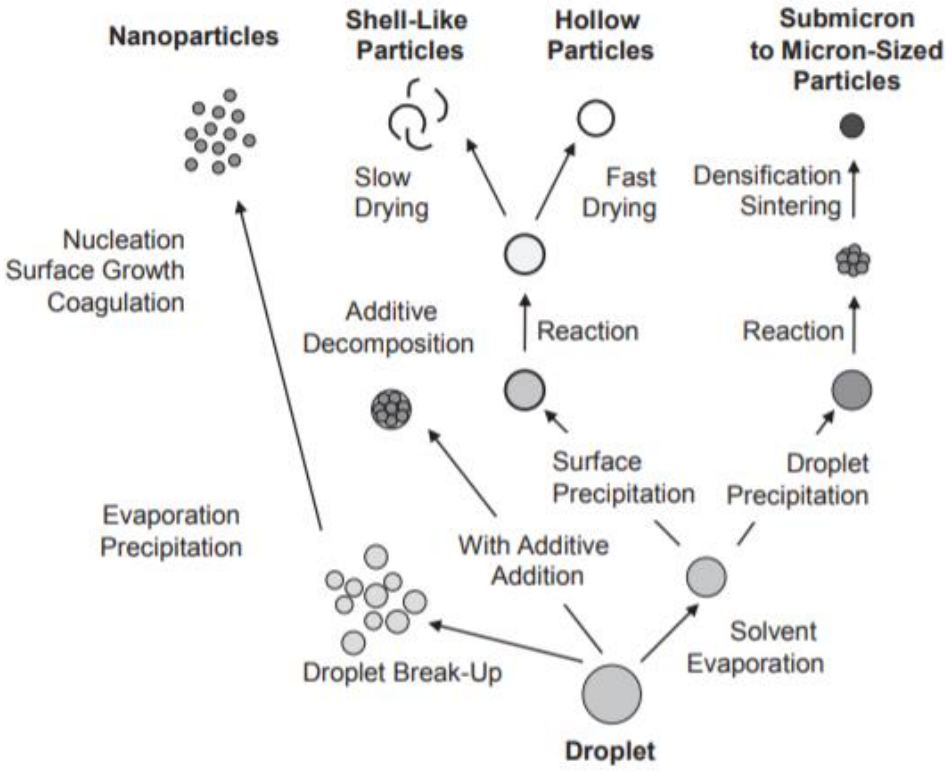

Figure 10. Schematic of the spray-flame synthesis of particles starting from droplets.[88]

The droplet-to-particle conversion leads to typically non-desired, shell-like, hollow and/or micron-size solid particles through different processes involving the surface/droplet precipitation, drying, densification and sintering. Nevertheless, the droplet-to-particle conversion and in general, the formation of particles using solutions of complex precursors is not understood in detail yet. The use of different combinations of metal precursors (e.g., metal nitrates) with single solvents (e.g., ethanol) has been linked to the mixed formation of particles through the gas-to-particle and the droplet-to-particle conversions, leading to the selection of organic-based metal precursors when the droplet-to-particle conversion needs to be avoided in a research-scale experiment.[17] Nevertheless, metal nitrates are usually the low-cost option[12, 89] and thus the selected precursors for an economic flame synthesis of particles. Thus, the understanding of this type of precursors and the design of nitrate-based solutions which promote the gas-to-particle

formation of nanoparticles is a current and interesting topic of research in the spray-flame synthesis community. Jossen et al.[90]proposed different criteria – involving the use of combustion enthalpies and boiling points of solvents, and melting/decomposition points of metal nitrates – to try to explain the formation of inhomogeneous or homogeneous particles in the spray-flame process. The authors analyzed the synthesis of Bi_2O_3 (among other materials) using bismuth nitrate as precursor and considering different liquids (methanol, ethanol, methoxy-2-propanol, ethoxy-ethanol, propylene glycol propylether, and diethylene glycol-monoethylether) mixed with a water-based HNO_3 solution (15 Vol. %) as solvents. Both homogeneous (i.e., solid nanoparticles) and inhomogeneous (i.e., mixture of hollow/solid large particles and solid small nanoparticles) Bi_2O_3 samples were reported. For each synthesized material and based on the combustion enthalpy of the given solvent, the total volumetric flow rate of each solution supplied to the reactor, and the volumetric flow rate of the dispersion gas, the authors proposed a parameter – the combustion enthalpy density (kJ/g_{gas}) – and correlated it to the observed formation of homogeneous or inhomogeneous Bi_2O_3 particles. This parameter was defined as the ratio of the liquid-fed combustion enthalpy (kJ/min) over the total gas flow rate through the nozzle (g_{gas}/min). By changing the volumetric flow rate of the precursor solution, the authors explored three values – 2.2, 4, and 4.7 kJ/g_{gas} – of the combustion enthalpy density to synthesize Bi_2O_3 using each of the mentioned alcohols/glycol ethers as solvent. It was proposed that a value ≥ 4.7 kJ/g_{gas} was effective to generate solid and homogeneous Bi_2O_3 nanoparticles. Towards the same goal, the authors also proposed that the ratio of the boiling point (T_{bp}) of the solvent(s) over the decomposition/melting point ($T_{d/mp}$) of the metal precursor should be ≥ 1.05 to prevent the formation of large or hollow particles. This means (assuming an ideal solution where the boiling point is not influenced by the solute), the formation of a solid precursor precipitate is prevented when the liquid evaporates as the remaining precursor either decomposes or remains liquid at the respective temperature. Even though this descriptors or criteria have been broadly used and adopted [79, 91-95], they do not take into account many relevant aspects of the spray-flame synthesis which are presented as follows:

- The different alcohols/glycol ether mixtures used are considered solely as energy sources, the solubility/chemistry of bismuth nitrate in each solvent and the chemical effect of the water-based HNO_3 solution were not considered. For example, it is known that bismuth nitrate readily hydrolyses in water to form oxy- and hydroxy-nitrate precipitates.[96] Additionally, bismuth nitrate is insoluble in pure ethanol. As the addition of HNO_3 helps stabilizing water-based solutions of bismuth nitrate, a similar effect is most likely occurring in methanol- and ethanol-based solutions. In contrast, bismuth nitrate is expected to be stable in solutions of glycol ethers (methoxy-2-propanol, ethoxy-ethanol, propylene glycol propylether, and diethylene glycol-monoethylether) by most likely forming bismuth alkoxides.[97] For combustion enthalpy densities of 2 and 4 kJ/g_{gas}, Jossen et al.[90] reported that the Bi_2O_3 particles synthesized using methanol and ethanol as solvents were inhomogeneous while those samples synthesized using glycol ethers were homogeneous. This was attributed to the comparatively higher boiling points of the glycol ethers in comparison to those of methanol and ethanol. Nevertheless, the formation of large Bi_2O_3 particles from the droplet-to-particle mechanism is – as explained before – highly dependent on the chemical stability of the precursor solution even at room temperature. The boiling point of the solvent is relevant for many other phenomena but it is most likely not – when considered out of chemical context – a parameter to evaluate/predict the formation of homogeneous/inhomogeneous particles.
- Jossen et al.[90] reported that the increase of the combustion enthalpy density from 4 to 4.7 kJ/g_{gas} was effective to produce homogeneous Bi_2O_3 using methanol or ethanol as solvent. Nevertheless,

the classification of Bi_2O_3 as homogeneous was based on the assumption that the XRD diffractogram of the ethanol-synthesized sample at 4.7 kJ/g_{gas} did not present a bimodal character in comparison with the sample synthesized at 2 kJ/g_{gas} (the sample synthesized at 4 kJ/g_{gas} was not included in the analysis) which presented a pronounced broadening of the bottom of the peaks. In contrary, this might be an indication of a higher content and size of large particles in the Bi_2O_3 sample synthesized at 4.7 kJ/g_{gas} based on the higher intensity of the diffraction peaks of this sample in comparison with the sample synthesized at 2 kJ/g_{gas}. Furthermore, the increase of the BET-derived particle size from 17 nm (4 kJ/g_{gas}) to 23 nm (4.7 kJ/g_{gas}) was explained based on the increase of the flame height (higher residence time and sintering of particles in the flame). Nevertheless, the effect of large particles on the BET specific surface area and derived particle size was not considered. Large particles have an important influence on BET results and their decrease or absence should most likely hint to a decrease of the BET-derived particle size of the samples synthesized at 4.7 kJ/g_{gas}, which was not the case.

- For each solvent analyzed, the variation of the combustion enthalpy density from 2 to 4.7 kJ/g_{gas} was done by increasing the volumetric flow rate of each precursor solution while maintaining the dispersion gas flow rate constant. In other words, the fuel/oxygen equivalence ratio was modified. This indicates a variation of the oxidation/reduction conditions of the flame and its temperature profiles. Furthermore, the increase of the volumetric flow rate of the precursor solution is most likely related with the variation of the droplet size distribution, leading to larger droplet sizes at high solution flow rates which might lead to larger particle sizes from the droplet-to-particle mechanism and a delayed evaporation of the precursor droplets and thus a different temperature history for the product on its path through the flame.
- Regarding the ratio of the boiling point (T_{bp}) of the solvent(s) over the decomposition/melting point ($T_{d/mp}$) of the metal precursor as proposed by Jossen et al.[90], the first point to consider is the melting point of the metal precursor. While the concept of the melting point can be applied for solids (e.g., $Bi(NO_3)_3 \cdot 5H_2O$), it is not applicable for solutions (e.g., bismuth nitrate dissolved in water) as they already are in a liquid physical state. Upon dissolution of a metal precursor in a given solvent, multiple reactions take place (e.g., ligand-exchange, formation of (oxy)hydroxides or complexes) even at room temperature, indicating as well that the melting point of the original metal precursor does not necessarily provide information relevant for the particle formation from the droplet-to-particle mechanism.

  The second point is related to the difference between melting point and decomposition point of metal precursors. Jossen et al.[90] used both terms interchangeably. The decomposition of a metal precursor (e.g., metal nitrate) occurs over a temperature range and depends on the atmosphere used (e.g., N_2, air, O_2). Depending on the metal nitrate, decomposition temperatures can range from ~140 to ~870°C.[98] If the $T_{bp}/T_{d/mp}$ values presented in Figure 11 are corrected by the decomposition temperatures of the metal nitrates, the $T_{bp}/T_{d/mp}$ ratios would be considerably lower than 1.05.

  Considering only metal nitrates as precursors, Jossen et al.[90] extended the discussion of the $T_{bp}/T_{d/mp}$ ratios including the results published by Tani et al.[99] regarding the spray-flame synthesis of CeO_2, ZnO, MgO, Al_2O_3, Fe_2O_3, and Y_2O_3. All these materials were synthesized using the corresponding metal nitrate dissolved in a mixture of water/kerosene/hexa(2-hydroxy-1,3-propylene glycol) in a 65/35/2 ratio, generating an emulsion of a hydrolyzed precursor. All synthesized oxides were identified as inhomogeneous as it can be observed in Figure 11 correlating the results with the $T_{bp}/T_{d/mp}$ ratios using the boiling point of water as reference and the melting point of each

metal nitrate. The use of such hydrolyzed-precursor-based solutions would probably lead to inhomogeneous/large/hollow particles in the spray-flame through the precipitation of oxy-hydroxide species in the liquid phase. In this case and as presented before, the use of the melting point of metal nitrates does not make sense due to the different physical state and chemical composition of each solution. Furthermore, if the value of the boiling points of kerosene and hexa(2-hydroxy-1,3-propylene glycol) are taken into account to calculate the $T_{bp}/T_{d/mp}$ ratios, the values would be much greater than 1. And similarly, if the real decomposition temperatures of the metal nitrates are considered, the $T_{bp}/T_{d/mp}$ ratios would be considerably lower.

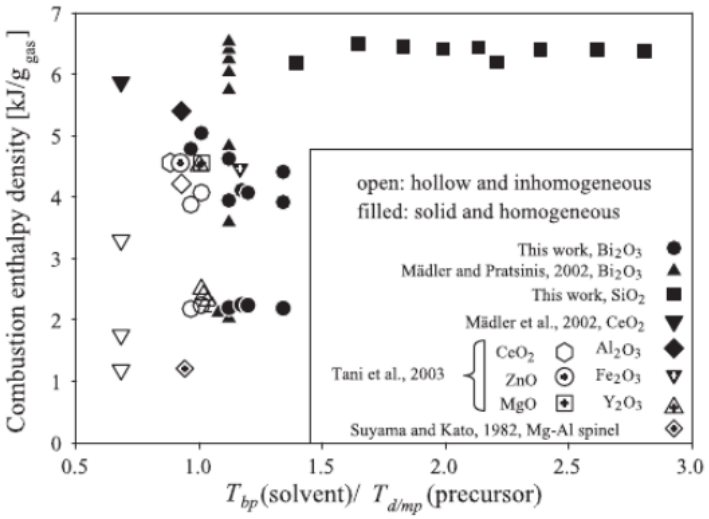

Figure 11. Combustion enthalpy density and $T_{bp}/T_{d/mp}$ ratio as criteria to identify the formation of inhomogeneous or homogeneous spray-flame synthesized metal oxides.[90]

Based on the previous points, it is concluded that parameters as the combustion enthalpy density and the $T_{bp}/T_{d/mp}$ ratio do not take into account the physical and chemical complexity of the spray-flame process in order to be used as universal criteria to predict the formation of homogeneous or inhomogeneous particles from the spray-flame synthesis. Instead, an extended analysis should be carried out involving, e.g., the precursor solution chemistry, the precursor decomposition, the flame characteristics (e.g., temperature, residence time), and the evaporation of oxides. Congruently, these aspects are analyzed in Chapter 3.2 for the spray-flame synthesis of different metal oxides. The discussion is focused on the use of metal nitrates as precursors – which fundamental chemical/physical aspects are presented in Chapter 3.2.1 – using ethanol (Chapter 3.2.2) or a mixture of ethanol and 2-ethylhexanoic acid (Chapter 3.2.3) as solvent for the synthesis of the different materials.

3.2 Metal nitrates as precursors for the spray-flame synthesis of single oxides

3.2.1 Chemistry and decomposition of metal nitrates

Hydrated metal nitrates have the general $M(NO_3)_x{\cdot}nH_2O$ form (e.g., $La(NO_3)_3{\cdot}nH_2O$, $Fe(NO_3)_3{\cdot}9H_2O$, $Co(NO_3)_2{\cdot}6H_2O$, $Mn(NO_3)_2{\cdot}4H_2O$), with x being the oxidation state of the metal ion and n being the number of crystallization water molecules.[100] The NO_3^- ion shares geometric similarities with the planar BO_3^- and CO_3^- ions and its structure can be explained – based on valance bond theory with three canonical forms (I, II, III)[101] as presented in Figure 12.

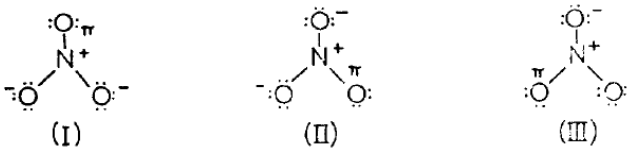

Figure 12. Canonical forms of the nitrate ion.[101]

The decomposition of hydrated metal nitrates is influenced by the gas atmosphere (e.g., air, H_2, N_2) – reducing or oxidizing conditions – at which it is done. Furthermore, metal nitrates count with a broad range of decomposition temperatures depending on the electronic interactions between the metal cation and the nitrate ion.[98, 102] Thermogravimetric analyses (TGA) of the decomposition of several metal nitrates under air is presented in Figure 13.

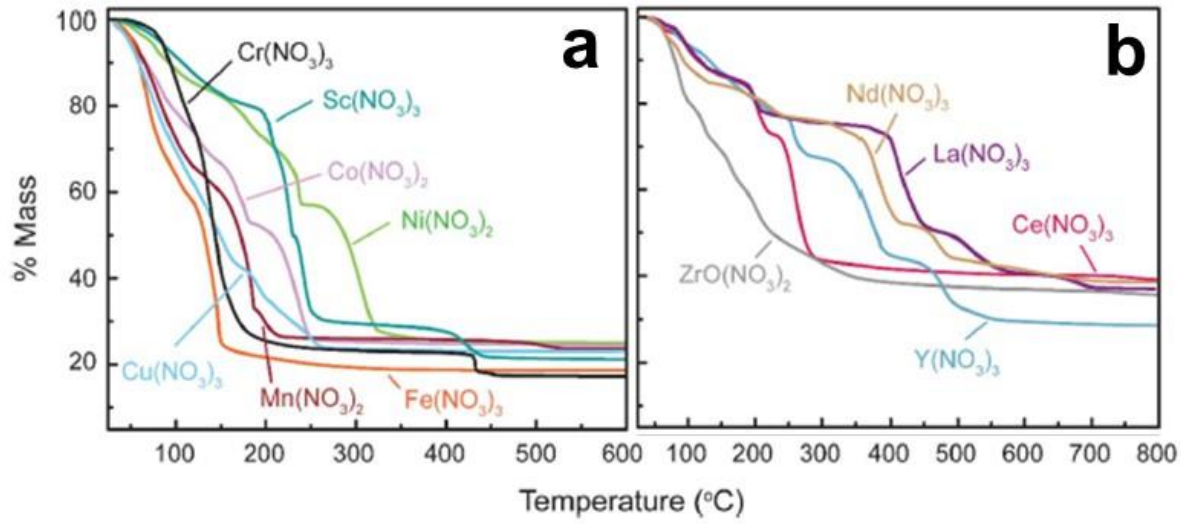

Figure 13. Thermogravimetric analysis (TGA) of the decomposition of metal nitrates under air. (a) Transition-metal nitrates. (b) Rare-earth nitrates. Adapted from Cochran et al.[102]

Most of the hydrated metal nitrates melt (formation of a highly concentrated solution of the metal nitrate using released hydration water as solvent) at low temperatures (<75 °C). The decomposition of the metal nitrates involves several steps and different reactions starting with the formation of $M(OH)_x(NO_3)_y(H_2O)_z$, HNO_3 and H_2O species until a temperature of 120 °C is reached. Higher temperatures – in the 200 to 500 °C regions of Figure 13a and Figure 13b – cause the formation of metal hydroxides, NO_x, O_2, and H_2O. The formation of metal oxides proceeds through the decomposition of the formed metal hydroxides and the release of water.[102] The decomposition temperature (T_d) – defined by Cochran et al.[102] as the temperature at which the initial metal nitrate compounds have lost 75 % of their mass – is related to the charge density of the metal cations. As presented in Figure 14, cations with high charge density – which can be understood as cations with high attraction of the nitrate ion electron density – count with low decomposition temperatures and vice versa. Additionally, metal cations with large ionic radii have low charge densities and thus, high decomposition temperatures. Congruently, lanthanum nitrate[102] has a T_d of ~440 °C, while iron, cobalt and manganese nitrates have decomposition temperatures of 140, 220, and 180 °C, respectively.

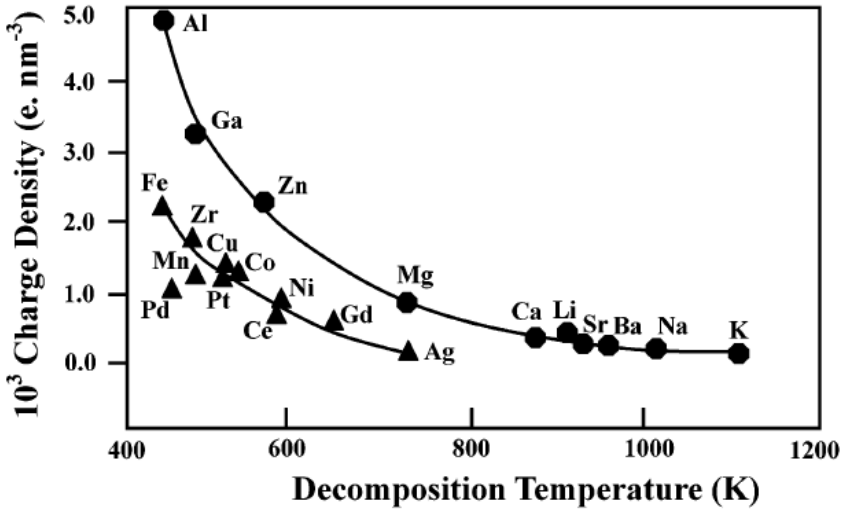

Figure 14. Charge density and decomposition temperature of metal nitrates.[98]

Metal nitrates are soluble in water and in polar organic solvents such as ethanol. The dissolution of metal nitrates in water is accompanied with multiple reactions and diverse speciation. The metal cations interact with the lone electron pairs of oxygen in water molecules. A high attraction between the metal cations and the oxygen from water would create positive-charged hydrogen species and would lead to a hydrolysis reaction and to metal cation acidity.[102] The deprotonation hydrolysis reaction[103] proceeds according to reaction (3.1).

$$[\mathrm{M(OH_2)_N}]^{z+} + \mathrm{hH_2O} \rightarrow [\mathrm{M(OH)_h(OH_2)_{N-h}}]^{(z-h)+} + \mathrm{hH_3O^+} \quad (3.1)$$

$$\mathrm{M^{z+}} + \mathrm{nH_2O} \rightarrow \mathrm{M^{z+}(aq)} \quad (3.2)$$

$$[\mathrm{M(OH_2)_N}]^{z+} + \mathrm{NO_3^-} \rightarrow [\mathrm{M(NO_3)(OH_2)_{N-1}}]^{(z-1)+} + \mathrm{H_2O} \quad (3.3)$$

Hydroxylated precursors as the $[\mathrm{M(OH)_h(OH_2)_{N-h}}]^{(z-h)+}$ species from the hydrolysis reaction lead to the condensation (precipitation) of metal ions through olation (e.g., formation of M–OH–M structures) – which is the dominant mechanism for low-valence (+2,+3) metal cations – or oxolation (e.g., formation of M–O–M structures). The speciation of metal cations in water is pH-, concentration-, and temperature-dependent. The speciation of aluminum (Al^{3+}) and iron (Fe^{3+}) are presented in Figure 15 as Pourbaix diagrams in order to analyze the dominant species at equilibrium conditions based on concentration and pH.

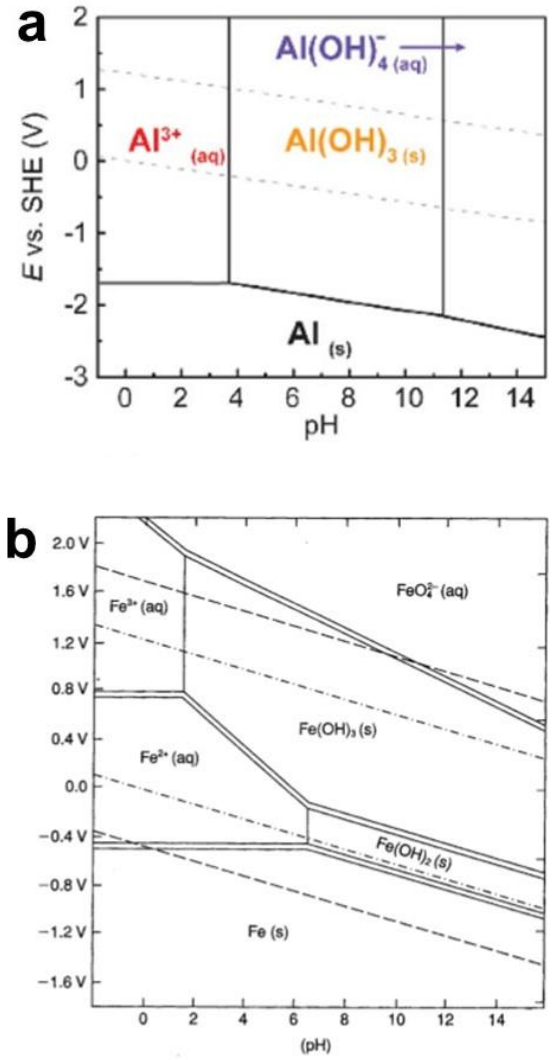

Figure 15. Pourbaix diagrams depicting the speciation of (a) aluminum (Al^{3+})[102] at 0.1 mol/l and 25 °C and (b) iron (Fe^{3+})[104] at 1 mol/l and 25 °C under different potentials and pH values.

Al^{3+} cations are stable in the aqueous form at pH below ~4. Above this pH, solid aluminum hydroxide species form. For Fe^{3+} cations and according to Figure 15b, a pH above ~2 is already sufficient to cause the fast formation of low-molecular-weight hydrolysis products as $Fe(OH)^{2+}$, $Fe(OH)_2^{+,}$ and $Fe_2(OH)_2^{4+}$, which are the precursors for solid species. Nevertheless, instead of precipitating as a hydroxide as indicated in Figure 15b, iron tends to form amorphous solid oxy-hydroxide compounds (e.g., $MO(OH)(OH_2)$). When considering the effect of the nitrate ions in aqueous solutions, the formation of metal nitrate complexes depends on the type of metal cation in solution and as presented by Cochran et al.[102], it can be analyzed with two parameters: The free energy of hydration (ΔG_{hyd}) in the reaction presented in reaction (3.2) and the water-exchange rate constant (k_{H2O}) taking the reaction presented in reaction (3.3) as reference. For different metal cations, the free energy of hydration and the water-exchange rate constant at 25 °C are presented in terms of the cation ion radius in Figure 16a and in Figure 16b, respectively.

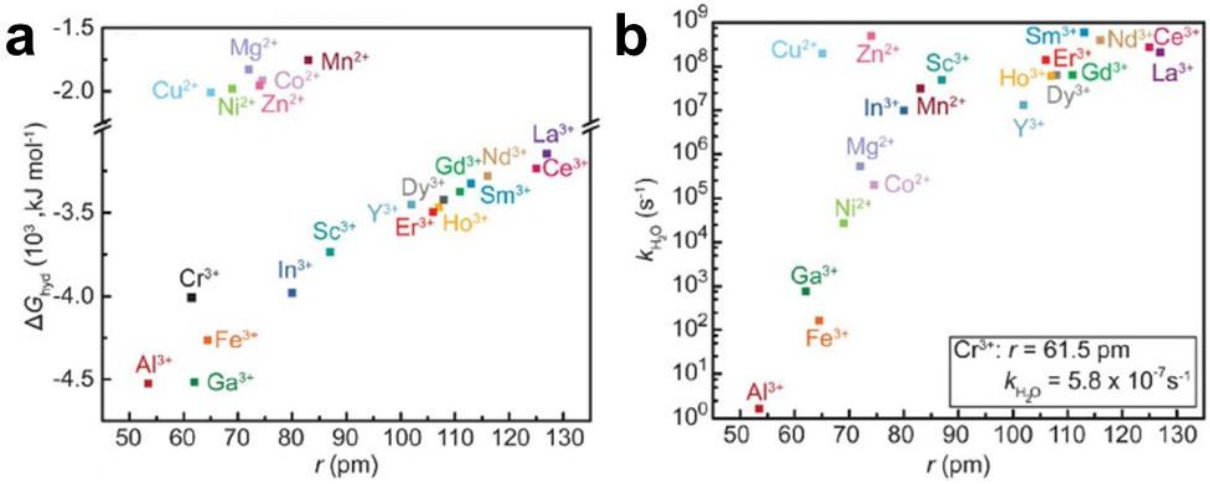

Figure 16. (a) Free enthalpy of hydration and (b) water-exchange rate constant at 25 °C for different metal cations coming from nitrates in water in function of the ionic radius (r). Adapted from Cochran et al.[102]

The stability of hydrated metal cations can be evaluated with the free energy of hydration. Metal ions as Al^{3+}, Ga^{3+} and Fe^{3+} form very stable hydrated complexes (low ΔG_{hyd}) while metal cations such as Zn^{2+}, Mg^{2+}, Mn^{2+}, Co^{2+} and La^{3+} do not present the formation of such stable hydrated complexes. Additionally, the water-exchange rate constant is helpful to analyze how fast water molecules from the inner coordination sphere of the metal cation can be exchange by nitrate ions in order to form metal-nitrate complexes. Congruently, metal cations as Al^{+3} and Fe^{3+} have a low exchange and other cations like Zn^{2+}, La^{3+} and Mn^{2+} have a high exchange rate, happening in a matter of seconds. Putting the two parameters together, metal cations with low ΔG_{hyd} and low k_{H2O} are expected to be especially prone to hydrolysis. This is relevant for the design of nitrate-based solutions for the spray-flame synthesis of metal oxides as hydrolysis reactions might induce the early formation of solid species acting as seed for the precipitation of compounds in the droplets promoting the non-desired droplet-to-particle conversion (Figure 10). However, the effect of organic solvents as ethanol on the hydrolysis of metal cations has not been studied in detail yet. Ho et al.[105] studied the effect of adding ethanol (21.2 Wt.% and 44.4 Wt.%) to water-based solutions of nickel nitrate on the hydrolysis of the nickel cations. Interestingly, the addition of ethanol increases the formation rate of species as $Ni_4(OH)_4^{4+}$. Additionally, the effect of the temperature of the solution was also evaluated. Compared to 25 °C, a temperature of 75 °C increases 10^6 times the formation constant of $Ni_4(OH)_4^{4+}$ in an aqueous solution. The temperature of the solution is also an important parameter in the spray-flame synthesis as the temperature of the droplets would increase from the initial temperature of supplying to the boiling point of the solvent or mixture of solvents until they are completely evaporated.

An approximation to the direct observation of hydrated metal cations in the gas-phase has been possible through techniques like the electrospray ionization mass spectroscopy (ESI-MS), which is identified as a method that enables the transfer of ionic species from a solution to the gas phase.[106] Important advantages and drawbacks of the method have been identified by Di Marco et al.[107] One example to consider is the ESI under mild conditions of aqueous solutions of cobalt nitrate performed by Schröder et al.[106] identifying $[Co(H_2O)_n]^{2+}$, $[Co(NO_3)(H_2O)_n]^{+}$ and $[Co(OH)(H_2O)_n]^{+}$ species as hydrolysis products. ESI-MS might be considered for future studies in order to link the hydrolysis reaction in the liquid phase with the gas phase.

3.2.2 Spray-flame synthesis of single oxides using metal nitrates as precursors and ethanol as solvent

When using nitrates as metal precursors for the spray-flame synthesis of single oxides, ethanol is the typical choice to prepare the solutions of precursors. The high solubility of the metal nitrates in ethanol and its low cost are the main reasons behind. But the use of solutions of metal nitrates in ethanol is associated with the mixed formation of large particles – from the droplet-to-particle conversion – and small particles – from the gas-to-particle conversion – in the spray-flame synthesis of metal oxides. The contribution of the droplet-to-particle conversion is usually high, leading to oxides with low BET SSAs. Some examples of TEM images displaying the final particles from single metal oxides are presented in Figure 17.

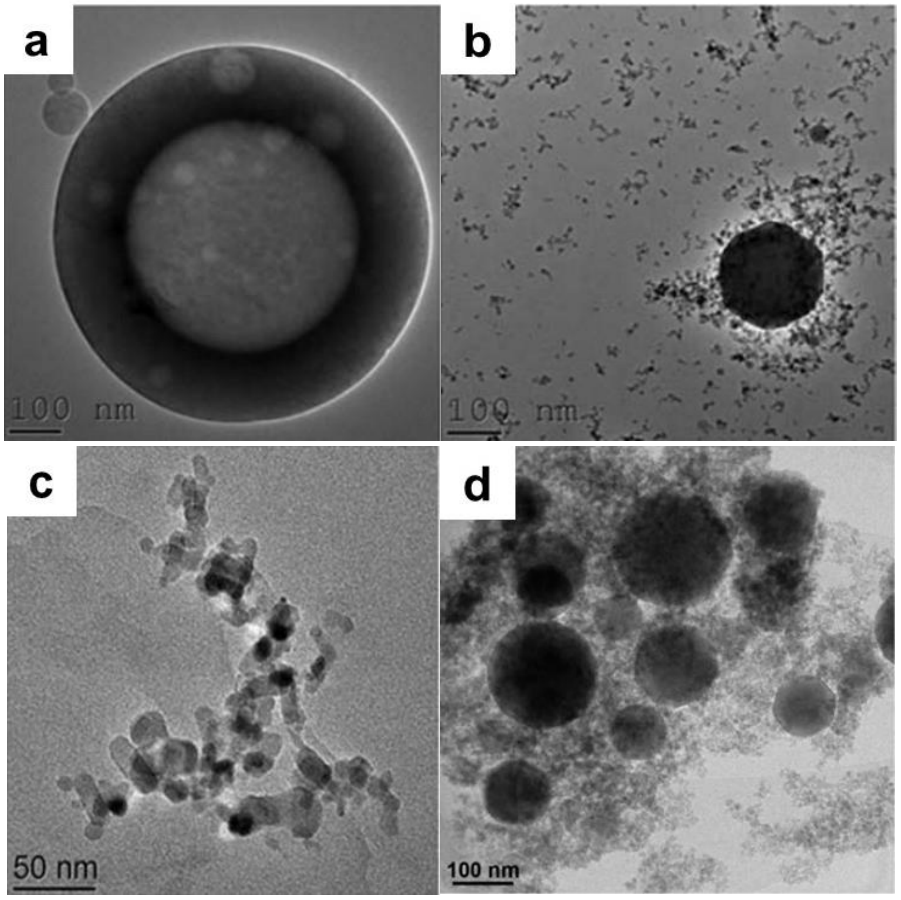

Figure 17. TEM images of (a) Al_2O_3, (b) Fe_xO_y, (c) ZnO, and (d) Co_xO_y particles spray-flame synthesized using metal nitrates as precursors and ethanol as solvent. Images (a), (b) and (c) adapted from Rosebrock et al.[13] and image (d) adapted from Strobel et al.[14].

It has been identified that for single oxides such as Al- (Figure 17a), Fe- (Figure 17b), and Co-oxides (Figure 17d), large particles are formed in most cases. However, Zn-oxide (Figure 17c) does not usually form this kind of large particles from the droplet-to-particle conversion. To analyze the reasons behind these differences, some properties of ethanol along with the characteristics of a spray-flame must be first presented. At 1 bar (abs.), ethanol has a boiling point of 78.3 °C (351.5 K)[108] and a standard heat of combustion of –1367.7 kJ/mol (-23.4 kJ/ml)[109]. At the same pressure and at stoichiometric conditions, the adiabatic flame temperature of ethanol using oxygen is ~2680 °C.[110] Using ethanol in the spray-flame process and considering the *SpraySyn* burner as reference, the temperature of the liquid-phase (droplets) varies between the initial temperature of the supplied solution and the boiling point of ethanol as it can be observed in Figure 18a.[111] By contrast, the gas-phase temperature – without considering the effect of the

pilot-flame (yellow region in Figure 18b) – reaches up to ~1750 °C.[80] The pilot-flame (pre-mixed CH_4/O_2) presents higher temperatures, up to ~2730 °C according to Figure 18b. The temperature values can be modified by the variation of the different liquid or gas flows (different equivalence ratios), e.g., an ethanol/O_2 flame temperature of ~2300 °C measured at 7 mm above the nozzle – without differentiating the effect of the pilot flame – has also been reported.[112]

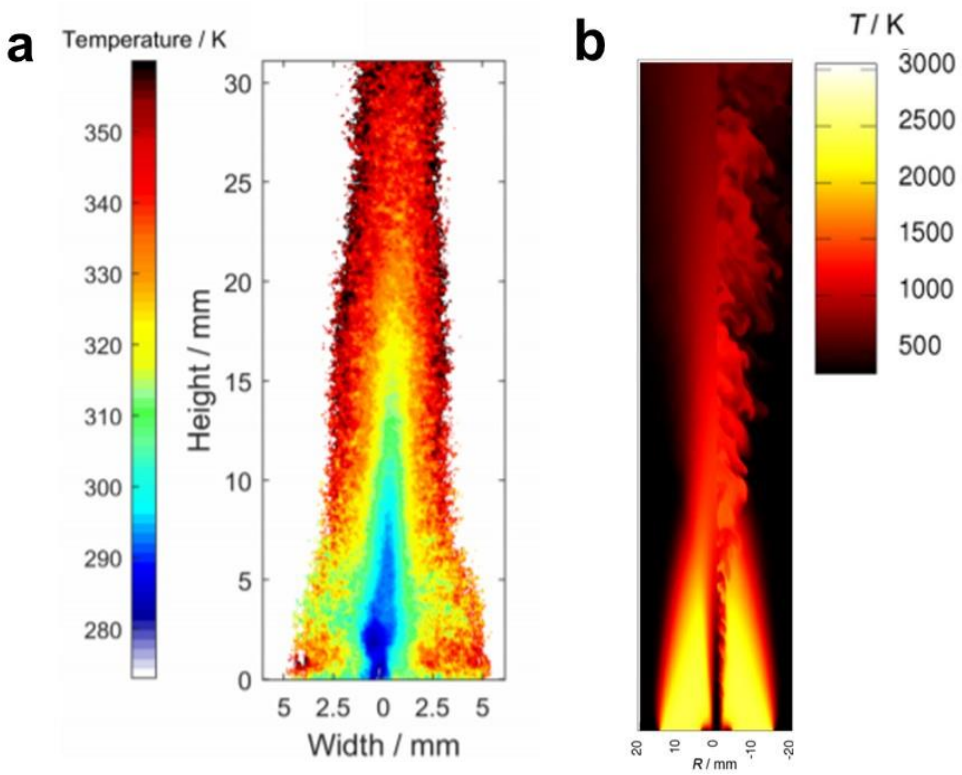

Figure 18. (a) Liquid-phase temperature of an ethanol spray in a spray-flame experiment using laser-induced fluorescence (LIF).[111] (b) Simulation of the gas-phase temperature of a spray-flame of ethanol using the SpraySyn burner (adapted from Schneider et al.[80]).

The first consideration to have into account is related to the chemistry of the metal nitrates in ethanol-based solutions. Based on Chapter 3.2.1, compounds prone to hydrolysis at low temperature as aluminum and iron nitrates might generate metal (oxy)-hydroxide species before and during the evaporation of ethanol in the droplets. As the boiling point of ethanol is lower than that of water, condensation of water from the gas phase is possible and might also affect the hydrolysis process. By contrast, compounds such as zinc nitrate are not expected to form stable (oxy)-hydroxides like Al nitrate at low temperature, limiting the early formation of precipitating species in the liquid phase. The second consideration involves the solubility of the metal nitrates. As ethanol evaporates from the droplets and depending on the concentration, some metal nitrate compounds recrystallize easier than others, e.g., lanthanum nitrate is less soluble than cobalt nitrate in ethanol. An early recrystallization would lead to the formation of large particles from droplets.

The size of the droplets is the next consideration. For ethanol sprays using the *SpraySyn* burner (liquid flow of 2 mL min^{-1} and dispersion gas (O_2) flow of 10 slm), at 15 mm above the burner, droplet sizes range from 2 μm to 30 μm following a log-normal distribution with a maximum at ~3 μm.[113] By contrast, when using a liquid flow of 7.5 mL min^{-1} and a dispersion gas flow of 7.5 slm, droplet sizes range from 2 μm to 65 μm at 10 mm above the burner.[114] Considering ethanol-based droplets with three different sizes (3, 30, 60 μm) containing 0.2 mol/l of iron nitrate nonahydrate and supposing that iron oxide (Fe_2O_3) would be

formed from the droplet-to-particle conversion, the final spherical particles would have a diameter of 434, 4340, and 8680 nm corresponding to the initial droplet sizes of 3, 30, and 60 μm, respectively. This approximation is helpful to visualize that avoiding the formation of large droplets (e.g., >3 μm, depending of the initial concentration of metal precursors in solution) and improving the quality of the spray would also help in reducing the formation of large particles from the droplet-to-particle conversion. In a two-fluid external atomization nozzle like the one used in the *SpraySyn* burner, the droplet size can be modified by changing, e.g., the dispersion gas flow. However, this must be carefully done as high flow might decrease the flame temperature and reduce the residence time of particles in the flame and their crystallinity.

The next consideration is related to the difference in thermal decomposition of the metal nitrates. As presented previously and in Figure 14, compounds as lanthanum nitrate (T_d = ~440 °C) require high temperatures for a complete decomposition to oxides. On the other hand, compounds such as iron, cobalt, or manganese nitrate require comparatively lower temperatures (<250 °C). Compounds with higher decomposition temperatures might require hotter flames and longer residence times. Assuming a decomposition from metal nitrates, the formed metal oxides count with different melting and boiling points and dissociation temperatures. The question in this case is at which temperatures metal-atom-bearing gas species might be formed from the metal oxide in the condensed state (solid or liquid). For example, ZnO has a melting point of ~1975 °C, but the formation of the gas phase species Zn(g) and O_2(g) at 1400 °C – or at even lower temperatures – has been reported.[115] Nevertheless, a temperature of at least ~1600 °C is required to have acceptable decomposition rates.[116] These temperatures are easily attainable with the spray-flame process and the decomposition of even large ZnO particles to form Zn and O_2 gas species is expected as it has been previously proposed.[117] The evaporation of metal oxides can proceed congruently (metal cation to oxygen atomic ratio (M/O) = 1 in both the condensed and the vapor phases) or incongruently (M/O different than 1 in the vapor phase with respect to the condensed phase). The evaporation can also happen associatively, leading to only one species in the gas phase or dissociatively, leading to more than one species in the gas phase. Some examples of metal oxides that present a congruent dissociative evaporation are Al_2O_3, MnO and NiO. By contrast, TiO, TiO_2, CuO, and La_2O_3 are examples of metal oxides with an incongruent evaporation. The vaporization temperatures of metal oxides have been studied basically under vacuum or using inert gases as N_2 or Ar in techniques as the Knudsen-cell effusion mass spectrometry.[118] These measurements can be used as an approximation to the relative volatility of metal oxides, providing reference information for the spray-flame process. Equilibrium partial pressures at different temperature of metal gas species over metal oxides under vacuum are presented in Figure 19.

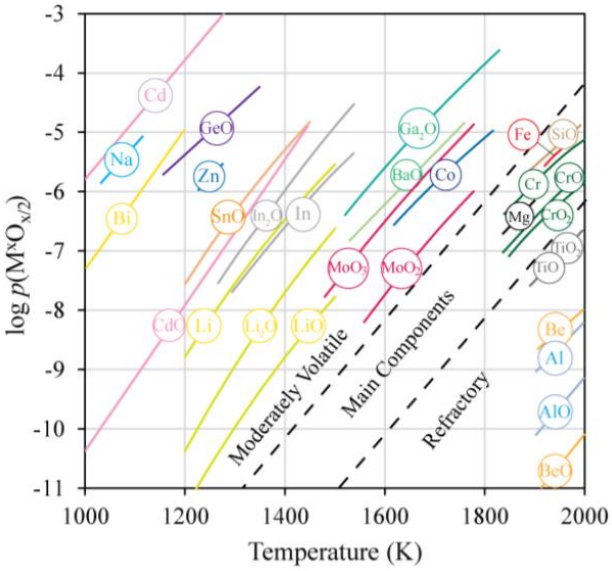

Figure 19. Equilibrium partial pressures at different temperatures of main metal gas species over metal oxides under vacuum.[118]

According to Figure 19, gas species as Na, Zn or Li are highly volatile. By contrast, Al, AlO or BeO are non-volatile/refractory gas species. Two interesting cases can be compared: ZnO and Al_2O_3 Large/hollow .Al_2O_3 particles and small ZnO nanoparticles are usually formed in the spray-flame synthesis as it can be observed in Figure 17a (Al_2O_3) and Figure 17c (ZnO), respectively. As gas species from Al_2O_3 (boiling point of ~2050 °C, boiling point of ~3000 °C) cannot be easily produced, the vaporization of – if formed – large particles is highly unlikely when ethanol is used as solvent in the spray-flame process. By contrast and as presented earlier, the vaporization of ZnO is expected to occur leading to small particles from the gas-to-particle conversion. ZnO and Al_2O_3 oxides are two opposite cases and not only regarding their decomposition at high temperatures. As presented in Figure 16, the hydrolysis of aluminum in the liquid phase – that might lead to the formation of large particles from the droplet-to-particle conversion – is energetically favorable. On the other hand, the hydrolysis of Zn in the liquid phase is highly unlikely to occur. In conclusion, the formation of metal oxide particles in the spray-flame is a multiparametric process that involves the formation of the spray (e.g., droplet size, spray quality, velocity of droplets and gases), the chemistry of the solution of precursors (e.g., solubility, stability, hydrolysis, redox reactions), the flame characteristics (e.g., temperature profiles, residence time, turbulence), the decomposition of solvents and precursors (e.g., release of water, gases, formation of oxides) and the vaporization of oxides (e.g., volatility, melting/boiling points). All these effects are usually coupled and the design of metal oxides using the spray-flame synthesis must take all of them into account.

Several methodologies have been used in the past to improve the quality (e.g., minimize the formation of large particles, improve the crystallinity, maximize the content of a given polymorph) of spray-flame synthesized single oxides. One successful approach has been the addition of 2-ethylhexanoic acid (2-EHA) as a solvent to ethanol-based solutions of metal nitrates. In the next chapter, the mixture of ethanol and 2-EHA as solvent for the spray-flame synthesis of single oxides using metal nitrates will be analyzed. Initially, some physical/chemical considerations of the ethanol/2-EHA mixture will be presented followed by some examples of metal oxides synthesized by this approach.

3.2.3 Spray-flame synthesis of single oxides using metal nitrates as precursors and mixtures of ethanol and 2-ethylhexanoic acid (2-EHA)

As presented in Figure 17, the use of pure ethanol as solvent and metal nitrates leads to large particles of spray-flame synthesized single oxides. The different reasons behind were outlined in Chapter 3.2.2. By contrast, the incorporation of 2-ethylhexanoic acid (2-EHA) in ethanol-based solutions of metal-nitrates has been identified as beneficial for the formation of small, unimodal and crystalline single oxides. TEM images of three oxides (Al-, Fe- and Co-oxides)[14] spray-flame synthesized using a mixture of ethanol/xylene/DEGBE/2-EHA are presented in Figure 20.

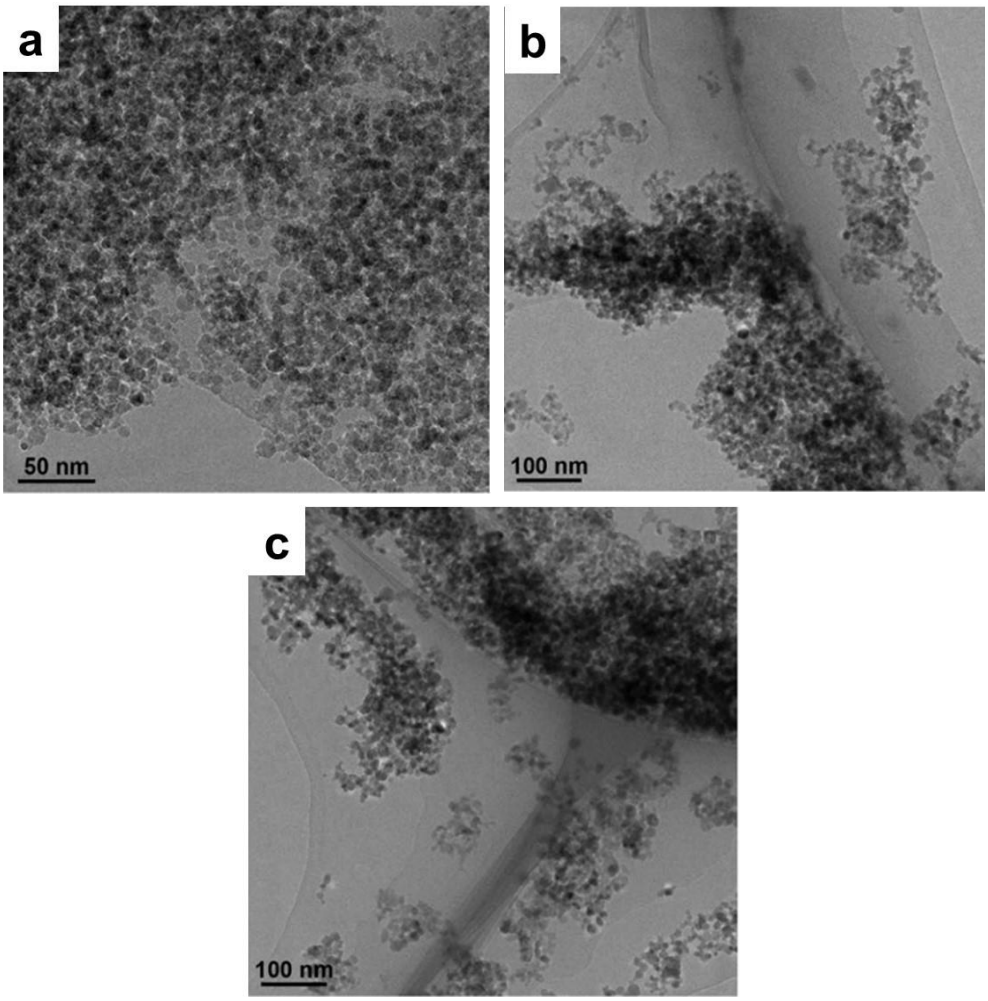

Figure 20. TEM images of (a) Al-oxide, (b) Co-oxide and (c) Fe-oxide spray-flame synthesized using solutions of metal nitrates dissolved in the ethanol/xylene/DEGBE/2-EHA mixture (1:1:1:1). Adapted from Strobel et al.[14]

Strobel et al.[14] proposed that the synthesis of small and homogenous oxides – through the gas-to-particle conversion – as the presented in Figure 20, was happening through the formation and decomposition of metal carboxylates. Additionally, it has been proposed that low-temperature decarboxylation of metal carboxylates might lead to the formation of CO_2 bubbles in droplets which can cause their sudden fragmentation (e.g., micro-explosion). The experiments done by Strobel et al.[14] were carried out using a pre-mixed methane and oxygen pilot flame. Using a pre-mixed hydrogen/oxygen pilot flame, Harra et al.[119] investigated the effect of the concentration of 2-EHA on the spray-flame synthesis of Al_2O_3 – SEM (top row) and TEM (bottom row) images are presented in Figure 21 – from metal-nitrate- and ethanol-based solutions.

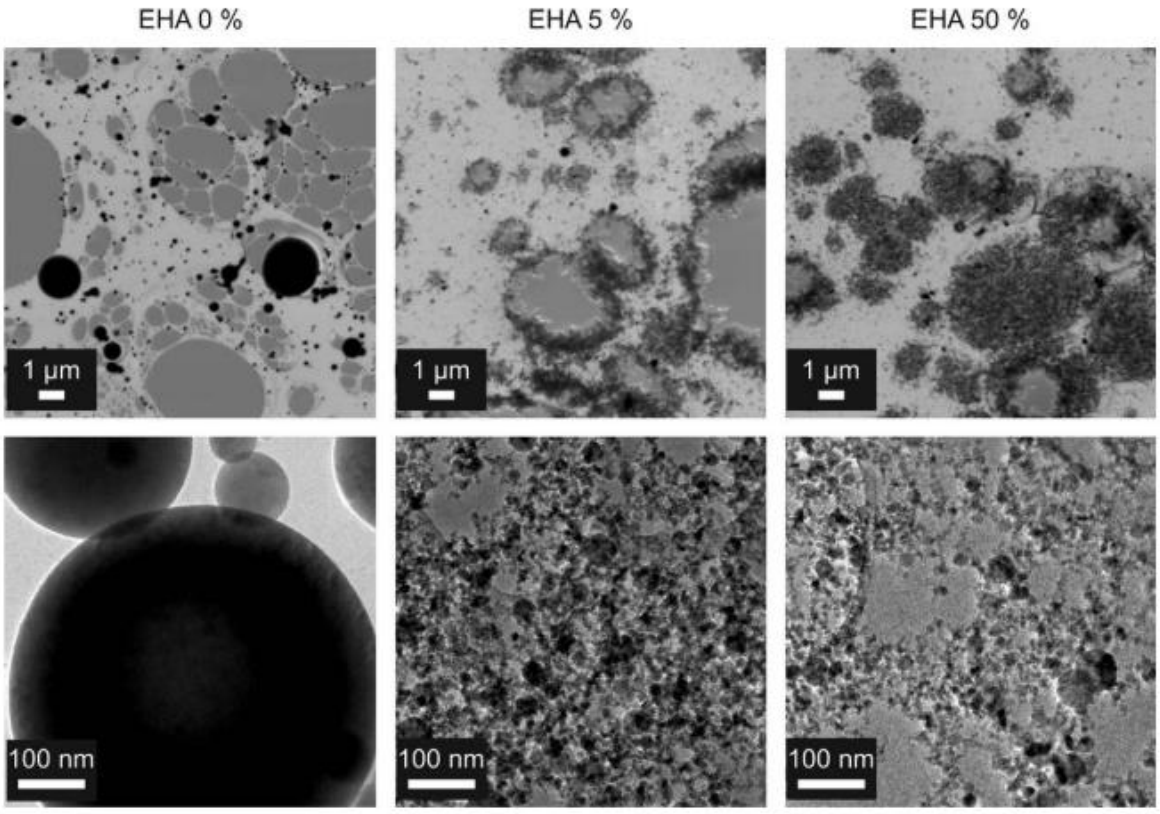

Figure 21. SEM (top row) and TEM (bottom row) images of Al_2O_3 particles spray-flame synthesized from ethanol-based solutions of aluminum nitrate using different contents of 2-EHA: Left column: 0 Vol.%, center column: 5 Vol.%, right column: 50 Vol.%.[119]

Interestingly, Harra et al.[119] identified that when hydrogen/oxygen pre-mixed pilot flames – given their higher temperatures compared to methane/oxygen flames – are used, a content of 2-EHA of 5 % is already sufficient to prevent the formation of large Al_2O_3 particles (case EHA 0 % in Figure 21 and similarly presented in Figure 17a) and to obtain small and homogeneous particles. When 2-EHA is added to ethanol-based solutions of metal nitrates, the improvement of the spray-flame synthesized materials is clear as it is evidenced in the absence/reduction of large particles leading to oxides with high specific surface areas. The explanation of the 2-EHA effect cannot be reduced to a single phenomenon. Instead, the use 2-EHA in the precursor solutions has consequences that range from the chemistry of the liquid-phase (e.g., droplets) or the gas-phase to the formation of the spray, droplet disruption, or the decomposition of precursors. Different physical and chemical considerations related to the ethanol/2-EHA mixture are discussed in the following sections in the context of the spray-flame synthesis of single oxides.

3.2.3.1 Physical considerations of the ethanol/2-ethylhexanoic acid (2-EHA) mixture

2-Ethylhexanoic acid (2-EHA) is a carboxylic acid with the formula $CH_3(CH_2)_3CH(C_2H_5)COOH$ (Figure 22). After acetic acid and propionic acid, it is – by volume – the third most produced carboxylic acid worldwide. In 2012, the European Union (EU) consumed 85,000 t of this acid. 2-EHA-derived products (e.g., metal 2-ethylhexanoates) are compounds used in the industry as, e.g., drying agents, thickeners for resins and paints, gelling agents and antibiotics synthesis precursors.[120]

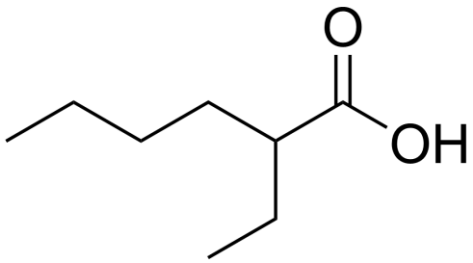

Figure 22. Structure of 2-ethylhexanoic acid (2-EHA).

2-EHA is a dense, viscous and high-boiling point liquid.[121] Some of its physical properties are presented in Table 1. By contrast, ethanol is a low-viscosity and low-boiling point alcohol which properties are also presented in Table 1.

Table 1. Physical properties of ethanol and 2-ethylhexanoic acid (2-EHA).[92, 109, 120]

	Ethanol	**2-Ethylhexanoic acid (2-EHA)**
Molecular weight	46.07	144.21
Boiling point / °C	78.25	226–228
Density at 20 °C/ g/ml	0.789	0.903
Viscosity at 20 °C / mPa s	1.14	8.4
Vapor pressure at 20 °C / kPa	5.95	0.004
Volumetric heat of combustion / kJ/ml	–23.4	–30

Taking into account the higher density and viscosity of 2-EHA in comparison to ethanol, the first consideration of using ethanol/2-EHA mixtures in the spray-flame process would be the effect on the spray formation (e.g., droplet size). In this regard, phase-Doppler anemometry (PDA) – an explanation of this method is presented in Appendix C – measurements performed by Bieber et al.[113] considering spray-flames of ethanol and of a mixture of ethanol (35 Vol.%) and 2-EHA (65 Vol.%) with and without iron nitrate (0.2 mol/l) are presented in Figure 23.

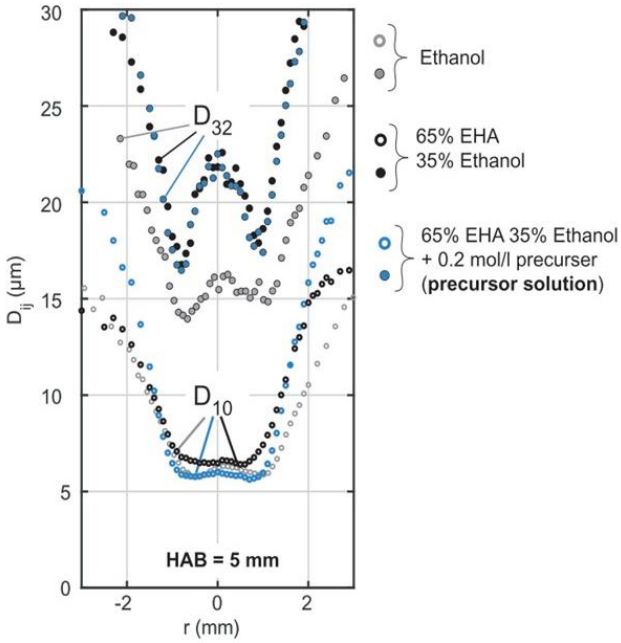

Figure 23. Arithmetic (D_{10}) and Sauter (D_{32}) mean droplet diameter from phase-Doppler anemometry (PDA) measurements of burning sprays of ethanol and a mixture of ethanol (35 Vol.%) and 2-EHA (65 Vol.%) without and with 0.2 mol/l of iron nitrate nonahydrate (precursor solution) using the SpraySyn burner. Adapted from Bieber et al.[113]

At HAB = 5 mm (Figure 23) and in comparison with pure ethanol as solvent, the use of the mixture of ethanol (35 Vol.%) and 2-EHA (65 Vol.%) did not importantly affect the arithmetic mean diameter (D_{10}) of the burning spray at the center position. However, larger Sauter mean diameters were obtained when using the ethanol/2-EHA mixture (D_{32} = ~23 µm at r = 0 mm) in comparison with ethanol (D_{32} = ~17 µm at r = 0 mm) indicating a higher concentration number of large droplets in the ethanol/2-EHA case as it might be expected given the density and viscosity of 2-EHA. The addition of a precursor – iron nitrate nonahydrate (0.2 mol/l) – to the ethanol/2-EHA mixture did not cause an appreciable variation of the droplet size in the –2 mm < r < 2 mm region.

As 2-EHA has a higher volumetric heat of combustion than ethanol, the use of a mixture of both solvents in a spray-flame experiment is expected to produce hotter flames when comparing with the use of only ethanol as solvent. For example, using a modified Hencken-type flat flame burner with a spray system adaptation, Wei et al[92] measured flame temperatures up to ~1200 K when using an ethanol/2-EHA (50 Vol.% : 50 Vol.%) mixture in contrast with temperatures up to ~1000 K when using only ethanol. Even though the measured temperatures are comparatively lower to the ones presented in Figure 18b (simulations using the *SpraySyn* burner as reference), they provide an idea of the order of magnitude expected when 2-EHA is incorporated as a fuel/solvent in a spray-flame experiment. The higher flame temperatures that can be reached with ethanol/2-EHA mixtures are important when metal precursors or metal oxides with high decomposition or evaporation temperatures must be synthesized. Based on Figure 19, at higher temperatures, higher partial pressures of metal-containing gas species can be obtained, probably supporting the gas-to-particle conversion in the spray-flame synthesis. Not only the temperature of the flame is affected by the addition of 2-EHA, the temperature of the liquid-phase (e.g., droplets) is also expected to change as the boiling point of 2-EHA is considerably higher than that of ethanol (see Table 1). The effect of the difference of volatilities of ethanol and 2-EHA in a binary fuel mixture on the total vaporization time of the droplets must be considered. As in the spray-flame synthesis the flame temperatures are high (Figure 18b), the formed droplets are exposed to a rapid heating process. Depending on the fuel and the operation conditions, the magnitude of the heat-transfer from the gas phase to the surface and then to

the interior of the droplets can greatly differ from the magnitude of the mass-transfer of the liquid from the center to the surface of the droplet. When the heat-transfer and mass-transfer are balanced in the droplet, the Lewis (*Le*) number – ratio of heat to mass transport – is equal to 1. However, the Lewis number is usually greater than 1 when considering the combustion of droplets, which indicates that the heat-transfer is higher than the mass-transfer and that the interior of the droplet is rapidly heated up. The *Le* > 1 condition in a binary fuel droplet (e.g., ethanol/2-EHA) can cause superheating of the most volatile component leading to the nucleation and fast growth of bubbles which might produce the abrupt disruption (e.g., micro-explosion) of the droplet.[122] The practical superheating limit (temperature) of pure liquids is close to 88–90 % of their critical temperature, i.e., ethanol has a measured superheating temperature of 189.5°C at atmospheric pressure. As this temperature is lower than the boiling point (Table 1) of 2-EHA, the ethanol superheating condition can be achieved. In a boiling liquid, vapor bubbles are unstable and usually collapse. By contrast, when the liquid is superheated, the vapor bubbles can be formed overcoming the minimum work required to create the bubble surface and to transfer molecules from the liquid to the bubble.[123] The nucleation of a bubble in a binary-fuel droplet can proceed homogeneously – governed by the liquid's properties – or heterogeneously – affected by surface effects.[122, 124] The homogeneous nucleation is considered to be stochastic indicating that the micro-explosion of a droplet falls in a probability (P_{ME}) function. It has been identified that this probability strongly depends on the initial droplet diameter – the higher the initial diameter, the higher the probability of a micro-explosion to occur. This is beneficial for the spray-flame synthesis as the largest formed droplets – the ones from which large particles can be formed from the droplet-to-particle conversion – have a higher probability to micro-explode when mixtures of ethanol and 2-EHA are used. The presence of surfaces, particles or impurities – which decrease the energy required for the formation of bubbles – can influence the heterogeneous nucleation/formation of bubbles.

The entrainment of air in the formation of droplets or in their collisions is another aspect that should be considered. For example, air entrapped in water/hexadecane droplets was identified as one of the mechanisms from which a micro-explosion can proceed through heterogeneous nucleation.[125] The effect of the metal precursors, their chemistry in the liquid-phase and their decomposition must be also taken into account. Rosebrock et al.[13] proposed the formation of a viscous shell of liquid or solid intermediates in burning droplets that would also facilitate the formation of vapor bubbles via heterogeneous nucleation – through the superheating of low-volatility components – and the eventual micro-explosion of the droplets.

The occurrence of micro-explosions in nitrate-based burning single-droplets has been recorded using high-speed cameras. Rosebrock et al.[15] presented the micro-explosion of droplets containing iron nitrate or aluminum nitrate dissolved in a mixture (volume ratio 1:1:1:1) of ethanol, xylene, diethyleneglycol monobutylether (DEGBE) and 2-EHA as presented in Figure 24.

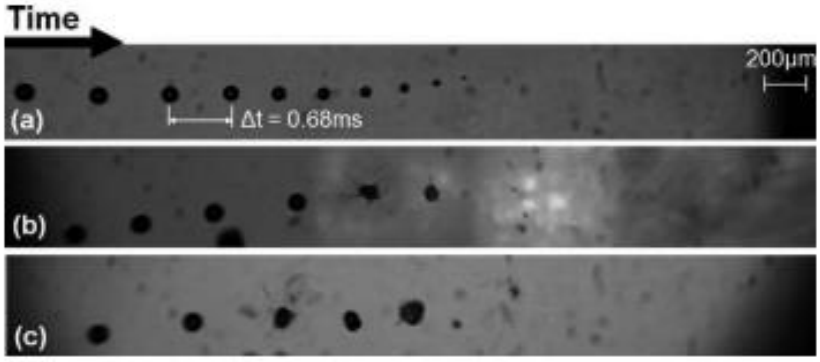

Figure 24. Time-dependent images of burning single-droplets containing (a) a precursor-free mixture of ethanol/xylene/DEGBE/2-EHA, with (b) 0.5 mol/l of iron nitrate dissolved or (c) aluminum nitrate dissolved in the mixture.[15]

As it can be observed in Figure 24a, the ethanol/xylene/DEGBE/2-EHA mixture did not present a micro-explosion episode. By contrast, the inclusion of iron nitrate (Figure 24b) or aluminum nitrate (Figure 24c) generated a micro-explosion of the single-droplet. In these two cases (Fe, Al), the authors did not attribute the micro-explosion to the stand-alone effect of the mixture of solvents (e.g., bubble nucleation through the superheating of ethanol) but to the formation of metal carboxylates (e.g., metal 2-ethylhexanoates) from the reaction of metal nitrates with 2-ethylhexanoic acid. This was suggested by the identification of two exothermic events at T > ~225 °C from thermogravimetric analyses (TGA) of the Fe- and Al-based solutions. The events were related to the decomposition of the carboxylates but further evidence of the formation of the metal 2-ethylhexanoates was not included. As it is presented in Chapter 3.2.3.2, the formation of carboxylates is possible but other reactions might also play a role. For example, ethanol and 2-EHA might react to form an ester compound (ethyl 2-ethylhexanoate) and water. Similarly, DEGBE – also known as 2-(2-butoxyethoxy)ethanol – might also react with 2-EHA to form a long-chain (e.g., high boiling point) ester compound and water. The role of these compounds in the micro-explosions or in the spray-flame synthesis of metal oxides is not clear yet and is a matter of current research. Chemical considerations resulting from the addition of 2-EHA to ethanol-based solutions of metal nitrates are presented as follows in Chapter 3.2.3.2.

3.2.3.2 Chemical considerations of the ethanol/2-ethylhexanoic acid (2-EHA) mixture

The addition of 2-EHA to ethanol-based solutions of metal nitrates has several chemical consequences. The acidic character of 2-EHA, which increases the concentration of protons in ethanol-based solutions, affects the speciation of metal-derived compounds by decreasing the pH of the solution. As presented in Figure 15, low pH values are required to avoid the formation of metal-hydroxide species from hydrolysis.

2-ethylhexanoic acid (2-EHA) might react with metal nitrates to form metal 2-ethyhexanoates. However, when metal nitrates are used to synthesize metal alkanoates (e.g., 2-ethylhexanoates), sodium or ammonium alkanoates are commonly used (e.g., metathesis reactions) instead of 2-EHA. Typical starting materials used in the synthesis of metal alkanoates by ligand-exchange reactions using an alkanoic acid (e.g., 2-EHA) in the presence of a catalyst are metal oxides, hydroxides, chlorides or acetates.[126] Metal nitrates are not usually used and the information about their effectivity to form metal 2-ethylhexanoates using 2-EHA is scarce and will be examined in more detail in the course of this thesis (Chapters 4.3.1, 5.3.1, and 6.3.1).

2-EHA might not only react with metal precursors, it also participates in an esterification reaction with ethanol to form ethyl 2-ethylhexanoate and water as presented in reaction (3.4).

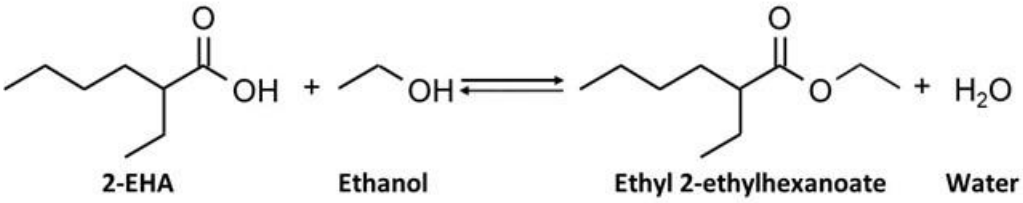

(3.4)

Volumetric concentrations of 27 % of ethanol and 73 % of 2-EHA are required for a stoichiometric reaction. Even though this reaction has not been studied in detail yet, for obtaining high yields of the ester compound and water, a catalyst might be required. Da Silva et al[127] reported the use of metal nitrates – Lewis acid compounds – as catalysts for the esterification of β-citronellol with acetic acid to produce β-citronellyl acetate and water. Iron nitrate – followed by aluminum nitrate and copper nitrate – was identified as the most active catalyst for that reaction given its ability in generating H^+ species from the carboxylic acid. Such effect might also be expected in the metal-nitrate-based solutions of ethanol and 2-EHA which are used for the spray-flame synthesis of metal oxides. The question arising is if this esterification is beneficial or detrimental for the spray-flame process. From one side, the formation of water as it was explained in chapter 3.2.1, might promote the hydrolysis of the metal ions and the early formation of solid (amorphous or crystalline) species from which large particles can be formed. From the other side, the formation energetic compounds (e.g., nitrate esters) that might influence the generation of droplet micro-explosions in these solutions has not been studied yet.

Based on the presented physical and chemical considerations of using mixtures of ethanol and 2-EHA as solvents in nitrate-based solutions for the synthesis of single oxides, this thesis explores the use of such mixtures for the spray-flame synthesis of $LaFeO_3$ (chapters 4 and 6), $LaCoO_3$ (chapters 4 and 6) and $LaMnO_3$ (chapters 5 and 6) perovskites. Over the years, other approaches – that have been explored for the spray-flame synthesis of different perovskites – are presented in the following section (chapter 3.3) in order to understand additional challenges related to the synthesis of these compounds.

3.3 Spray-flame synthesis of perovskites

One of the earliest reports by Kriegel et al.[128] of the spray-flame synthesis of a perovskite material ($SrMnO_3$) dates back to 1994. Using a hydrogen/oxygen pilot-flame, the authors produced the perovskite using solutions containing carbonates (e.g., $SrCO_3$ and $MnCO_3$) as metal precursors and water, acetic acid and N_2H_4 as solvents. Even though the crystallographic information of the $SrMnO_3$ sample was not presented in detail, particles of ~25 nm were obtained, and the synthesized sample proved to be more active for the catalytic oxidation of methane when compared with a $SrMnO_3$ sample synthesized by a solid-state method. In 1999, Saracco et al.[129] reported the spray-flame synthesis of $LaMnO_3$ using a solution containing lanthanum nitrate and manganese acetate dissolved in ethanol. The authors identified both the formation of large aggregates and particles with sizes up to ~2 μm and small-size particles (<200 nm). Additionally, the dispersion gas flow (air) was modified as a way to control the flame temperature and the authors found that low air flows led to the formation of the $LaMnO_3$ orthorhombic phase, while higher flows led to the formation of the $LaMnO_3$ rhombohedral phase. However, the phases were only analyzed by XRD and particle size-polymorph relationships were not established.

Based on available information, Prof. Forni (Department of Physical Chemistry and Electrochemistry, University of Milan) investigated the spray-flame synthesis of perovskites ($LaFeO_3$, $LaCoO_3$, $LaMnO_3$, $LaNiO_3$ and different A- and B-site-substituted perovskites) for gas-phase oxidation catalysis leading to publications between 1998 and 2012.[130-133] In 2007, Chiarello et al.[16, 17] evaluated the spray-flame synthesis of

Spray-flame synthesis

$LaCoO_3$ using metal nitrates as precursors dissolved in methanol, ethanol, propanol or in a mixture of propanol and propionic acid. The authors obtained in all cases materials with a relatively low-purity and a low specific surface area of ~20 m^2/g which was attributed to the high volatility of the alcohols and the high decomposition temperature of the nitrate-based precursors. In contrast, the use of metal acetates as precursors and different carboxylic acids as solvents – including pure 2-EHA – led to the formation of purer $LaCoO_3$ materials with higher specific surface areas (~40 – ~70 m^2/g). Using also metal acetates as precursors, Chiarello et al.[134] evaluated the effect of the nozzle – convergent and convergent/divergent – operation parameters (e.g., liquid flow rates, solution concentration, dispersion oxygen linear velocity and flow rate) for the spray-flame synthesis of $LaCoO_3$. A summary of the findings is presented in Table 2.

Table 2. Effect of selected spray-flame synthesis operation parameters on the properties of $LaCoO_3$ perovskite.[134]

Increasing of	SSA	Particle size	Crystal-linity	Catalytic activity	Thermal stability
Liquid flow rate					
Const. ϕ	≈	≈	≈	≈	≈
Const. O_2 flow rate	↓	↑	↑	↓	↑
Solution concentration	↓[a]	↑	↑	↓	↑
O_2 linear velocity	↑	↓	↓	↑	↓
O_2 flow rate					
Below P_c	↑	↓	↓	↑	↓
Above P_c[b]	≈	≈	≈	≈	≈

Note: $\Phi = \frac{(\text{mol } O_2/\text{mol fuel})_{real}}{(\text{mol } O_2/\text{mol fuel})_{stoich}}$; P_c = nozzle critical pressure; ≈ = almost no effect.

[a] For concentration ⩾0.05 M.

[b] For $\phi > 3$ too low crystallinity was observed.

As expected, the increase of the oxygen dispersion flow (Table 2)[134] – lower flame temperature and height – caused the increase of the specific surface area (SSA) – from ~30 to ~65 m^2/g using an oxygen flow from 3 to 8 slm – of the $LaCoO_3$ materials, the decrease of their crystallinity and the increase of their activity of the oxidation of methane. Even though large particles were also identified, their effect on the SSA or crystallographic results was not analyzed. The increase of parameters as the liquid flow rate and the concentration of precursors in the solution led to similar effects: low SSAs, high crystallinity, and low catalytic activity. It is evident than the increase in specific surface area occurs at the expense of crystallinity and vice versa. This is, as in the spray-flame synthesis of single oxides, an important challenge.

Coming from another research hub related to the spray-flame synthesis of perovskites (Laboratory for High Performance Ceramics – EMPA in Switzerland) and using metal nitrates as precursors, Heel et al.[135] studied the effect of the addition of acetic acid – from 0 to 70 Vol.% – to water-based solutions on the spray-flame synthesis of the $La_{0.6}Sr_{0.4}CoO_{3-\delta}$ materials. Even though a phase-pure perovskite was not obtained (e.g., the $(La, Sr)_2CoO_4$ Ruddlesden-Popper phase was identified at concentrations up to 27 Wt.%), the increase of acetic acid in solution was effective to increase the specific surface area of the materials (up to ~40 m^2/g). The authors attributed the improvement in SSA to higher flame temperatures while the chemical effects of water and acetic acid on the solution of metal precursors were not analyzed.

The spray-flame synthesis of A- and B-site-substituted perovskites has also been studied. Aegerter et al.[136] from the Paul Scherrer Institute, EMPA, and ETH in Switzerland investigated the effect of the operation parameters on the spray-flame synthesis of the $Ba_{0.5}Sr_{0.5}Co_{0.8}Fe_{0.2}O_{3-\delta}$ perovskite. The authors used barium carbonate and strontium, cobalt and iron nitrates as metal precursors dissolved in a mixture of water and acetic acid (75:25 volume ratio). It was identified that high precursor solution flows (50 ml/min) and low

dispersion gas flows (25 slm) led – through the formation of large droplets and the incomplete decomposition of the precursors – to the formation of secondary phases and low specific surface areas. In this case, chemical effects of the solvents and metal precursors were also not studied.

In the previous chapters, several challenges related to the spray-flame synthesis of perovskite materials were identified. The first one is related to the formation of secondary phases as it was also identified in chapter 2.6. The formation of these phases is connected to the type of metal precursors and solvents used and with the operation parameters of the synthesis. The chemistry of the solutions – reactions between solvents or among the dissolved precursors with solvents – has not been investigated in detail yet or related with the formation of perovskites in the spray-flame synthesis method. Similar to single oxides, the synthesis of perovskites using metal nitrates as precursors typically leads to multimodal particle size distributions resulting from mixed particle formation from the droplet-to-particle and from the gas-to-particle conversion routes. This particle size multimodality is the second identified challenge, which – as presented in chapter 3.2.3 for single oxides – can be tackled with the use of ethanol/2-EHA mixtures. For that reason, such mixtures are evaluated in this thesis for the spray-flame synthesis of $LaFeO_3$, $LaCoO_3$, and $LaMnO_3$ perovskites. In chapter 4, the effect of the addition 2-EHA (0, 50, and 65 Vol.%) to ethanol-based solutions of metal nitrates on the spray-flame synthesis of La(Fe, Co)O_3 perovskites for catalytic CO oxidation is presented and discussed. In chapter 5, the spray-flame synthesis of $LaMnO_3$ is analyzed using only ethanol and a 1:1 volumetric mixture of ethanol and 2-EHA and the crystallographic structure and catalytic activity of the synthesized materials are analyzed in higher detail. In both chapters 4 and 5, the chemistry of the solutions is analyzed with ATR-FTIR spectroscopy and for the Mn-based solutions, UV-Vis spectroscopy measurements were also carried out to identify and to analyze the redox chemistry of manganese. Using solutions of metal nitrates dissolved in an ethanol/2-EHA (35 Vol.%/65 Vol.%), the effect of the dispersion gas flow rate (5, 6, 7, and 8 slm) and the esterification reaction between ethanol and 2-EHA on the droplet size and the particle size homogeneity the three $LaFeO_3$, $LaCoO_3$, and $LaMnO_3$ perovskites is analyzed in chapter 6.

4 Spray-flame synthesis of La(Fe, Co)O_3 nano - perovskites from metal nitrates

The content of this chapter was published in AIChE Journal:

> **Angel, S.**; Neises, J.; Dreyer, M.; Friedel Ortega, K.; Behrens, M.; Wang, Y.; Arandiyan, H.; Schulz, C.; Wiggers, H., Spray-flame synthesis of La(Fe, Co)O_3 nano-perovskites from metal nitrates. AIChE J. 2019, 66, e16748.

Further information related to this chapter is presented in Appendix A (Chapter 11.1), including the Figure A 1 and Figure A 2.

My contribution in this work includes: Research conceptualization, synthesis, characterization of precursors and materials, analysis of data including the catalytic results, writing of the manuscript. J. Neises contributed with FTIR measurements. M. Dreyer, K. Friedel-Ortega, M. Behrens, Y. Wang and H. Arandiyan contributed with catalytic measurements/analysis. C. Schulz and H. Wiggers contributed to the conceptualization, the interpretation, and the writing of the manuscript.

4.1 Introduction

Perovskite-type mixed oxides, composed of lanthanum as a rare-earth ion, and iron ($LaFeO_3$) or cobalt ($LaCoO_3$) as a d-orbital transition-metal ion, have high thermal stability and are remarkably tolerant to the formation of anionic or cationic vacancies (as in $LaCo_{1-x}Fe_xO_3$).[137] This enables the modification of the oxidation state of the transition metals and the oxygen availability,[138] thus adapting the materials for specific catalytic reactions.[26] Perovskite materials are currently being explored as potential low-cost alternatives to noble-metal catalysts for environmental reactions.[139] Among others, iron- and cobalt-based perovskites attract scientific interest with respect to catalytic applications, e.g., the oxidation of CO and hydrocarbons, the reduction of NO_x, and energy conversion in reactions such as water splitting and the dry reforming of methane.[140-142]

The synthesis method of the perovskites significantly affects their structure, surface area, and catalytic properties.[143] Conventional production methods include solid-state reactions, precipitation/co-precipitation from solution, sol-gel and hydrothermal synthesis.[144, 145] Solid-state reactions are one of the oldest synthesis routes for the preparation of perovskites. They, however, often face challenges with broad particle-size distribution and lack of purity.[146] Sol-gel techniques and the Pechini method can better control the phase purity of the formed perovskites.[146] Nevertheless, all the mentioned methods are batch processes that require a multistage post-treatment including filtration, drying and calcination.[136] Continuous processes offer advantages such as reproducible quality and the ability to synthesize spherical particles,[137] which might be advantageous in catalytic applications as they permit the packing of the particles without decreasing substantially the total surface area (related to the catalytic activity) while minimizing the pressure loss in, e.g., packed bed reactors.[147] Additionally, they provide the potential to scale-up to high production rates and low-cost production. Among the continuous processes, spray-flame synthesis (SFS) is most promising for the generation of mixed oxides and allows the preparation of perovskites in a single step.[74, 75, 134]

Spray-flame synthesis of metal oxides such as ZrO_2, TiO_2, Fe_2O_3, SnO_2, among others, has been studied in detail[76, 90] with specific focus on the selection of the precursors and organic solvents used. When selecting soluble precursors, metal nitrates are of specific interest from an economical point of view when compared to metal-organic precursors. When used in SFS, nitrate solutions often lead to the formation of a

mixture of two materials classes composed of nanoparticles with a small and narrow particle-size distribution – resulting from a gas-to-particle process – and micrometer-sized particles that are sometimes hollow or fragmented, resulting from a droplet-to-particle conversion.[148] Here, the formation of large-scale hollow and porous particles – which for some applications could be of high value – is not desired.

As nitrates require polar solvents, alcohols, are frequently selected as a low-cost compound. SFS of precursor dissolved in ethanol, however, frequently leads to unwanted particle morphology as a result of the droplet-to-particle mechanism. In order to shift to the formation of nanoscale particles, one common strategy involves the use of combined solvents including diethylene glycol monobutyl ether, xylene, and 2-ethylhexanoic acid (2-EHA). For the synthesis of Fe_2O_3, Al_2O_3, and Co_3O_4, Strobel et al.[14] postulated a reaction of the carboxylic acid, 2-EHA, with the corresponding metal nitrates resulting in metal carboxylates. This reaction in the precursor solution prior to the SFS process might facilitate the formation of particles through gas-to-particle conversion. Strobel et al. observed the formation of iron carboxylates in solution at room temperature, which was verified with ATR-FTIR analysis. Respective cobalt carboxylate compounds were not identified under the experimental conditions.

Besides the modification of the chemical structure of the precursor solution, solvent mixtures can also influence spray formation and evaporation. In single-droplet experiments, Rosebrock et al.[15] observed that the addition of 2-EHA to the ethanolic metal nitrate solution generates cascade-like micro-explosions of the burning droplets and observed the same behavior when metal 2-ethylhexanoate precursors were used. Explosive droplet evaporation is well known also in spray combustion of hydrocarbon mixtures without inorganic solutes. This effect has been studied, e.g., in the context of biofuel-containing hydrocarbon fuels for internal combustion engines.[149] It is attributed to preferential evaporation of high-vapor pressure components leading to their depletion near the droplet surface with subsequent flash-boiling of the light fractions in the center of the droplet during heat up.[149] The main requirement for micro-explosions to occur is that the superheating temperature of the most volatile component at ambient pressure does not exceed the boiling point of the other component.[15] A binary system that complies with this requirement is the ethanol and 2-EHA mixture.

Chiarello et al demonstrated the spray-flame synthesis of $LaCoO_3$ for an application in catalytic flame-less combustion of methane.[16, 17] They focused on the best-suited operating conditions for the SFS and on the effect of different solvents and metal precursors (nitrates and acetates). When using metal nitrates in alcohols (methanol, ethanol, and propanol) and mixtures of propionic acid and propanol, secondary phases as La_2O_3 and La_2CoO_4 could not be avoided, thus leading to particles with inhomogeneous elemental composition.

In the present work, we investigate the effect of solvent mixtures – ethanol and 2-EHA – on the characteristics of $LaFeO_3$ and $LaCoO_3$ made from nitrates by spray-flame synthesis. Using temperature-dependent liquid-phase ATR-FTIR studies, we investigated the modifications of the respective precursor solutions and correlated the occurrence of pre-reactions in the liquid phase with the properties of the synthesized materials that were characterized by TEM, BET, EDX, and XRD. Moreover, the catalytic performance of the samples was analyzed for the low-temperature catalytic oxidation of carbon monoxide.

4.2 Materials and methods

4.2.1 Synthesis

The perovskite materials were synthesized in an enclosed spray-flame reactor (described in detail in Chapter 3.1 and in previous publications[80, 150, 151]). For $LaFeO_3$ and $LaCoO_3$ synthesis, metal nitrates were used as precursors: $La(NO_3)_3{\cdot}x\ H_2O$ (AppliChem Panreac, >99.0 % purity), $Fe(NO_3)_3{\cdot}9\ H_2O$ (VWR, >98 % purity) and $Co(NO_3)_2{\cdot}6\ H_2O$ (Honeywell, > 99.0 % purity). Ethanol (VWR, >99.9 % purity) and 2-ethylhexanoic acid

(2-EHA) (Alfa Aesar, >99 % purity) were used as solvents. Using the respective metal nitrates in a total concentration of 0.2 mol/l, three solutions were prepared for each material system employing different mixtures of solvents: **(I)** ethanol, **(II)** a mixture of ethanol (50 Vol.%) and 2-EHA (50 Vol.%) and **(III)** a mixture of ethanol (35 Vol.%) and 2-EHA (65 Vol.%). Solutions with concentrations of 2-EHA higher than 65 Vol.% could not be processed at the selected reactors' operation parameters due to stability problems related to high viscosity of the mixtures.

4.2.2 Solution and particle characterization

As-prepared nitrate solutions with different solvent mixtures were heated from room temperature to 50 and 70 °C, maintaining each temperature for 15 min. At each temperature and for each solution, an aliquot was taken and measured with Fourier-transform infrared spectroscopy (FTIR, Vertex 80, Bruker) using standard optical components consisting of a KBr beam splitter, a DigiTect DLaTGS detector, and a mid-infrared light source from 400 to 4000 cm^{-1} in combination with an ATR sample holder.
Gas chromatogram and mass spectrum of ethyl 2-ethylhexanoate in a solution of ethanol (50 Vol.%) and 2-EHA (50 Vol.%) were measured using a GC/MS (Agilent 7890A and MSD 5975C) equipped with a HP5-MS column for separation of species and connected to a quadrupole mass spectrometer (QMS).
The crystal structure of the materials was analyzed by X-ray diffraction (PANalytical X´Pert PRO) operated with Cu-K_α radiation (0.15406 nm, 40 kV, 40 mA). The diffraction intensity was recorded at diffraction angles 2θ between 10 and 100° with a step size of 0.05°.
The morphology, particle size, and composition of the materials were studied by transmission electron microscopy (TEM-EDX-SAED; JEOL JEM- 2200FS). The mean particle sizes were measured using the program *ImageJ*. The histograms of the particle diameters were fitted to log-normal size distributions using the program *Origin*, from where the count median diameter and the geometric standard deviation were extracted in each case.

4.2.3 Catalytic activity

Each perovskite sample was heated in air at 250 °C for 1 h to remove organic residues from the surface as measured by TGA analysis. Depending on synthesis conditions, a weight loss between 7 Wt.% (only ethanol) and about 11 Wt.% (ethanol and 2-EHA) was observed.
For catalytic testing, 100 mg (sieve fraction 251–355 µm) of each heat-treated catalyst sample diluted with 500 mg of silicon carbide (> 355 µm) was placed inside a U-shaped quartz tube reactor (inner diameter: 8 mm). Each sample was heated at 3 °C/min in 20 % O_2/80 % He (99.9999 %, Air Liquide) from room temperature to 200 °C, which was kept constant for 1 h. Thereafter, the sample was cooled down in He to 35 °C. Before starting the catalytic experiments towards CO oxidation, the catalyst/SiC mixture was purged for 15 min with 3 % CO and 6 % O_2 in He to equilibrate the gas composition. Thereafter, the temperature to start CO oxidation was increased to 300 °C at a heating rate of 3 °C/min. The total gas flow was 80 ml_n/min. The reactor off-gas was analyzed with a MicroGC (Agilent Technologies 490) equipped with a 5-Å molecular sieve and a Pora Plot Q column for the detection of CO, O_2, and CO_2. The catalytic activities of the samples were evaluated by determining the temperature T_{50}, required for 50 % CO conversion.

4.3 Results

4.3.1 Temperature-dependent ATR-FTIR analysis of solutions

In spray-flame synthesis, the boiling points of the solvents and the decomposition mechanisms and temperatures of the precursors influence the formation, size homogeneity, and phase of the final particles.[17, 90] Reactions between dissolved precursors and solvent during droplet heating and combustion might either initiate or accelerate the nucleation and precipitation of species in the droplets which can then lead to the formation of large particles. The interaction might also be beneficial to support the formation of particles that are homogeneous in size as well as in chemical composition through gas-to-particle processes. In order to gain insight in such interactions, a liquid-phase temperature-dependent ATR-FTIR study of the processes in the precursor solutions prior to the spray-flame process was carried out.

4.3.2 Iron nitrate and lanthanum nitrate

To minimize solvent evaporation during heating, the maximum temperature in all experiments was limited to 70 °C. The ATR-FTIR spectra of iron nitrate in ethanol are presented in Figure 25a. While most of the signals remained unchanged, the intensity of a weak band at 1558 cm^{-1} (23 °C) that is attributed to organic nitro compounds[152] decreased with increasing temperature, while two new bands developed at 1287 and 948 cm^{-1}. The two latter are assigned to the formation of nitric acid (HNO_3).[153, 154] Through the released crystal water of the iron nitrate ($Fe(NO_3)_3 \cdot 9\ H_2O$), the formation of these peaks can be explained from the hydrolysis of the Fe(III) hexa-aqua ion at low pH. The H^+ ion is released during the formation of the $[(Fe(OH)(OH)_2)_5]^{2+}$ cation, which is in equilibrium with $[Fe(OH_2)_6]^{3+}$.[155] H^+ then reacts with NO_3^- to form HNO_3 because this acid behaves as a weak electrolyte in ethanolic solutions.[156]

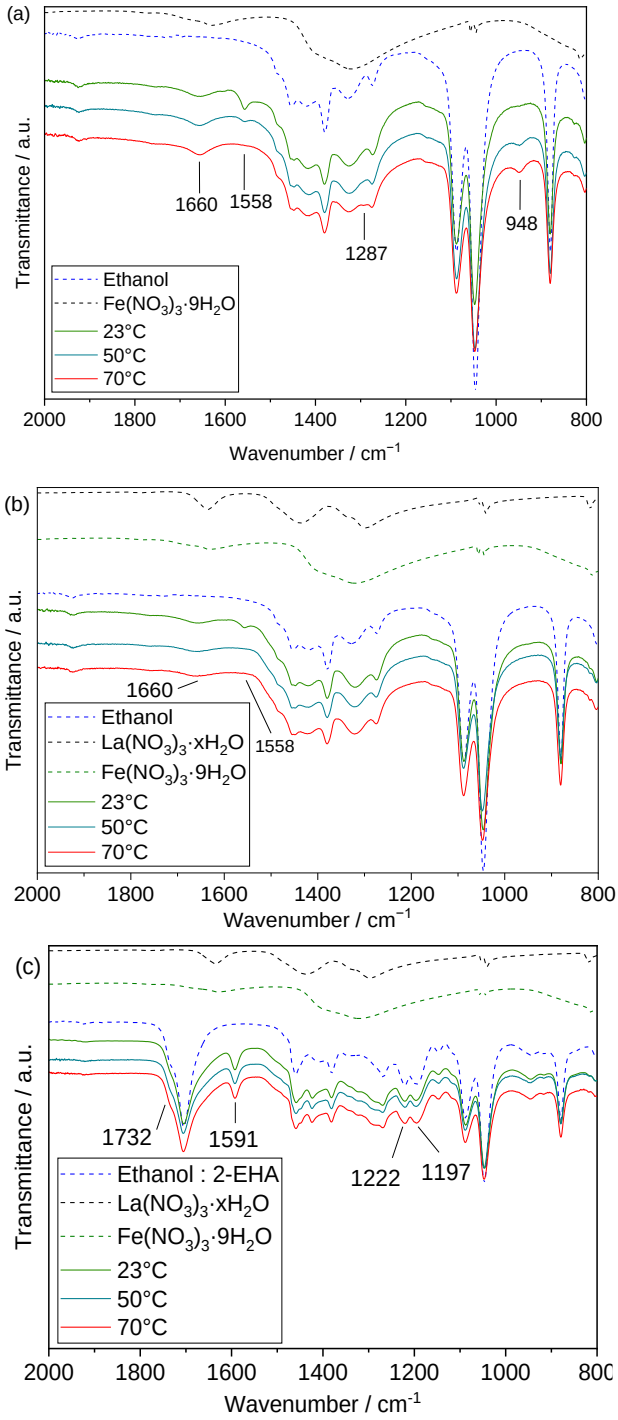

Figure 25. ATR-FTIR spectra of 0.2 mol/l precursor solutions that have been heated to different temperatures. (a) Iron nitrate in ethanol. (b) Lanthanum and iron nitrate in ethanol. (c) Lanthanum and iron nitrate in a 1:1 mixture of ethanol and 2-ethylhexanoic acid. For comparison, the FTIR spectra of pure nitrates and solvents are also given.

The IR absorption spectra of the solutions of lanthanum nitrate and iron nitrate in ethanol are presented in the Figure 25b. With the addition of lanthanum nitrate, the weak band at 1558 cm^{-1} also disappears at higher temperature. The bands at 1287 and 948 cm^{-1}, however, do not appear in this case, indicating the suppression of the formation of nitric acid. The lanthanum nitrate hydrate added to the solution counts with a number of water molecules between four and five according to TGA analysis (not shown). The coordination number of the La^{3+} ion is 9[157] while the trivalent iron ion tends to have a coordination number

of 6 in complexes.[158] The excess water coming from the iron nitrate nonahydrate is likely coordinating with the lanthanum ions and hence decreasing the potential for the hydrolysis of iron.

The ATR-FTIR spectra of the ethanol/2-EHA solutions containing lanthanum nitrate and iron nitrate are presented in Figure 25c. The spectra of the precursor-free ethanol/2-EHA mixture show in contrast to ethanol three specific bands at 1732, 1222, and 1197 cm^{-1}. These bands are assigned to the ester C=O (1732 cm^{-1})[159] and C–O (1222 and 1197 cm^{-1})[160-162] stretching vibrations. The appearance of these peaks suggests an esterification reaction (see reaction (3.4)) of 2-EHA with ethanol. The products of this endothermic and reversible reaction are ethyl 2-ethylhexanoate and water as confirmed by GC/MS, see Figure A 1 in Appendix A. The three vibration bands are also present in the spectra of the solutions containing lanthanum and iron nitrate. Even though the ester's characteristic bands can be seen in the reference spectra of the mixture of ethanol and 2-EHA without the addition of metal nitrates, the esterification of carboxylic acids with alcohols is strongly increased by acids. In this case, iron nitrate, specifically Fe^{3+} acts as a Lewis acid[127, 163] and it has previously been used as a catalyst for the esterification of β-citronellol and acetic acid. Besides the use of iron nitrate, da Silva et al. also used other transition metal nitrates as Lewis acids including cobalt and manganese nitrates but obtaining lower selectivities in comparison with iron nitrate.[127]

The measured absorption band at 1591 cm^{-1} is assigned to the asymmetric vibration of a C=O group coordinated with a metal ion, specifically iron.[164] In a solution without iron nitrate, containing only lanthanum nitrate (not shown), this signal is not present. The interaction of the Fe^{3+} ion with the C=O group has been explained as part of the mechanism to form esters starting from the coordination of the iron ion with the carbonyl group of the carboxylic acid. Subsequent steps involve the reduction of Fe^{3+} to Fe^{2+}, the alcohol addition, water formation, and the oxidation of iron to its original +3 state in order to form the ester.[165] In summary, the band at 1591 cm^{-1} is most likely related to the formation of an iron carboxylate.[14, 166] This type of carboxylates has also been observed in other studies, for example as a product of the reaction between titanium tetraisopropoxide (TTIP) and 2-EHA resulting in a bidentate chelating complex (COO– Ti*) with an FTIR band at 1600 cm^{-1}.[93]

4.3.3 Cobalt nitrate and lanthanum nitrate

The ATR-FTIR spectra of all solutions consisting of a nitrate and ethanol show a weak band at 1660 cm^{-1} (Figure 25a and b, Figure 26a and b). We assume that this band indicates the interaction between ethanol and the NO_3^- group as this weak band has been associated with the formation of nitrate esters.[167, 168] These compounds are explosive and might play a role as low-temperature initiators in the micro explosions of droplets containing nitrates.

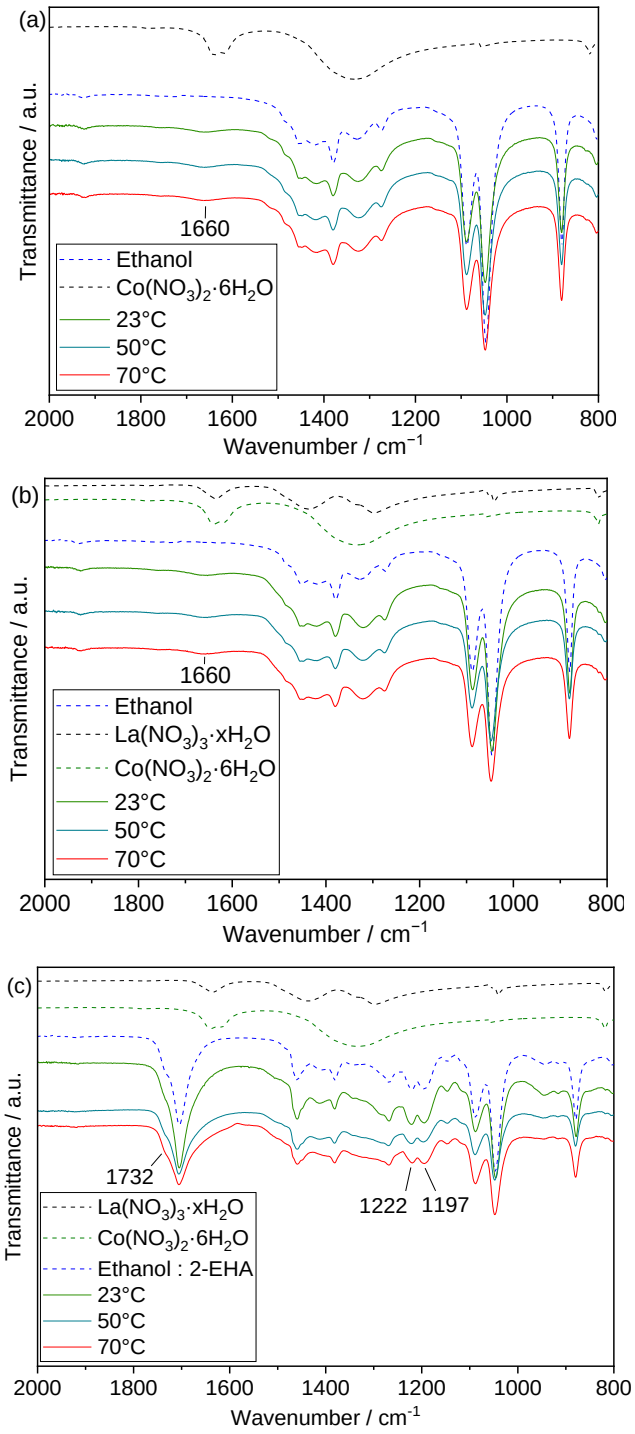

Figure 26. ATR-FTIR spectra of pure ethanol, pure cobalt and lanthanum nitrate, and solutions of 0.2 mol/l cobalt nitrate in ethanol at different temperatures (a); solutions of 0.2 mol/l lanthanum and cobalt nitrate in ethanol at different temperatures (b); and solutions of 0.2 mol/l lanthanum and cobalt nitrate in a 1:1 mixture of ethanol and 2-EHA (c).

In contrast to iron nitrate in ethanol, the two main absorption bands indicating the formation of HNO_3 (1287 and 948 cm^{-1}) were absent in the spectra of cobalt nitrate in ethanol (neither with nor without lanthanum nitrate, Figure 26a and b), indicating a lower degree of hydrolysis of the cobalt in comparison with the iron nitrate.

The FTIR spectra of the solutions of lanthanum and cobalt nitrate in ethanol/2-EHA (50/50 v/v) also clearly indicate the carboxylic acid (1706 cm^{-1}) and the formation of the C=O and C–O ester bonds, see peaks at 1732, 1222, and 1197 cm^{-1} (Figure 26c). This indicates that also cobalt nitrate is active for the esterification reaction. The band at 1591 cm^{-1} related to the formation of metal carboxylates was absent in the spectra of this solution, indicating that this band is specific for the iron nitrate solution. Based on this finding the formation of metal carboxylates in the solutions of lanthanum nitrate, cobalt nitrate, ethanol and 2-EHA cannot be discarded. However, this might be indicative for the higher tendency of iron nitrate to form such compounds in solution at lower temperatures and under the applied conditions.

4.3.4 Effect of the concentration of 2-EHA on iron nitrate/lanthanum nitrate and cobalt nitrate/lanthanum nitrate solutions

The ATR-FTIR analysis concerning the esterification of the precursor solutions for $LaFeO_3$ and $LaCoO_3$ was performed at 50 °C with 2-EHA amounts from 0 Vol.% (only ethanol as solvent) to 70 Vol.% 2-EHA. In the case of solutions containing iron and lanthanum nitrates (Figure 27a), the characteristic ester bands at 1732, 1222, and 1197 cm^{-1} [159-161] develop with increasing 2-EHA concentration. Even at low 2-EHA concentrations, the formation of the absorption band at 1591 cm^{-1} (asymmetric C=O vibration in coordination with iron (iron carboxylate)[164]) is already present. This indicates a selectivity towards the formation of iron carboxylates compared to the ester formation at 2-EHA concentrations below 30 Vol.%.

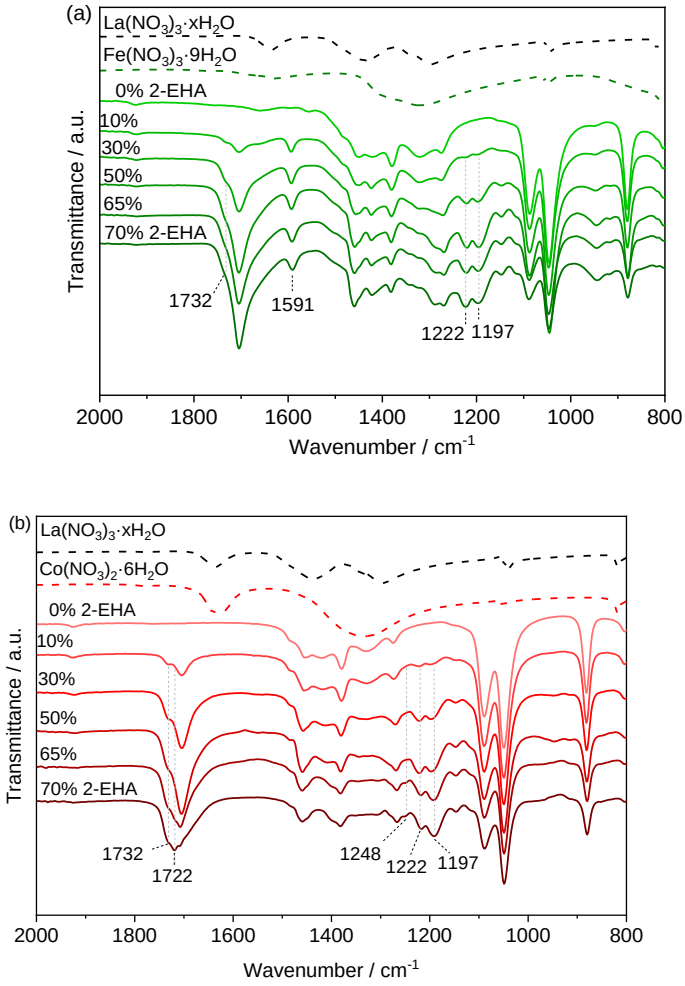

Figure 27. ATR-FTIR spectra of ethanol/2-EHA precursor solutions measured at 50 °C containing 0.20 mol/l of iron and lanthanum nitrates (a) and 0.20 mol/l of cobalt and lanthanum nitrates (b), respectively, with 2-EHA amounts ranging from 0 to 70 Vol.%.

In contrast to the solutions containing iron nitrate, a significant increase of the absorption band at 1732 cm^{-1} is observed for cobalt containing solutions with increasing amount of 2-EHA (Figure 27b) and is attributed to the formation of free C=O ester carbonyl groups.[169] For 2-EHA concentrations above 50 %, two additional absorption bands develop. A band at 1722 cm^{-1}, assigned to (α, β) unsaturated esters,[161, 169] and a band at 1248 cm^{-1}, assigned to C-O-C stretching vibrations.[170] Furthermore, the intensity of the ester CO band at 1197 cm^{-1} [160] increased in comparison with the band at 1222 cm^{-1}, what has been related to isomerism in the ester group,[162] hinting to the formation of ordered interlinked ester structures. To summarize: esterification is preferred in case of cobalt-containing solutions while iron shows some trend towards formation of carboxylates. In addition, esterification at very high concentration of 2-EHA (73 Vol.%), leads to the formation of two phases.

4.3.5 Particle-size homogeneity and phase characterization

The spray-flame synthesis of the $LaFeO_3$ and $LaCoO_3$ perovskites was done as described in materials and methods section (chapter 4.2.1), using the same reactor operating conditions in all cases (if not otherwise indicated) and supplying the respective solution to the reactor. In all cases, the total concentration of metal nitrates in the solutions was constant (0.20 M), but the solvent or mixture of solvents was varied. For each perovskite system, three cases were analyzed: (I) only ethanol as solvent, which is a reference case in which typically a multimodal particle-size distribution is obtained[16]; (II) a mixture of ethanol (50 Vol.%) and 2-EHA (50 Vol.%),[14] which has been reported previously for the preparation of single oxides; (III) and a mixture of ethanol (35 Vol.%) and 2-EHA (65 Vol.%), which is close to the stoichiometric esterification proportions of ethanol:2-EHA (27:73) without the solubility problems related to the dissolution of mainly lanthanum nitrate in high 2-EHA containing solutions at room temperature. These three cases were selected to analyze the effect of the incorporation of 2-EHA in the solutions on the particle-size distribution of the as-synthesized particles and their phase purity, using the information and findings from the ATR-FTIR analysis.

The particle-size distributions were analyzed for both perovskite systems with TEM images from the as-synthesized samples as collected from the filter (Figure 28). As also found in literature,[14, 16] the use of ethanol as solvent for the nitrates results in products with a quite inhomogeneous particle size distribution. This effect is more pronounced for $LaFeO_3$ perovskite (Figure 28a-I) with particle sizes ranging between 3 and 600 nm. The fine particle fraction (detailed distribution presented in Figure 28a-I) shows mainly soft agglomerates with a primary particle count median diameter (fitted to the histogram data) of 4.9 nm. As mentioned before, two main mechanisms have been proposed for the formation of the particles by spray-flame synthesis: Small nanoparticles are assumed to evolve from gas-to-particle transition while large nanoparticles are a result of droplet-to-particle formation.[75] According to the current results, the formation of a multimodal particle-size distribution and large nanoparticles is assumed to be also caused – especially in case of $LaFeO_3$ – by the hydrolysis of the iron precursor. The water molecules required for the hydrolysis process come from two main sources: the crystal water from the metal nitrates and from the SFS process, in which water produced from combustion can be absorbed by the droplets as the boiling point of ethanol (78 °C) is below that of water. This would facilitate the hydrolysis of the iron nitrate and hence, the precipitation of hydroxide species within the droplets already at low temperatures which most likely initiate the formation of large-size particles during spray combustion. The relationship between the hydrolysis degree of precursors and the formation of multi-modal particle size distributions have been previously analyzed for spray-flame synthesized $Li_4Ti_5O_{12}$ by Meierhofer et al. Similar to our findings, they observed the formation of HNO_3 and lithium alcoholate in solutions containing lithium nitrate and ethanol.[93]

a.) $LaFeO_3$

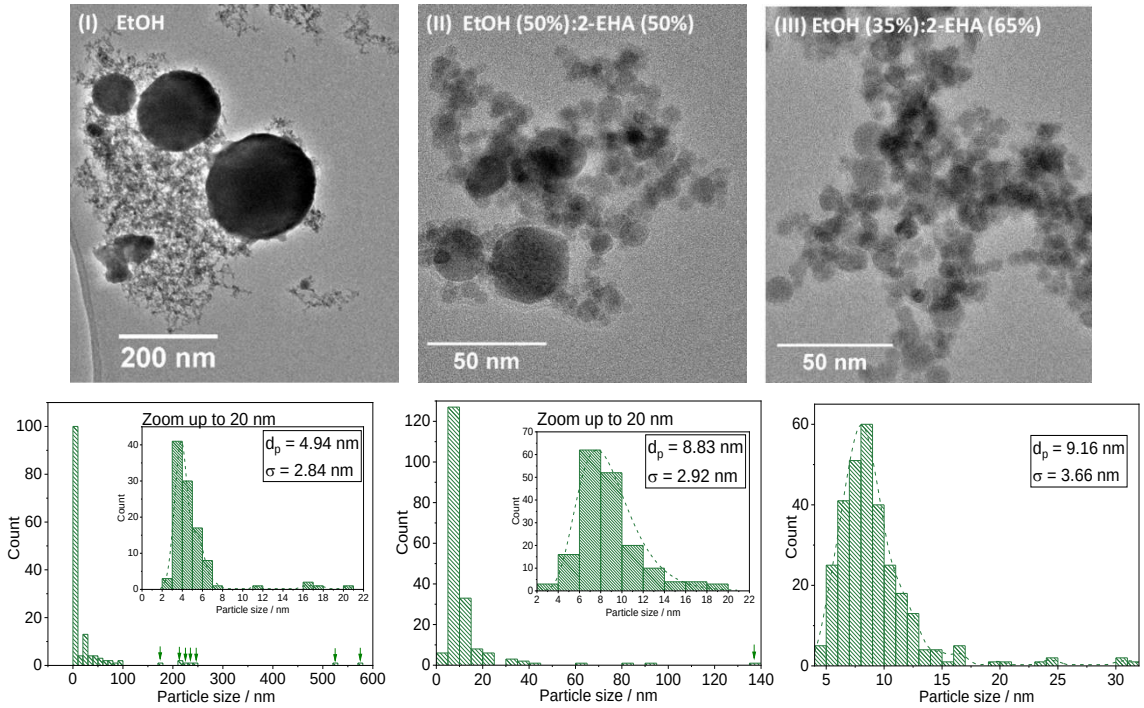

b.) $LaCoO_3$

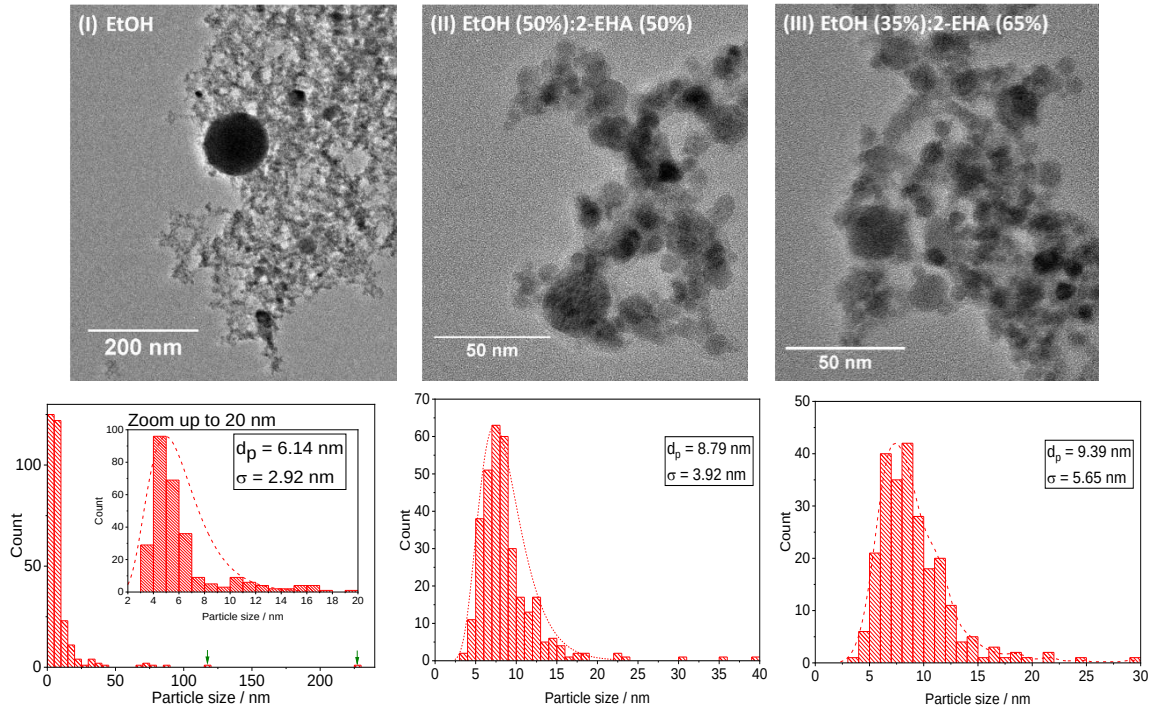

Figure 28. TEM images of $LaFeO_3$ (upper row) and $LaCoO_3$ particles (lower row) synthesized using ethanol (left), ethanol/EHA 50/50 (by volume), and ethanol/EHA 35/65 as solvent. The increase in the concentration of 2-EHA generates a more homogeneous particle size distribution minimizing the formation of particles with a size higher than 20 nm.

For the $LaCoO_3$ perovskite from the ethanol solution (Figure 28b-I), a respective effect on the particle-size distribution can be observed. Nevertheless, the distribution is not as broad as for the $LaFeO_3$. According to the TEM images, the particle size ranges between 3 and 250 nm. The fine particles (sizes up to 20 nm)

have an average size of 6.1 nm. Also in this case, the distribution of the particle size is multimodal. As it was analyzed in the ATR-FTIR section, solutions containing cobalt nitrate and ethanol did not evolve nitric acid with an increase of temperature, indicating a lower hydrolysis degree and a lower formation of metal hydroxide species which are precursors of high-size particles. This helps explaining the reduced presence of large $LaCoO_3$ particles in comparison with $LaFeO_3$ particles.

Figure 28a-II and Figure 28b-II show TEM images of $LaFeO_3$ and $LaCoO_3$ samples synthesized using an ethanol/2-EHA (50/50 by volume) mixture. When 2-EHA is incorporated at this proportion, the particle-size distribution for both perovskite systems becomes narrower. For the $LaFeO_3$ perovskite, the maximum particle size, as seen in the TEM pictures, is decreased from 600 nm (case a-I) to 140 nm. The size of most of the particles ranges from 3 to 20 nm with a count average of 8.8 nm in this interval, larger than in the a-I case. This hints to a different formation mechanism of the particles by the in presence of 2-EHA.

A unimodal particle size distribution is obtained for the $LaCoO_3$ perovskite (Figure 28b-II). In this case, the average particle size is 8.8 nm. According to the TEM analysis, the 50/50 volume proportion of ethanol and 2-EHA seems to be more effective for the $LaCoO_3$ than for the $LaFeO_3$ perovskite in regard to obtaining a homogeneous particle size distribution. According to the previously mentioned FTIR results, carboxylates are formed in the solutions containing lanthanum and iron nitrate. Nevertheless, the resulting $LaFeO_3$ particles were not as narrow in size distribution as $LaCoO_3$ despite the fact that also the lanthanum nitrate and cobalt nitrate solutions did not show indications of low-temperature formation of carboxylates. As indicated in other studies, carboxylate formation might happen at higher temperatures in the droplets.[14] However, one common effect was found in all solutions containing the metal nitrates, ethanol and 2-EHA: The esterification reaction forming ethyl 2-ethylhexanoate. The micro-explosion of the droplets containing ethanol and 2-EHA is possible as the superheating temperature of pure ethanol (189.5 °C[15]) is lower than the boiling point of 2-EHA (228 °C[13]). A study by Rosebrock et al. showed that the droplets without metal precursors and which contained ethanol, 2-EHA, xylene, and diethylene glycol monobutyl ether did not micro-explode, but when metal nitrates, as iron nitrate, were incorporated, the droplets displayed micro-explosions.[15] Different phenomena might promote the conditions for the beginning of the micro-explosions: The decomposition of metal carboxylates (e.g., iron (iii) 2-ethylhexanoate) and the decomposition of ester compounds.

Increasing the concentration of 2-EHA to 65 Vol.%, was beneficial for $LaFeO_3$ leading to a further decrease of the maximum particle size to 30 nm and to a narrowed particle-size distribution, with an average of 9.2 nm (Figure 28a-III). In this case, a lower concentration of ethanol in the droplets means a lower degree of hydrolysis of the iron which is also correlated with a higher boiling temperature of the droplets suppressing water absorption in the droplets from the gas-phase. For $LaCoO_3$, the particle-size distribution also narrows, but the average particle size increases from 8.8 nm (50 Vol.% 2-EHA) to 9.4 nm (65 Vol.% 2-EHA). These values almost exactly match with the particle sizes calculated from the BET area assuming spherical, monodisperse particles and the bulk density of $LaCoO_3$ (7.29 g/cm^3), resulting in 8.7 nm (95 m^2/g, 50 Vol.% 2-EHA) and 9.5 nm (87 m^2/g, 65 Vol.% 2-EHA). As presented in the FTIR analysis, solutions containing cobalt and high concentrations of 2-EHA start to develop ordered interlinked ester structures that might affect the particle sizes. Furthermore, in the solutions containing lanthanum and cobalt nitrate, the effect of hydrolysis is not as strong as in the solutions of iron nitrate. This slightly higher combustion enthalpy of the 2-EHA-rich solutions can be related to higher flame temperatures and therefore, the formation of larger particles.[16] Additionally, as the viscosity of 2-EHA is seven times higher than that of ethanol at room temperature, the Sauter Mean Diameter (SMD) of the droplets is expected to be 42 % higher in the presence of 50 Vol.% 2-EHA compared to pure ethanol (based on the Elktob et al. correlation

for external mixing of air-assisted atomizers[171, 172]). When the 2-EHA concentration is increased to 65 Vol.%, the SMD is expected to further increase by 32 %. Nevertheless, increasing the SMD is considered beneficial for the occurrence of micro-explosions of the droplets because the underlying accumulation of low-boiling compounds in the center of the droplet is more prominent in larger droplets. Therefore, as presented by Mikami et al.,[122] the initial droplet diameter has a fifth-power dependence on the micro-explosions probability.

The effect of the solvent composition on the particle size can be further understood with the BET surface areas (see Figure A 2 in Appendix A). For case I (ethanol as solvent), the BET surface areas of $LaFeO_3$ and $LaCoO_3$ are 15 and 23 m^2/g, respectively. In agreement with the TEM information, the BET surface areas increase for the case II (50 Vol. % 2-EHA), reaching values of 89 m^2/g for the $LaFeO_3$ perovskite, and 95 m^2/g for the $LaCoO_3$ perovskite. Further increasing the concentration of 2-EHA to 65 Vol.% does not significantly influence the specific surface area of the perovskites. Nevertheless, a slight increment from 89 to 92 m^2/g is noticed for the $LaFeO_3$ system in agreement with the TEM results, which indicates a reduction in the number of particles with sizes above 20 nm when a mixture of solvents containing 65 Vol.% of 2-EHA is used, thus contributing to an increase of the SSA. For the $LaCoO_3$ perovskite, the SSA decreases to 87 m^2/g (case III), which matches the particle-size distribution obtained from the TEM pictures (Figure 28b-III).

The use of pure ethanol as solvent not only generates a multimodal particle-size distribution, it also affects the phase composition of the samples. In order to analyze the phase composition of the samples and the effect of 2-EHA, powder XRD patterns are presented in Figure 29a and Figure 30a for $LaFeO_3$ and $LaCoO_3$, respectively. The elemental distribution of lanthanum and iron and lanthanum and cobalt can be seen in the EDX images from Figure 29b and Figure 30b for the $LaFeO_3$ and $LaCoO_3$ perovskites, respectively.

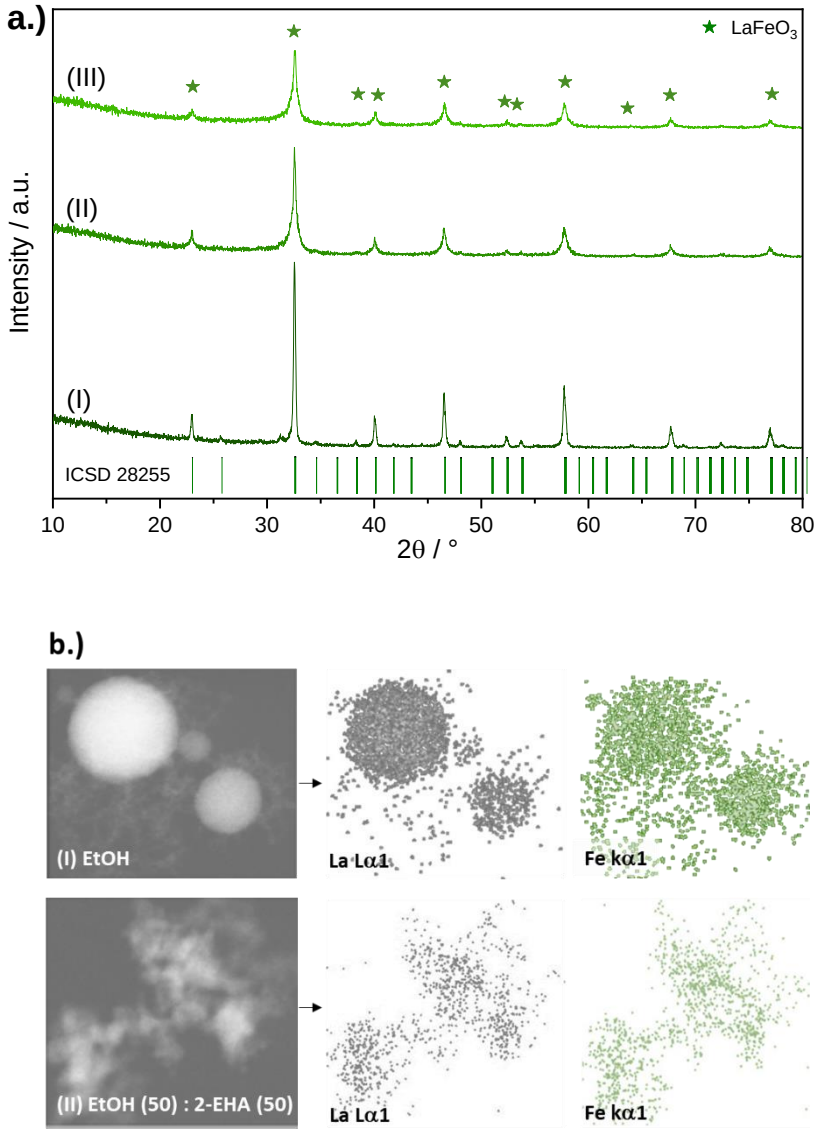

Figure 29. a.) Powder XRD patterns and b.) EDX images of the $LaFeO_3$ perovskites synthesized using (I) ethanol, (II) ethanol/2-EHA (50/50 by vol.) or (III) /ethanol/2-EHA (35/65 by vol.) as solvents.

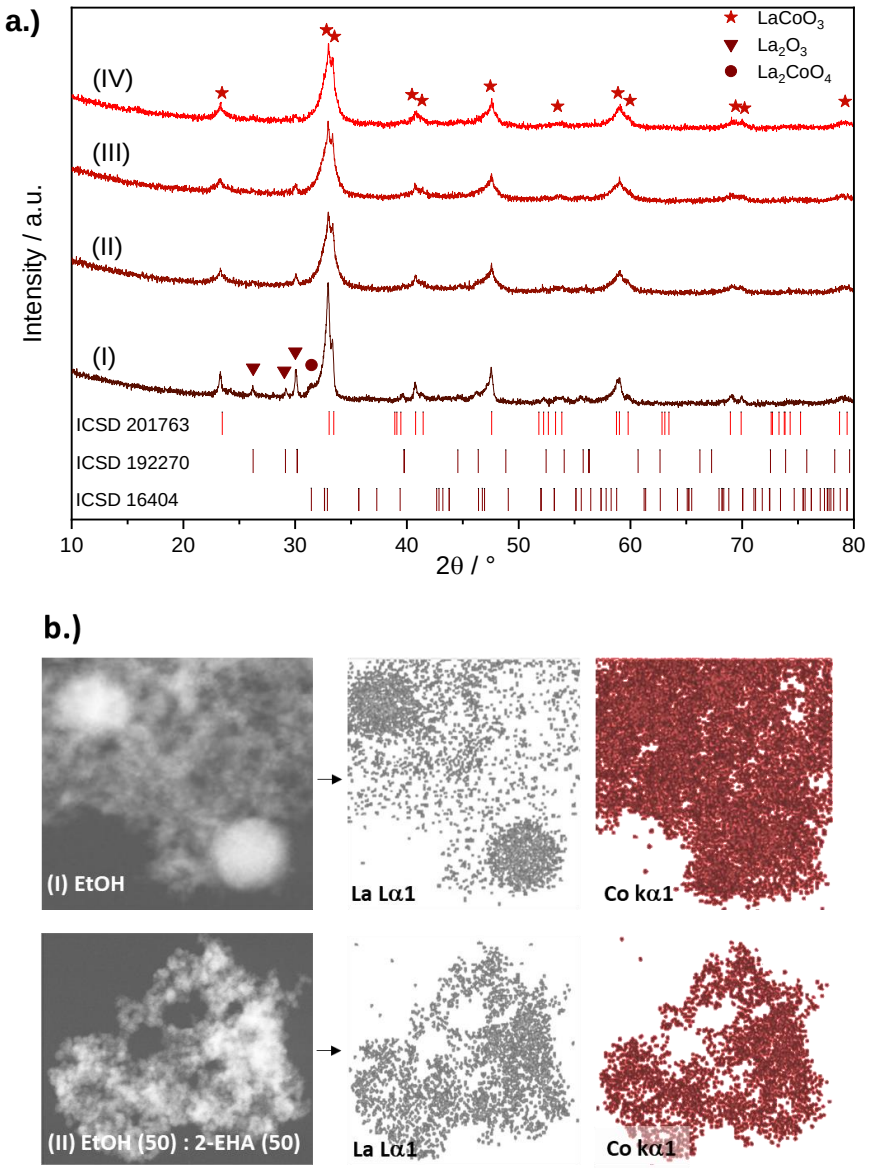

Figure 30. a.) XRD diffractograms and b.) EDX images of the $LaCoO_3$ perovskites synthesized using (I) ethanol, (II) ethanol/2-EHA (50/50 by vol.) or (III) ethanol/2-EHA (35/65 by vol.) as solvents. In cases I, II, and III, a dispersion-gas flow of 7 slm of O_2 was used. The perovskite of case (IV) presented in the XRD results, was synthesized using also an ethanol/2-EHA (35/65 by vol.) mixture but a reduced dispersion gas flow (6 slm) to avoid the formation of La_2O_3.

For the $LaFeO_3$ system and according to the XRD results from the Figure 29a, the use of ethanol as solvent generates mainly the indexed orthorhombic $LaFeO_3$ phase with a space group *Pbnm* (62) (ICSD 28255). In this case, the particles with a size above 80 nm contain more than 99 % of the mass. When 2-EHA is used as solvent, the $LaFeO_3$ particles are phase pure and the lower contribution of large particles is evidenced in the broadening of the peaks and in TEM results (Figure 28a). In this case, the elemental distribution of lanthanum and iron is also improved as presented in Figure 29b-II from EDX analysis.

The $LaCoO_3$ system showed a larger diversity of secondary phases than the $LaFeO_3$ when ethanol was used as solvent. The phases La_2O_3 (ICSD 192270) and La_2CoO_4 (ICSD 16404) were identified besides the rhombohedral $LaCoO_3$ (ICSD 201763) perovskite phase. Small cobalt oxide particles are also expected in this case, which are usually surrounding large lanthanum-rich particles, as seen in Figure 30b-I. The Rietveld refinements of the XRD pattern showed a mean crystallite size of 8 and 9 nm for the $LaCoO_3$ samples

prepared with a dispersion gas flow of 7 and 6 slm, respectively. These values are slightly lower than the results obtained from TEM and BET measurements. Moreover, Rietveld refinement revealed a slight decrease of La_2O_3 content from 2 Wt.% (7 slm) to 1.4 Wt.% (6 slm). However, these values are at the limit of the characterization method. However, as mentioned before, the particle-size distribution in case of $LaCoO_3$ synthesis is more homogeneous than for the $LaFeO_3$.

In the EDX image (Figure 30b-I), it can be seen that the large particles are lanthanum-rich while the surrounding smaller particles are cobalt-rich. In order to verify the phase of these zones, TEM images and Selected Area Electron Diffraction (SAED) patterns were recorded for a 73 nm lanthanum-rich nanoparticle (Figure 31a and b) and for a region of low-size (<10 nm), cobalt-rich nanoparticles (Figure 31c and d). For the lanthanum-rich nanoparticle, the d-spacing values correspond to the crystal structure of the La_2O_3 (ICSD 192270) phase with a space group *P-3m1* (164). For the cobalt-rich region, the d-spacing values correspond to the (220), (311), (222) and (511) planes of the Co_3O_4 cubic structure (ICSD 28158) with a space group *Fd-3mS* (227). This verifies the assumed presence of small size cobalt oxide particles in the sample synthesized using ethanol as solvent.

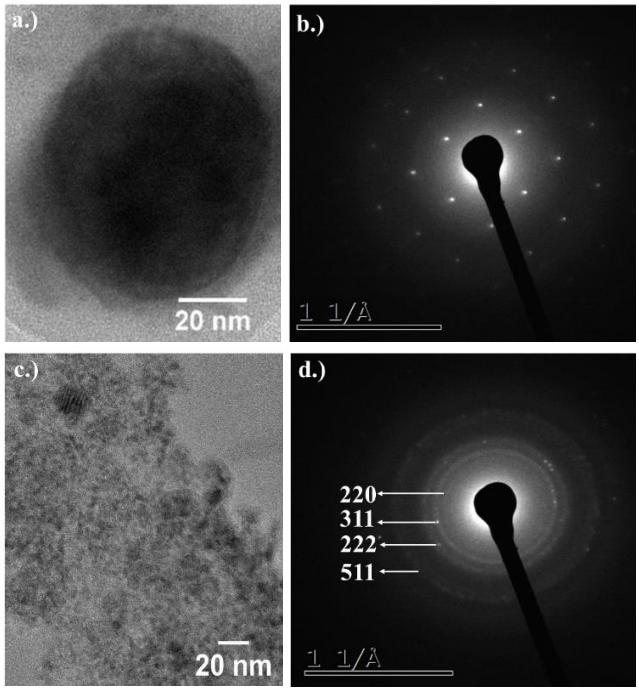

Figure 31. TEM images and SAED patterns of a lanthanum-rich nanoparticle (a, b) and of a cobalt-rich region of nanoparticles (c, d) from a polydisperse $LaCoO_3$ sample synthesized using ethanol as solvent. Based on the lattice spacing, the La-rich nanoparticle was identified as La_2O_3 while the Co-rich region is mainly composed of Co_3O_4.

The incorporation of 2-EHA in solution avoids the formation of the La_2CoO_4 phase while the weight fraction of the La_2O_3 phase decreases with increasing content of 2-EHA in solution. In order to further decrease the La_2O_3 content, the dispersion gas flow was decreased from 7 slm (Figure 30a-III) to 6 slm (Figure 30a-IV). This enabled to increase the flame temperature and the initial diameter of the droplets, and thus also increases the probability for micro-explosions.

4.3.6 Temperature-programmed CO oxidation of the $LaMO_3$ (M = Fe, Co) perovskites

$LaFeO_3$ and $LaCoO_3$ perovskites were tested in the catalytic oxidation of carbon monoxide. As can be seen, the group of $LaCoO_3$ perovskites presents a higher activity for the conversion of CO to CO_2 than the $LaFeO_3$ group (Figure 32a). The light-off temperature of the $LaCoO_3$ perovskites is about 100 °C lower than that

of the $LaFeO_3$ perovskites. 50 % CO conversion is reached at around 160 °C for the best-performing $LaCoO_3$ sample that was generated from a precursor solution in an ethanol/2-EHA (35/65) solution and a dispersion gas flow of 6 slm. This sample also shows the lowest light-off temperature (95 °C) with 10 % CO conversion at about 100 °C and a complete CO conversion was reached at 206 °C. The perovskite structure wasn't affected by the catalytic test as shown in the X-ray diffraction patterns (Figure 32b).

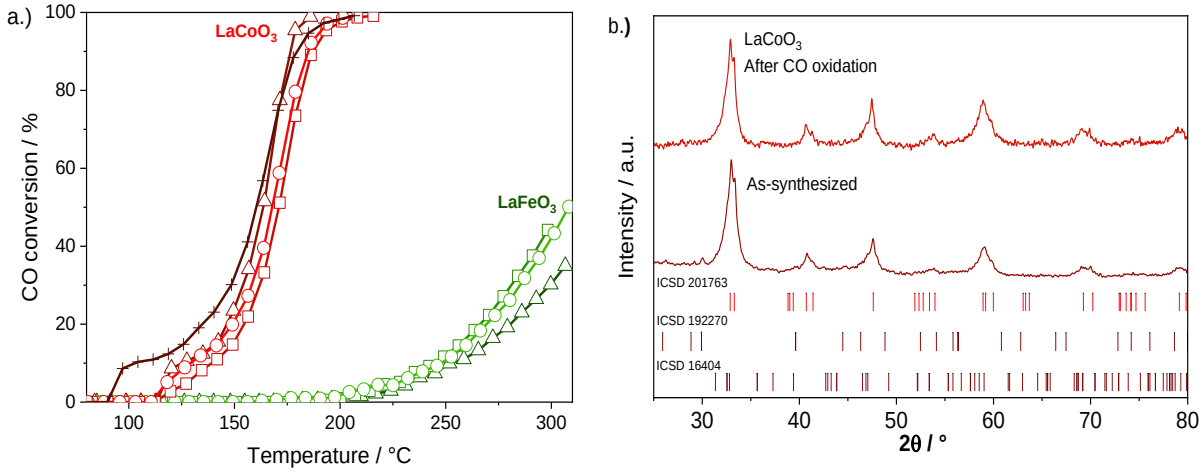

Figure 32. (a) CO oxidation of the $LaFeO_3$ and $LaCoO_3$ perovskites. Cases: Ethanol (△), ethanol/2-EHA (50/50 by vol.) (□), ethanol/2-EHA (35/65 by vol.) (○). Case (+): additional sample of $LaCoO_3$ synthesized using 6 slm O_2 as dispersion gas with ethanol/2-EHA (35/65 by vol.). All other samples were synthesized with O_2 dispersion gas flow of 7 slm. (b) Powder XRD patterns of $LaCoO_3$ as-synthesized and after CO oxidation.

By contrast, in case of the $LaFeO_3$ perovskites, 50 % CO conversion is not even obtained at 300 °C. Several reports agree with the higher activity of the $LaCoO_3$ over $LaFeO_3$ perovskites for the CO oxidation.[8, 173] However, both materials show a very high catalytic activity compared to literature. For comparison, perovskites synthesized by batch processes (e.g., Pechini or Sol-Gel method) typically present much lower activities for CO oxidation, e.g., 50 % CO conversion at 240 °C for the $LaCoO_3$ perovskite[174] and at 430 °C for the $LaFeO_3$ perovskite.[61]

The La^{3+} ion is assumed to be inactive[27, 175] for CO oxidation, with the 3d transition metal ion, Co^{3+} being active. Fierro et al. indicated that the CO oxidation over perovskites happens basically as a suprafacial process.[27] This means that the symmetry and energy of the orbitals near the Fermi level determine efficiency of the catalyst.[176] According to a study of Jia et al, the compounds $LaCoO_3$ and $LaFeO_3$ have band gaps of 0.80 and 2.20 eV, respectively.[177] In addition to these electronic considerations, the Lewis acidity of the surface due to the transition metal cations will also change with the composition and may affect the adsorption properties, e.g., the interaction of CO with the Lewis acid sites distributed on the surface of $LaCoO_3$ catalysts has been previously studied and demonstrated using DRIFTS.[178] Therefore, a higher redox activity of the $LaCoO_3$ perovskites is expected. From the mechanisms proposed for the CO oxidation on the $LaCoO_3$ perovskite, the Co^{3+} species (Lewis acidic sites) act as active sites for the adsorption of CO, while the Co^{2+} sites, which originate from the formation oxygen vacancies,[49] preferentially adsorb molecular oxygen.[8]

For the $LaFeO_3$ samples, a higher activity was found for the samples synthesized using mixtures of ethanol and 2-EHA instead of using only ethanol. In this case, this is thought to be associated with the high specific surface areas, 89 and 92 m^2/g, of the samples, which were synthesized with 50 and 65 Vol.% 2-EHA, respectively. In contrast, the BET SSA of the sample made using only ethanol as solvent was 15 m^2/g).

4.4 Conclusions

This work presents the spray-flame synthesis of single-phase $LaFeO_3$ and $LaCoO_3$ perovskite nanoparticles with narrow size distribution and high specific surface area using nitrates as precursors. This was achieved by the addition of 2-ethylhexanoic acid (2-EHA) to the solutions of the corresponding metal nitrates in ethanol. 2-EHA has been previously related to cascade-like micro-explosions of droplets in the spray flame process through the superheating of ethanol.

In this work, the effect of 2-EHA in the solutions prior to the spray-flame processes was investigated in order to understand the chemical interactions of metal nitrate precursors, ethanol and 2-EHA. Modifications of the precursor solutions were analyzed by liquid-phase temperature-dependent ATR-FTIR for the corresponding metal nitrates dissolved in ethanol, ethanol/2-EHA (50/50 by vol.), and ethanol/2-EHA (35/65 by vol.). It was identified that HNO_3 can be formed when the temperature is increased to 70 °C in the solutions containing iron nitrate and ethanol, indicating a high degree of hydrolysis. In the solutions containing lanthanum nitrate, iron nitrate (or cobalt nitrate) and ethanol, HNO_3 was not identified.

It was found that when 2-EHA is added to the ethanol-containing solutions of lanthanum nitrate and iron nitrate (or cobalt nitrate), esterification occurs producing ethyl 2-ethylhexanoate and water. In this reaction, the transition metal nitrates are probably acting as low-temperature catalysts as it has been indicated in other report for the reactions of β-citronellol and acetic acid. The coordination of a carboxyl group with a metal ion could only be identified in the solutions containing iron from room temperature until 70 °C. This analysis expresses the importance of early stage reactions (catalytic esterification, formation of carboxylates, nitrate-ester interaction) in the solutions as possible promoters of micro-explosions and thus narrow nanoparticle size distributions.

The width of the particle-size distribution of both perovskite materials was significantly reduced when 2-EHA was incorporated in the solution. In the case of $LaFeO_3$, decreasing the content of ethanol in solution to 35 %, helps lowering the degree of hydrolysis of the iron precursor and hence, the formation of large particles from the droplet-to-particle mechanism. For $LaCoO_3$, the particle-size distribution was unimodal even with a 50 % ethanol in solution, indicating a higher effectivity of the utilization of 2-EHA for this material in comparison to $LaFeO_3$.

The formation of secondary phases as La_2O_3 and La_2CoO_4 was evident in the $LaCoO_3$ case when only ethanol was used as solvent. It was identified by EDX that in this case, the large particles (>80 nm) were lanthanum-rich, with cobalt-rich particles in the range of 3 to 20 nm. Besides improving the particle size homogeneity, the incorporation of 2-EHA in solution was effective to improve the atomic La and Co distribution in the particles, avoiding the formation of La_2CoO_4 and helping in the control of the La_2O_3 secondary phase, which content was further reduced by decreasing the oxygen dispersion gas flow in the reactor from 7 to 6 slm.

The $LaFeO_3$ and $LaCoO_3$ perovskites were tested for their activity in low-temperature catalytic oxidation of carbon monoxide (CO). In agreement with several reports, the $LaCoO_3$ perovskites are more active for this reaction than the $LaFeO_3$ compounds. The temperature required for a 50 % CO conversion in the $LaCoO_3$ case was around 160 °C, almost half of the temperature required for the same conversion level in the $LaFeO_3$ case.

5 Spray-flame synthesis of $LaMnO_3$ nanoparticles for selective CO oxidation (SELOX)

The content of this chapter was published in Energy & Fuels:

> **Angel, S.**; Tapia, J. D.; Gallego, J.; Hagemann, U.; Wiggers, H., Spray-Flame Synthesis of $LaMnO_{3+\delta}$ Nanoparticles for Selective CO Oxidation (SELOX). *Energy & Fuels* **2021** *35* (5),4367-4376.

Further information related to this chapter is presented in Appendix B (Chapter 11.2), including Figure B 1 to Figure B 5, Table B 1, and Table B 2.

My contribution in this work includes: Research conceptualization, synthesis, characterization of precursors and materials, analysis of data including the catalytic results, writing of the manuscript. U. Hagemann contributed with XPS measurements/analysis. J.D. Tapia and J. Gallego contributed with catalytic measurements/analysis. H. Wiggers contributed to conceptualization, result interpretation, and writing.

5.1 Introduction

Lanthanum-containing manganites ($LaMnO_3$) are perovskite-type oxides that have been studied over the years for their diverse and interesting magnetic and electrochemical properties, e.g., colossal magnetoresistance in doped manganites[179, 180] and high-energy storage and power densities in Li-ion batteries.[181, 182] Recently, these compounds also attracted growing attention for their versatile catalytic properties combined with chemical stability, especially regarding their potential as low-cost substitutes of noble-metal catalysts for environmentally relevant reactions as CO oxidation and CO selective oxidation (SELOX)[8, 183, 184]. They can be applied for, e.g., removing CO from enclosures and residue gases[185] to avoid the poisoning of catalysts in proton-exchange membrane fuel cells for H_2 production.[8, 186]

The oxidation activity of $LaMnO_{3+\delta}$ perovskites has been mainly attributed to the oxygen mobility within the lattice[187] and the redox capability[183] of the Mn cations ($Mn^{3+} \rightleftharpoons Mn^{4+}$). The Mn^{4+} content (percentage of the total manganese species) in the $LaMnO_{3+\delta}$ perovskite flexibly varies and stabilizes in function of structure polymorphs[51]. According to Tomaszewski et al, the orthorhombic phase *Pnma II* counts with a Mn^{4+} content lower than 14 % (abbreviated as *O')*, followed by the orthorhombic phase *Pnma I*, with a Mn^{4+} content ranging between 14 and 26 % (abbreviated as *O)*, while the Mn^{4+} content of the rhombohedral phase with R-3c space group is usually higher than 26 % but lower than 30 % (abbreviated as *R)*[55]. The formation of a specific polymorph depends on the selected synthesis technique[188]. In order to produce rhombohedral/orthorhombic-$LaMnO_{3+\delta}$ nanoparticles, typically batch processes as sol-gel[181] or the citrate method[188] are used. These processes count with a final calcination step involving temperatures usually higher than 600 °C[183, 189] and long annealing periods of > 2h, making the formation of crystalline manganites with high surface area and thus low-size particles (ideally < 20 nm) a challenge. As an alternative to common batch processes, the spray-flame synthesis (SFS) is a versatile, continuous and scalable technique that allows to produce oxide materials with high crystallinity, high specific surface areas and with a controlled chemical and phase composition.[74, 76] It is used for the synthesis of perovskites using either organometallic precursors (e.g., lanthanum(III) 2-ethylhexanoate or lanthanum(III) acetate, strontium(II) acetate, iron(II) naphtenate or iron(II) acetate, cobalt(II) acetylacetonate, barium(II) acetate)[190-192] or inorganic metal precursors (e.g., lanthanum(III) nitrate, cobalt(II) nitrate and iron(III) nitrate).[17, 193] Regardless of the type of metal precursor, avoiding the formation of undesired secondary phases is always a challenge for the SFS of perovskites. Moreover, when low-cost inorganic metal precursors (e.g., metal nitrates)

are used in combination with polar solvents as EtOH, unwanted multimodal particle size distributions are often obtained in SFS.[14, 17]

Recently, we successfully synthesized phase pure mixed oxides with unimodal particle size distributions (PSD) using metal nitrates as precursors and a mixture of EtOH and 2-ethylhexanoic acid (2-EHA) as solvent.[194] While the use of such solvent mixtures in SFS has been proven to be beneficial for improving the quality (e.g., phase purity and PSD) of single (e.g., Al_2O_3, Co_3O_4[14], Fe_2O_3[195]) and mixed oxides (e.g., $Li_4Ti_5O_{12}$[93], $LaCoO_3$, $LaFeO_3$[194]), the understanding of the chemical/physical phenomena behind this effect is a matter of current multidisciplinary research.[80, 196, 197] For starting, as the superheating temperature of ethanol (189.5 °C[123]) is lower than the boiling point of 2-EHA (227.5 °C[198]) at 1 bar abs., droplets containing the EtOH/2-EHA mixture have the potential to undergo a sudden fragmentation (e.g., micro explosion) through the superheating EtOH enabled by the high heat transfer from the exterior to the center of the droplets in contrast with a low mass transfer of ethanol from the center to the surface of the droplets (e.g., mixture of solvents with Lewis (Le) numbers much greater than unity[199]). Additionally, as 2-EHA has a higher combustion enthalpy than ethanol, the flame temperature increases when EtOH/2-EHA mixtures are used in comparison with EtOH-based solutions,[92] most likely influencing the particle size and crystallinity of the spray-flame-synthesized materials.

From a chemical point of view, the use of 2-EHA-based solutions in SFS has been related to the formation of attractive metal carboxylates (e.g., 2-ethylhexanoates)[74] due to ligand-exchange reactions of metal nitrate precursors with 2-EHA. Nevertheless, it was shown that in solutions containing La, Fe- and La, Co-nitrates in EtOH/2-EHA mixtures, the ligand-exchange reaction depends on the transition metal and usually proceeds slowly at the reported conditions.[194] EtOH/2-EHA mixtures are also subject to catalyzed esterification depending on the transition metal.[114, 200] The formation of water in this reaction might lead to the hydrolysis of metal ions and the low-temperature precipitation of metal hydroxide species in the droplets causing the generation of high-size particles via a droplet-to-particle mechanism.[75] To summarize, the use of EtOH/2-EHA mixtures is a promising but complex approach for the SFS of metal oxides with several associated challenges. In particular, the role of chemical interactions at low temperatures with redox-active metal ions is not yet fully understood and is therefore also of particular interest for Mn-containing solutions. Such interactions might affect the solution composition and thus the particle size distribution/homogeneity and the formation of specific $LaMnO_3$ polymorphs.

This study explores the spray-flame synthesis of the $LaMnO_3$ perovskite from solutions containing metal nitrate precursors and (i) ethanol as a reference case or (ii) a mixture of ethanol and 2-ethylhexanoic acid (2-EHA) (1/1 v/v) as solvent. The precursor solutions were analyzed using temperature-dependent infrared (ATR-FTIR) and UV-Vis spectroscopic studies in order to investigate their stability and thus possible effects on the synthesized materials while the particles were characterized by X-ray diffraction (XRD), Raman spectroscopy, transmission electron microscopy (TEM), energy-dispersive X-ray spectroscopy (EDX), temperature programmed desorption of oxygen (O_2-TPD), hydrogen temperature programmed reduction (H_2-TPR), Brunauer, Emmett, and Teller specific surface area (BET SSA) and X-ray photoelectron spectroscopy (XPS). Additionally, in order to remove residual organics and water adsorbed on the particles surface, the samples were heat-treated under air at 500 °C and compared with the as-synthesized perovskites. Finally, the heat-treated materials were tested regarding their catalytic activity for CO oxidation and CO selective oxidation (SELOX).

5.2 Experimental section

5.2.1 Spray-flame synthesis

The spray-flame synthesis of the $LaMnO_3$ samples was performed in a self-developed and enclosed reactor which diagram is presented in Figure 9. The precursor solutions were prepared by dissolving $La(NO_3)_3{\cdot}xH_2O$ (AppliChem Panreac, >99.0 %) and $Mn(NO_3)_2{\cdot}4H_2O$ (Alfa Aesar, >98 %) in pure ethanol or in a mixture of 50 Vol.% of ethanol (VWR, >99.9 % purity) and 50 Vol.% of 2-ethylhexanoic acid (2-EHA) (Alfa Aesar, >99 % purity) in order to obtain a total metal-ion concentration [La + Mn] of 0.2 mol/l.

Each corresponding solution was filled in a syringe pump and supplied to the reactor at a constant flow rate of 2 ml/min via a hollow needle located at the center of an external mixing two-fluid atomizing nozzle.[150, 151] Using oxygen (Air Liquide, 99.95 %) as dispersion gas, a fine spray was formed and ignited by a continuously burning premixed pilot flame (3 slm CH_4 (Air Liquide, N25, 99.5 %) and 5 slm O_2 (Air Liquide, 99.95 %)). The flame was stabilized by a sheath-gas flow (140 slm, compressed air) added via a porous sintered bronze plate (10 cm diameter), coaxially surrounding the spray nozzle. The pressure in the reactor chamber was kept constant at 970 mbar abs., and an additional stream of quenching gas flow (230 slm, compressed air) was supplied downstream the reaction zone in order to avoid condensation of water and to reduce the temperature of the off-gas for protecting the filter used to collect the nanoparticles. To investigate whether the sample preparation for the catalytic tests affects the particle morphology and phase composition, the collected samples were heat-treated at 500 °C for 1 h under a continuous air flow (500 l/h) in a Nabertherm L 1/12/R6 muffle furnace. This standard procedure was used in advance of the catalytic tests to remove adsorbates.

5.2.2 Characterization of precursor solutions

As possible reactions among metal ion precursors and solvents might influence the stability of the solutions and thus the particle formation during the spray-flame synthesis, the prepared solutions were analyzed by Fourier-transform infrared spectroscopy (FTIR) and ultraviolet-visible spectroscopy (UV-Vis) from room temperature up to 70 °C.

First, closed vials containing 20 ml of each prepared solution were put into a stirred water bath heated at 30, 50, and 70 °C, respectively. After maintaining each temperature for 15 min, an aliquot of each corresponding solution was extracted using a probing pipette which allowed to place the sample of interest directly on the ATR holder to measure the FTIR spectra or inside a quartz cuvette to measure the UV-Vis spectra, in order to identify temperature-related non-reversible chemical transitions during heating. The Fourier-transform infrared (FTIR) spectra were obtained from the average of 32 scans recorded in ~1.7 min (~3.2 s/scan) from 400 to 4000 cm^{-1} with a resolution of 4 cm^{-1} using a Bruker Vertex 80 with standard optical components (KBr beam splitter, DigiTect DLaTGS detector, Attenuated Total Reflectance (ATR) sample holder). Ultraviolet-visible (UV-Vis) spectra were recorded from 200 to 800 nm with a high-performance dual-beam Varian Cary 400 spectrophotometer (silica overcoated optics, Schwarzschild coupling optics, PbS detector), using a scan rate of 600 nm/min and a step size of 1 nm.

5.2.3 Characterization of as-synthesized and heat-treated samples

The particles were analyzed with transmission electron microscopy instrument (JEOL JEM 2200FS) to study the particle size, morphology and elemental composition by EDX mapping (energy dispersive x-ray spectroscopy).

X-ray diffractograms (XRD) were measured at 2θ = 10–70° with a step size of 0.05° using a PANalytical X´Pert PRO device operated with Cu-Kα radiation (0.15406 nm, 40 kV, 40 mA). Phase characterization of the samples was also performed with Raman spectroscopy using a Renishaw InVia confocal Raman microscope with a 633 nm laser operating at 1 % of the total laser power (15 mW) in order to avoid the oxidation of the samples.

X-ray photoelectron spectra (XPS) were recorded using an ULVAC-PHI device (Versaprobe II) using a monochromatic Al Kα radiation source and a pass energy of 11.75 eV, a spot size of 100 µm and an energetic resolution of ~0.5 eV. The calibration of the spectra was done using the C1s adventitious carbon C–C binding energy (284.8 eV).

The specific surface (SSA) area of the perovskite samples was determined with a Quantachrome Nova2000 device using the Brunauer, Emmet, Teller (BET) method after outgassing the samples for 18 h in vacuum at 250 °C.

5.2.4 Catalytic CO oxidation and selective oxidation (SELOX) of CO

In order to investigate both the reducibility and the formation of active oxygen species on the materials surface, temperature-programmed reduction (H_2-TPR) and temperature-programmed desorption (O_2-TPD) experiments were applied to the heat-treated samples using a Chemisorption AutoChem 2920 Micromeritics® equipment equipped with a thermal conductivity detector (TCD). The heat-treated samples (100 mg) were inserted into a U quartz reactor and pretreated at 500 °C for 15 min under the flow of a mixture of gases (10 Vol.% O_2 in Ar). The H_2-TPR experiments were performed with a mixture of 5 Vol.% H_2 in Ar (30 ml/min) while increasing the temperature from room temperature to 500 °C at 10 °C/min. The TPD-O_2 experiments were performed under pure argon flow (30 ml/min).

In order to investigate the catalytic activity, temperature-programmed reactions (TPR) were carried out in a vertical microreactor using 100 mg of the heat-treated oxides. The reaction gas mixture consisted of 5 Vol.% CO, 5 Vol.% O_2, 20 Vol.% H_2 for the SELOX reaction or 0 Vol.% for the normal CO oxidation, and He balance. A total gas flow rate of 100 ml/min was used in all cases. The reaction conditions gave a gas hourly space velocity (GHSV) of 10000 h^{-1}. The reactor off gas was analyzed with a quadrupole mass spectrometer (Pfeiffer QMS OmniStar 300) and the intensity of M/Z signals: 2, 15, 18, 28, 30, 32, and 44, corresponding to: H_2^+, CH_4^+, H_2O^+, CO^+, $HCOH^+$, O_2^+, and CO_2^+, respectively, were monitored continuously while raising the temperature from room temperature to 500 °C at a heating rate of 10 °C/min.

5.3 Results and discussion

5.3.1 Temperature dependent ATR-FTIR/UV-Vis analysis of solutions containing the metal nitrates and the combination of solvents

The ATR-FTIR spectra of a solution containing $La(NO_3)_3{\cdot}x\ H_2O$ and $Mn(NO_3)_2{\cdot}4\ H_2O$ in EtOH heated at different temperatures are presented in Figure 33a. Besides the characteristic bands of EtOH, which reference spectrum is also shown, two bands were identified at 735 and 819 cm^{-1} (not to be confused with the EtOH characteristic vibration band at 804 cm^{-1}), corresponding to typical out-of-plane and in-plane nitrate group vibrations.[201-204] Increasing the temperature from 30 to 70 °C did not affect the spectra.

ATR-FTIR spectra of the 1:1 ethanol:2-ethylhexanoic acid solutions (EtOH/2-EHA) are presented in Figure 33b. As previously observed in case of iron nitrate precursor,[194] the solution mixture reacted forming ethyl 2-ethylhexanoate ester and water. The weak ester C=O antisymmetric vibration band at 1732 cm^{-1} and

the ester C–O vibration bands at 1222 and 1197 cm^{-1} did not present an apparent modification when the temperature was raised from 30 to 70 °C. Nevertheless, the visual inspection of the solution while heating revealed a distinct color transition suggesting a redox reaction of the metal ions (see Figure B 1 from Appendix B). At room temperature and at 30 °C, the solution presented a pale pink tone which is the characteristic color of the Mn^{2+} aqueous complex $[Mn(H_2O)_6]^{2+}$ in neutral/acidic solutions[205]. At temperatures above 35 °C, the color started to change, reaching a pale black tone at 50 °C and an intense darker tone at 70 °C. This transition might be an indication of the formation of Mn(II)-2-ethylhexanoate from manganese nitrate and 2-EHA but was excluded due to the absence of its characteristic IR-bands at 1589 cm^{-1} (CO_2 antisymmetric stretch) and at 1550 cm^{-1} (antisymmetric shoulder)[206] in the spectra shown in Figure 33b.

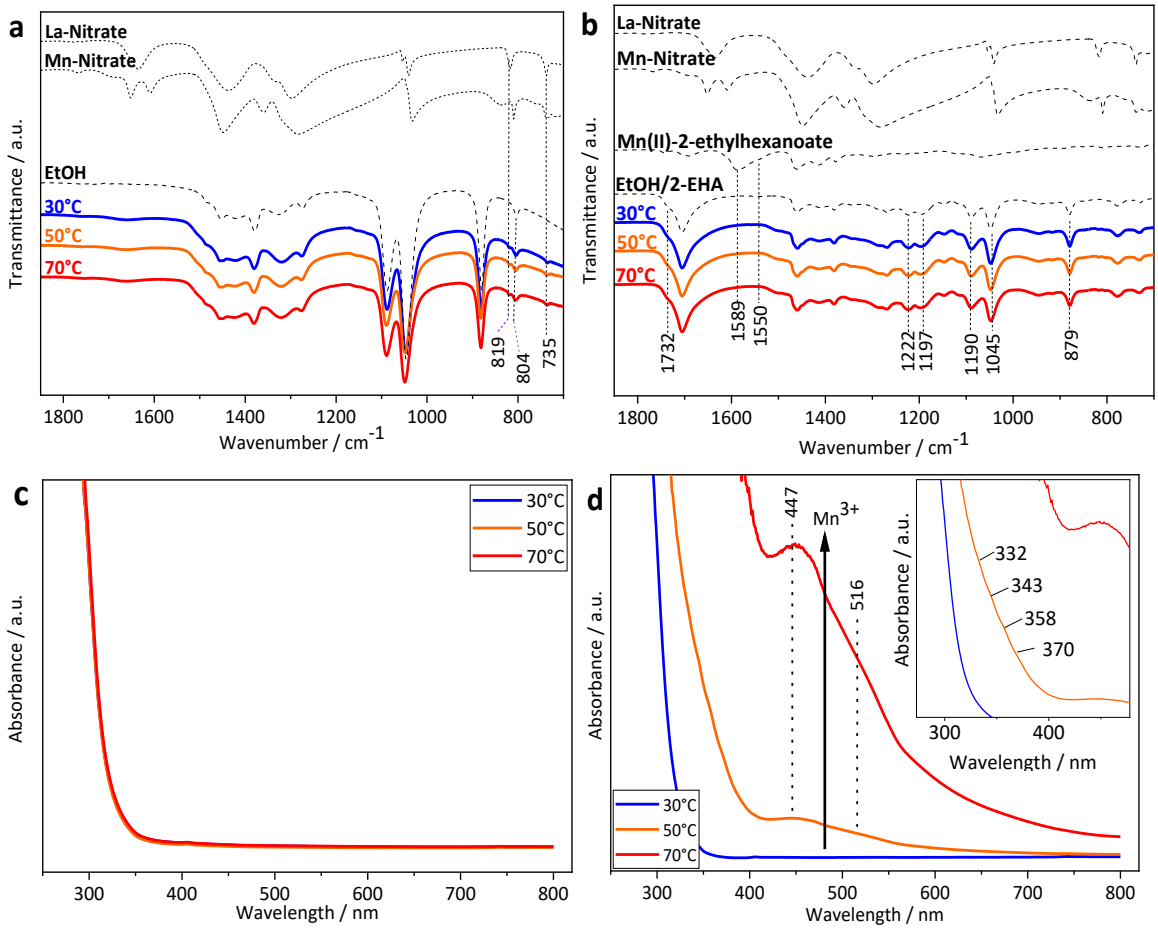

Figure 33. Temperature-dependent ATR/FTIR and UV/VIS measurements of metal-nitrate-based solutions prepared using either ethanol as solvent (**a** and **c**) or a 1/1 mixture of ethanol and 2-EHA (**b** and **d**).

UV-Vis absorption spectra of the metal nitrate solutions in EtOH and EtOH/2-EHA are presented in Figure 33c and d, respectively. For the precursor solution in EtOH (Figure 33c), the spectra exhibited an ultraviolet feature below 300 nm due to the cut-off wavelength of ethanol,[207] but no features were observed in the visible, indicating only the presence of Mn^{2+} species in solution[208] regardless of the temperature. This was also the case for the precursor solution in the EtOH/2-EHA mixture heated at 30 °C (Figure 33d). Heating at higher temperature caused the development of one main peak at λ = 447 nm and a shoulder at λ = 516 nm that can be associated with manganese complexes counting with a mixed oxidation state of Mn^{2+} and Mn^{3+}.[208-210] This indicates the oxidation of Mn^{2+} to Mn^{3+} and the stabilization of Mn^{3+} (possibly Mn^{2+}-Mn^{3+}) complexes. This process is most likely happening through the release and reduction of nitrate

groups (NO_3^-/NO_x), previously identified in solutions of $Mn(NO_3)_2$ in 2-picolinic acid and acetic acid.[208] The explanation is supported by four very weak shoulders at λ = 333, 345, 357, and 371 nm presented in the inset of Figure 33d, indicating the formation of nitrous acid (HNO_2).[211] We attributed the formation of NO_2 (N-oxidation state = +4) to the reduction of NO_3^- (N-oxidation state = +5), balancing the oxidation of Mn^{2+} to Mn^{3+}. However, the oxidation process did not affect the stability of the solution.

5.3.2 Particle size and phase characterization of as-synthesized materials

TEM investigation of materials produced from ethanol solution clearly showed the formation of a multi-modal particle size distribution with sizes ranging from 4 nm until almost 2 μm in diameter, as it can be observed in Figure 34a. In strong contrast, the use of the mixture of ethanol and 2-EHA as solvent led to the formation of a much more homogeneous particle size distribution (Figure 34b), mainly consisting of nanoparticles with sizes ranging between 4 nm and 15 nm with an average particle size (d_p) of 8 nm ($d_{3,2}$ = 9.4 nm, $d_{4,3}$ = 10.5 nm) according to the TEM histogram presented in Figure B 4 (Appendix B). Only a very few particles in the 200 nm range could be found and bigger particles are completely missing.

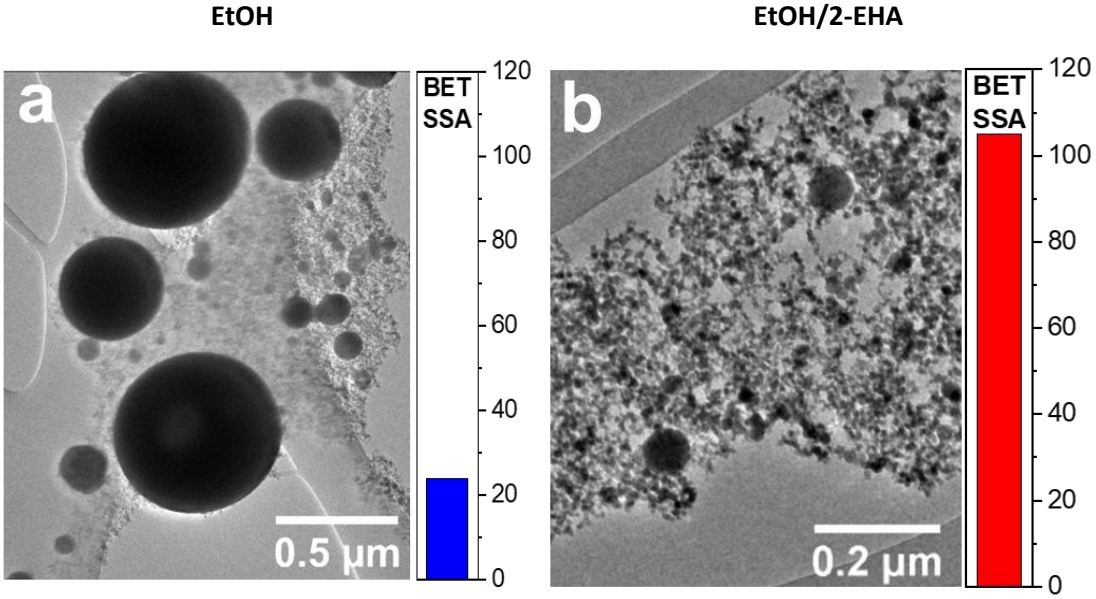

Figure 34. TEM images of $LaMnO_3$ particles from spray-flame-synthesis using (a) EtOH and (b) a mixture of EtOH and 2- EHA. At the right side of each image, a bar chart indicates the BET specific surface area (SSA) of each sample (unit: m^2/g). While the use of EtOH as solvent led to the formation of a multimodal particle size distribution (PSD) with a low SSA, the use of the EtOH/2-EHA mixture promoted the formation of a much more homogeneous PSD avoiding the formation of micron-sized particles.

BET specific surface area measurements (SSA) support the findings regarding the particle sizes. While the use of only EtOH as solvent generated a low BET SSA (24 m^2/g, bar chart at the right side of Figure 34a), the use of the EtOH/2-EHA mixture produced a sample with a BET SSA 4.4 times higher (105 m^2/g, bar chart in Figure 34b). Since the as-synthesized particles are mainly spherical, a SSA-derived particle size was calculated for the latter assuming a monodisperse size and considering the $LaMnO_3$ bulk density (≈ 6.6 g/cm). The calculated particle size of 9 nm is quite close to the TEM results (Figure B 4, Appendix B) and supports the finding that only few bigger particles are produced. Due to the multimodal size distribution of the material synthesized from pure EtOH solution, the calculation of a BET-derived particle size is not appropriate.

The X-ray diffractograms presented in Figure 35 reveal significant differences in crystallinity and phase composition of the samples. It is obvious that the material synthesized from the EtOH-based solution shows a much higher crystallinity, which is in line with the high number of big particles. The analysis indicates the formation of mainly orthorhombic $LaMnO_3$ (space group *Pnma II*, abbreviated as *O',* ICSD Nr. 83761). Besides this main phase, a low content of La_2O_3 (ICSD 192270) was also identified.

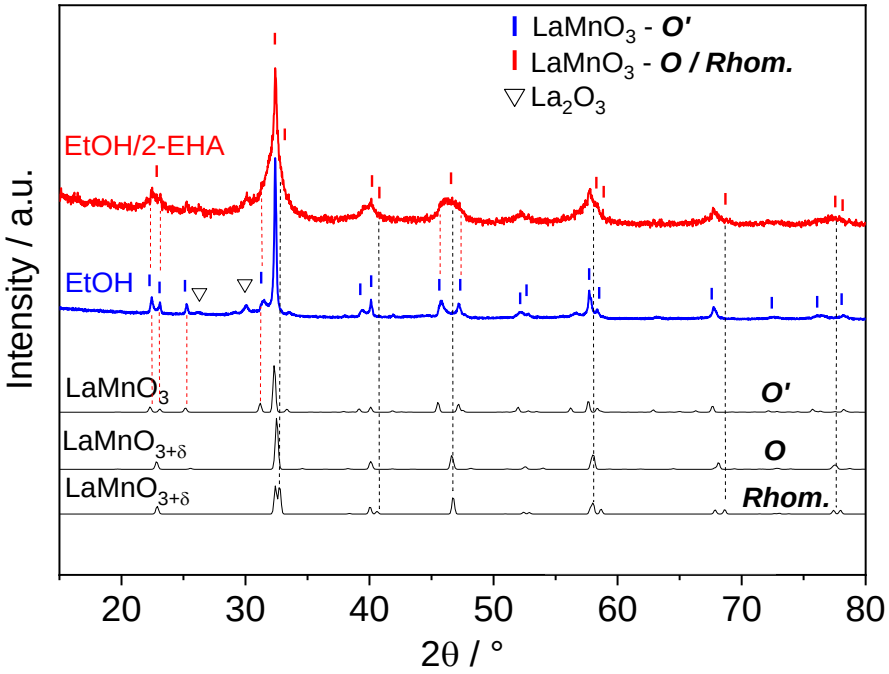

Figure 35. X-ray diffractograms of the spray-flame-synthesized samples using ethanol or a mixture of ethanol and 2-EHA as solvent.

The $LaMnO_3$ sample synthesized with the ethanol/2-EHA mixture also showed the characteristic peak positions of the *O'* phase, however, the main phase contribution was identified to come from one or two additional phases: the orthorhombic $LaMnO_{3+\delta}$ (space group *Pnma I* abbreviated as *O,* ICSD 51653) and/or the rhombohedral $LaMnO_{3+\delta}$ (space group R-3c, abbreviated as *R,* ICSD 80370). A qualitative and reliable differentiation of the *O* and *R* phases could not be obtained in the current case from the XRD pattern alone for several reasons: (1) the peak broadening because of small crystallite sizes, (2) the presence of the *O'* phase, and (3) the similarity of the peak positions (2θ) of both phases as shown in the reference diffractograms (Figure 35).[55]

All the possible three phases (*O', O* and rhombohedral), usually denominated as excess-oxygen phases, present cation (La, Mn) deficiencies.[180] The *O'* phase with a Mn^{4+} content lower than 14 % is commonly used and accepted as *$LaMnO_3$*, also used here. The electroneutrality of the phases is maintained by the oxidation of Mn^{3+} to Mn^{4+}, with the concentration of Mn^{4+} in the structure being equivalent to 2δ (expressed in %). The high Mn^{3+}/Mn^{4+} ratio of the orthorhombic *O'* phase leads to the occurrence of Jahn-Teller (J-T) distortions of the MnO_6 octahedra (two shorter and four longer Mn–O bond lengths)[54], also present in the *O*-phase.[212] As a result, the Raman modes in the orthorhombic structures related to the Jahn-Teller distortions (e.g., A_g and B_{2g} modes) are enhanced [213], which allows to distinguish the orthorhombic phases from the rhombohedral phase.[214] Consequently, Raman spectra (Figure 36) were measured for the sample prepared from ethanol/2-EHA solution.

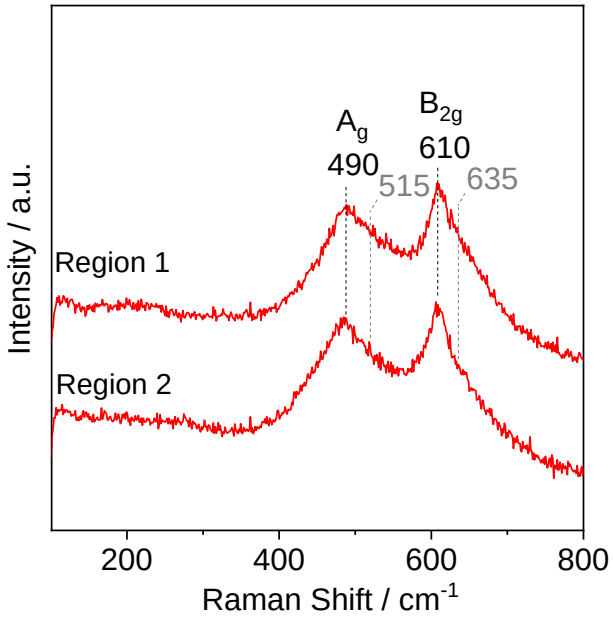

Figure 36. Raman spectra measured at two different regions of the sample synthesized using a mixture of ethanol and 2-EHA.

Two characteristic spectra measured at different positions are presented in Figure 36. The main bands were identified at 490 cm^{-1} (A_g mode) and at 610 cm^{-1} (B_{2g} mode), corresponding to the orthorhombic perovskite structure.[212] Additionally, the rhombohedral structure, which counts with two bands centered at ~515 and ~635 cm^{-1}, could not be identified with the performed Raman measurements.[212] In summary, the Raman results and the previous XRD results point to the presence of mainly orthorhombic *O'* and *O* structures for the sample that was synthesized using the ethanol/ 2-EHA solution.

Based on the qualitative determination of the phase composition of both $LaMnO_3$ samples, Rietveld refinements were performed (see Appendix B). For both samples, the shape of the peaks of the diffractograms (broad bottom, narrow top) presented in Figure 35 and specifically observable for the ethanol/2-EHA sample indicates the contribution of at least two different crystallite sizes. The Rietveld refinement of the XRD pattern (ethanol-prepared sample, Figure B 2a) revealed 59.5 Wt. % of the *O'*-phase with an average crystallite size (d_C) of 40 nm, 37.6 Wt.% of the *O'*-phase (d_C = 864 nm), and 2.9 Wt.% of the La_2O_3 phase (d_C = 100 nm). Regarding the sample prepared from EtOH/2-EHA (Figure B 3a), the Rietveld refinement indicated 89 Wt. % of the *O*-phase (d_C = 10 nm), 9 Wt. % of the *O'*-phase (d_C = 167 nm) and 2 Wt.% of the La_2O_3 (d_C = 100 nm). The results regarding the particle size are in very good coincidence with the TEM investigations (Figure B 4). As a main finding of the XRD analysis it is found that the EtOH/2-EHA solution is not only effective to generate small nanoparticles with a narrow particle size distribution but also promotes the *O*-phase formation containing a higher amount of Mn^{4+} than the material synthesized from pure ethanol. Interestingly, the Mn^{4+} rich *O* phase is mainly related to the small nanoparticles (d_C = 10 nm) while the *O'* phase is connected with the bigger particles (d_C = 167 nm).

The poor homogeneity of the material made from pure ethanol was also found in TEM-EDX elemental mapping of lanthanum and manganese (Figure 37). While the very small particles tend to be rich in manganese, the bigger ones are rich in lanthanum. In contrast, a very homogeneous La and Mn distribution was observed for particles made from ethanol/2-EHA.

I - Ethanol

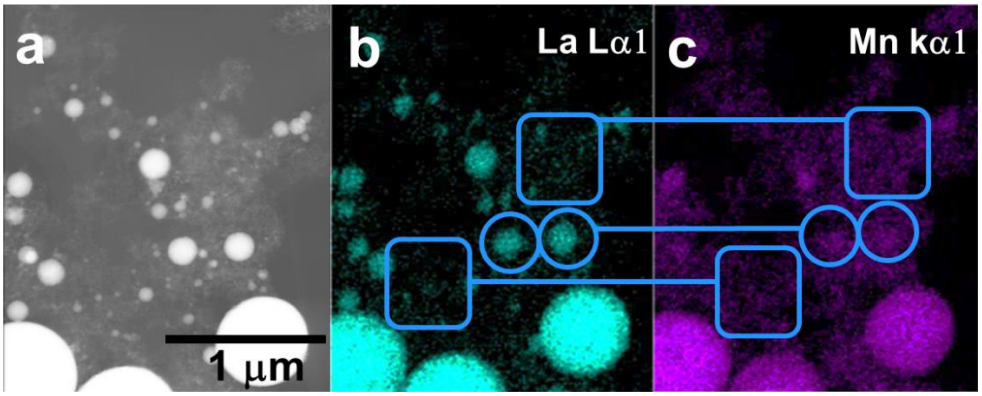

II - EtOH/2-EHA

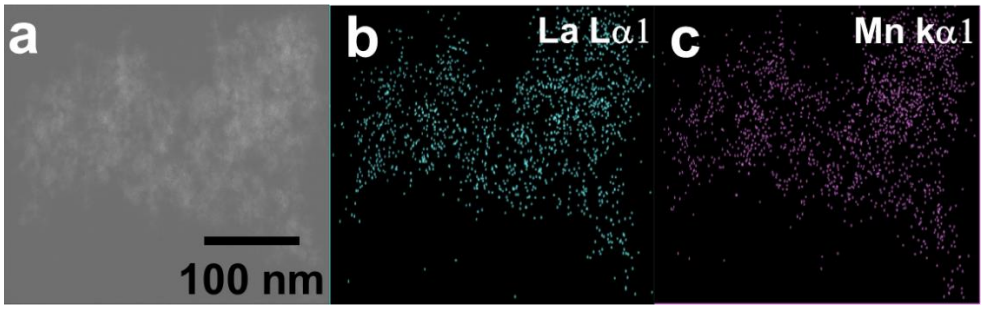

Figure 37. TEM/EDX images of perovskite samples synthesized using (I) ethanol or a (II) ethanol/2-EHA mixture as solvent with their corresponding (a) dark-field TEM image, (b) La $L_{\alpha}1$ elemental mapping and (c) Mn $K_{\alpha}1$ elemental mapping.

The findings regarding the inhomogeneity of the materials made from ethanol are further supported by XPS measurements. Former investigations on SFS-made materials have shown that as-prepared particles are covered with adsorbates[93, 215] originating from combustion products and (partly) unburned fuel. Thus, different oxygen-containing species can be identified. O1s XPS enables the analysis of these species and allows the identification of the nature of lattice oxygen close to the particle surface. The respective spectra shown in Figure 38 indicate significant differences between the samples prepared from EtOH and EtOH/2-EHA, respectively. While the spectrum of the EtOH-made sample is dominated by oxygen – mainly bound in water, carbonates, and single oxides (lattice oxygen binding energy of 529,8 eV[216]) – the spectrum of EtOH/2-EHA-made material clearly shows a different oxygen species. Besides the oxygen-related surface-adsorbed species (OH/CO/O_2) identified at 531.1 eV,[183, 217] the oxygen peak at 529.1 eV can be assigned to lattice oxygen pertaining to the perovskite structure.[25]

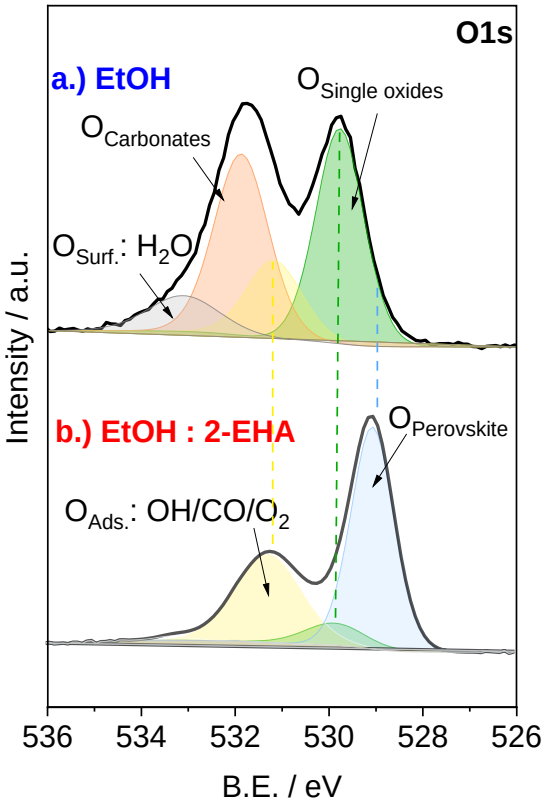

Figure 38. O 1s XPS spectra of samples spray-flame synthesized using (a) EtOH and (b) EtOH/2-EHA mixture as solvent.

In summary, the materials characterization shows that the use of pure ethanol alone did not only lead to the formation of a multimodal particle size distribution, it also comes along with an inhomogeneous La and Mn distribution in the particles and consequently, the formation of multiple phases. The orthorhombic *O'* $LaMnO_3$ structure observed in XRD is related to the big particles, while the small-size particles (< 10 nm) were found to be poorly crystalline and manganese-rich. Using ethanol/2-EHA as a solvent not only leads to the formation of a much more homogeneous product, it also supports the formation of materials with manganese in a higher oxidation state. We attribute this to the fact that oxidation of Mn^{2+} to $Mn^{3+/4+}$ is not limited to the particle formation step in the flame but starts much earlier when droplets are heated in advance of the combustion as shown by UV-VIS spectroscopy of the respective solutions.

5.3.3 Heat-treated materials: Particle-size and characterization

To remove adsorbates from the particle surface previous to catalytic testing, the synthesized materials were heat-treated under a continuous flow of air at 500 °C for 1h. Given that the heating process might modify the particle size and phase composition/concentration of the samples, the heat-treated samples were again characterized by XRD, Raman, TEM, and XPS.

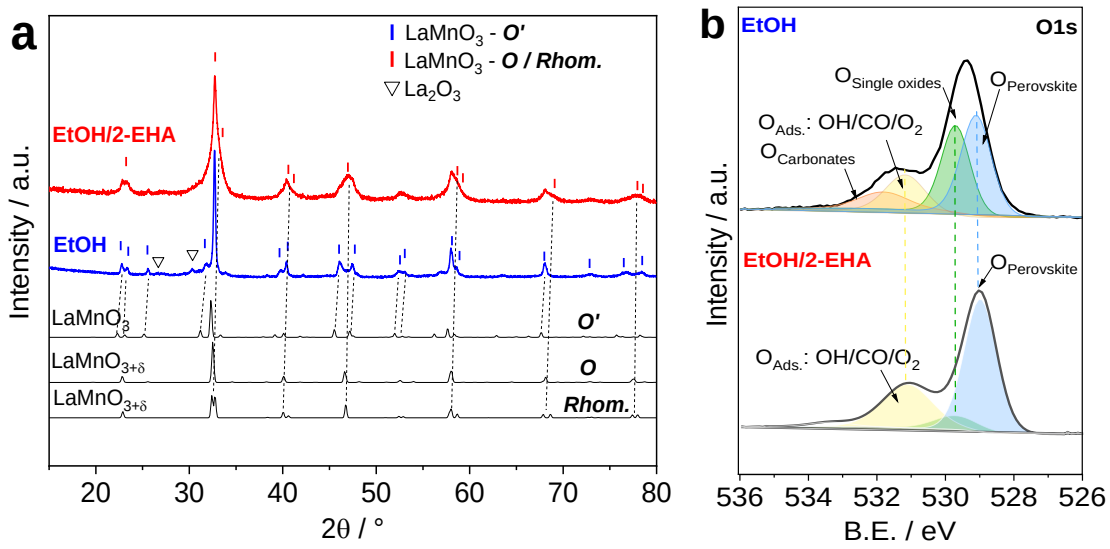

Figure 39. (a) X-ray diffractograms and (b) O1s XPS spectra of the heat-treated (500 °C, 1 h, air) samples that were synthesized using ethanol or a mixture of ethanol and 2-EHA as solvent.

The material made from ethanol/2-EHA remained almost unaffected regarding its phase composition, the contribution of at least two different perovskite phases can be observed in the XRD diffractogram (Figure 39a). This result is also supported by Raman measurements (not shown). As before, the phase content of the *O* and *R* phase could not be separated by Rietveld refinement, however, a small increase in crystallite size from 10 to 13 nm was observed (Figure B 3, Table B 2), matching closely the particle size obtained from TEM measurements (Figure B 4). Regarding the ethanol-made material, the peak positions shifted towards higher 2θ-values when compared with the reference positions of the *O'*-orthorhombic $LaMnO_3$ phase (Figure 39a). This can be related to some oxidation of Mn^{3+} to Mn^{4+} ions in the perovskite structure, decreasing the unit cell volume, which is well-known from literature.[53, 218, 219] A phase transition of the *O'*-phase towards the *O* or *R* phase containing an amount of Mn^{4+} higher than 14 % could not be identified.

The deconvoluted O 1s XPS spectra of the heat-treated samples are presented in Figure 39b. The lattice oxygen peak at B.E. = 529.1 eV corresponding to the perovskite structure, absent in the as-synthesized sample made from EtOH solution (Figure 38), could now be identified. Nevertheless, the contribution of the single-oxide lattice oxygen peak at 529.8 eV[216] was found to be still prominent, corresponding to ~45 mol% of the near-surface lattice oxygen. As expected, the heat-treatment caused an important decrease of the oxygen content related to metal carbonate structures (B.E. = 531.9 eV)[216], also observed in FTIR measurements (Figure B 5), decreasing from ~35 mol% (as-synthesized sample) to ~10 mol% (heat-treated sample) of the total measured oxygen. In contrast, the lattice oxygen of the ethanol/2-EHA-made sample related to the perovskite phase did not change while the content of oxygen species related to adsorbates is reduced as expected, also identified with FTIR measurements (Figure B 5).

5.3.4 Catalysis tests

CO oxidation tests, as presented in Figure 40a, were conducted in order to compare the activity of the two heat-treated samples. Both samples presented a typical sigmoidal evolution, however, the ethanol/2-EHA sample presented a significantly higher catalytic activity for the oxidation of CO.

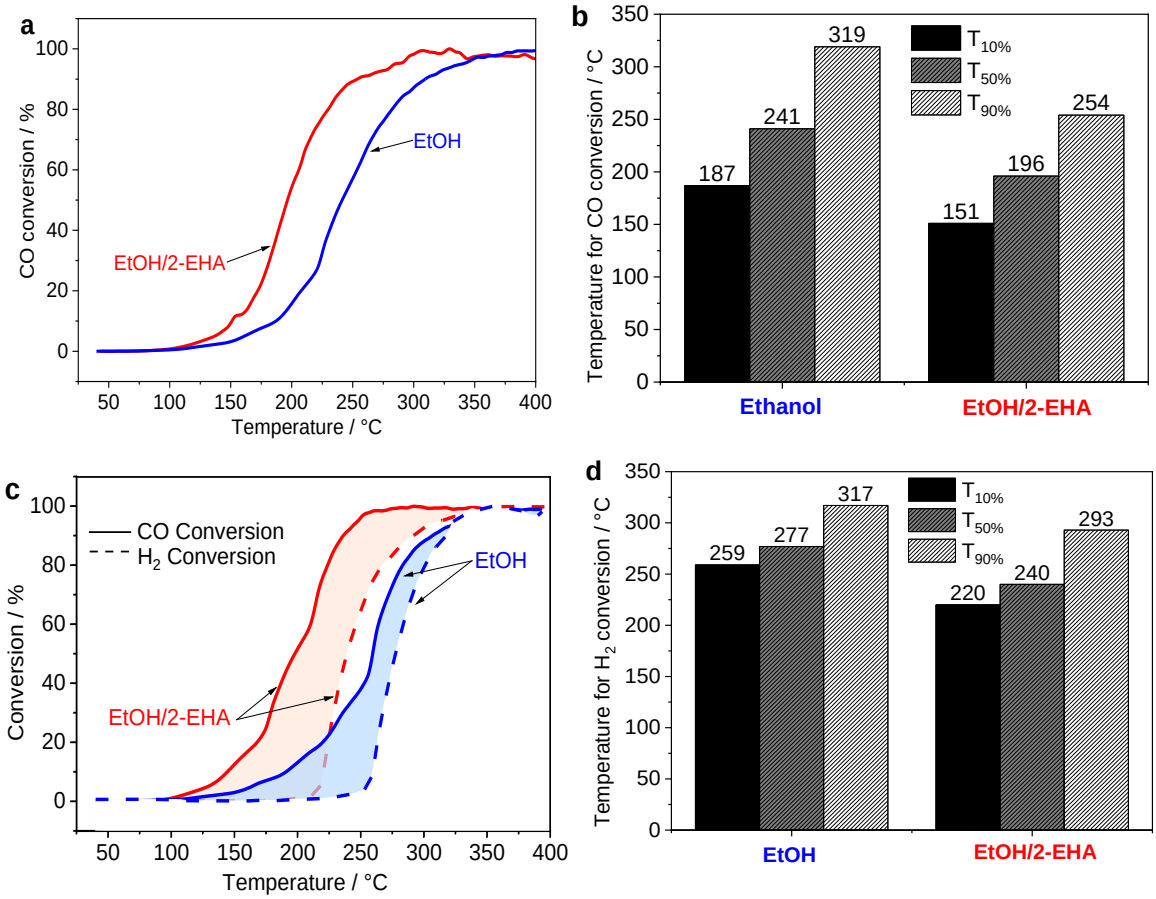

Figure 40. Catalytic performance of the heat-treated samples synthesized either with EtOH as solvent or with a mixture of EtOH (50 Vol.%) and 2-EHA (50 Vol.%): (a and b) CO conversion percentage and temperatures. (c) CO and H_2 conversions and (d) H_2 conversion temperatures on the selective oxidation (SELOX) of CO.

The required temperatures for 10, 50, and 90 % conversion of CO are presented in Figure 40b for the two measured samples. The EtOH/2-EHA sample reached a 50 and a 90 % CO conversion at 196 and 254 °C, respectively, while the EtOH sample required higher temperatures, reaching the same conversions at 241 and at 319 °C, respectively.

Concerning the CO SELOX reaction (Figure 40c), the EtOH/2-EHA sample also outperforms the ethanol sample, reaching almost 80 % of CO conversion at 220 °C while the H_2 conversion was only of 10 % (Figure 40d). For the ethanol sample, at 259 °C, corresponding to the temperature for the 10 % conversion of H_2, a CO conversion of only 40 % was reached.

The catalytic activity of lanthanum-based perovskites for CO oxidation and CO SELOX reactions is reported in literature discussing three main aspects: (i) defect nature and density, (ii) reducibility, and (iii) oxygen adsorbed species.[8] Regarding the CO oxidation, the reaction proceeds through a suprafacial mechanism, in which CO molecules react with adsorbed active oxygen species that were formed through the activation of O_2 from the gas phase on the surface of the catalyst. This occurs via a redox process of the B-site element of the perovskite[178], in this case, the interplay of Mn^{4+} and Mn^{3+} ions. Thus, the catalytic activity of lanthanum-based perovskites, e.g., $LaMnO_{3+\delta}$, is mainly dependent on the activation and control of adsorbed oxygen species and on the reducibility of the cations. In order to understand the influence of both of these factors, O_2-TPD and H_2-TPR measurements were performed and are presented in Figure 41a and b, respectively.

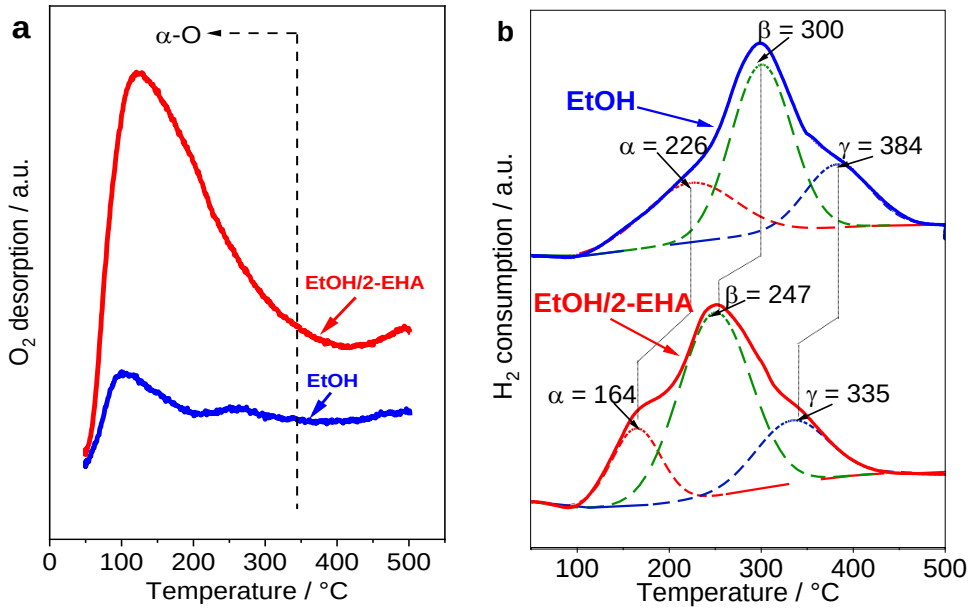

Figure 41. (a) O_2-TPD and (b) H_2-TPR- results from heat-treated samples that were synthesized either with ethanol as solvent or with a mixture of ethanol and 2-EHA.

The O_2-TPD region up to 350 °C is related to the so-called α-O, which is a measure of weakly chemisorbed/physisorbed oxygen upon oxygen vacancies,[220] the most active oxygen species for the catalytic oxidation of CO. According to the O_2-TPD results shown in Figure 41a, the EtOH/2-EHA sample presented a higher oxygen activation degree and adsorption amount (1282 μmol/g / 17 μmol/m^2) than the ethanol sample (253 μmol/g / 11 μmol/m^2), in agreement with the CO oxidation results from Figure 40a. The respective results are summarized in Table 3.

Table 3. BET specific surface areas, oxygen desorption (O_2-TPD) and hydrogen consumption (H_2-TPR) from $LaMnO_3$ samples synthesized either with ethanol as solvent or with a mixture of ethanol and 2-EHA (EtOH/2-EHA).

Catalyst (heat-treated samples)	**BET SSA m^2/g**	**O_2-TPD μmol g^{-1} (μmol/m^2)**	**H_2-TPR μmol/g (μmol/m^2)**			
			α	*β*	*γ*	**Total**
$LaMnO_3$-ethanol	23.1	253 (11)	214 (9)	412 (18)	161 (7)	786 (34)
$LaMnO_3$-EtOH/2-EHA	77.6	1282 (17)	220 (3)	761 (10)	262 (3)	1242 (16)

Regarding the H_2-TPR results presented in Figure 41b, three main reduction events are observed[221]: *α*, which is related to the removal of physically/chemically adsorbed surface oxygen species; *β*, which indicates the reduction of Mn^{4+} ions to Mn^{3+} ions and; γ, which is related to the Mn^{3+} to Mn^{2+} reduction in coordination with unsaturated microenvironments. The ethanol/2-EHA sample presented a higher reducibility with a total H_2 consumption of 1242 μmol/g while the ethanol sample had a total H_2 consumption of 786 μmol/g. The difference is mainly related to the process indicated as β (Table 3), associated with the reduction of Mn^{4+} ions to Mn^{3+}. The results show a pronounced Mn^{4+}/Mn^{3+} redox capability of the ethanol/2-EHA sample, involving not only the surface of the particles but also the perovskite lattice. Congruently, the temperatures at the maximum points of the β-peaks of both samples, 247 °C (ethanol/2-EHA) and 300 °C (EtOH), correspond roughly to the temperatures at the 90 % CO conversion as it can be observed in Figure 40a and c.

The higher CO oxidation activity of the ethanol/2-EHA sample was expected as this sample mainly consists of the Mn^{4+}-rich *O*/*R* phase while the ethanol sample presented mainly the orthorhombic *O'*-phase. Nevertheless, the low reducibility of the ethanol sample is beneficial in avoiding a premature hydrogen oxidation as it can be observed in Figure 40c.

Despite the lower H_2-TPR temperatures of the ethanol/2-EHA sample which are also related with the undesired lower temperature to oxidize H_2 (Figure 40c and d) the ethanol/2-EHA sample still presents a better catalytic activity for the CO-SELOX reaction than the ethanol sample. The reason behind is the higher effectivity of the ethanol/2-EHA sample to generate active oxygen species on the catalyst surface.

5.4 Conclusions

The spray-flame synthesis of the $LaMnO_3$ perovskite using metal nitrates as precursors and ethanol as solvent led to the formation of a multimodal particle size distribution with sizes ranging from 4 nm up to 2 μm. The formation of the big particles is suggested to be related with a droplet-to-particle conversion. The use of a solvent mixture (ethanol/2-ethylhexanoic acid (2-EHA) 50/50 v/v) generated the formation of a narrow and homogeneous particle size distribution (sizes ranging mainly between 4 and 15 nm). The use of ethanol/2-EHA also led to the oxidation of Mn^{2+} in solution as observed with UV-VIS spectroscopy. The phase composition of the samples was also affected by the solvent. While the sample synthesized using ethanol as solvent was identified to mostly consist of the *orthorhombic O'* phase, the sample synthesized from ethanol and 2-EHA solution was identified to count mainly with phases rich in Mn^{4+}.

The higher amount of Mn^{4+} resulted in a better catalytic performance for the oxidation of CO and the selective oxidation of CO compared to the sample synthesized from ethanol solution. A CO conversion of 50 % was reached at 196 °C, while the EtOH sample required a temperature of 241 °C to reach the same conversion. The same trend was observed for the SELOX reaction, where the ethanol/2-EHA sample reached 80 % CO conversion at 220 °C. The better performance could be explained based on O_2-TPD and H_2-TPR measurements, which also identified the Mn^{3+}/Mn^{4+} redox reaction as main driver for high catalytic activity.

6 Spray-flame synthesis of $LaMO_3$ (M = Mn, Fe, Co) perovskite nanomaterials: Effect of spray droplet size and esterification on particle size distribution

The content of this chapter was published in Proceedings of the Combustion Institute:

> **Angel, S.**; Schneider, F.; Apazeller, S.; Kaziur-Cegla, W.; Schmidt, T. C.; Schulz, C.; Wiggers, H., Spray-flame synthesis of $LaMO_3$ (M = Mn, Fe, Co) perovskite nanomaterials: Effect of spray droplet size and esterification on particle size distribution. Proc. Combust. Inst. 38 (2021) 1279-1287.

Further information related to this chapter is presented in Appendix C (Chapter 11.3), including Figure C 1 to Figure C 12.

My contribution in this work includes: Research conceptualization, synthesis, characterization of precursors and materials, analysis of data including the catalytic results, writing of the manuscript. F. Schneider and S. Apazeller contributed with PDA measurements. W. Kaziur-Cegla and T.C. Schmidt contributed with headspace GC/MS measurements. C. Schulz and H. Wiggers contributed to conceptualization, results interpretation, and writing.

6.1 Introduction

Perovskites are mixed oxides with the general formula ABO_3, in which A is generally a lanthanide metal ion and B is a transition metal ion such as manganese ($LaMnO_3$), iron ($LaFeO_3$), or cobalt ($LaCoO_3$) [146]. Given their diversity of physical and chemical properties,[27] these materials are currently being studied in the field of heterogeneous catalysis as they are promising alternatives to costly noble-metal based catalysts containing, e.g., platinum, palladium, rhodium, or iridium.[26, 222] Transition metal-based perovskite catalysts are of high interest in multiple reactions such as the oxygen-evolution reaction (OER), alkaline electrolysis,[223] alcohol oxidation towards aldehydes and ketones,[224] or photocatalytic CO_2 reduction.[225]

There are multiple routes to prepare and synthesize perovskite-type oxides, usually involving precipitation, complexation, and gelation in the liquid phase,[226] or solid-state synthesis based on blending, grinding, and sintering of solid-state precursors. These methods usually involve additional pre- and post-processing steps such as drying and calcination.[76] In contrast, gas-phase processes such as spray-flame synthesis, offer an attractive alternative to produce perovskite materials in a single step.[16] This method, in which typically spherical particles can be generated at high production rates, offers additional advantages over the previously described batch processes such as scalability and reproducibility of the continuous production process.[77]

In spray-flame synthesis, oxide nanoparticles are generated by combustion of a solution of metal salts in combustible liquids. Size homogeneity and phase purity of the synthesized materials depend on the selection of the metal precursors and solvents. Synthesis from metal nitrates dissolved in low-cost polar solvents as ethanol often results in bimodal particle-size distributions. Large particles with sizes up to several hundred nanometers are produced via a droplet-to-particle conversion mechanism involving precipitation inside the droplet prior to evaporation, while in parallel, small particles (below 50 nm) are produced via a gas-to-particle mechanism where gas-phase precursor species are formed and then nucleate from the gas phase.[90, 227] In the case of the synthesis of multinary materials systems such as perovskites, secondary phases such as La_2O_3 and La_2CoO_4 can form as unwanted side products.[16]

Spray-flame synthesis of LaMO3 (M = Mn, Fe, Co) perovskite nanomaterials: Effect of spray droplet size and esterification on particle size distribution

It has been shown that the use of solvent mixtures consisting of ethanol and 2-ethylhexanoic acid (2-EHA) is beneficial for the spray-flame synthesis of unimodal and narrow particle-size distributions, which also enables the synthesis of phase-pure multinary oxides from nitrates.[15, 93] The positive effect of the addition of 2-EHA has been attributed to the generation of cascade-like micro-explosions during the combustion of burning droplets [13] as a result of concentration gradients forming inside the evaporating droplets. These micro-explosions considerable decrease the droplet lifetime and thus promote the gas-to-particle mechanism. Recently we reported that mixtures containing 50 Vol.%:50 Vol. and 35 Vol.%:65 Vol.% of ethanol:2-EHA could be successfully used to directly synthesize phase-pure $LaCoO_3$ and $LaFeO_3$ perovskites from metal nitrate precursors.[194] In addition, it was discussed that liquid-phase reactions at low temperature, particularly a catalyzed esterification already taking place upstream of the droplet combustion, may cause precipitation inside the droplets, thus affecting the particle-size distribution of the product.

Micro-explosions and liquid-phase reactions depend on the temperature history of the evaporating droplets in the flame and thus on the initial droplet size and velocity. Consequently, the effect of the dispersion gas flow (5–8 slm O_2), which is used to atomize the solution, is analyzed in the current study. This is done for the spray-flame synthesis of the three perovskite-forming systems. In all cases, mixtures of the corresponding metal nitrates were dissolved in a mixture of 35 Vol.% ethanol and 65 Vol.% 2-EHA. The dispersion gas flow has been also related to modifications of the flame temperature, residence time, and thus sintering of the particles [228].

We investigated the characteristics of the burning spray of a mixture of 35 Vol. %:65 Vol. % ethanol:2-EHA without precursors using phase Doppler anemometry (PDA) to quantify the droplet-size distribution as a function of the dispersion gas flow. Using GC/MS, we analyzed the effect the metal precursors have on the liquid-phase esterification of ethanol and 2-EHA in a semi-quantitative way. These investigations, were used to understand the effect of the spray-flame process on the particle-size distribution and the characteristics of the synthesized perovskite nanoparticles that were analyzed by transmission electron microscopy (TEM), X-ray diffraction (XRD), and nitrogen adsorption (BET).

6.2 Materials and methods

6.2.1 Spray-flame synthesis

An enclosed spray-flame reactor (previously described in Refs.[77, 151]) was used to synthesize $LaMnO_3$, $LaFeO_3$, and $LaCoO_3$ perovskite nanomaterials. A process flow/component diagram of the reactor system is presented in Figure 9b. Metal nitrates were used as precursors: $La(NO_3)_3{\cdot}xH_2O$ (AppliChem Panreac, >99.0 %), $Mn(NO_3)_2{\cdot}4H_2O$ (Alfa Aesar, >98 %), $Fe(NO_3)_3{\cdot}9H_2O$ (VWR, >98 %), $Co(NO_3)_2{\cdot}6H_2O$ (Honeywell, > 99.0 %) and dissolved in a mixture of 35 Vol.% ethanol and 65 Vol.% 2-EHA. The precursor solutions contained a total metal-ion concentration of 0.2 mol/l.

The solutions were supplied via a syringe pump at a constant flow rate of 2 ml/min to a two-fluid nozzle installed at the bottom of a closed reactor chamber. A spray was formed from the solution by an O_2 dispersion gas flow. The spray is ignited by a continuously burning premixed pilot flame (3 slm CH_4 (Air Liquide, N25, 99.5 %) and 5 slm O_2), stabilized on a sintered bronze plate (10 cm diameter) coaxially surrounding the spray nozzle. The pilot flame itself is surrounded by a sheath-gas flow (140 slm, compressed air) to stabilize the flame and shield it from the reactor walls. An additional quenching gas flow (230 slm, compressed air) was added downstream the reaction zone to control the reactor off-gas temperature to

values below 130 °C to prevent thermal damage of the filter from which the particles were collected at the end of each synthesis.

6.2.2 Phase Doppler anemometry (PDA)

A metal-precursor-free solvent mixture was supplied to the burner used for the spray-flame synthesis in this study. The PDA measurements (for details about the principle of measurement, see Appendix C) were performed as described by Schneider et al.[80] and a schematic of the used setup is presented in Figure C 3 from Appendix C. Droplet velocities and size distributions in the spray flame were measured using a commercial fiber-based dual PDA system (Dantec Dynamics). By using two lasers operated at 20 mW, two velocity components *u* and *v* (corresponding to the height above burner, HAB axis and the radial *y*-axis, respectively) can be measured simultaneously, but only the velocity *u* (HAB axis) was used in this study. A minimum HAB of 10 mm could be probed in the used configuration.

6.2.3 Headspace GC/MS (Gas Chromatography-Mass Spectrometry) measurement of metal-nitrate solutions

Ethanol/2-EHA solvent mixtures containing the metal-precursors were prepared and 1 ml of each solution was transferred to 20 ml amber vials and investigated by GC/MS in triplicates. Blanks with 1 ml ethanol were measured after each triplicate. A GCMS-QP2010 Ultra (Shimadzu Deutschland GmbH, Germany) with a Restek Rxi-5ms (30 m × 0.25 mm × 0.25 µm) as analytical column was used for separation and quantification of the organics. Samples were injected with a PAL RTC autosampler, equipped with a headspace tool with a 2.5 ml gas-tight headspace syringe (CTC Analytics AG, Switzerland). The vials with the samples were transferred to an agitator, where they were heated to 40 °C and agitated continuously (500 rpm) to ensure temperature equilibration. During the incubation time, the headspace syringe was flushed with N_2 for 9 min. Afterwards, it was heated to 60 °C to ensure a complete injection without any residues in the syringe body and 300 µl of the solution were injected into the GS/MS. The sample was desorbed at 250 °C for 1 min (splitless) with helium as carrier gas at a column flow of 1 ml/min. The temperature in the column oven started from 50 °C with 1 min hold time and increased to 150 °C with a rate of 10 °C/min. This program led to the best separation and time efficient detection of the desired analytes. The interface between GC and MS as well as the ion source temperature were set at 250 °C as recommended by the manufacturer. The solvent cut time was 7 min. To determine the analyte, the total ion current of the QMS was monitored (*m*/*z* range of 50–400). The mass spectra were compared with those of solutions of commercial ethyl-2-ethylhexanoate (abcr GmbH, Germany).

6.2.4 Particle characterization

Transmission electron microscopy was used (TEM-EDX-SAED; JEOL JEM-2200FS) and the images were analyzed using ImageJ. Histograms of the particle sizes were plotted and fitted to log-normal distributions. X-ray diffraction patterns were recorded in a PANalytical X´Pert PRO operated with Cu-K_α radiation (0.15406 nm, 40 kV, 40 mA). The diffraction intensity was recorded at 2θ = 10–100° with a step size of 0.05°. BET (Brunauer Emmet Teller) specific surface areas were measured by nitrogen adsorption (Quantachrome, Nova2000).

6.3 Results

6.3.1 Particle-size distribution and phase characterization

The $LaMnO_3$, $LaFeO_3$ and $LaCoO_3$ perovskite materials were analyzed concerning the effect of the dispersion gas flow on particle size and morphology. Therefore, the O_2 dispersion gas flow rates were varied from the lowest flow at which the spray-flame was stable enough and considering four consecutive integer values (5, 6, 7, and 8 slm), while the other operating parameters were kept constant.

For all as-synthesized materials, particle-size distributions were derived from TEM measurements (Figure 42). The materials consisted of mostly agglomerated, spherical particles with primary particle sizes between 2 and 30 nm. The TEM images from experiments with 6 slm O_2 show typical particle morphologies that were observed for all experimental conditions. The mean particle sizes (d_p), the standard deviation (SD) and the Sauter mean diameters (d_{32}) were calculated and indicated in each distribution.

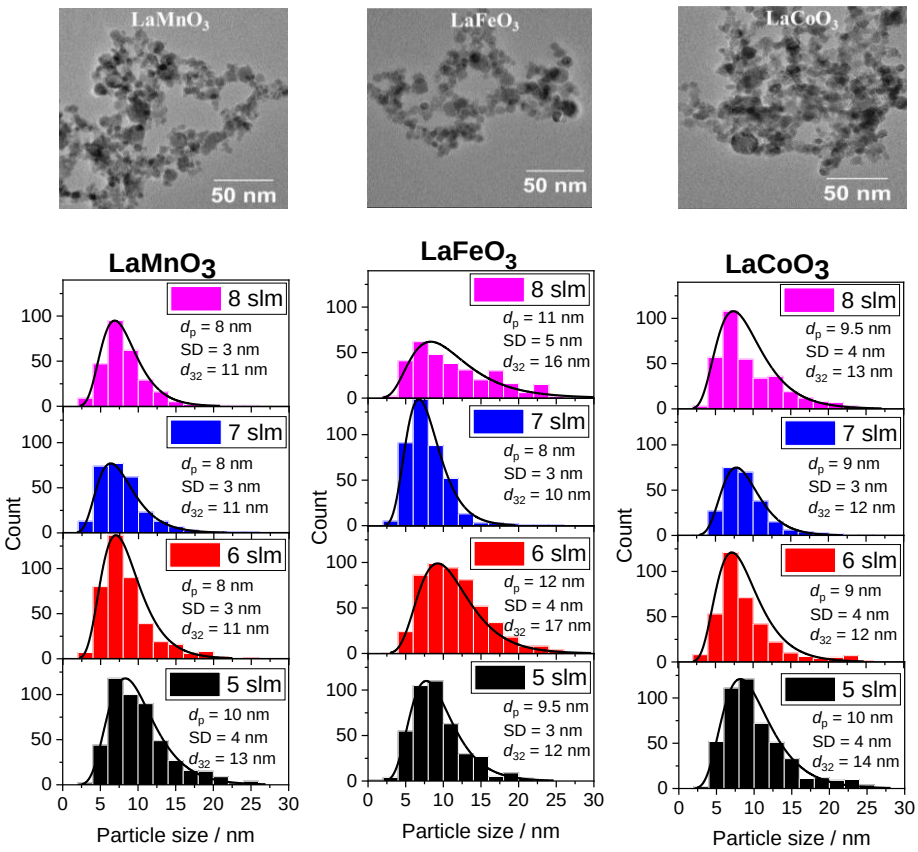

Figure 42. Example TEM images (6 slm O_2) and particle-size distributions of the $LaMnO_3$, $LaFeO_3$, and $LaCoO_3$ spray-flame-synthesized perovskites.

For the $LaMnO_3$ and $LaCoO_3$ perovskites, the effect of the dispersion gas flow on the particle-size distribution was very similar. The mean particle size of both perovskite systems synthesized with a 5 slm flow was 10 nm. Given a slight increase in the count of particles from 20 to 30 nm, the d_{32} of $LaCoO_3$ was slightly higher, 14 nm, than that of the $LaMnO_3$ perovskite, 13 nm. The mean particle sizes and Sauter mean diameters were found to be almost identical for flows from 6 to 8 slm (d_p = 8 nm and d_{32} = 11 nm for $LaMnO_3$, d_p = 9 nm and d_{32} = 12 nm for $LaCoO_3$), thus, no trend was observable. In the $LaFeO_3$ case, it was found that the mean particle sizes varied between 8 and 12 nm but also without a clear trend related to the dispersion gas flow.

For all materials, few large spherical particles up to 200 nm were observed (Figure 43, examples from materials synthesized with 7 slm O_2 – TEM images from the samples synthesized with other dispersion gas flow rates are shown in Figure C 11 from Appendix C), however, they were not included in the particle-size distributions from Figure 42 as the counted numbers from these large particles is not statistically significant.

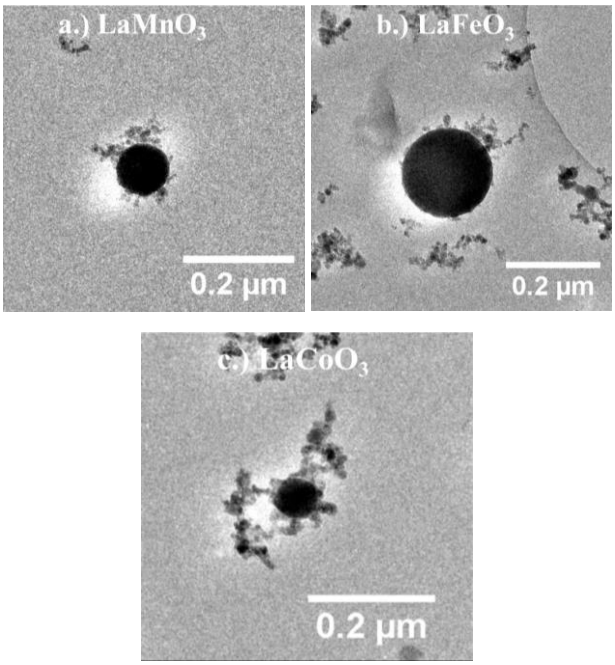

Figure 43. Examples of large particles of a) $LaMnO_3$, b) $LaFeO_3$ (larger sizes found compared with the other materials), and c) $LaCoO_3$ perovskite materials synthesized with a dispersion gas flow of 7 slm O_2.

The phase composition characterized by XRD confirms the findings from the TEM analysis. The diffraction pattern as well as the signal shape and width are almost unaffected regarding the dispersion gas flow (Figure 44). In the $LaMnO_3$ case, three main phases could be identified from the XRD patterns (Figure 44a): the orthorhombic *Pnma II* (*Ortho II*) (ICSD 50334), the orthorhombic *Pnma I* (*Ortho I*) (ICSD 51653) and the rhombohedral *R-3c* (ICSD 75070) phases. The *Ortho II* phase could be unequivocally identified from the XRD patterns, it presented well defined peak positions and intensities which also qualitatively indicated a higher crystallite size than that of the other two possible phases. The presence of the *Ortho I* or the rhombohedral phase cannot be excluded from the qualitative analysis of XRD alone. This is due to the strong unit cell symmetrization [55] of the *Ortho I* phase, indicating that its diffraction peaks present a small splitting with 2θ positions that match those of the rhombohedral phase at, e.g., 23.3° and 47.1°. Raman measurements (Figure C 4) suggest that both the *Ortho I* and rhombohedral phases are most likely present in the $LaMnO_3$ samples besides the *Ortho II* phase.

In case of $LaFeO_3$, the diffraction pattern perfectly matches the orthorhombic (ICSD 28255) $LaFeO_3$ phase without the presence of secondary phases. The diffraction patterns for the materials synthesized are virtually congruent and no major variations were developed with the change of the dispersion gas flow. In the $LaCoO_3$ case, the main phase indexed was the rhombohedral (ICSD 201763) $LaCoO_3$ structure while traces of the (ICSD 192270) La_2O_3 phase could also be identified. Again, no specific change could be observed with increasing dispersion gas flow.

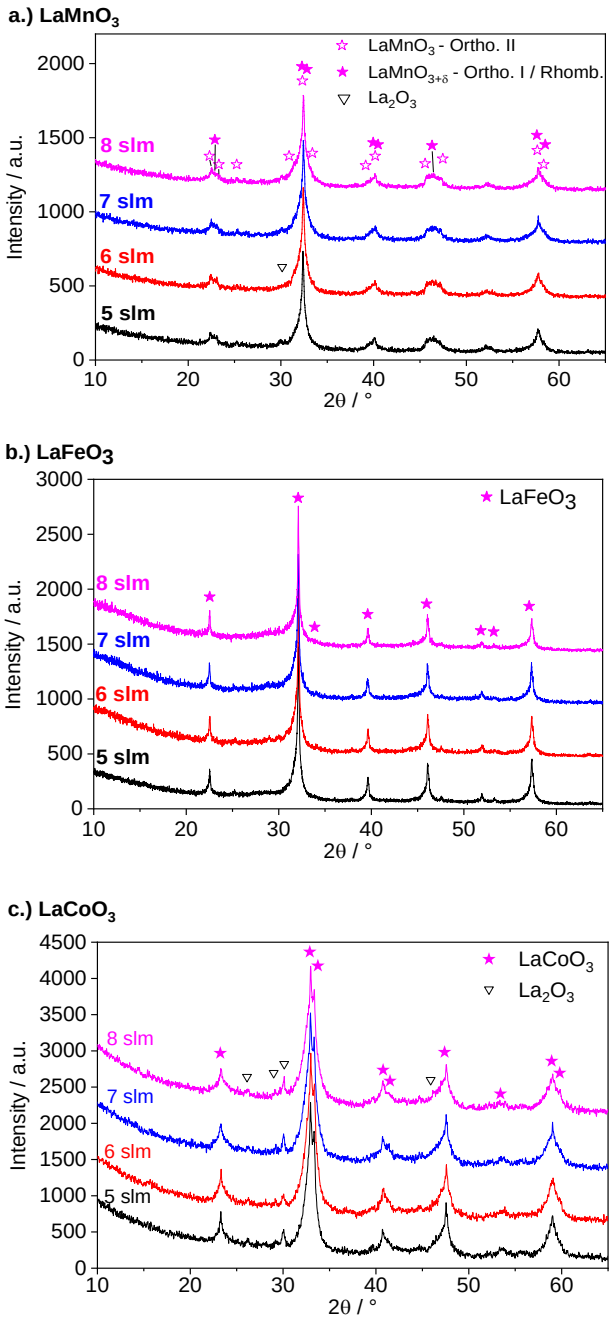

Figure 44: XRD of the a) $LaMnO_3$, b) $LaFeO_3$, and c) $LaCoO_3$ perovskites synthesized using dispersion gas flows from 5 to 8 slm.

Surprisingly, the characterization of the specific surface area (SSA) with BET measurements draws a different picture. In contrast to the almost identical results presented so far for the materials synthesized at different dispersion gas flow rates, the BET results show a clear trend for $LaMnO_3$ and $LaCoO_3$ towards an increasing SSA with increasing flow rate as presented in Figure 45. As evidenced in the TEM pictures from Figure 42, particles are mainly assumed as spherical and monomodal. Considering the bulk density of the materials produced, a mean BET-based particle size (d_{BET}) can be obtained from the measured SSA and is also presented for each sample in Figure 45. A big mismatch between particle sizes obtained from TEM histograms and the BET-based estimation of the mean particle size indicates a bimodal size distribution as shown in Figure 43. Thus, BET measurements are an easy method to identify the presence of large

particles. From these results presented in Figure 45 it must be concluded that the dispersion gas affects the particle formation process in the spray flame. In case of 8 slm dispersion gas, the particle sizes calculated from the SSA match almost perfectly with the results from TEM analysis. However, the results also suggest that the mass ratio of the big particles cannot be neglected for lower flow rates despite the fact that there are only very few.

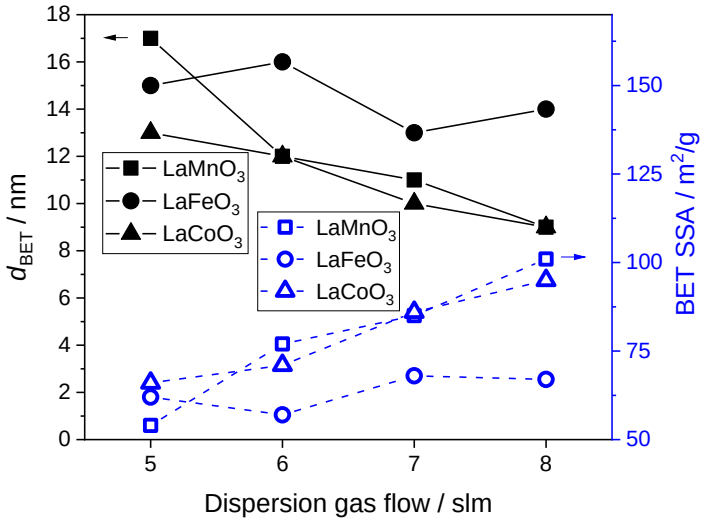

Figure 45. BET specific surface areas and derived diameters from the synthesized $LaMnO_3$, $LaFeO_3$, and $LaCoO_3$ perovskite materials.

Particle formation in spray flames occurs either via a gas-to-particle or a liquid-to-particle process [14]. In the latter, particles are formed via precipitation inside the droplets, especially in large ones. Thus, we investigated droplet formation and their disappearance through evaporation during combustion for different dispersion gas flow rates.

6.3.2 PDA measurements of droplets in the burning spray

Phase Doppler anemometry measurements were performed along the axial centerline between 10 and 50 mm. At HAB = 10 mm, the arithmetic mean droplet size (D_{10}) was 16 µm regardless of the dispersion gas flow and did not change much for HAB = 20 mm (D_{10} = 16 µm) and HAB = 50 mm (D_{10} = 19 µm). The slight increase in D_{10} from HAB = 20 mm to 50 mm is attributed to the preferential and fast vaporization of small droplets. The droplet count number significantly decreases with increasing HAB (Figure 46a and b) as expected due to evaporation and dilution of droplets. The droplet-size distribution at HAB = 20 mm as a function of the dispersion gas flow is presented in Figure C 12.

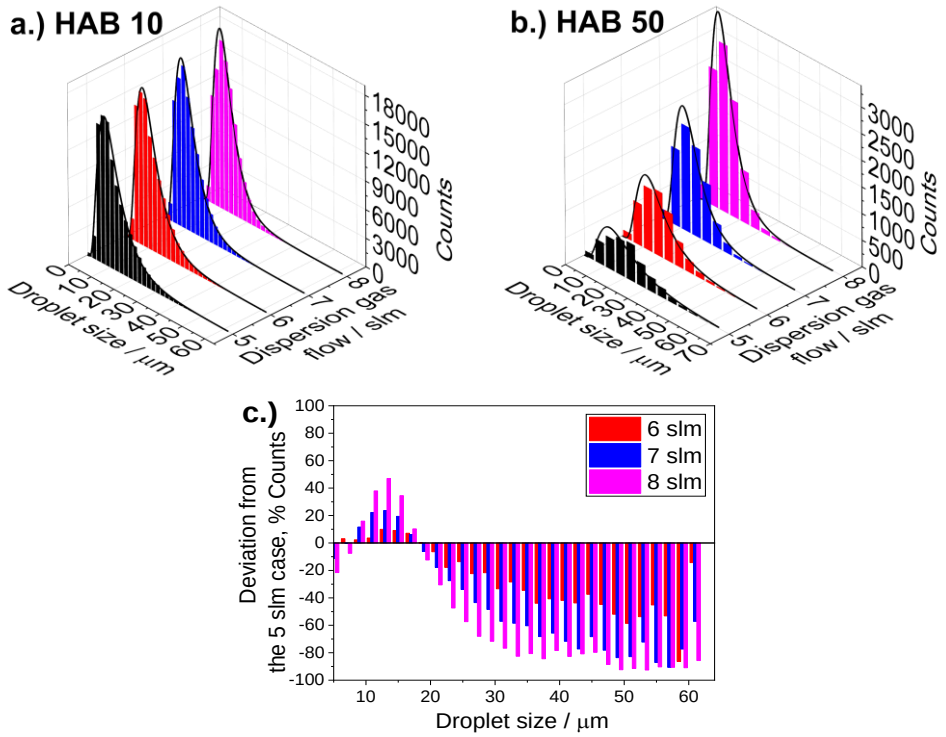

Figure 46. Droplet-size distributions as a function of the dispersion-gas flow rate (5 slm: black, 6 slm: red, 7 slm: blue, 8 slm: magenta) at a) HAB = 10 mm and b) HAB = 50 mm. c) Relative change in number concentration for 6, 7, and 8 slm compared to 5 slm at HAB = 10 mm.

As the droplet count at HAB = 10 mm was the same for dispersion gas flows from 5 to 8 slm, the number concentration of droplets along the size distribution was analyzed exemplarily for HAB = 10 mm. For better comparison, the counts for each section of the measurements for 5 slm were set as reference and the relative change was plotted for 6, 7, and 8 slm (Figure 46c). It is obvious that the most important changes occur for droplets > 30 µm and especially between 45 and 65 µm where the number concentration is reduced by about 90 % for 8 slm compared to 5 slm. As a consequence, it can be concluded that the particle formation process is increasingly shifted from the droplet-to-particle to the gas-to-particle process in the $LaMnO_3$ and $LaCoO_3$ cases, which can also explain the very good agreement between the particle diameters obtained from BET and TEM measurements for a dispersion-gas flow rate of 8 slm.

In contrast to the results discussed for $LaMnO_3$ and $LaCoO_3$, the SSA of $LaFeO_3$ did not systematically increase with the dispersion gas flow. SSA values are comparably low and range from 57 to 68 m^2/g. A more detailed inspection of the XRD patterns, especially of $LaFeO_3$, also reveals that the signal profiles do not well match to a Lorentz shape but seem to consist of two overlapping modes (Figure 44). A similar XRD profile was observed when synthesizing titania nanoparticles in a spray-flame reactor at reduced pressure, where poor atomization caused a bimodal particle-size distribution.[151] Thus, Rietveld analyses (Figure C 5 to Figure C 10) of $LaMnO_3$, $LaFeO_3$, and $LaCoO_3$ XRD patterns were performed[229] considering a bimodal crystallite-size distribution with a small- (crystallite sizes: ~10 nm) and a large-particle mode (50–220 nm).

For $LaMnO_3$, a small-particle mode (~10.5 nm) was identified contributing ~83 Wt.% of the sample. Neither the average crystallite sizes nor the concentration of the small-particle mode was significantly influenced by the dispersion-gas flow rate. In the large-particle mode in contrast, the average size decreased from 215 nm (5 slm) to 83 nm (8 slm) while its concentration remained stable (~15 Wt.%, Figure C 6). Similar to $LaMnO_3$, the $LaCoO_3$ samples contained a small-particle fraction (~9 nm, 85 Wt.%) which was

not affected by of the dispersion-gas flow rate, while, the average size of the large-particle fraction decreased from 85 nm (5 slm) to 55 nm (8 slm) with a constant mass fraction of 15 Wt.% (Figure C 10). This observation agrees with the TEM results that showed a constant number of small particles (Figure 42) and with the increase of the SSA of $LaMnO_3$ and $LaCoO_3$ with increasing dispersion-gas flow rate through the decrease of the size of the large particles. The small-particle fraction of $LaFeO_3$ had an average size of ~10 nm (76 Wt.%) while the large crystallites had an average size of 178 nm, that – unlike the $LaMnO_3$ and $LaCoO_3$ cases – did not depend on the dispersion-gas flow rate (Figure C 8). Furthermore, the average concentration of the large crystallites of the $LaFeO_3$ samples was higher (24 Wt.%) than that of the other materials systems. This information is consistent with the SSA of the $LaFeO_3$ samples (Figure 45) that did not depend on the dispersion-gas flow rate. The origin of the specific role of $LaFeO_3$ is still unclear.

6.3.3 Esterification reaction of ethanol and 2-EHA in the precursor solutions

In previous studies, we proposed that the iron-containing precursor solution shows some catalytic activity towards the esterification of ethanol and 2-EHA for producing ethyl-2-ethylhexanoate and water.[194] Mainly the content of water – together with the water of crystallization of the iron nitrate precursor – is expected to force the hydrolysis of the metal ions, especially iron, and the subsequent formation of particles within the droplets before their evaporation occurs, thus boosting the droplet-to-particle mechanism.[194]

The chemical interaction of the different components of the solutions (lanthanum nitrate, the corresponding transition metal nitrate, ethanol and 2-ethylhexanoic acid) might influence the formation and combustion of the droplets as well as the low-temperature formation of species prompted to precipitate in the liquid-phase in advance of the droplet combustion leading to the formation of large particles.

In a previous study,[194] it was found from an ATR-FTIR analysis that in solutions containing lanthanum and iron nitrates, the hydrolysis of iron leading to iron-hydroxide species was reduced by decreasing the ethanol concentration in the solution from 50 to 35 Vol. %, narrowing the particle-size distribution (TEM) of $LaFeO_3$. Solutions containing lanthanum and cobalt nitrates were also analyzed, finding that given the lower degree of hydrolysis of cobalt, solutions containing 50 Vol.% ethanol led to the formation of $LaCoO_3$ with a unimodal particle size distribution.

Without the presence of a catalyst, esterification reactions are typically slow at room temperature.[165] However, we previously observed that transition metals – especially iron – can act as a catalyst for this reaction.[194] To quantify the effect of the precursor solution composition on the esterification reaction, we applied GC/MS for a quantitative comparison of the ethyl-2-ethylhexanoate content produced for the various precursor systems (Figure 47).

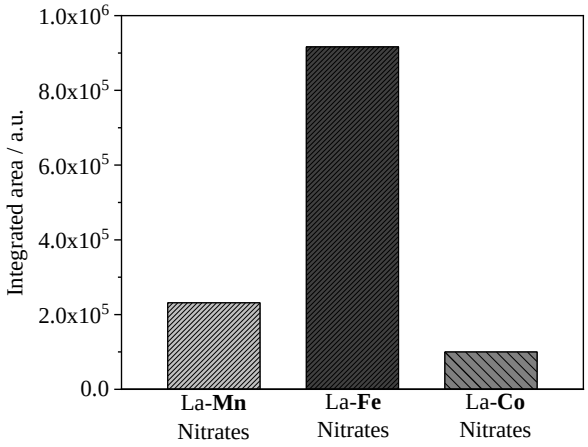

Figure 47. Integrated GC/MS signal of ethyl-2-ethylhexanoate as a measure for their relative concentration in the precursor solutions.

Solutions containing lanthanum and iron nitrates showed by far the highest trend towards forming ethyl-2-ethylhexanoate with a concentration four times higher than in solutions of lanthanum and manganese nitrates and nine times higher than in solutions of lanthanum and cobalt nitrates. The esterification is directly related to the release of water, thus the water content originating from the esterification is also 4–9 times higher than in the solutions with cobalt and manganese. Additionally, the content of water of crystallization is also the highest for iron nitrate ($Fe(NO_3)_3 \cdot 9H_2O$). In contrast, cobalt and manganese nitrates have 6 and 4 molecules of water of crystallization, respectively. Therefore, iron nitrate solutions will reach a water content (from released water of crystallization and esterification) 6–10 times higher than solutions of cobalt or manganese nitrate. The formation of ethyl-2-ethylhexanoate and water is expected to affect the temperature history and vaporization characteristics of the droplets in the spray flame. As ethanol is consumed and water is produced, the boiling point of the mixture will increase and additional energy will be required for heating up the droplets and for the evaporation of water. Moreover, liquid-phase separation might occur due to the low solubility of the ester and the acid in water, dividing also the precursors in water-soluble such as nitrates and ester/acid-soluble, e.g., iron-carboxylate, which formation has been previously studied.[14] We assume that a significant amount of the metal ions will accumulate in the water phase, especially in solutions containing iron nitrate, and hydrolyze before the droplet is completely burned/evaporated. As a consequence, the formation of large particles from the $LaFeO_3$ perovskites can be attributed to the high water-content and related hydrolysis of metal ions and thus the variation of the dispersion-gas flow (and thus the decrease of initial droplet size) would not greatly increase the SSA of the product because particle precipitation also occurs rapidly in small droplets.

6.4 Conclusions

In this paper, we identified spray-flame reaction conditions that lead to the formation of perovskite nanoparticles with a bimodal size distribution. For $LaMnO_3$ and $LaCoO_3$, the dispersion gas flow (6–8 slm) did not affect the primary particle size of the small-particle mode (up to 30 nm). This was evidenced in the mean particle size (8 nm in $LaMnO_3$ and 9 nm in $LaCoO_3$) obtained from TEM images (Figure 42), which was almost independent on the dispersion-gas flow rate. A low flow rate of 5 slm slightly increased the mean particle size of both materials systems to 10 nm due to an increase in the fraction of particles in the 20–30 nm regime. In case of $LaFeO_3$, the mean particle size varied from 8 to 12 nm depending on the

dispersion-gas flow rate. In addition, few large particles (up to 200 nm) were encountered for all three materials.

Even though the mean particle size obtained from the analysis of TEM images was almost invariant, the increase of the dispersion-gas flow rate caused an increase of the BET specific surface areas (SSA) of the $LaMnO_3$ (from 54 to 101 m^2/g at 5 to 8 slm, resp.) and $LaCoO_3$ perovskites (from 66 to 95 m^2/g from 5 to 8 slm, resp.), indicating a reduction of the fraction of large particles with increasing dispersion-gas flow rate. This effect was not seen for $LaFeO_3$, where the SSA remained constant at ~65 m^2/g.

PDA measurements of the burning sprays from a mixture of 35 Vol.% ethanol and 65 Vol.% 2-ethylhexanoic acid without precursors revealed droplet sizes ranging from 2 to 65 μm, and a mean droplet size of 16 μm. Most importantly, the measurements revealed that the number concentration of large droplets (45–65 μm) is reduced by about 90 % when increasing the dispersion-gas flow rate from 5 to 8 slm. We conclude that in case of $LaMnO_3$ and $LaCoO_3$, increasing the dispersion-gas flow rate shifts the formation of particles from the droplet-to-particle to the gas-to-particle mechanism, explaining the increase in the specific surface areas.

Our experiments verified the previous hypothesis that the esterification reaction of ethanol with 2-EHA towards ethyl-2-ethylhexanoate and water is catalyzed by the transition-metal precursors in the solution. From GC/MS measurements we found that the concentration of ethyl-2-ethylhexanoate, and hence water, is four times and nine times higher in solutions containing La/Fe nitrates than in solutions containing La/Mn and La/Co nitrates, respectively. The high content of water specifically affects the hydrolysis of iron and the formation of precipitates in the droplets, generating the formation of high-size particles. This explains the rather low and invariant BET specific surface area of the $LaFeO_3$ perovskite with the dispersion gas flow.

7 Discussion summary

This work presents the spray-flame synthesis (SFS) of three lanthanum-based perovskite-like oxides – $LaMnO_3$, $LaFeO_3$ and $LaCoO_3$ – using nitrates as metal precursors. The effect of two solvents – ethanol and 2-ethylhexanoic acid (2-EHA) – mainly on the particle size distribution, specific surface area (SSA) and phase composition of the synthesized materials is analyzed.

The use of ethanol as solvent produced perovskite materials with low BET SSAs of 24, 15, and 23 m^2/g for the $LaMnO_3$ (Figure 34a), $LaFeO_3$ and $LaCoO_3$ oxides (see Figure A 2 in Appendix A), respectively. TEM images of the different materials indicate the formation of particle-size distributions consisting of two modes: small particles with sizes ranging between 2 and 20 nm and large spherical particles reaching up to 2 μm in diameter. The formation of such large particles is responsible for the identified low SSAs of the synthesized materials. As presented in chapter 3.2.2, the formation of large particles when ethanol is used as solvent – as in the synthesis of single oxides – has been associated with the direct droplet-to-particle formation route, which is closely related to the chemistry of the metal nitrate precursors in the ethanol-based solutions. To identify such chemical effects, temperature-dependent ATR-FTIR measurements of the corresponding precursor solutions for the spry-flame synthesis of the three perovskite systems were performed. In the lanthanum-free iron-nitrate-based solution (Figure 25a), IR bands related to the formation of HNO_3 were identified when the temperature of the solution was increased from 23 to 70 °C. The formation of HNO_3 is related to the hydrolysis of the Fe(III) hexa-aqua ion (chapter 4.3.2) and the generation of (oxy)-hydroxides, which are precipitating species in the liquid-phase. Cobalt nitrate (Figure 25) or manganese nitrate (Figure 33) – regardless of the presence of lanthanum nitrate – ethanol-based solutions did not display the formation of IR bands related to the formation of HNO_3, indicating a weaker hydrolysis degree than the iron-based solution. A stronger degree of hydrolysis (i.e., formation of stable hydrated complexes) of iron nitrate is expected as it has – taking water-based solutions as reference – a lower free energy of hydration (Figure 16a) and water exchange rate constant (Figure 16b) than La-, Co-, or Mn-nitrate. The study of the chemistry of metal nitrates in ethanol-based solutions points to the hydrolysis of the metal ions – especially of iron – in solution and the formation of precipitating hydroxide species as promoters of the formation of large particles directly from droplets in the spray-flame process.

The use of ethanol alone a solvent does not only affect the particle-size distribution of the spray-flame synthesized materials, it also affects the elemental distribution of La/Mn, La/Fe and La/Co throughout the formed particles. An enrichment of lanthanum in large particles can be observed in the TEM/EDX images of the spray-flame synthesized $LaMnO_3$ (Figure 37-I), $LaFeO_3$ (Figure 29b-I), and $LaCoO_3$ (Figure 30b-I). This lanthanum enrichment is likely driven by different phenomena, e.g., the higher decomposition temperature of lanthanum nitrate in comparison with Mn-, Fe-, or Co-nitrate (see chapter 3.2.1) and the lower solubility of lanthanum nitrate in ethanol in comparison with the other metal nitrates which might cause an early recrystallization of lanthanum nitrate with the evaporation of ethanol from the droplets (chapter 3.2.2). The consequence of the lack of elemental homogeneity throughout the particles is the formation of secondary phases as La_2O_3 besides the formation of the $LaCoO_3$ (Figure 30) or the $LaMnO_3$ (Figure 35) perovskite.

The use of metal-nitrate-based solutions of ethanol/2-EHA (50/50 by vol.) caused an important increase of the BET SSAs of the spray-flame synthesized $LaMnO_3$, $LaFeO_3$ and $LaCoO_3$ perovskites to 105 (Figure 34a), 89, and 95 m^2/g (chapter 4.3.5), respectively. The improvement of the SSAs is explained through the radical decrease – compared with using only ethanol as solvent – of the concentration number of large particles (> 100 nm) in the synthesized materials, especially for the $LaMnO_3$ (Figure 34b) and $LaCoO_3$ (Figure 28b-II) cases. For the $LaFeO_3$ case (Figure 28a-II), few large particles (>100 nm) were identified. Nevertheless, the increase of the concentration of 2-EHA to 65 Vol.% was effective to further decrease the concentration number of such particles (Figure 28a-III). The reasons behind the beneficial effect of the ethanol/2-EHA mixtures in the SFS of oxides (chapter 3.2.3) have been attributed to different physical (see chapter 3.2.3.1) – as droplet micro-explosions and high flame temperatures – and chemical (chapter 3.2.3.2) phenomena such as the formation of metal carboxylates. To further understand the chemical interactions among the metal nitrates and the ethanol/2-EHA mixture, temperature-dependent ATR-FTIR measurements of the corresponding precursor solutions were performed. In all solutions containing metal nitrates, ethanol and 2-EHA, IR bands (Figure 25c, Figure 26c, Figure 33b) characteristic for ester compounds were identified and using GC/MS (see Figure A 1 in Appendix A), the ester compound was identified as ethyl 2-ethylhexanoate, as proposed in reaction (3.4). As esterification reactions are typically catalyzed by, e.g., Lewis acid compounds (chapter 3.2.3.2), the transition metal ions (Fe^{3+}, Mn^{2+}, or Co^{2+}) in solution were proposed as potential catalysts for the identified formation of the ester compound. The formation of characteristic IR bands of the C=O carbonyl group in the solutions containing iron (Figure 25c) hinted to a stronger interaction of Fe^{3+} ions – compared to that of cobalt or manganese ions – with the carbonyl group of the carboxylic acid, which has been identified as important part in the mechanisms of catalyzed esterification reactions. For solutions containing lanthanum and manganese nitrate, the presence of 2-EHA generated as well the oxidation of Mn^{2+} to Mn^{3+} – supported by UV-Vis measurements (Figure 33d) – at temperatures above 35 °C (chapter 5.3.1), happening through the release and reduction of nitrate groups. As consequence, the liquid-phase oxidation of manganese allowed the formation of the $LaMnO_{3+\delta}$ perovskite-like oxide which counts with a Mn^{4+}-rich orthorhombic *O*-phase as identified by XRD (Figure 35) and Raman measurements (Figure 36). Furthermore, the incorporation of 2-EHA in solution caused a more homogeneous – in comparison with using only ethanol as solvent – elemental distribution of La and Mn throughout the particles (see TEM/EDX pictures from Figure 37-II). This higher degree of elemental distribution was also observed in the $LaFeO_3$ (Figure 29b-II) and $LaCoO_3$ (Figure 30b-II) perovskites synthesized using the ethanol/2-EHA mixture.

Using solutions of the corresponding metal nitrates dissolved in the ethanol/2-EHA (35/65 by vol.) solvent mixture, the effect of the dispersion gas – which is used to atomize the solution flow into fine droplets – flow rate (5, 6, 7, and 8 slm) on the particle size distribution of the spray-flame synthesized $LaMnO_3$, $LaFeO_3$, and $LaCoO_3$ perovskites was analyzed. Increasing the dispersion gas flow rate from 5 to 8 slm caused the increase of the BET SSAs (Figure 45) of the $LaMnO_3$ and $LaCoO_3$ perovskites from 54 to 101 m^2/g and from 66 to 95 m^2/g, respectively. On the other hand, the BET SSA (Figure 45) of the $LaFeO_3$ perovskite did not present any important variation – constant value of ~65 m^2/g – with the change of the dispersion gas flow rate. Rietveld refinements of the $LaMnO_3$ (Figure C 5), $LaFeO_3$ (Figure C 7) and $LaCoO_3$ (Figure C 9) perovskites synthesized with dispersion gas flow rate of 5 slm evidenced a bimodal particle size distribution – also observed in TEM pictures from Figure 43 – consisting of small crystallite size (<12 nm) nanoparticles (~85 Wt.%) and large crystallite size (~200 nm for the $LaMnO_3$ and $LaFeO_3$ samples and ~85 nm for the $LaCoO_3$ sample) particles (~15 Wt.%). While the size and concentration of the small-crystallite-size nanoparticles and the concentration of the large-crystallite-size particles did not present an important variation, the increase of the dispersion gas flow rate to 8 slm caused the decrease of the size of the large-

crystallite particles of the $LaMnO_3$ and $LaCoO_3$ samples to ~75 nm (Figure C 6b) and ~60 nm (Figure C 10b), respectively. By contrast, the size of the large-crystallite particles of the $LaFeO_3$ samples was not modified – explaining the invariability of the BET SSAs –with the change of the dispersion gas flow rate, remaining at a high value of ~200 nm (Figure C 8b). As presented in chapter 3.1, the formation of large particles in the spray-flame synthesis is associated with the droplet-to-particle conversion mechanism, which indicates that the initial droplet size is a relevant parameter to be understood and controlled. In this regard, phase Doppler anemometry (PDA) measurements (Chapter 6.3.2) of metal-nitrate-free burning sprays were conducted along the axial centerline of the burner in order to quantify the droplet size distribution as a function of the dispersion gas flow rate. At a height-above-burner (HAB) of 10 mm and using a dispersion gas flow rate of 5 slm, the droplet size (Figure 46a) ranges between 2 and 65 μm (arithmetic mean droplet size (D_{10}) of 16 μm). Even though D_{10} is not modified when the dispersion gas flow rate is increased to 8 slm, the number concentration of droplets with sizes between 45 and 65 μm is decreased by 90 % (Figure 46c). This is in agreement with the results concerning the $LaMnO_3$ and $LaCoO_3$ cases, as the increase of the dispersion gas flow rate shifts the particle formation process from droplet-to-particle to gas-to-particle route, causing the decrease of large particles and consequently, the increase of the BET SSAs. In order to understand the different behavior – invariability of BET SSAs and large particle size with the change of the dispersion gas flow rate – of the $LaFeO_3$ samples, the previously mentioned hypothesis related to the catalytic role of the transition metals in solutions for the esterification of reaction between ethanol and 2-EHA was explored.

Using headspace GC/MS measurements (Chapter 6.3.3), the ethanol/2-EHA (35/65 by vol.)-based solution containing lanthanum and iron nitrates was identified to present the highest concentration of ethyl 2-ethylhexanoate (Figure 47), four times higher than a La/Mn-based solution and nine times higher than a La/Co-based solution. This indicates that the iron-based solution has a remarkable catalytic activity in the esterification reaction between ethanol and 2-EHA. Furthermore, water is also produced in the reaction and the Fe-based solution also contains four or nine times more water coming from the esterification than the Mn- or Co-based solutions, respectively. Considering the higher tendency of iron ions to hydrolyze – lower free energy of hydration and water-exchange rate constant compared to Co, Mn, or La ions as presented in Figure 16 – and the high concentration of water in the Fe-based solutions, a higher formation of precipitating (oxy)-hydroxide species is expected, leading to a higher influence of the droplet-to-particle conversion route as it was observed in the spray-flame synthesis of $LaFeO_3$ perovskite-like oxides.

Concerning the catalytic activity of the spray-flame synthesized materials for the oxidation of CO, the $LaCoO_3$ perovskite oxides presented – as expected and previously presented in Figure 6b – the highest activity ($LaCoO_3$ > $LaMnO_3$ > $LaFeO_3$), reaching a 50 % CO conversion at ~160 °C (Figure 32a). By contrast, the $LaFeO_3$ oxides reached the same conversion at ~300 °C (Figure 32a). Regarding the $LaCoO_3$ and $LaFeO_3$ oxides, the samples synthesized with only ethanol or with an ethanol/2-EHA mixture did not perform radically different in the catalytic CO oxidation. This was not the case for the $LaMnO_3$ oxides as the sample synthesized with an ethanol/2-EHA (50/50 by vol.) mixture reached a 50 % CO conversion at 196 °C (chapter 5.3.4 for more details) while the sample synthesized with ethanol reached the same conversion at 241 °C (Figure 40a, b). As previously indicated, the $LaMnO_3$ sample synthesized with the ethanol/2-EHA counts with a Mn^{4+}-rich orthorhombic (*O*) structure which was identified to have both an increased capability to adsorb oxygen species (e.g., generation of active α-O oxygen species as presented in Figure 41a) and a higher reducibility at lower temperatures (Figure 41b), explaining the higher activity of this sample – compared to the $LaMnO_3$ oxide prepared using ethanol as solvent – for the catalytic oxidation of CO.

Furthermore, $LaMnO_3$ samples were also tested for the selective oxidation of CO (Figure 40c, d) as presented in Chapter 5.3.4. Also in this case and attributed to its high capability to generate active oxygen species on the catalyst surface (Figure 41a), the sample synthesized using an ethanol/2-EHA mixture as solvent presented a higher catalytic activity reaching ~80 % of CO conversion at 220 °C while the H_2 conversion was only of 10 %.

8 Outlook

The spray-flame synthesis of $LaFeO_3$, $LaMnO_3$, and $LaCoO_3$ perovskite nanomaterials for catalytic CO oxidation was presented in this thesis. Using metal-nitrate-based solutions, the effect of two solvents was analyzed: ethanol and 2-ethylhexanoic acid. Several aspects that can potentially help to synthesize materials of higher quality in terms of phase purity and particle size homogeneity were identified and are described as follows:

Regarding hydrolysis, micro explosions and the use of 2-ethylhexanoic acid

- To avoid the formation of large particles from droplets when metal nitrates are used as precursors, two issues must be studied in parallel: the improvement of the nozzle/burner and the control of hydrolysis of metal ions. The improvement of the nozzle, specifically related to the spray-formation directed towards controlling the droplet size, requires multiple aspects: a preparation of several nozzle design options with their respective modeling (e.g., CFD to understand velocities and pressures), the fast and precise manufacture of the parts (e.g., evaluate the possibility of 3D printing of nozzle parts) and a testing methodology which involves the measurement of droplets' sizes and velocities, gas velocity and spraying angles – in a test/design feedback loop – with concrete goals, e.g., a maximum droplet size of 7 μm.

  The hydrolysis of metal ions should also be studied and related with the spray-flame synthesis of oxides. One interesting case would be the synthesis of Al_2O_3 from aluminum nitrate. The first study idea comes from the identified esterification reaction of ethanol with 2-EHA which produces the ester compound ethyl 2-ethylhexanoate and water. In order to eliminate water or to displace the equilibrium reaction to the left (reaction (3.4)), ester compounds can be directly added to the solutions. This is a non-explored field in the design of solutions for the spray-flame synthesis of metal oxides. Other potential water scavengers are ortho esters[230] (e.g., trimethyl orthoformate, TMOF) or acid anhydrides[231] (e.g., acetic anhydride reacts with water to form acetic acid). The addition of esters and acid anhydrides can be studied for the spray-flame synthesis of Al_2O_3, analyzing particle sizes and specific surfaces areas. All these analyses must be done taking into account the chemistry of the solutions, different spectroscopic methods can be used (e.g., IR, UV-Vis, MS, NMR). The identification of hydrolysis-derived chemical species must also be considered, an alternative here might be the use of methods as the electrospray ionization mass spectroscopy (ESI-MS), which is identified as a method that allows the transfer of ionic species from a solution to the gas-phase.[106]

  Another alternative to control the hydrolysis of the metal nitrates can be the use of ligands stronger than H_2O in solution (e.g., NH_3, NO_2^-). Here, attention must be paid to other reactions (e.g., formation of sols and gels) that might affect the final quality of the particles.

  Avoiding the formation of large droplets and controlling hydrolysis would not only serve to avoid the formation of large particles, it would also help avoiding the formation of secondary phases, especially when mixed oxides (e.g., perovskites) are being produced. As identified in this thesis, large particles tend to be La-rich forming phases as La_2CoO_4 or La_2O_3. This is evident from multiple points of view: The low solubility of lanthanum nitrate in different solvents compared with transition metal nitrates and the volatility of, e.g., Co gas-phase species.

- To form small and monomodal nanoparticles and to obtain phase pure perovskite materials, the use of the ethanol/2-ethylhexanoic acid mixtures was very effective. The underlying chemical and physi-

cal phenomena, however, must be further explored. The effect of the metal precursors and intermediaries on the droplet micro explosions can be investigated by modifying the concentration of the precursors in the prepared solution and by recording high-speed videos of the formed droplets (single droplet and spray) in a way that the frequency of the micro-explosions could be quantified. This point is also related with the role of the presence of traces of elements/species that can influence the heterogeneous nucleation of bubbles in the droplets, e.g., addition of extremely low quantities to the solutions of carbon-derived compounds, Al_2O_3 nanoparticles, or of the same final desired compound.

The heterogeneous nucleation of bubbles in droplets can also be encouraged using various approaches as, e.g., saturating[232] the prepared solutions with gases (e.g., CO_2, O_2, N_2) or pressurizing the solution container to facilitate the superheating of ethanol. Lasers can be also used to generate micro-explosions of droplets. For example, Wood et al.[233] used a pulsed CO_2 laser to cause the micro-explosions of ethanol and water droplets.

- The formation of metal carboxylates (e.g., metal 2-ethylhexanoates) from the reaction of metal nitrates with 2-ethylhexanoic acid must be better understood. Until now, the analysis of these compounds in the solutions used for the spray-flame synthesis has been done basically using qualitative methods (e.g., characteristic bands in FTIR). Quantitative analysis can be performed using, e.g., liquid chromatography – mass spectroscopy (LC-MS) or micro-extraction techniques coupled with gas chromatography/spectroscopy. The quantification of metal carboxylates will help also to clarify aspects of the micro-explosion phenomenon and the role of these compounds in the formation of homogeneous nanoparticles.

- Alternatives to 2-ethylhexanoic acid can be also explored.[120] Within the branched chain acids family there two interesting options: 2-propylpentanoic acid (boiling point: 219–220 °C) and 3,5,5-trimethylhexanoic acid (boiling point: 230–240 °C). The latter option might be especially interesting given its high boiling point and higher branching degree. Within the straight chain acids family, options as the n-heptanoic acid, n-octanoic acid or n-nonanoic acid can be tested.

Regarding the synthesis, characterization and the use of perovskites

- Avoiding the formation of large droplets/particles will greatly help improving the phase purity of perovskite materials. A careful design of the solutions of precursors should be always performed, understanding, e.g., the chemistry and decomposition of precursors in order to identify important differences, the effect of solvents in the solution and in the flame characteristics (e.g., temperatures, residence time).

- For catalytic applications, the surface of the perovskites should be as clean as possible. Chemical species (e.g., unburned solvents, CO, CO_2, H_2O) that are adsorbed on the surface of the materials should be minimized. Until now, this is commonly done by heating the materials in ovens at, e.g., 250 °C for some hours. Instead, the heating can be done directly in the reactor and under vacuum. As low pressures can be reached in the reactor system, the samples can be left in the filter with a continuous flow of N_2/O_2 and at a temperature of ~150 °C, as with vacuum, lower temperatures are required to desorb the species. Heating at low temperatures is also important in order to limit the sintering of the particles. Nevertheless, this process – as the normal heating in ovens at mild temperatures – is not effective to decrease the content of carbonates.

Outlook

- The understanding of the electronic structure of the perovskites must be increased to develop better catalysts. Characterization techniques as EXAFS (extended X-ray absorption fine structure) and XANES (X-ray absorption near-edge structure) can be performed using synchrotron radiation in order to identify, e.g., interatomic distances, coordination numbers and valence states. These measurements should go from sporadic to frequent and should be related with the studied applications.
- As stated by Royer et al.[26], the future in the use of perovskites as catalysts might be more related to the production of hybrid catalysts (e.g., (noble)metal/perovskite). However, many other alternatives can be tested. For example, the synthesis of perovskites in a high-entropy configuration[234] (e.g., $La(Co_{0.2}Cr_{0.2}Fe_{0.2}Mn_{0.2}Ni_{0.2})O_3$, $(Sr_{0.5}Ba_{0.5})(Zr_{0.2}Sn_{0.2}Ti_{0.2}Hf_{0.2}Nb_{0.2})O_3$) is an emerging promising field that can be explored.

Various ideas regarding the use of hydrogen, organization of information, and digitalization

- The use of hydrogen in the pilot flame of the spray-flame synthesis should be further explored. As hydrogen is currently being worldwide explored for several applications, the spray-flame synthesis method can be easily coupled with several alternatives. For example, if carbon contamination of the synthesized material needs to be reduced, water can be used as the main solvent to prepare the precursor solutions. In this case, a H_2/O_2 supporting flame would provide the required energy for the spray-flame synthesis without introducing – contrary to CH_4/O_2 flames – additional carbon sources to the process and final material.

  Linking the characterization of materials with the synthesis operation parameters (e.g., liquid and gas flow rates, concentration of precursors) is a simple task but time demanding and very manual. A more complex – but also normally done and manual – activity is relating the spray-flame characteristics (e.g., droplet sizes, temperatures, chemical species) with the materials characterization (e.g., particle sizes, crystallographic phase, surface characteristics). Getting to a level at which the spray-flame and materials characteristics could be automatically compared is not a simple task. One approach might be to organize all characterization results in a database and in a parametric way. For example, a folder of the spray-flame synthesis of $LaCoO_3$ will contain the XRD, FTIR, XPS results of the materials – in a format that can be analyzed by a computer program – and the flame temperatures, droplet sizes from LII or PDA measurements. All these data should be correlated and the program could be able to identify, e.g., the presence of secondary phases in XRD, and to relate these issues with flame parameters. The development of such databases will give the potential to develop machine learning – and eventually, artificial intelligence – alternatives, in which the program might be able to predict the best operation conditions to synthesize a given material. Another alternative here is related to the in-situ crystallographic characterization of materials in the spray-flame reactor. One way of achieving this might be using a soft X-ray free electron laser[235] in order to obtain in-situ diffraction patterns of materials. However, this requires a powerful X-ray source (Beamline) and considering having the continuous presence of a spray-flame reactor in a beamline.

9 References

1. Armaroli, N.; Balzani, V., Solar Electricity and Solar Fuels: Status and Perspectives in the Context of the Energy Transition. *Chemistry* **2016,** 22, 32-57.

2. Droege, P., Urban Energy Transition: An Introduction. In *Urban Energy Transition*, Droege, P., Ed. Elsevier: 2008; pp 1-14.

3. Schlogl, R., E-Mobility and the Energy Transition. *Angewandte Chemie International Edition* **2017,** 56, 11019-11022.

4. Artz, J.; Muller, T. E.; Thenert, K.; Kleinekorte, J.; Meys, R.; Sternberg, A.; Bardow, A.; Leitner, W., Sustainable Conversion of Carbon Dioxide: An Integrated Review of Catalysis and Life Cycle Assessment. *Chemical Reviews* **2018,** 118, 434-504.

5. Yang, Z.; Zhang, J.; Kintner-Meyer, M. C.; Lu, X.; Choi, D.; Lemmon, J. P.; Liu, J., Electrochemical energy storage for green grid. *Chemical Reviews* **2011,** 111, 3577-613.

6. Palys, M. J.; Daoutidis, P., Using hydrogen and ammonia for renewable energy storage: A geographically comprehensive techno-economic study. *Computers & Chemical Engineering* **2020,** 136, 106785.

7. Song, J.; Wei, C.; Huang, Z. F.; Liu, C.; Zeng, L.; Wang, X.; Xu, Z. J., A review on fundamentals for designing oxygen evolution electrocatalysts. *Chemical Society Reviews* **2020,** 49, 2196-2214.

8. Granger, P.; Parvulescu, V.; Kaliaguine, S.; Prellier, W., *Perovskites and Related Mixed Oxides*. Wiley-VCH Verlag GmbH & Co. KGaA: 2016; p 1019.

9. Suntivich, J.; May, K. J.; Gasteiger, H. A.; Goodenough, J. B.; Shao-Horn, Y., A perovskite oxide optimized for oxygen evolution catalysis from molecular orbital principles. *Science* **2011,** 334, 1383-5.

10. Kucharczyk, B., Catalytic Oxidation of Carbon Monoxide on Pd-Containing $LaMnO_3$ Perovskites. *Catalysis Letters* **2015,** 145, 1237-1245.

11. Wang, Y.; Cui, X.; Li, Y.; Chen, L.; Shu, Z.; Chen, H.; Shi, J., High surface area mesoporous $LaFe_xCo_{1-x}O_3$ oxides: synthesis and electrocatalytic property for oxygen reduction. *Dalton Transactions* **2013,** 42, 9448-52.

12. Mädler, L., Liquid-fed Aerosol Reactors for One-step Synthesis of Nano-structured Particles. *KONA Powder and Particle Journal* **2004,** 22, 107-120.

13. Rosebrock, C. D.; Riefler, N.; Wriedt, T.; Mädler, L.; Tse, S. D., Disruptive burning of precursor/solvent droplets in flame-spray synthesis of nanoparticles. *AIChE Journal* **2013,** 59, 4553-4566.

14. Strobel, R.; Pratsinis, S. E., Effect of solvent composition on oxide morphology during flame spray pyrolysis of metal nitrates. *Physical Chemistry Chemical Physics* **2011,** 13, 9246-52.

15. Rosebrock, C. D.; Wriedt, T.; Mädler, L.; Wegner, K., The role of microexplosions in flame spray synthesis for homogeneous nanopowders from low-cost metal precursors. *AIChE Journal* **2016,** 62, 381-391.

16. Chiarello, G. L.; Rossetti, I.; Forni, L.; Lopinto, P.; Migliavacca, G., Solvent nature effect in preparation of perovskites by flame pyrolysis. *Applied Catalysis B: Environmental* **2007,** 72, 227-232.

17. Chiarello, G. L.; Rossetti, I.; Forni, L.; Lopinto, P.; Migliavacca, G., Solvent nature effect in preparation of perovskites by flame-pyrolysis. *Applied Catalysis B: Environmental* **2007,** 72, 218-226.

18. Ortega-San-Martin, L., Introduction to Perovskites: A Historical Perspective. In *Revolution of the Perovskite: Synthesis, properties and applications*, Arul, N. S.; Nithya, V. D., Eds. Springer: 2020.

19. Chakhmouradian, A. R.; Woodward, P. M., Celebrating 175 years of perovskite research: a tribute to Roger H. Mitchell. *Physics and Chemistry of Minerals* **2014,** 41, 387-391.

20. Katz, E. A., Perovskite: Name Puzzle and German-Russian Odyssey of Discovery. *Helvetica Chimica Acta* **2020,** 103, e2000061.

21. Long, Y. W., A-site ordered quadruple perovskite oxides $AA'_3B_4O_{12}$. *Chinese Physics B* **2016,** 25, 078108.

22. Ishihara, T., Structure and Properties of Perovskite Oxides. In *Perovskite Oxide for Solid Oxide Fuel Cells*, 2009; pp 1-16.

23. Tiley, R. D., The ABX_3 Perovskite Structure. In *Perovskites: Structure-Property Relationships*, John Wiley & Sons, ltd: 2016; pp 11-26.

24. Mitchell, R. H.; Welch, M. D.; Chakhmouradian, A. R., Nomenclature of the perovskite supergroup: A hierarchical system of classification based on crystal structure and composition. *Mineralogical Magazine* **2018,** 81, 411-461.

25. Arandiyan, H. Methane Combustion over Lanthanum-based Perovskite Mixed Oxides. Tsinghua University, Beijing, China, 2015.

26. Royer, S.; Duprez, D.; Can, F.; Courtois, X.; Batiot-Dupeyrat, C.; Laassiri, S.; Alamdari, H., Perovskites as substitutes of noble metals for heterogeneous catalysis: dream or reality. *Chemical Reviews* **2014,** 114, 10292-368.

27. Pena, M. A.; Fierro, J. L., Chemical structures and performance of perovskite oxides. *Chemical Reviews* **2001,** 101, 1981-2017.

28. Dixon, C. A. L.; Kavanagh, C. M.; Knight, K. S.; Kockelmann, W.; Morrison, F. D.; Lightfoot, P., Thermal evolution of the crystal structure of the orthorhombic perovskite $LaFeO_3$. *Journal of Solid State Chemistry* **2015,** 230, 337-342.

29. Kumar, A. Synthesis and characterization of $LaFeO_3$ using high energy ball milling. Master, Thapar University, India, 2011.

30. Povoden-Karadeniz, E.; Grundy, A. N.; Chen, M.; Ivas, T.; Gauckler, L. J., Thermodynamic Assessment of the La-Fe-O System. *Journal of Phase Equilibria and Diffusion* **2009,** 30, 351-366.

31. Feng, J.; Liu, T.; Xu, Y.; Zhao, J.; He, Y., Effects of PVA content on the synthesis of $LaFeO_3$ via sol–gel route. *Ceramics International* **2011,** 37, 1203-1207.

32. Gildo-Ortiz, L.; Reyes-Gómez, J.; Flores-Álvarez, J. M.; Guillén-Bonilla, H.; Olvera, M. d. l. L.; Rodríguez Betancourtt, V. M.; Verde-Gómez, Y.; Guillén-Cervantes, A.; Santoyo-Salazar, J., Synthesis, characterization and sensitivity tests of perovskite-type $LaFeO_3$ nanoparticles in CO and propane atmospheres. *Ceramics International* **2016,** 42, 18821-18827.

33. Küpferling, M.; Corral Flores, V.; Grössinger, R.; Matutes Aquino, J., Preparation and characterization of hexaferrite. *Journal of Magnetism and Magnetic Materials* **2005,** 290-291, 1255-1258.

34. Zhu, Z.; Peelaers, H.; Van de Walle, C. G., Electronic and protonic conduction in $LaFeO_3$. *Journal of Materials Chemistry A* **2017,** 5, 15367-15379.

35. Thirumalairajan, S.; Girija, K.; Hebalkar, N. Y.; Mangalaraj, D.; Viswanathan, C.; Ponpandian, N., Shape evolution of perovskite $LaFeO_3$ nanostructures: a systematic investigation of growth mechanism, properties and morphology dependent photocatalytic activities. *RSC Advances* **2013,** 3, 7549–7561.

36. Li, X.; Zhang, H.; Liu, X.; Li, S.; Zhao, M., XPS study on O(1s) and Fe(2p) for nanocrystalline composite oxide $LaFeO_3$ with the perovskite structure. *Materials Chemistry and Physics* **1994,** 38, 355-362.

37. Blanck, D.; Berrier, E.; Paul, J.-F., First-Principles Investigation of the Relevant Surfaces Exposed by Polycrystalline $LaFeO_3$. *ChemCatChem* **2017,** 9, 2383-2389.

38. Sun, L.; Hu, J.; Qin, H.; Zhao, M.; Fan, K., Influences of Ca Doping and Oxygen Vacancy upon Adsorption of CO on the $LaFeO_3$ (010) Surface: A First-Principles Study. *The Journal of Physical Chemistry C* **2011,** 115, 5593-5598.

39. Kobayashi, Y.; Mitsunaga, T.; Fujinawa, G.; Arii, T.; Suetake, M.; Asai, K.; Harada, J., Structural Phase Transition from Rhombohedral to Cubic in $LaCoO_3$. *Journal of the Physical Society of Japan* **2000,** 69, 3468-3469.

40. Zhang, W.-W.; Povoden-Karadeniz, E.; Xu, H.; Chen, M., Thermodynamic Modeling of the La-Co-O System. *Journal of Phase Equilibria and Diffusion* **2019,** 40, 219-234.

41. Hansteen, O. H.; Fjellvåg, H., Synthesis, Crystal Structure, and Magnetic Properties of $La_4Co_3O_{10+\delta}$ ($0.00 \leqslant \delta \leqslant 0.30$). *Journal of Solid State Chemistry* **1998,** 141, 212-220.

42. Nowroozi, M. A.; Ivlev, S.; Rohrer, J.; Clemens, O., La_2CoO_4: a new intercalation based cathode material for fluoride ion batteries with improved cycling stability. *Journal of Materials Chemistry A* **2018,** 6, 4658-4669.

43. Yuste, M.; Perez-Flores, J. C.; de Paz, J. R.; Azcondo, M. T.; Garcia-Alvarado, F.; Amador, U., New perovskite materials of the $La_{(2-x)}Sr_{(x)}CoTiO_6$ series. *Dalton Transactions* **2011,** 40, 7908-15.

44. Dimitrovska-Lazova, S.; Aleksovska, S.; Mirceski, V.; Pecovska-Gjorgjevich, M., Correlation between composition, electrical and electrochemical properties of $LnCo_{1-x}Cr_xO_3$ (Ln = Pr, Gd and x = 0, 0.5 and 1) perovskites. *Journal of Solid State Electrochemistry* **2019,** 23, 861-870.

45. Tomiyasu, K.; Koyama, S.-I.; Watahiki, M.; Sato, M.; Nishihara, K.; Takahashi, Y.; Onodera, M.; Iwasa, K.; Nojima, T.; Nojiri, H.; Okamoto, J.; Huang, D.-J.; Yamasaki, Y.; Nakao, H.; Murakami, Y., Microscopic Examinations of Co Valences and Spin States in Electron-Doped $LaCoO_3$. *Journal of the Physical Society of Japan* **2016,** 85, 094702.

46. Simbock, J.; Ghiasi, M.; Schonebaum, S.; Simon, U.; de Groot, F. M. F.; Palkovits, R., Electronic parameters in cobalt-based perovskite-type oxides as descriptors for chemocatalytic reactions. *Nature Communications* **2020,** 11, 652.

47. Yang, Q.; Wang, D.; Wang, C.; Li, X.; Li, K.; Peng, Y.; Li, J., Facile surface improvement method for $LaCoO_3$ for toluene oxidation. *Catalysis Science & Technology* **2018,** 8, 3166-3173.

48. Wang, C.; Zeng, L.; Guo, W.; Gong, C.; Yang, J., Enhancing oxygen and hydrogen evolution activities of perovskite oxide $LaCoO_3$ via effective doping of platinum. *RSC Advances* **2019,** 9, 35646-35654.

49. Khan, S.; Oldman, R. J.; Cora, F.; Catlow, C. R.; French, S. A.; Axon, S. A., A computational modelling study of oxygen vacancies at $LaCoO_3$ perovskite surfaces. *Physical Chemistry Chemical Physics* **2006,** 8, 5207-22.

50. Rivero, P.; Meunier, V.; Shelton, W., Electronic, structural and magnetic properties of $LaMnO_3$ phase transition at high temperature. *Physical Review B* **2016,** 93, 024111.

51. Sedykh, V.; Shekhtman, V. S.; Zverkova, I. I.; Dubovitskii, A. V.; Kulakov, V. I., Reversibility of structure phase transitions in $LaMnO_{3+\delta}$ manganite under heat treatment. *Physica C: Superconductivity* **2006,** 433, 189-194.

52. Grundy, A. N.; Chen, M.; Gauckler, L. J.; Hallstedt, B., Assessment of the La-Mn-O system. *Journal of Phase Equilibria and Diffusion* **2005,** 26, 131-151.

53. Bogush, A. K.; Pavlov, V. I.; Balyko, L. V., Structural phase transitions in the $LaMnO_{3+\lambda}$ system. *Crystal Research and Technology* **1983,** 18, 589-598.

54. Qiu, X.; Proffen, T.; Mitchell, J. F.; Billinge, S. J., Orbital correlations in the pseudocubic O and rhombohedral R phases of $LaMnO_3$. *Physical Review Letters* **2005,** 94, 177203.

55. Tomaszewski, P. E.; Miniajluk, N.; Zawadzki, M.; Trawczyński, J., X-ray study of structural phase transitions in nanocrystalline $LaMnO_{3+\delta}$ perovskite. *Phase Transitions* **2019,** 92, 525-536.

56. Pilania, G.; Ramprasad, R., Adsorption of atomic oxygen on cubic $PbTiO_3$ and $LaMnO_3$ (001) surfaces: A density functional theory study. *Surface Science* **2010,** 604, 1889-1893.

57. Shi, C.; Sun, L.; Qin, H.; Wang, X.; Li, L.; Hu, J., Adsorption properties of CO molecule on the orthorhombic structure $LaMnO_3$ (0 1 0) surface. *Computational Materials Science* **2015,** 98, 83-87.

58. Wang, T.; Zhang, C.; Wang, J.; Li, H.; Duan, Y.; Liu, Z.; Lee, J. Y.; Hu, X.; Xi, S.; Du, Y.; Sun, S.; Liu, X.; Lee, J.-M.; Wang, C.; Xu, Z. J., The interplay between the suprafacial and intrafacial mechanisms for complete methane oxidation on substituted $LaCoO_3$ perovskite oxides. *Journal of Catalysis* **2020,** 390, 1-11.

59. Levasseur, B.; Kaliaguine, S., Methanol oxidation on $LaBO_3$ (B=Co, Mn, Fe) perovskite-type catalysts prepared by reactive grinding. *Applied Catalysis A: General* **2008,** 343, 29-38.

60. Tascón, J. M. D.; González Tejuca, L., Catalytic activity of perovskite-type oxides $LaMeO_3$. *Reaction Kinetics and Catalysis Letters* **1980,** 15, 185-191.

61. Xiao, P.; Zhong, L.; Zhu, J.; Hong, J.; Li, J.; Li, H.; Zhu, Y., CO and soot oxidation over macroporous perovskite $LaFeO_3$. *Catalysis Today* **2015,** 258, 660-667.

62. Magalhães, R. N. S. H.; Toniolo, F. S.; da Silva, V. T.; Schmal, M., Selective CO oxidation reaction (SELOX) over cerium-doped $LaCoO_3$ perovskite catalysts. *Applied Catalysis A: General* **2010,** 388, 216-224.

63. Huang, X.; Zhao, G.; Wang, G.; Irvine, J. T. S., Synthesis and applications of nanoporous perovskite metal oxides. *Chemical Science* **2018,** 9, 3623-3637.

64. Yu, J.; Ran, R.; Zhong, Y.; Zhou, W.; Ni, M.; Shao, Z., Advances in Porous Perovskites: Synthesis and Electrocatalytic Performance in Fuel Cells and Metal–Air Batteries. *Energy & Environmental Materials* **2020,** 3, 121-145.

65. Zhang, R.; Alamdari, H.; Kaliaguine, S., Water vapor sensitivity of nanosized $La(Co, Mn, Fe)_{1-x}(Cu, Pd)_xO_3$ perovskites during NO reduction by C_3H_6 in the presence of oxygen. *Applied Catalysis B: Environmental* **2007,** 72, 331-341.

66. Thuy, N. T.; Minh, D. L., Size Effect on the Structural and Magnetic Properties of Nanosized Perovskite $LaFeO_3$ Prepared by Different Methods. *Advances in Materials Science and Engineering* **2012,** 2012, 1-6.

67. Dai, J.; Zhu, Y.; Zhong, Y.; Miao, J.; Lin, B.; Zhou, W.; Shao, Z., Enabling High and Stable Electrocatalytic Activity of Iron‐Based Perovskite Oxides for Water Splitting by Combined Bulk Doping and Morphology Designing. *Advanced Materials Interfaces* **2018,** 6, 1801317.

68. Sokolowski, M.; Sokolowska, A.; Michalski, A.; Gokieli, B., The "in-flame-reaction" method for Al_2O_3 aerosol formation. *Journal of Aerosol Science* **1977,** 8, 219-230.

69. Ulrich, G. D., Theory of Particle Formation and Growth in Oxide Synthesis Flames. *Combustion Science and Technology* **1971,** 4, 47-57.

70. Barthel, H.; Rsch, L.; Weis, J., Fumed Silica - Production, Properties, and Applications. In *Organosilicon Chemistry II*, 1995; pp 761-778.

71. Pratsinis, S. E., Flame aerosol synthesis of ceramic powders. *Progress in Energy and Combustion Science* **1998,** 24, 197-219.

72. Kammler, H. K.; Mädler, L.; Pratsinis, S. E., Flame Synthesis of Nanoparticles. *Chemical Engineering & Technology* **2001,** 24, 583-596.

73. Nielsen, M. L.; Hamilton, P. M.; Walsh, R. J., ULTRAFINE METAL OXIDES BY DECOMPOSITION OF SALTS IN FLAME. *Journal of the Electrochemical Society* **1961,** 108, C64-C64.

74. Teoh, W. Y.; Amal, R.; Madler, L., Flame spray pyrolysis: An enabling technology for nanoparticles design and fabrication. *Nanoscale* **2010,** 2, 1324-47.

75. Strobel, R.; Pratsinis, S. E., Flame aerosol synthesis of smart nanostructured materials. *Journal of Materials Chemistry* **2007,** 17, 4743–4756.

76. Koirala, R.; Pratsinis, S. E.; Baiker, A., Synthesis of catalytic materials in flames: opportunities and challenges. *Chemical Society Reviews* **2016,** 45, 3053-68.

77. Schulz, C.; Dreier, T.; Fikri, M.; Wiggers, H., Gas-phase synthesis of functional nanomaterials: Challenges to kinetics, diagnostics, and process development. *Proceedings of the Combustion Institute* **2019,** 37, 83-108.

78. Mäkelä, J. M.; Haapanen, J.; Harra, J.; Juuti, P.; Kujanpää, S., Liquid Flame Spray—A Hydrogen-Oxygen Flame Based Method for Nanoparticle Synthesis and Functional Nanocoatings. *KONA Powder and Particle Journal* **2017,** 34, 141-154.

79. Li, S.; Ren, Y.; Biswas, P.; Tse, S. D., Flame aerosol synthesis of nanostructured materials and functional devices: Processing, modeling, and diagnostics. *Progress in Energy and Combustion Science* **2016,** 55, 1-59.

80. Schneider, F.; Suleiman, S.; Menser, J.; Borukhovich, E.; Wlokas, I.; Kempf, A.; Wiggers, H.; Schulz, C., SpraySyn-A standardized burner configuration for nanoparticle synthesis in spray flames. *Review of Scientific Instruments* **2019,** 90, 085108.

81. Roth, P., Particle synthesis in flames. *Proceedings of the Combustion Institute* **2007,** 31, 1773-1788.

82. Kluge, S.; Deng, L.; Feroughi, O.; Schneider, F.; Poliak, M.; Fomin, A.; Tsionsky, V.; Cheskis, S.; Wlokas, I.; Rahinov, I.; Dreier, T.; Kempf, A.; Wiggers, H.; Schulz, C., Initial reaction steps during flame synthesis of iron-oxide nanoparticles. *CrystEngComm* **2015,** 17, 6930-6939.

83. Karakaya, Y.; Kluge, S.; Wiggers, H.; Schulz, C.; Kasper, T., Investigation of the combustion of iron pentacarbonyl and the formation of key intermediates in iron oxide synthesis flames. *Chemical Engineering Science* **2021,** 230, 116169.

84. Kluge, S.; Wiggers, H.; Schulz, C., Mass spectrometric analysis of clusters and nanoparticles during the gas-phase synthesis of tungsten oxide. *Proceedings of the Combustion Institute* **2017,** 36, 1037-1044.

85. Gurav, A.; Kodas, T.; Pluym, T.; Xiong, Y., Aerosol Processing of Materials. *Aerosol Science and Technology* **1993,** 19, 411-452.

86. Wiggers, H.; Fikri, M.; Wlokas, I.; Roth, P.; Schulz, C., Synthesis of Tailored Nanoparticles in Flames: Chemical Kinetics, In Situ Diagnostics, Numerical Simulation, and Process Development. In *Nanoparticles from the Gasphase*, 2012; pp 3-48.

87. Meierhofer, F.; Mädler, L.; Fritsching, U., Nanoparticle evolution in flame spray pyrolysis—Process design via experimental and computational analysis. *AIChE Journal* **2019,** 66, e16885.

88. Purwanto, A., Fabrication of functional nanomaterials using flame assisted spray pyrolysis. In 2014; pp 48-51.

89. Kuai, L.; Wang, J.; Ming, T.; Fang, C.; Sun, Z.; Geng, B.; Wang, J., Aerosol-spray diverse mesoporous metal oxides from metal nitrates. *Scientific Reports* **2015,** 5, 9923.

90. Jossen, R.; Pratsinis, S. E.; Stark, W. J.; Madler, L., Criteria for Flame-Spray Synthesis of Hollow, Shell-Like, or Inhomogeneous Oxides. *Journal of the American Ceramic Society* **2005,** 88, 1388-1393.

91. Pokhrel, S.; Madler, L., Flame-made Particles for Sensors, Catalysis, and Energy Storage Applications. *Energy Fuels* **2020,** 34, 13209-13224.

92. Wei, J.; Li, S.; Ren, Y.; Zhang, Y.; Tse, S. D., Investigating the role of solvent formulations in temperature-controlled liquid-fed aerosol flame synthesis of YAG-based nanoparticles. *Proceedings of the Combustion Institute* **2019,** 37, 1193-1201.

93. Meierhofer, F.; Li, H.; Gockeln, M.; Kun, R.; Grieb, T.; Rosenauer, A.; Fritsching, U.; Kiefer, J.; Birkenstock, J.; Madler, L.; Pokhrel, S., Screening Precursor-Solvent Combinations for $Li_4Ti_5O_{12}$ Energy Storage Material Using Flame Spray Pyrolysis. *ACS Applied Materials & Interfaces* **2017,** 9, 37760-37777.

94. Pokhrel, S.; Birkenstock, J.; Schowalter, M.; Rosenauer, A.; Mädler, L., Growth of Ultrafine Single Crystalline WO3 Nanoparticles Using Flame Spray Pyrolysis. *Crystal Growth & Design* **2009,** 10, 632-639.

95. Akurati, K. K.; Vital, A.; Dellemann, J.-P.; Michalow, K.; Graule, T.; Ferri, D.; Baiker, A., Flame-made WO_3/TiO_2 nanoparticles: Relation between surface acidity, structure and photocatalytic activity. *Applied Catalysis B: Environmental* **2008,** 79, 53-62.

96. Kuvshinova, T. B.; Skorikov, V. M.; Volodin, V. D., Reaction of bismuth nitrate with sodium citrate in water-glycerol solutions. *Russian Journal of Inorganic Chemistry* **2009,** 54, 1816-1819.

97. Rogers, R. D.; Bond, A. H.; Aguinaga, S., Alcoholysis of bismuth(III) nitrate pentahydrate by polyethylene glycols. Comparison with bismuth(III) nitrate crown ether complexation. *Journal of the American Chemical Society* **2002,** 114, 2960-2967.

98. Yuvaraj, S.; Fan-Yuan, L.; Tsong-Huei, C.; Chuin-Tih, Y., Thermal Decomposition of Metal Nitrates in Air and Hydrogen Environments. *The Journal of Physical Chemistry B* **2003,** 107, 1044-1047.

99. Tani, T.; Watanabe, N.; Takatori, K.; Pratsinis, S. E., Morphology of oxide particles made by the emulsion combustion method. *Journal of the American Ceramic Society* **2003,** 86, 898-904.

100. Zyrichev, N. A.; Shlenskii, O. F., Kinetics of decomposition of hydrated nitrates by short contact time plasma heating. *High Energy Chemistry* **2000,** 34, 40-46.

101. Field, B. O.; Hardy, C. J., Inorganic nitrates and nitrato-compounds. *Quarterly Reviews, Chemical Society* **1964,** 18, 361-388.

102. Cochran, E. A.; Woods, K. N.; Johnson, D. W.; Page, C. J.; Boettcher, S. W., Unique chemistries of metal-nitrate precursors to form metal-oxide thin films from solution: materials for electronic and energy applications. *Journal of Materials Chemistry A* **2019,** 7, 24124-24149.

103. Henry, M.; Jolivet, J. P.; Livage, J., Aqueous chemistry of metal cations: Hydrolysis, condensation and complexation. In *Chemistry, Spectroscopy and Applications of Sol-Gel Glasses*, 1992; pp 153-206.

104. Graham, N.; Jiang, C. C.; Li, X. Z.; Jiang, J. Q.; Ma, J., The influence of pH on the degradation of phenol and chlorophenols by potassium ferrate. *Chemosphere* **2004,** 56, 949-56.

105. Ho, C.-H.; Van Zee, J. W., Effect of Ethanol and Temperature on the Hydrolysis of a Nickel(II) Ion in Ethanol−Water Solutions. *Industrial & Engineering Chemistry Research* **2000,** 39, 752-758.

106. Schröder, D.; de Jong, K. P.; Roithová, J., Gas-Phase Model Studies Relevant to the Decomposition of Transition-Metal Nitrates $M(NO_3)_2$ (M = Co, Ni) into Metal-Oxo Species. *European Journal of Inorganic Chemistry* **2009,** 2009, 2121-2128.

107. Di Marco, V. B.; Bombi, G. G., Electrospray mass spectrometry (ESI-MS) in the study of metal-ligand solution equilibria. *Mass Spectrometry Reviews* **2006,** 25, 347-79.

108. Pachghare, P. R.; Mahalle, A. M., Thermal Performance of Closed Loop Pulsating Heat Pipe Using Pure and Binary Working Fluids. *Frontiers in Heat Pipes* **2013,** 3, 033002

109. Chao, J.; Rossini, F. D., Heats of Combustion, Formation, and Isomerization of Nineteen Alkanols. *Journal of Chemical & Engineering Data* **1965,** 10, 374-379.

110. Jones, M.; Li, C. H.; Afjeh, A.; Peterson, G., Experimental study of combustion characteristics of nanoscale metal and metal oxide additives in biofuel (ethanol). *Nanoscale Research Letters* **2011,** 6, 246.

111. Prenting, M. M.; Bin Dzulfida, M. I.; Dreier, T.; Schulz, C., Characterization of tracers for two-color laser-induced fluorescence liquid-phase temperature imaging in sprays. *Experiments in Fluids* **2020,** 61, 77.

112. Mädler, L.; Kammler, H. K.; Mueller, R.; Pratsinis, S. E., Controlled synthesis of nanostructured particles by flame spray pyrolysis. *Journal of Aerosol Science* **2002,** 33, 369-389.

113. Bieber, M.; Tischendorf, R.; Schmid, H.-J. S.; Reddemann, M.; Kneer, R., Influence of precursor concentration on spray and particle formation in flame spray pyrolysis. In *29th Conference on Liquid Atomization and Spray Systems*, Paris, France, 2019; pp 1-8.

114. Stodt, M. F. B.; Kiefer, J.; Fritsching, U., Ethanol droplet formation, dynamics and combustion mode in the flame of the SpraySyn-nozzle. *Experiments in Fluids* **2019,** 60, 125.

115. Palumbo, R.; Léde, J.; Boutin, O.; Elorza Ricart, E.; Steinfeld, A.; Möller, S.; Weidenkaff, A.; Fletcher, E. A.; Bielicki, J., The production of Zn from ZnO in a high-temperature solar decomposition quench process—I. The scientific framework for the process. *Chemical Engineering Science* **1998,** 53, 2503-2517.

116. Haueter, P.; Moeller, S.; Palumbo, R.; Steinfeld, A., The production of zinc by thermal dissociation of zinc oxide—solar chemical reactor design. *Solar Energy* **1999,** 67, 161-167.

117. Hembram, K.; Sivaprakasam, D.; Rao, T. N.; Wegner, K., Large-scale manufacture of ZnO nanorods by flame spray pyrolysis. *Journal of Nanoparticle Research* **2013,** 15, 1461.

118. Sossi, P. A.; Fegley, B., Thermodynamics of Element Volatility and its Application to Planetary Processes. *Reviews in Mineralogy and Geochemistry* **2018,** 84, 393-459.

119. Harra, J.; Kujanpää, S.; Haapanen, J.; Juuti, P.; Mäkelä, J. M.; Hyvärinen, L.; Honkanen, M., Aerosol analysis of residual and nanoparticle fractions from spray pyrolysis of poorly volatile precursors. *AIChE Journal* **2017,** 63, 881-892.

120. Kubitschke, J.; Lange, H.; Strutz, H., Carboxylic Acids, Aliphatic. In *Ullmann's Encyclopedia of Industrial Chemistry*, 2014; pp 1-18.

121. Raju, R.; Prasad, K., Synthetic applications of 2-ethylhexanoic acid derived reagents. *Tetrahedron* **2012,** 68, 1341-1349.

122. Mikami, M.; Kojima, N., An experimental and modeling study on stochastic aspects of microexplosion of binary-fuel droplets. *Proceedings of the Combustion Institute* **2002,** 29, 551-559.

123. Blander, M.; Katz, J. L., Bubble nucleation in liquids. *AIChE Journal* **1975,** 21, 833-848.

124. Hasan, M.; Monde, M., Review of homogeneous nucleation boiling phenomena under non-equilibrium heating condition and a generalized model for boiling explosion. *Trends in Heat & Mass Transfer* **2013,** 13, 26.

125. Wang, C. H.; Lin, C. Z.; Hung, W. G.; Huang, W. C.; Law, C. K., On the Burning Characteristics of Collision-Generated Water/Hexadecane Droplets. *Combustion Science and Technology* **2004,** 176, 71-93.

126. Mishra, S.; Daniele, S.; Hubert-Pfalzgraf, L. G., Metal 2-ethylhexanoates and related compounds as useful precursors in materials science. *Chemical Society Reviews* **2007,** 36, 1770–1787.

127. da Silva, M. J.; Ayala, D. A. M., Unravelling transition metal-catalyzed terpenic alcohol esterification: a straightforward process for the synthesis of fragrances. *Catalysis Science & Technology* **2016,** 6, 3197-3207.

128. Kriegel, R.; Töpfer, J.; Preu, N.; Grimm, S.; Böer, J., Flame pyrolysis: A preparation route for ultrafine powders of metastable?-$SrMnO_3$ and $NiMn_2O_4$. *Journal of Materials Science Letters* **1994,** 13, 1111-1113.

129. Saracco, G.; Geobaldo, F.; Mazza, D.; Baldi, G., New method for catalyst powder manufacturing based on solvent combustion. *Journal of Thermal Analysis and Calorimetry* **1999,** 56, 1435-1442.

130. Ferri, D.; Forni, L., Methane combustion on some perovskite-like mixed oxides. *Applied Catalysis B: Environmental* **1998,** 16, 119-126.

131. Giacomuzzi, R. A. M.; Portinari, M.; Rossetti, I.; Forni, L., A new method for preparing nanometer-size perovskitic catalysts for CH_4 flameless combustion. In *12th International Congress on Catalysis, Proceedings of the 12th ICC*, 2000; pp 197-202.

132. Buchneva, O.; Rossetti, I.; Oliva, C.; Scavini, M.; Cappelli, S.; Sironi, B.; Allieta, M.; Kryukov, A.; Forni, L., Effective Ag doping and resistance to sulfur poisoning of La–Mn perovskites for the catalytic flameless combustion of methane. *Journal of Materials Chemistry* **2010,** 20, 10021–10031

133. Campagnoli, E.; Tavares, A.; Fabbrini, L.; Rossetti, I.; Dubitsky, Y.; Zaopo, A.; Forni, L., Effect of preparation method on activity and stability of $LaMnO_3$ and $LaCoO_3$ catalysts for the flameless combustion of methane. *Applied Catalysis B: Environmental* **2005,** 55, 133-139.

134. Chiarello, G.; Rossetti, I.; Forni, L., Flame-spray pyrolysis preparation of perovskites for methane catalytic combustion. *Journal of Catalysis* **2005,** 236, 251-261.

135. Heel, A.; Holtappels, P.; Graule, T., On the synthesis and performance of flame-made nanoscale $La_{0.6}Sr_{0.4}CoO_{3-\delta}$ and its influence on the application as an intermediate temperature solid oxide fuel cell cathode. *Journal of Power Sources* **2010,** 195, 6709-6718.

136. Aegerter, D.; Borlaf, M.; Fabbri, E.; Clark, A. H.; Nachtegaal, M.; Graule, T.; Schmidt, T. J., Tuning the Co Oxidation State in $Ba_{0.5}Sr_{0.5}Co_{0.8}Fe_{0.2}O_{3-\delta}$ by Flame Spray Synthesis Towards High Oxygen Evolution Reaction Activity. *Catalysts* **2020,** 10, 984.

137. Tejuca, L. G.; Fierro, J. L. G., *Properties and Applications of Perovskite-Type Oxides*. Taylor & Francis Group: 1992.

138. Orge, C. A.; Órfão, J. J. M.; Pereira, M. F. R.; Barbero, B. P.; Cadús, L. E., Lanthanum-based perovskites as catalysts for the ozonation of selected organic compounds. *Applied Catalysis B: Environmental* **2013,** 140-141, 426-432.

139. Hwang, J.; Rao, R. R.; Giordano, L.; Katayama, Y.; Yu, Y.; Shao-Horn, Y., Perovskites in catalysis and electrocatalysis. *Science* **2017,** 358, 751-756.

140. Misono, M., Catalysis of Perovskite and Related Mixed Oxides. In *Heterogeneous Catalysis of Mixed Oxides - Perovskite and Heteropoly Catalysts*, 2013; pp 67-95.

141. Ashok, A.; Kumar, A.; Bhosale, R. R.; Almomani, F.; Malik, S. S.; Suslov, S.; Tarlochan, F., Combustion synthesis of bifunctional $LaMO_3$ (M = Cr, Mn, Fe, Co, Ni) perovskites for oxygen reduction and oxygen evolution reaction in alkaline media. *Journal of Electroanalytical Chemistry* **2018,** 809, 22-30.

142. Goldwasser, M. R.; Rivas, M. E.; Lugo, M. L.; Pietri, E.; Pérez-Zurita, J.; Cubeiro, M. L.; Griboval-Constant, A.; Leclercq, G., Combined methane reforming in presence of CO_2 and O_2 over $LaFe_{1-x}Co_xO_3$ mixed-oxide perovskites as catalysts precursors. *Catalysis Today* **2005,** 107-108, 106-113.

143. Lu, Y.; Eyssler, A.; Otal, E. H.; Matam, S. K.; Brunko, O.; Weidenkaff, A.; Ferri, D., Influence of the synthesis method on the structure of Pd-substituted perovskite catalysts for methane oxidation. *Catalysis Today* **2013,** 208, 42-47.

144. Perego, C.; Villa, P., Catalyst preparation methods. *Catalysis Today* **1997,** 34, 281-305.

145. Purwanto, A.; Wang, W. N.; Okuyama, K., Flame Spray Pyrolysis. In *Handbook of Atomization and Sprays*, 2011; pp 869-879.

146. Athayde, D. D.; Souza, D. F.; Silva, A. M. A.; Vasconcelos, D.; Nunes, E. H. M.; Diniz da Costa, J. C.; Vasconcelos, W. L., Review of perovskite ceramic synthesis and membrane preparation methods. *Ceramics International* **2016,** 42, 6555-6571.

147. Allison, J. D. Catalyst and method of making micrometer sized spherical particles. 2003.

148. Rudin, T.; Wegner, K.; Pratsinis, S. E., Towards carbon-free flame spray synthesis of homogeneous oxide nanoparticles from aqueous solutions. *Advanced Powder Technology* **2013,** 24, 632-642.

149. Basu, S.; Miglani, A., Combustion and heat transfer characteristics of nanofluid fuel droplets: A short review. *International Journal of Heat and Mass Transfer* **2016,** 96, 482-503.

150. Hamid, N. A.; Wennig, S.; Hardt, S.; Heinzel, A.; Schulz, C.; Wiggers, H., High-capacity cathodes for lithium-ion batteries from nanostructured $LiFePO_4$ synthesized by highly-flexible and scalable flame spray pyrolysis. *Journal of Power Sources* **2012,** 216, 76-83.

151. Hardt, S.; Wlokas, I.; Schulz, C.; Wiggers, H., Impact of Ambient Pressure on Titania Nanoparticle Formation During Spray-Flame Synthesis. *Journal of Nanoscience and Nanotechnology* **2015,** 15, 9449-56.

152. Djonev, B.; Tsyntsarski, B.; Klissurski, D.; Hadjiivanov, K., IR spectroscopic study of NO adsorption and NO–O_2 coadsorption on Co^{2+}/SiO_2 catalysts. *Journal of the Chemical Society, Faraday Transactions* **1997,** 93, 4055-4063.

153. Johnson, A. T. A Combined Cyanex ‑ 923 and HEH[EHP] Process for Partitioning Used Nuclear Fuels: Characterizing Complex Interactions. Washington State University, 2014.

154. Kunov-Kruse, A. J.; Thomassen, P. L.; Riisager, A.; Mossin, S.; Fehrmann, R., Absorption and Oxidation of Nitrogen Oxide in Ionic Liquids. *Chemistry* **2016,** 22, 11745-55.

155. Durães, L.; Benedini, L.; Costa, B. F. O.; Portugal, A., Sol-gel synthesis and washing of amorphous g-FeO(OH) xerogels. *Materialwissenschaft und Werkstofftechnik* **2012,** 43, 427-434.

156. Murray-Rust, D. M.; Brewer Hartley, H., The dissociation of acids in methyl and in ethyl alcohol. *Proceedings of the Royal Society of London. Series A, Containing Papers of a Mathematical and Physical Character* **1997,** 126, 84-106.

157. Voleišienė, B. R., D, Investigation of the hydration phenomenon in 3–1 electrolyte solutions. *Ultrasound* **2007,** 6, 41-45.

158. Bauer, I.; Knölker, H. J., Iron Complexes in Organic Chemistry. In *Iron Catalysis in Organic Chemistry: Reactions and Applications*, Plietker, B., Ed. Wiley-VCH Verlag GmbH & Co. KGaA: Weinheim, Germany, 2008; Vol. 1, pp 1-24.

159. Mowla, O.; Kennedy, E.; Stockenhuber, M., In-situ FTIR study on the mechanism of both steps of zeolite-catalysed hydroesterification reaction in the context of biodiesel manufacturing. *Fuel* **2018,** 232, 12-26.

160. Olewnik, E.; Nowaczyk, J.; Garman, K.; Czerwinski, W., Influence of ozone treatment on structure and thermal properties of bis-2-hydroxyethyl terephthalate-based copolymers. *Journal of Thermal Analysis and Calorimetry* **2012,** 112, 697-702.

161. Socrates, G., *Infrared and Raman Characteristic Group Frequencies Contents*. 3rd ed.; John Wiley & Sons: 2004; p 366.

162. Trapeznikova, O. N.; Belopolskaya, T. In *Investigation of the Rotation of Molecular Groups in Polymers of Methyl Acrylate and Vinyl Acetate by the Method of IR-Spectroscopy*, 1987.

163. Savela, R. Iron(II) as Lewis Acid Catalyst in Organosilicon and Carbonyl Chemistry. Åbo Akademi - Åbo Akademi University, 2015.

164. Bao, L.; Low, W.-L.; Jiang, J.; Ying, J. Y., Colloidal synthesis of magnetic nanorods with tunable aspect ratios. *Journal of Materials Chemistry* **2012,** 22, 7117.

165. Rajabi, F.; Abdollahi, M.; Luque, R., Solvent-Free Esterification of Carboxylic Acids Using Supported Iron Oxide Nanoparticles as an Efficient and Recoverable Catalyst. *Materials (Basel)* **2016,** 9, 557.

166. Xu, Z. H.; Li, C. J.; Wu, J. G.; Xu, G. X.; Butler, I. S., Infrared spectroscopic study of the surface interactions of cyclopentadienyliron dicarbonyl dimer with acidic, neutral, and basic alumina supports. *Vibrational Spectroscopy* **1995,** 8, 457-460.

167. Cakic, S.; Raskovic, L.; Lacnjevac, C.; Rajkovic, M.; Barac, M.; Stojanovic, M., Physical-mechanical properties of nitrodopes affected by ultra-violet radiation. *Sensors* **2007,** 7, 2139-2156.

168. Hiskey, M. A.; Hatch, M. J.; Oxley, J. C., Nitrato Amine Nitrates: Nitrate ester explosives with reduced impact sensitivity. *Propellants, Explosives, Pyrotechnics* **1991,** 16, 40-42.

169. Yilgor, I.; Yilgor, E.; Guler, I. G.; Ward, T. C.; Wilkes, G. L., FTIR investigation of the influence of diisocyanate symmetry on the morphology development in model segmented polyurethanes. *Polymer* **2006,** 47, 4105-4114.

170. Raju, K.; Kishore, K.; Narayan, R., Synthesis and characterization of waterborne hyperbranched UV cured polyurethane ‑ silica hybrids coatings. In *The Waterborne Symposium*, Rawlins, J.; Storey, R., Eds. DEStech Publications: New Orleans, 2012.

171. Elkotb, M. M.; Mahdy, M. A. E.; Montaser, M. E. In *Atomization Quality of Twin Fluid Atomizers for Gas Turbines*, ASME 1982 International Gas Turbine Conference and Exhibit, ASME: 1982; p 10.

172. Ashgriz, N., *Handbook of Atomization and Sprays*. 1st ed.; Springer US: 2011; p XVI, 935.

173. Levasseur, B.; Kaliaguine, S., Effects of iron and cerium in $La_{1-y}Ce_yCo_{1-x}Fe_xO_3$ perovskites as catalysts for VOC oxidation. *Applied Catalysis B: Environmental* **2009,** 88, 305-314.

174. Chagas, C. A.; Toniolo, F. S.; Magalhães, R. N. S. H.; Schmal, M., Alumina-supported $LaCoO_3$ perovskite for selective CO oxidation (SELOX). *International Journal of Hydrogen Energy* **2012,** 37, 5022-5031.

175. Femina, P.; Sanjay, P., $LaCoO_3$ perovskite catalysts for the environmental application of Auto motive CO oxidation. *Research Journal of Recent Sciences* **2012,** 1, 178-184.

176. Voorhoeve, R. J. H.; Remeika, J. P.; Trimble, L. E., Defect chemistry and catalysis in oxidation and reduction over perovskite-type oxides. *Annals of the New York Academy of Sciences* **1976,** 272, 3-21.

177. Jia, T.; Zeng, Z.; Lin, H. Q.; Duan, Y.; Ohodnicki, P., First-principles study on the electronic, optical and thermodynamic properties of ABO_3 (A = La,Sr, B = Fe,Co) perovskites. *RSC Advances* **2017,** 7, 38798-38804.

178. Natile, M. M.; Ugel, E.; Maccato, C.; Glisenti, A., $LaCoO_3$: Effect of synthesis conditions on properties and reactivity. *Applied Catalysis B: Environmental* **2007,** 72, 351-362.

179. Xue, K.; He, F.; Zhang, J.; Tang, L.; Chen, X.; Mao, Z., Nonequilibrium magnetic properties in oxygen-rich $LaMnO_3$ nanoparticles. *Journal of Physics-Condensed Matter* **2019,** 31, 355801.

180. Töpfer, J.; Goodenough, J. B., $LaMnO_{3+\delta}$ Revisited. *Journal of Solid State Chemistry* **1997,** 130, 117-128.

181. Shafi, P. M.; Bose, A. C.; Vinu, A., Electrochemical Material Processing via Continuous Charge-Discharge Cycling: Enhanced Performance upon Cycling for Porous $LaMnO_3$ Perovskite Supercapacitor Electrodes. *ChemElectroChem* **2018,** 5, 3723-3730.

182. Li, C.; Yu, Z.; Liu, H.; Chen, K., High surface area $LaMnO_3$ nanoparticles enhancing electrochemical catalytic activity for rechargeable lithium-air batteries. *Journal of Physics and Chemistry of Solids* **2018,** 113, 151-156.

183. Wang, Q.; Ma, L., NO oxidative activity of mesoporous $LaMnO_3$ and $LaCoO_3$ perovskite nanoparticles by facile molten-salt synthesis. *New Journal of Chemistry* **2019,** 43, 2974-2980.

184. Cimino, S.; Colonna, S.; De Rossi, S.; Faticanti, M.; Lisi, L.; Pettiti, I.; Porta, P., Methane Combustion and CO Oxidation on Zirconia-Supported La, Mn Oxides and $LaMnO_3$ Perovskite. *Journal of Catalysis* **2002,** 205, 309-317.

185. Zhou, Y.; Wang, Z.; Liu, C., Perspective on CO oxidation over Pd-based catalysts. *Catalysis Science & Technology* **2015,** 5, 69-81.

186. Al Soubaihi, R.; Saoud, K.; Dutta, J., Critical Review of Low-Temperature CO Oxidation and Hysteresis Phenomenon on Heterogeneous Catalysts. *Catalysts* **2018,** 8, 660.

187. Peng, Y.; Si, W.; Li, J.; Crittenden, J.; Hao, J., Experimental and DFT studies on Sr-doped $LaMnO_3$ catalysts for NO_x storage and reduction. *Catalysis Science & Technology* **2015,** 5, 2478-2485.

188. Miniajluk, N.; Trawczyński, J.; Zawadzki, M.; Tylus, W., $LaMnO_3$ ($La_{0.8}Sr_{0.2}MnO_3$) Perovskites for Lean Methane Combustion: Effect of Synthesis Method. *Advances in Materials Physics and Chemistry* **2018,** 08, 193-215.

189. Dhiman, T. K.; Singh, S., Enhanced Catalytic and Photocatalytic Degradation of Organic Pollutant Rhodamine ‐ B by $LaMnO_3$ Nanoparticles Synthesized by Non ‐ Aqueous Sol ‐ Gel Route. *physica status solidi (a)* **2019,** 216, 1900012.

190. Simmance, K.; Thompsett, D.; Wang, W.; Thiebaut, B., Evaluation of perovskite catalysts prepared by flame spray pyrolysis for three-way catalyst activity under simulated gasoline exhaust feeds. *Catalysis Today* **2019,** 320, 40-50.

191. Alkan, B.; Cychy, S.; Varhade, S.; Muhler, M.; Schulz, C.; Schuhmann, W.; Wiggers, H.; Andronescu, C., Spray ‐ flame ‐ synthesized $LaCo_{1-x}Fe_xO_3$ perovskite nanoparticles as electrocatalysts for water and ethanol oxidation. *ChemElectroChem* **2019,** 6, 4266-4274.

192. Tarasov, A.; Shvartsman, V. V.; Shoja, S.; Lewin, D.; Lupascu, D. C.; Wiggers, H., Spray-flame synthesis of $BaTi_{1-x}Zr_xO_3$ nanoparticles for energy storage applications. *Ceramics International* **2020,** 46, 13915-13924.

193. Rossetti, I.; Forni, L., Catalytic flameless combustion of methane over perovskites prepared by flame–hydrolysis. *Applied Catalysis B: Environmental* **2001,** 33, 345-352.

194. Angel, S.; Neises, J.; Dreyer, M.; Friedel Ortega, K.; Behrens, M.; Wang, Y.; Arandiyan, H.; Schulz, C.; Wiggers, H., Spray ‐ flame synthesis of La(Fe, Co)O_3 nano ‐ perovskites from metal nitrates. *AIChE Journal* **2019,** 66, e16748.

195. Hammad, M.; Fortugno, P.; Hardt, S.; Kim, C.; Salamon, S.; Schmidt, T. C.; Wende, H.; Schulz, C.; Wiggers, H., Large-scale synthesis of iron oxide/graphene hybrid materials as highly efficient photo-Fenton catalyst for water remediation. *Environmental Technology & Innovation* **2020**.

196. Aßmann, S.; Münsterjohann, B.; Huber, F. J. T.; Will, S., Droplet sizing in spray flame synthesis using wide-angle light scattering (WALS). *Applied Physics B* **2020,** 126.

197. Stodt, M. F. B.; Liu, C.; Li, S.; Mädler, L.; Fritsching, U.; Kiefer, J., Phase-selective laser–induced breakdown spectroscopy in flame spray pyrolysis for iron oxide nanoparticle synthesis. *Proceedings of the Combustion Institute* **2020**.

198. Steele, W. V.; Chirico, R. D.; Knipmeyer, S. E.; Nguyen, A., Vapor Pressure, Heat Capacity, and Density along the Saturation Line, Measurements for Cyclohexanol, 2-Cyclohexen-1-one, 1,2-Dichloropropane, 1,4-Di-tert-butylbenzene, (±)-2-Ethylhexanoic Acid, 2-(Methylamino)ethanol, Perfluoro-n-heptane, and Sulfolane. *Journal of Chemical & Engineering Data* **1997,** 42, 1021-1036.

199. Boateng, A. A., Combustion and Flame. In *Rotary Kilns*, 2016; pp 107-143.

200. Angel, S.; Schneider, F.; Apazeller, S.; Kaziur-Cegla, W.; Schmidt, T. C.; Schulz, C.; Wiggers, H., Spray-flame synthesis of $LaMO_3$ (M = Mn, Fe, Co) perovskite nanomaterials: Effect of spray droplet size

and esterification on particle size distribution. *Proceedings of the Combustion Institute* **2021,** 38, 1279-1287.

201. Vojisavljevic, K.; Chevreux, P.; Jouin, J.; Malic, B., Characterization of the Alkoxide-based Sol-gel Derived $La_{9.33}Si_6O_{26}$ Powder and Ceramic. *Acta Chimica Slovenica* **2014,** 61, 530-541.

202. Spichal, Z.; Necas, M.; Pinkas, J.; Zdrahal, Z., Binuclear complexes of lanthanides with 1,4-bis(diphenylphosphino)butane dioxide. *Polyhedron* **2006,** 25, 809-814.

203. Bollino, F.; Armenia, E.; Tranquillo, E., Zirconia/Hydroxyapatite Composites Synthesized Via Sol-Gel: Influence of Hydroxyapatite Content and Heating on Their Biological Properties. *Materials (Basel)* **2017,** 10, 757.

204. Smith C, B., *Infrared Spectral Interpretation : A Systematic Approach*. CRC Press: 1998; Vol. 1, p 282.

205. Collomb, M.-N.; Deronzier, A., Manganese: Inorganic & Coordination Chemistry. In *Encyclopedia of Inorganic Chemistry*, King, R. B.; Crabtree, R. H.; Lukehart, C. M.; Atwood, D. A.; Scott, R. A., Eds. John Wiley & Sons, Ltd.: 2006; p 13.

206. Zhu, H. J.; Hill, R. H., The photochemical metal organic deposition of manganese oxide films from films of manganese(II) 2-ethylhexanoate: a mechanistic study. *Journal of Non-Crystalline Solids* **2002,** 311, 174-184.

207. Gauglitz, G.; Vo ‑ Dinh, T., *Handbook of Spectroscopy*. WILEY-VCH Verlag GmbH & Co. KGaA: Weinheim, 2003.

208. Lagerblom, K.; Lagerspets, E.; Keskiväli, J.; Cook, C.; Ekholm, F.; Parviainen, A.; Repo, T., Practical Aerobic Oxidation of Alcohols: A Ligand-Enhanced 2,2,6,6-Tetramethylpiperidine-1-oxy/Manganese Nitrate Catalyst System. *ChemCatChem* **2017,** 9, 3880-3887.

209. Anderson, J. M.; Kochi, J. K., Manganese(III) complexes in oxidative decarboxylation of acids. *Journal of the American Chemical Society* **1970,** 92, 2450-2460.

210. Levy, L. B., Facile oxidation of manganese(II) to manganese(III) in long-chain carboxylic acids. *The Journal of Organic Chemistry* **1989,** 54, 253-254.

211. Finlayson-Pitts, B. J.; Wingen, L. M.; Sumner, A. L.; Syomin, D.; Ramazan, K. A., The heterogeneous hydrolysis of NO_2 in laboratory systems and in outdoor and indoor atmospheres: An integrated mechanism. *Physical Chemistry Chemical Physics* **2003,** 5, 223-242.

212. Rodriguez-Lamas, R.; Pla, D.; Chaix-Pluchery, O.; Meunier, B.; Wilhelm, F.; Rogalev, A.; Rapenne, L.; Mescot, X.; Rafhay, Q.; Roussel, H.; Boudard, M.; Jimenez, C.; Burriel, M., Integration of $LaMnO_{3+\delta}$ films on platinized silicon substrates for resistive switching applications by PI-MOCVD. *Beilstein Journal of Nanotechnology* **2019,** 10, 389-398.

213. Iliev, M. N.; Abrashev, M. V., Raman phonons and Raman Jahn-Teller bands in perovskite-like manganites. *Journal of Raman Spectroscopy* **2001,** 32, 805-811.

214. Iliev, M. N.; Abrashev, M. V.; Lee, H. G.; Popov, V. N.; Sun, Y. Y.; Thomsen, C.; Meng, R. L.; Chu, C. W., Raman spectroscopy of orthorhombic perovskite like $YMnO_3$ and $LaMnO_3$. *Physical Review B* **1998,** 57, 2872-2877.

215. Alkan, B.; Medina, D.; Landers, J.; Heidelmann, M.; Hagemann, U.; Salamon, S.; Andronescu, C.; Wende, H.; Schulz, C.; Schuhmann, W.; Wiggers, H., Spray-Flame-Prepared $LaCo_{1-x}Fe_xO_3$ Perovskite Nanoparticles as Active OER Catalysts: Influence of Fe Content and Low-Temperature Heating. *ChemElectroChem* **2020,** 7, 2564-2574.

216. Li, J. P. H.; Zhou, X.; Pang, Y.; Zhu, L.; Vovk, E. I.; Cong, L.; van Bavel, A. P.; Li, S.; Yang, Y., Understanding of binding energy calibration in XPS of lanthanum oxide by in situ treatment. *Physical Chemistry Chemical Physics* **2019,** 21, 22351-22358.

217. Yang, R.; Lu, X.; Zhang, Z.; Wang, X.; Tang, D.; Zhu, L., Three-dimensionally ordered macroporous $LaMnO_3$ with tunable oxygen vacancies via nitric acid-aided modulating and their catalytic combustion properties. *RSC Advances* **2015,** 5, 98404-98411.

218. Ritter, C.; Ibarra, M. R.; De Teresa, J. M.; Algarabel, P. A.; Marquina, C.; Blasco, J.; García, J.; Oseroff, S.; Cheong, S. W., Influence of oxygen content on the structural, magnetotransport, and magnetic properties of $LaMnO_{3+\delta}$. *Physical Review B* **1997,** 56, 8902-8911.

219. Dabrowski, B.; Dybzinski, R.; Bukowski, Z.; Chmaissem, O.; Jorgensen, J. D., Oxygen Content and Structures of $La_{1-x}Ca_xMnO_{3+\delta}$ as a Function of Synthesis Conditions. *Journal of Solid State Chemistry* **1999,** 146, 448-457.

220. Wang, L.; Xie, H.; Wang, X.; Zhang, G.; Guo, Y.; Guo, Y.; Lu, G., Preparation of $LaMnO_3$ for catalytic combustion of vinyl chloride. *Chinese Journal of Catalysis* **2017,** 38, 1406-1412.

221. Zhao, B.; Ran, R.; Sun, L.; Guo, X.; Wu, X.; Weng, D., NO catalytic oxidation over an ultra-large surface area $LaMnO_{3+\delta}$ perovskite synthesized by an acid-etching method. *RSC Advances* **2016,** 6, 69855-69860.

222. Zhu, H.; Zhang, P.; Dai, S., Recent Advances of Lanthanum-Based Perovskite Oxides for Catalysis. *ACS Catalysis* **2015,** 5, 6370-6385.

223. Cheng, X.; Fabbri, E.; Yamashita, Y.; Castelli, I. E.; Kim, B.; Uchida, M.; Haumont, R.; Puente-Orench, I.; Schmidt, T. J., Oxygen Evolution Reaction on Perovskites: A Multieffect Descriptor Study Combining Experimental and Theoretical Methods. *ACS Catalysis* **2018,** 8, 9567-9578.

224. Singh, S. J.; Jayaram, R. V., Oxidation of Alcohols to Aldehydes and Ketones Using TBHP as an Oxidant over $LaMO_3$ (M = Cr, Mn, Co, Ni, Fe) Perovskites. *Synthetic Communications* **2012,** 42, 299-308.

225. Zeng, S.; Kar, P.; Thakur, U. K.; Shankar, K., A review on photocatalytic CO_2 reduction using perovskite oxide nanomaterials. *Nanotechnology* **2018,** 29, 052001.

226. Schwarz, J. A.; Contescu, C.; Contescu, A., Methods for Preparation of Catalytic Materials. *Chemical Reviews* **1995,** 95, 477-510.

227. Rudin, T.; Wegner, K.; Pratsinis, S. E., Uniform nanoparticles by flame-assisted spray pyrolysis (FASP) of low cost precursors. *Journal of Nanoparticle Research* **2011,** 13, 2715-2725.

228. Kilian, D. P. Flame Spray Synthesis of Semiconducting Oxide Nanomaterials: Fundamental Process Characterization and Control of Product Properties. PhD, Friedrich-Alexander-Universität Erlangen-Nürnberg, 2016.

229. Uvarov, V.; Popov, I., An estimation of the correctness of XRD results obtained from the analysis of materials with bimodal crystallite size distribution. *CrystEngComm* **2015,** 17, 8300-8306.

230. Kesslin, G.; Bradshaw, R., Ortho Esters as Water Scavengers. *Industrial & Engineering Chemistry Product Research and Development* **1966,** 5, 27-29.

231. Fritzler, B. C.; Dharmavaram, S.; Hartrim, R. T.; Diffendall, G. F., Acetic Anhydride Hydrolysis at High Acetic Anhydride to Water Ratios. *International Journal of Chemical Kinetics* **2014,** 46, 151-160.

232. Antonov, D. V.; Shlegel, N. E.; Strizhak, P. A., Secondary atomization of gas-saturated liquid droplets as a result of their collisions and micro-explosion. *Chemical Engineering Research and Design* **2020,** 162, 200-211.

233. Wood, C. F.; Leach, D. H.; Zhang, J. Z.; Chang, R. K.; Barber, P. W., Time-resolved shadowgraphs of large individual water and ethanol droplets vaporized by a pulsed CO_2 laser. *Applied Optics* **1988,** 27, 2279-86.

234. Musicó, B. L.; Gilbert, D.; Ward, T. Z.; Page, K.; George, E.; Yan, J.; Mandrus, D.; Keppens, V., The emergent field of high entropy oxides: Design, prospects, challenges, and opportunities for tailoring material properties. *APL Materials* **2020,** 8, 040912.

235. Bogan, M. J.; Boutet, S.; Chapman, H. N.; Marchesini, S.; Barty, A.; Benner, W. H.; Rohner, U.; Frank, M.; Hau-Riege, S. P.; Bajt, S.; Woods, B.; Seibert, M. M.; Iwan, B.; Timneanu, N.; Hajdu, J.; Schulz, J., Aerosol Imaging with a Soft X-Ray Free Electron Laser. *Aerosol Science and Technology* **2010,** 44, i-vi.

236. Seiferth, O.; Wolter, K.; Dillmann, B.; Klivenyi, G.; Freund, H. J.; Scarano, D.; Zecchina, A., IR investigations of CO_2 adsorption on chromia surfaces: Cr_2O_3 (0001)/Cr(110) versus polycrystalline α-Cr_2O_3. *Surface Science* **1999,** 421, 176-190.

237. Smidt, E.; Eckhardt, K. U.; Lechner, P.; Schulten, H. R.; Leinweber, P., Characterization of different decomposition stages of biowaste using FT-IR spectroscopy and pyrolysis-field ionization mass spectrometry. *Biodegradation* **2005,** 16, 67-79.

238. Czylkowska, A.; Markiewicz, M., Synthesis, thermal behavior, and other properties of Y(III) and La(III) complexes with 4,4′-bipyridine and trichloro- or dibromoacetates. *Journal of Thermal Analysis and Calorimetry* **2012,** 109, 727-734.

239. Bernard, C.; Durand, B.; Verelst, M.; Lecante, P., Hydrothermal synthesis of $LaMnO_{3+\delta}$: F.T.I.R. and W.A.X.S. investigations of the evolution from amorphous to crystallized powder. *Journal of Materials Science* **2004,** 39, 2821-2826.

240. Roonasi, P. Adsorption and Surface Reaction Properties of Synthesized Magnetite Nano-Particles. Licentiate, Luleå University of Technology, Luleå, Sweden, 2007.

241. Klingenberg, B.; Vannice, M. A., Influence of Pretreatment on Lanthanum Nitrate, Carbonate, and Oxide Powders. *Chemistry of Materials* **1996,** 8, 2755-2768.

242. Ofner, B., Phase Doppler Anemometry (PDA). In *Optical Measurements*, 2001; pp 139-152.

10 Publications

Peer-reviewed publications

1. **Angel, S.**; Neises, J.; Dreyer, M.; Friedel Ortega, K.; Behrens, M.; Wang, Y.; Arandiyan, H.; Schulz, C.; Wiggers, H., Spray-flame synthesis of La(Fe, Co)O_3 nano-perovskites from metal nitrates. AIChE J. 2019, 66, e16748.
   Award: *Top downloaded paper 2018-2019. One of the most read papers in AIChE Journal. Wiley.*
2. **Angel, S.**; Schneider, F.; Apazeller, S.; Kaziur-Cegla, W.; Schmidt, T. C.; Schulz, C.; Wiggers, H., Spray-flame synthesis of $LaMO_3$ (M = Mn, Fe, Co) perovskite nanomaterials: Effect of spray droplet size and esterification on particle size distribution. Proc. Combust. Inst. 38 (2021) 1279-1287.
3. **Angel, S.**; Tapia, J. D.; Gallego, J.; Hagemann, U.; Wiggers, H., Spray-Flame Synthesis of $LaMnO_{3+\delta}$ Nanoparticles for Selective CO Oxidation (SELOX). Energy & Fuels 2021, 35, 4367-4376.
4. Carvajal, L.; Buitrago-Sierra, R.; Santamaria, A.; **Angel, S.**; Wiggers, H.; Gallego, J., Effect of Spray Parameters in a Spray Flame Reactor During Fe_xO_y Nanoparticles Synthesis. J. Therm. Spray Technology **2020**, 29, 368-383.
5. Wollny, P.; **Angel, S.**; Wiggers, H.; Kempf, A. M.; Wlokas, I., Multiscale Simulation of the Formation of Platinum-Particles on Alumina Nanoparticles in a Spray Flame Experiment. Fluids **2020**, 5, 201.

In preparation

6. **Angel, S.**; Braun, M., Alkan, B.; Landers, J.; Salamon, S.; Wende, H.; Andronescu, C.; Schulz, C., Wiggers, H., Spray-flame synthesis of $LaFe_xCo_{1-x}O_3$ (x = 0.2, 0.3) nanoparticles for OER: Effect of metal acetates and nitrates as precursors. *In preparation*. 2021.
7. Büker, J.; **Angel, S.**; Schulz, C.; Wiggers, H.; Peng, B.; Muhler, M., Cyclohexene oxidation over spray-flame synthesized $Co_xFe_{3-x}O_4$: Peroxide decomposition ability of Co-Fe-mixed spinel catalysts. *In preparation*. 2021.
8. Carvajal, L.; Pérez, S.; Buitrago-Sierra, R.; Santamaría, A.; Moreno, A.; **Angel, S.**; Wiggers, H.; Gallego, J., Spray-flame synthesis (SFS) and characterization of Fe_xO_y nanoparticles: Role of the metal precursor and concentration. *In preparation*. 2021.
9. **Angel, S.**; Waffel, D; Peng, B.; Muhler, M. Schulz, C.; Wiggers, H., Spray-flame synthesis of $LaMn_xFe_{1-x}O_3$ nanoparticles for the catalytic oxidation of benzyl alcohol, cinnamyl alcohol and styrene with *tert*-butyl hydroperoxide (TBHP) as oxidant. *In preparation*. 2021.
10. Hammad, M.; **Angel, S.**; Al-kamal, A.; Fortugno, P.; Asghar, A.; Kim, C.; Klippert, D.; Schmidt, T. C.; W. M. Kay, C.; Wiggers, H., Facile self-assembly synthesis of $LaCoO_3$/graphene nanocomposites as highly efficient peroxymonosulfate activator for degradation of organic pollutants. *In preparation*. 2021.

Oral presentations on conferences

- 05/2019: Spray-flame synthesis of the nanosized $LaMO_3$ (M = Fe, Co) perovskites from metal nitrate precursors, E-MRS (European Materials Research Society) Spring Meeting 2019, Nice, France
- 08/2019: Oxygen Evolution Reaction (OER) of $LaFe_xCo_{1-x}O_3$ (x = 0.1, 0.2, 0.3) perovskites made from metal acetate and nitrate solutions by spray-flame synthesis, EuropaCat 2019, Aachen, Germany
- 09/2019: Spray-flame synthesis (SFS) of the nanosized $LaMO_3$ (M = Fe, Co) perovskites from metal nitrate precursors: Influence of the mixture of ethanol and 2-ethylhexanoic acid on materials' homogeneity", Flammentag 2019, Bochum, Germany
- 03/2020: Effect of the metal precursors (acetates and nitrates) on the spray-flame synthesis of $LaFe_xCo_{1-x}O_3$ (x = 0.1, 0.2 and 0.3) for oxygen evolution reaction (OER) in water splitting. CENIDE conference 2020, Bergisch Gladbach, Germany
- 09/2020: Spray-flame synthesis of $LaMO_3$ (M = Mn, Fe, Co) perovskite nanomaterials: Effect of spray droplet size and catalyzed esterification on particle size distribution. European Aerosol Conference (EAC) 2020, Online (Originally planned in Aachen/Germany)

Poster presentations on conferences

- 05/2017: Spray-flame synthesis of nanoscale $LaCoO_3$ perovskite catalyst, E-MRS (European Materials Research Society) Spring Meeting 2017, Strasbourg, France
- 08/2017: Spray-flame synthesis of nanoscale $LaCoO_3$ perovskite catalyst for the CFC of methane, European Aerosol Conference (EAC) 2017, Zürich, Switzerland
- 11/2018: Spray-flame synthesis of the nanosized $LaMO_3$ (M = Fe, Co) perovskites from metal nitrate precursors, 8th NRW Nano Conference 2018, Dortmund, Germany
- 11/2018: Spray-flame synthesis of the nanosized $LaMO_3$ (M = Fe, Co) perovskites from metal nitrate precursors, MRS (Materials Research Society) Fall Meeting 2019, Boston, USA, awarded with the ***'Best Poster Award'***
- 05/2019: Preferential oxidation (PROX) of CO with spray-flame made $LaMnO_3$ perovskite nanoparticle, E-MRS (European Materials Research Society) Spring Meeting 2019, Nice, France
- 08/2019: Preferential oxidation (PROX) of CO with spray-flame made $LaMnO_3$ perovskite nanoparticle, EuropaCat 2019, Aachen, Germany

11 Appendix

11.1 Appendix A

The information presented in this appendix is related to the analysis from Chapter 4.

Spray-flame synthesis description

Each solution was supplied via a syringe pump at a constant flow rate of 2 ml/min to a two-fluid nozzle installed in the bottom part of a closed reactor chamber. A fine spray was formed from the solution by a flow of 7 slm (standard liters per minute, otherwise indicated) of O_2 (Air Liquide, technical). The main flame was supported by a premixed flat pilot flame (3 slm methane (Air Liquide, N25, 99.5 % purity) and 5 slm O_2) stabilized on a sintered bronze plate (10 cm diameter) coaxially surrounding the spray nozzle. The pilot flame is surrounded by a sheath-gas flow (140 slm, compressed air) to stabilize the flame and shield it from the reactor walls. An additional quenching gas flow (230 slm, compressed air) was supplied above the reaction zone to further control the reactor off-gas temperature to values below 130 °C to prevent thermal damage of the filter device used to collect the particles.

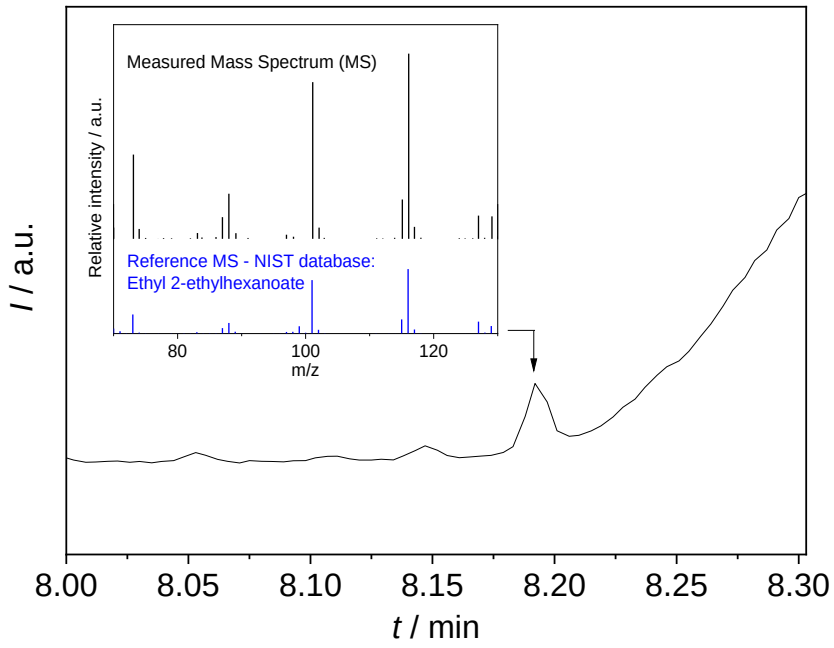

Figure A 1. Gas chromatogram and mass spectrum of ethyl 2-ethylhexanoate (retention time of 8.19 min) in a solution of ethanol/2-EHA 50/50 % v/v.

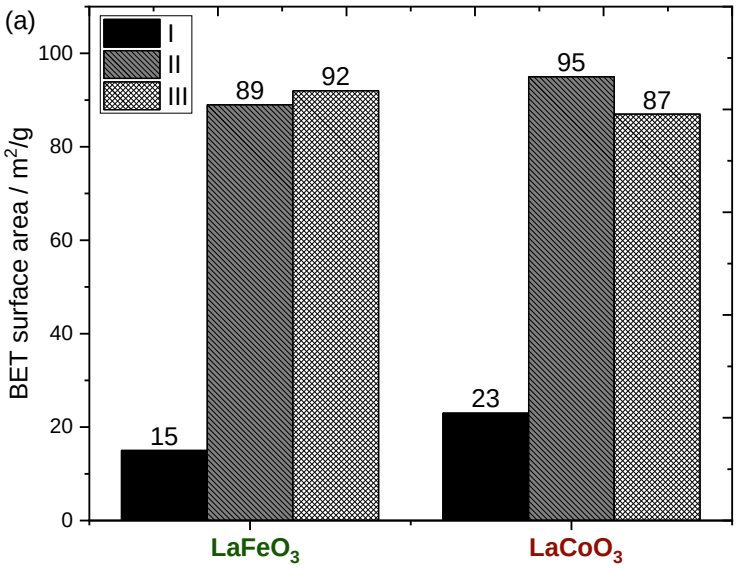

Figure A 2. BET surface areas of the perovskites $LaFeO_3$ and $LaCoO_3$. (I) Ethanol, (II) ethanol/2-EHA (50/50 by vol.) and (III) ethanol/2-EHA (35/65 by vol.). The specific surface area (SSA) of the nanoparticles was determined using the Brunauer, Emmet, Teller (BET) gas-adsorption method (Quantachrome Nova2000).

11.2 Appendix B

The information presented in this appendix is related to the analysis from Chapter 5.

- **Photographs of solutions of precursors at different temperatures**

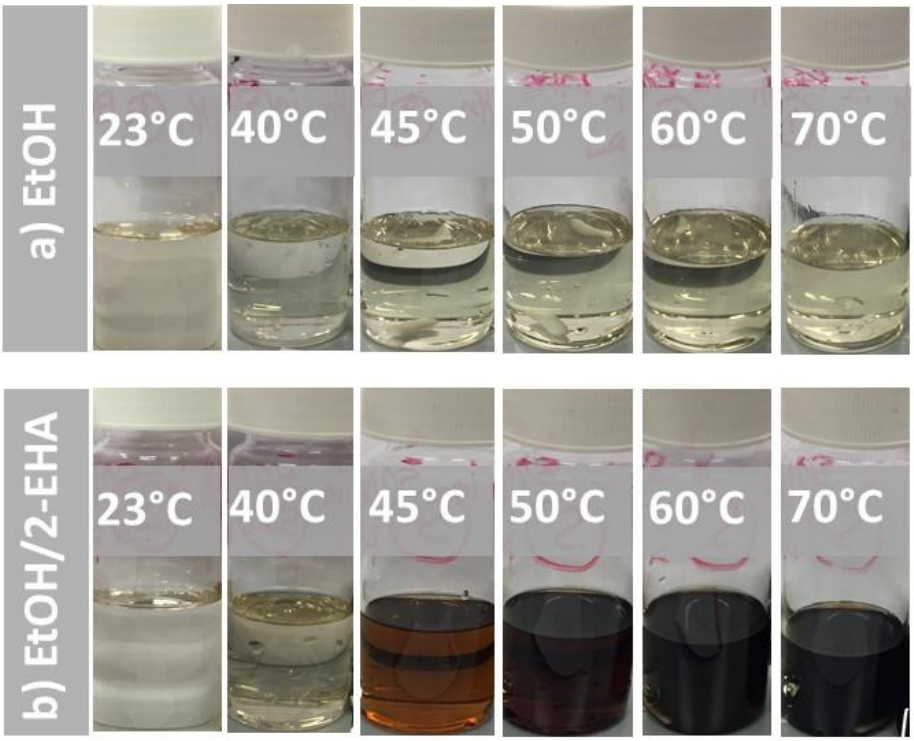

Figure B 1. Photographs of the nitrate-based solutions of precursors using a) ethanol (EtOH) and b) a mixture of ethanol/2-EHA as solvent.

- **Rietveld refinements**

Rietveld refinements were performed using the program Maud and the corresponding reference diffraction patterns from the ICSD database.

a. Ethanol as solvent

Regarding the as-synthesized and heat-treated samples spray-flame-synthesized using ethanol as solvent, their Rietveld refinements were done using the "double-phase model"[229] which consists in selecting/loading the same reference phase file twice ($LaMnO_3$ *Orthorhombic O'* in this case: (1) and (2) – ICSD: 83761) in order to obtain two different concentrations and crystallite sizes for the same phase. The reference phase of La_2O_3 (ICSD: 192270) was also included in the refinement of both samples. The refinements' results are presented in Figure B 2a (as-synthesized) and Figure B 2b (heat-treated). A summary of the concentrations and crystallite sizes of the different phases conforming both phases is presented in Table B 1.

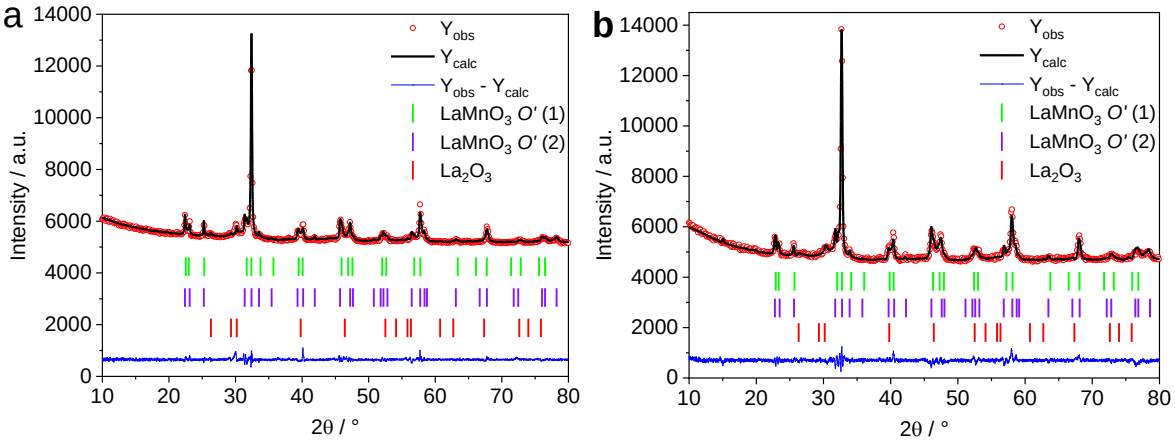

Figure B 2. Rietveld refinements of (a) as-synthesized and (b) heat-treated samples spray-flame synthesized using ethanol as solvent. Phases included: $LaMnO_3$ orthorhombic O' (1) and (2), La_2O_3.

Table B 1. Concentrations and crystallite sizes of as-synthesized and heat-treated samples spray-flame synthesized using ethanol as solvent.

	As-synthesized		Heat-treated	
	Concentration, Wt.%	Crystallite size/ nm	Concentration, Wt.%	Crystallite size/ nm
$LaMnO_3$ *O'* (1)	59.50	40	67	54
$LaMnO_3$ *O'* (2)	37.60	864	28	949
La_2O_3	2.90	100	5	110

b. Mixture of ethanol and 2-ethylhexanoic acid (2-EHA) as solvent

The Rietveld refinements of both the as-synthesized and heat-treated samples prepared using the mixture of ethanol and 2-EHA as solvent were performed including the following reference phases: $LaMnO_3$ *Orthorhombic O'* – ICSD: 83761, $LaMnO_3$ *Orthorhombic O* – ICSD: 51653 and La_2O_3 – ICSD: 192270). The refinements' results are presented in Figure B 3a (as-synthesized) and Figure B 3b (heat-treated). A summary of the concentrations and crystallite sizes of the different phases conforming both phases is presented in Table B 2.

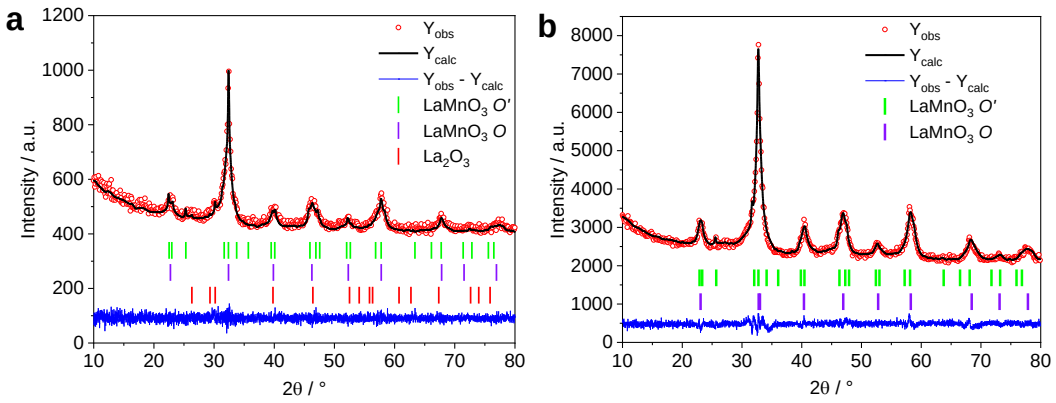

Figure B 3. Rietveld refinements of (a) as-synthesized and (b) heat-treated samples spray-flame synthesized using the mixture of ethanol and 2-EHA as solvent. Phases included: $LaMnO_3$ orthorhombic O', $LaMnO_3$ orthorhombic O and La_2O_3 for both the as-synthesized and heat-treated samples.

Table B 2. Concentrations and crystallite sizes of as-synthesized and heat-treated samples spray-flame synthesized using the mixture of ethanol and 2-EHA as solvent.

	As-synthesized		Heat-treated	
	Concentration, Wt.%	Crystallite size/ nm	Concentration, Wt.%	Crystallite size/ nm
$LaMnO_3$ *O'*	9.00	167	8	253
$LaMnO_3$ *O*	89.0	10	92	13
La_2O_3	2.00	100		

Particle size distributions of $LaMnO_3$ samples synthesized using the EtOH/2-EHA mixture

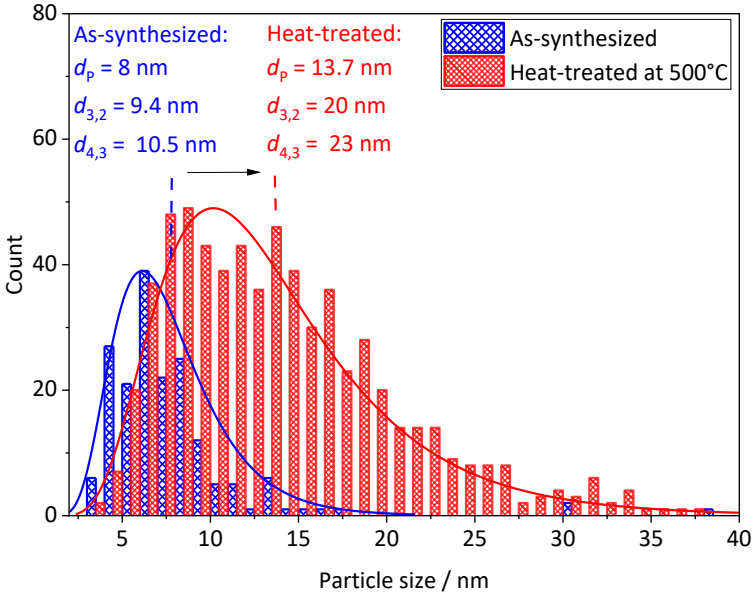

Figure B 4. Particle size distributions of as-synthesized (ethanol/2-EHA) and heat-treated $LaMnO_3$ samples obtained from the analysis of TEM images.

ATR-FTIR analysis of $LaMnO_3$ samples

ATR-FTIR spectra of the synthesized $LaMnO_3$ samples – and their corresponding heat-treated samples (500 °C, air, 1 h) – using ethanol and a mixture of ethanol/2-EHA as solvent are presented in Figure B 5a and in Figure B 5b, respectively.

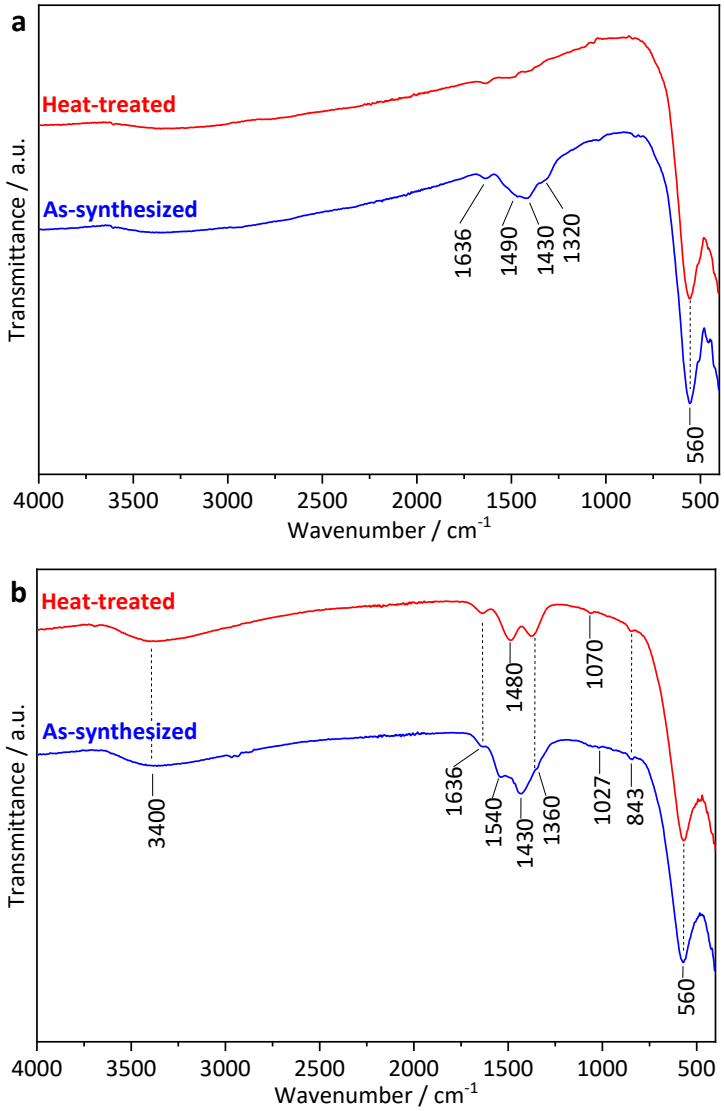

Figure B 5. FTIR spectra of as-synthesized and heat-treated $LaMnO_3$ samples that were synthesized using a.) ethanol or a mixture of b) ethanol/2-EHA as solvent.

Regarding the synthesized $LaMnO_3$ sample using ethanol as solvent (Figure B 5a), the bands centered at 1320 and 1490 cm^{-1} were assigned to characteristic vibrations of unidentate carbonates.[236] The band at 1430 cm^{-1} has been attributed in the literature to the symmetric (COO) stretch vibration of carboxylates and it has been also related to the CH_2 group in aliphatic alkanes.[237] The band at 1636 cm^{-1} was assigned to asymmetric (COO) carboxylate vibrations[238]. The heat-treatment at 500 °C under air of the ethanol-synthesized sample reduced almost completely the intensity of the mentioned vibration bands indicating the effective extraction of adsorbed carbonates and carboxylate species from the surface of the sample. The band centered at 560 cm^{-1}, assigned to the M-O vibration of the $LaMnO_3$ perovskite structure[239] and also identified in the $LaMnO_3$ sample synthesized with the ethanol/2-EHA, was not affected by the heat-treatment.

The spray-flame synthesized $LaMnO_3$ sample using the ethanol/2-EHA mixture presented bands at 1540 and 1430 cm^{-1} assigned to the asymmetric and symmetric (COO) carboxylate vibrations, respectively.[240] The heat-treatment (500 °C, air) of the sample caused the total reduction of the afore-mentioned vibrations, leaving weak bands centered at 1580, 1360, 1070, 1027, and 843 cm^{-1}, which correspond to typical vibrations of carbonate species.[240, 241]

11.3 Appendix C

The information presented in this appendix is related to the analysis from chapter 6.

Phase-Doppler anemometry (PDA) principle and experimental setup

- Measurement principle

Phase-Doppler anemometry is a laser-based optical technique which allows to measure simultaneously the velocity and size of spherical particles (e.g., droplets).[242] The measurement principle is based on light-scattering interferometry. Light-scattering can be analyzed with the help of ray-tracing diagrams as those presented in Figure C 1.

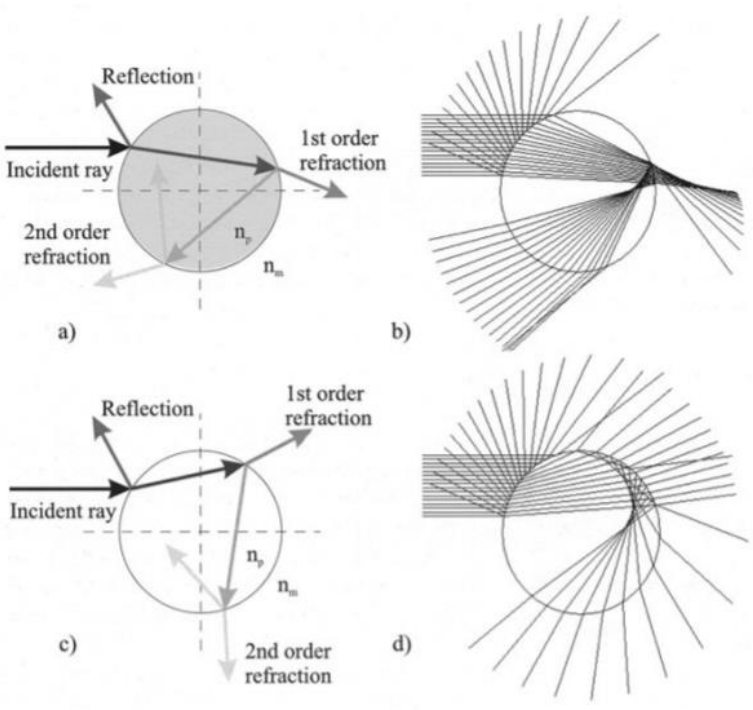

Figure C 1. Light scattering by droplets (a, b) and by bubbles (c, d).[242]

The most important scattering modes for the PDA are reflection, the 1st and the 2nd refraction orders as indicated in Figure C 1a,b for water droplets in air refractive index of the particle (n_p) > than that of the medium (n_m) and in Figure C 1c,d for air bubbles in air refractive index of the particle (n_p) < than that of the medium (n_m). The angle (see Figure C 2) of the receiving optics (photo-detectors) is selected based on the n_p/n_m ratio and in order to ensure that a given scattering mode is dominant, e.g., angles between 30° and 70° are commonly used for first-order refraction.

In order to calculate the velocity and size of moving droplet, two incident laser beams of equal intensity and frequency intercept and interfere at 2θ as presented in Figure C 2forming a fringe pattern.

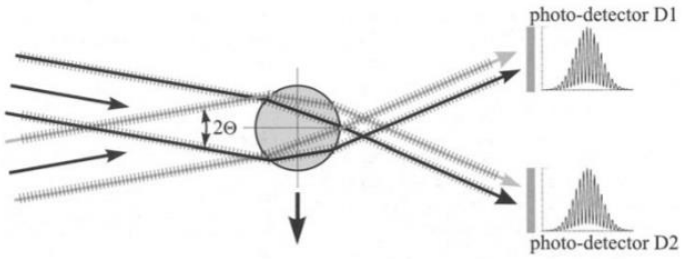

Figure C 2. Light scattered by a droplet and Doppler bursts generated in the photo-detectors.[242]

When a droplet passes through the interception, light waves coming from the two beams are scattered. As each incident beam has a different orientation related to the position of the photodetectors and the direction of the droplet, the frequency shifts of the light scattered from each beam are slightly different. In the photodetectors, the two scattered bursts are superimposed forming a Doppler burst (signal periodically rising and falling with a frequency which is equal to half of the difference between the frequency shifts of the light scattered from each laser beam). The velocity of the droplet is proportional to the Doppler burst frequency. As the photo-detectors are located at different positions, each detector receives the same Doppler burst (same frequency) but with a phase difference, which is used to calculate the diameter of the droplet based on the scattering mode.

- Experimental setup

Droplet size distributions and velocities in the spray-flame were measured using a commercial fiber-based dual Phase-Doppler anemometry (PDA) system (Dantec Dynamics). It consists of two monochrome diode lasers (532 nm and 561 nm) that are spatially overlapped by a lens (L1) to form the measuring volume (Figure C 3). An optical receiver (R) is collecting the scattered light through a collimating-lens (L2) from the droplets crossing the measuring volume. Through a detection mask (M), the signal is separated into four parts being focused on four fiber-coupled photo-detectors (PD) that are read-out and processed by a burst spectrum analyzer (BSA processor). Figure C 3 shows the setup for in situ measurements on the spray burner using first-order refraction on the droplets of the spray-flame. By using two lasers operated at 20 mW, two velocity components *u* and *v* (corresponding to the HAB-axis and *y*-axis, respectively) can be measured simultaneously, however, only the axial velocity *u* is presented in this study. Due to the focal length of the focusing-lens (L1) of 300 mm and the outer diameter of the burner system (100 mm), a minimum height above the burner (HAB) of 10 mm can be probed in the presented configuration. The applied mask enables the measurement of droplets in the range from 1–63 µm. For the measurements, droplets were either counted for a fixed time slot of 60 s or until a number count of 100,000 validated droplets was reached.

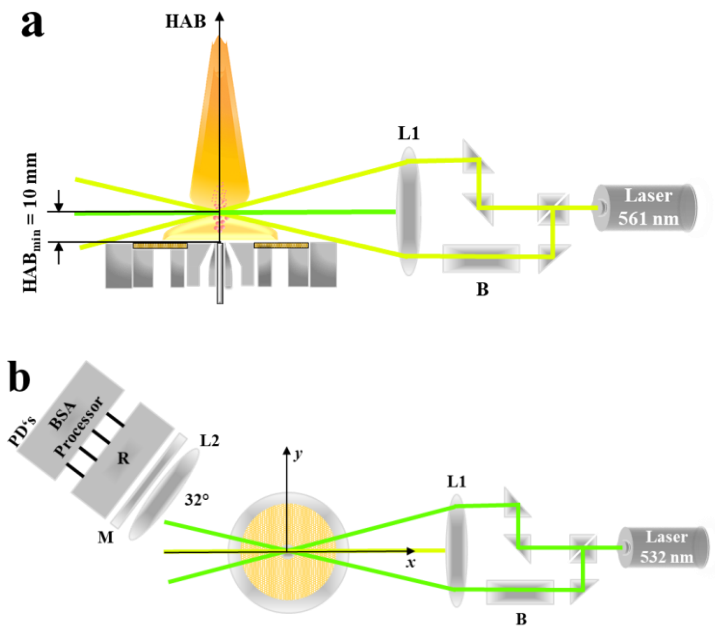

Figure C 3. Fiber-based dual PDA setup applied to the burner indicating the axis definitions (*x, y*, HAB) used. The top view (b) shows the probe, the photo detectors (PD) and the BSA processor that is omitted in the side view (a) for better clarity.

Samples transfer to TEM grids and XRD holders

For TEM measurements, dispersions of the collected samples were prepared in ethanol. Each dispersion was homogenized in an ultrasonic bath for 10 min. Afterwards and working inside a protecting fume hood, a droplet of each dispersion was deposited onto a corresponding carbon supported copper TEM grid from which ethanol was allowed to be dried for 5 min before transferring the grid to the TEM specimen holder. For XRD measurements, each sample was uniformly spread over a zero-background holder (ZBH) which was adapted to a steel support and placed in the XRD device rotating stage.

Raman measurements of the $LaMnO_3$ samples

Raman spectra were recorded from 100 to 800 cm^{-1} using a Renishaw inVia Reflex MicroRaman system with a laser wavelength of 633 nm and a laser power < 0.2 mW. Based on the XRD results presented in Figure 44a, three $LaMnO_3$ phases were identified: the orthorhombic *Pnma II* (*Ortho II*) (ICSD 50334), the orthorhombic *Pnma I* (*Ortho I*) (ICSD 51653) and the rhombohedral *R-3c* (ICSD 75070) phase. The *Ortho II* phase could be unequivocally identified from the XRD patterns, it presented well defined peaks' positions and intensities which also qualitatively indicated a higher crystallite size than that of the other two possible phases. The presence of the *Ortho I* or the rhombohedral phase cannot be excluded from the qualitative analysis of XRD alone. This is due to the strong unit cell symmetrization [55] of the *Ortho I* phase, indicating that its diffraction peaks present a small splitting with 2θ-positions that match those of the rhombohedral phase.

The Ortho I phase counts with a Mn^{4+} content ranging between 14 and 26 %, while the rhombohedral phase presents a Mn^{4+} content higher than 26 % [55], indicating that the Ortho I phase has a higher Mn^{3+} content than the rhombohedral phase. The Mn^{3+} ions in the MnO_6 non-linear octahedra of the perovskite structure allow Jahn-Teller (J-T) distortions [213]. The rhombohedral cation-deficient $LaMnO_3$ perovskite is

not compatible with the J-T distortion as the Mn-O bonds have the same length [213]. The Jahn-Teller distortions cause the enhancement of the Raman modes between 400 and 700 cm^{-1} in the orthorhombic structure, the A_g (~490 cm^{-1}) and B_{2g} (~600 cm^{-1}) Raman modes present narrow and intense bands [212-214]. By contrast, the rhombohedral structure presents broader and relatively weaker bands also at ~490 and ~600 cm^{-1}, which are not necessarily Raman modes but oxygen phonon branches from non-coherent Jahn-Teller distortions [213]. Raman measurements of $LaMnO_3$ perovskites spray-flame synthesized using different dispersion gas flow rates are presented in Figure C 4.

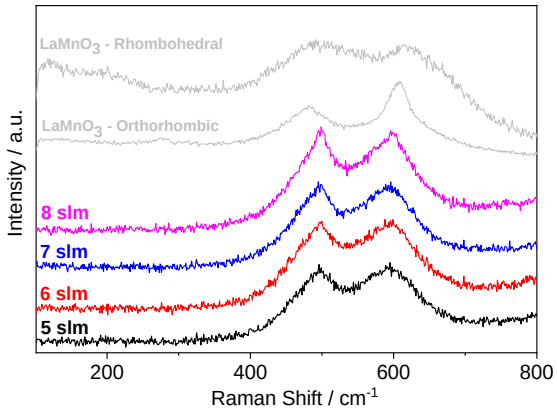

Figure C 4. Raman measurements of the $LaMnO_3$ samples. Two spectra from an orthorhombic and a rhombohedral phase are presented as reference.

The Raman spectra of all samples (5–8 slm) were similar, with two main bands centered at ~490 and ~600 cm^{-1}, which indicate the presence of both, orthorhombic and rhombohedral phases. The bands shape hint to a higher content of the orthorhombic structure. As the crystallite size of the low-content *Ortho II* phase is suspected to be much higher than the of the *Ortho I or R-3c* phases (confirmed in the following Rietveld refinements results) and the Raman spectra were taken in regions of low-size nanoparticles, the Raman results combined with the XRD results indicate the presence of the three proposed phases.

Rietveld refinements

The refinements were performed using the program Maud and the reference phases from the ICSD database. As presented in chapter 6.3.1, the particle size distributions are composed of a high fraction of low-size particles and a low fraction of high-size particles. Assuming this bimodal particle size distribution, the "double-phase model" [151, 229] was used in the refinements of the $LaFeO_3$ and $LaCoO_3$ samples. This method consists on using twice the same reference phase file for the fitting of each sample. As consequence, from one phase, two average crystallite sizes can be obtained with their corresponding mass concentrations.

For the $LaCoO_3$ samples, the rhombohedral (ICSD 201763) reference database CIF file was loaded twice to Maud. Additionally, La_2O_3 (ICSD 192270) was also included. For the $LaFeO_3$ samples, the orthorhombic (ICSD 28255) CIF file was loaded twice.

Regarding the $LaMnO_3$ samples and according to the XRD results, the high crystallite size orthorhombic *Pnma II (Ortho II*) (ICSD 50334) phase was identified. Additionally, two low crystallite size phases were identified as possible: the orthorhombic *Pnma I* (*Ortho I*) (ICSD 51653) phase and the rhombohedral *R-3c* (ICSD 75070) phase. The two low-crystallite size phases were verified with Raman measurements as presented in Figure C 4, which qualitatively indicated a higher proportion of the *Ortho I* phase over the *R-3c* phase. Based on this finding, the Rietveld refinement of the $LaMnO_3$ samples was performed using only

the two orthorhombic phases. This was additionally done because the strong unit cell symmetrization of the *Ortho I* phase and the presence of the other orthorhombic phase (*Ortho II*) do not allow to reliably distinguish them from the rhombohedral phase in the Rietveld refinement or qualitatively in the XRD patterns. As consequence, the *Ortho II* phase concentration and crystallite size are approximations to the average concentration and average crystallite size of the *Ortho II* and *R-3c* phases.

Based on the refinement results, two additional graphs were prepared for each perovskite system. In the first one, the mass concentration of each phase is presented as function of the dispersion gas flow rate. In the second one, the corresponding crystallite size is presented.

a. **$LaMnO_3$**

Rietveld refinements of $LaMnO_3$ samples are presented in Figure C 5.

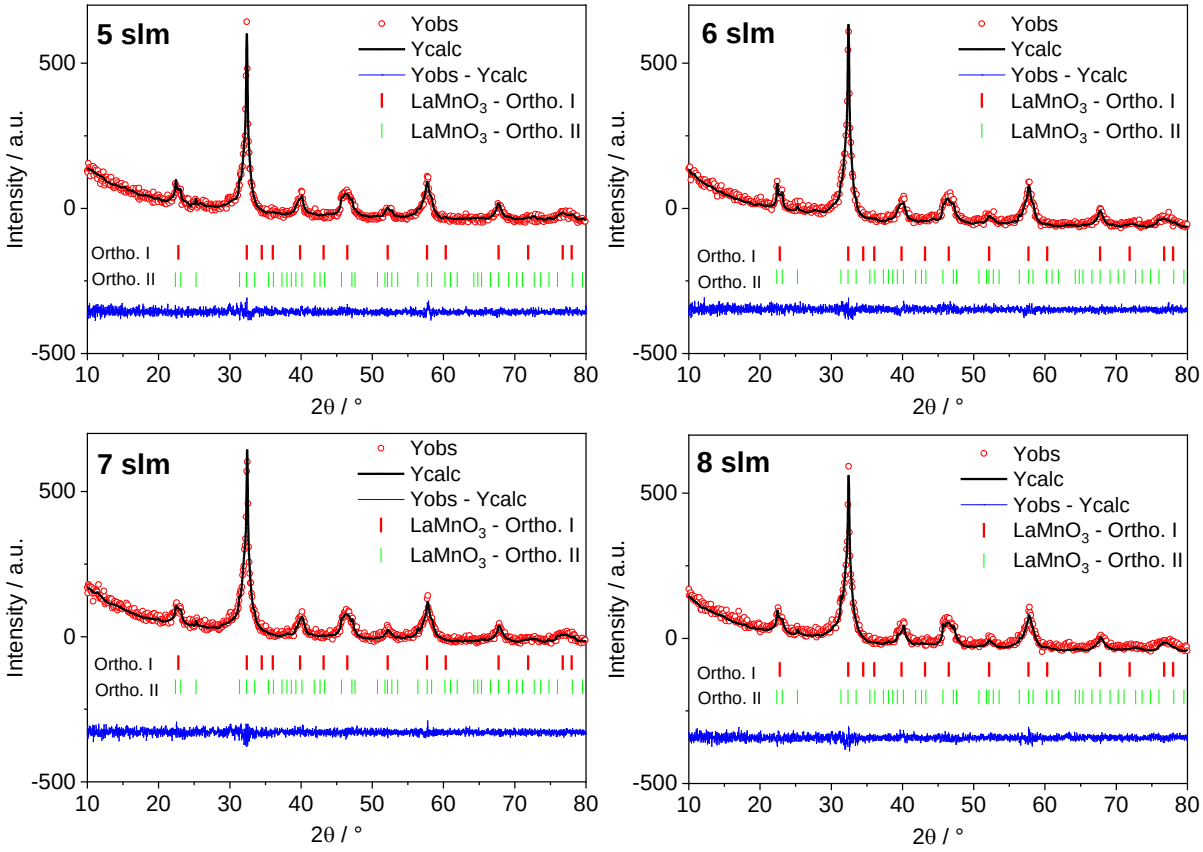

Figure C 5. Rietveld refinements of $LaMnO_3$ samples. Two phases were included: the orthorhombic Pnma I (Ortho. I) and the orthorhombic Pnma II (Ortho. II) phases.

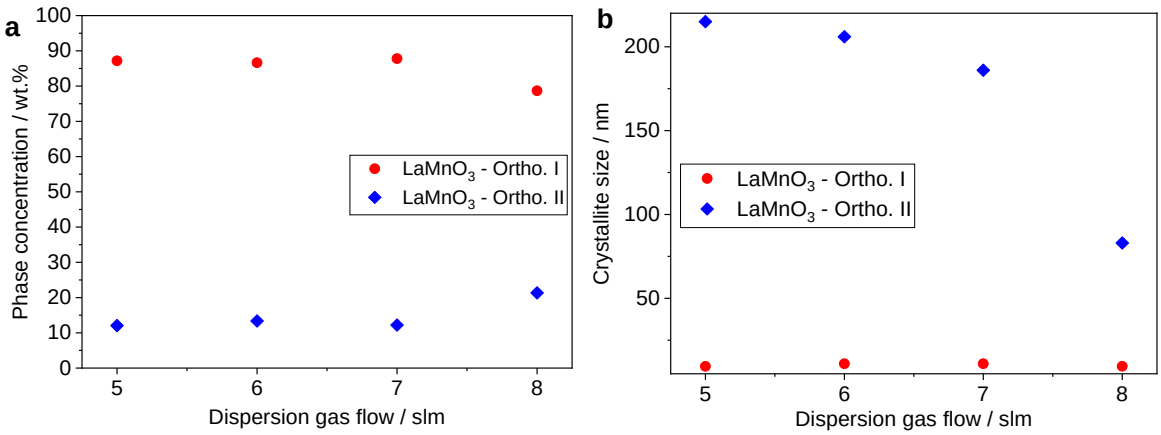

Figure C 6. (a) Concentration of each phase as a function of the dispersion gas flow. (b) Crystallite size of each phase as a function of the dispersion gas flow.

According to Figure C 6a, the *Ortho I* phase presented a concentration of about 87 Wt. % for the samples prepared using dispersion gas flows from 5 to 7 slm. This concentration slightly decreased to 78 Wt. % for the 8 slm case. As expected and as presented in the Figure C 6b, the *Ortho I* phase counted with a low crystallite size, about 10 nm, regardless of the used dispersion gas flow rate. In contrast, the concentration of the *Ortho II* phase (Figure C 6a) was about 13 Wt.% for dispersion gas flows between 5 and 7 slm, and increased to 22 Wt. % for the 8 slm case. The increase of the dispersion gas flow caused the decrease of the crystallite size of the *Ortho II* phase from 215 nm (5 slm) to 83 nm (8 slm) as it can be observed in Figure C 6b. These results are in line with the TEM and BET SSA results from the chapter 6.3.1 (Figure 42 and Figure 45), which indicated that the primary particle size as obtained from TEM images was not affected by the change of the dispersion gas flow, but the specific surface area increased with the increase of the flow.

b. $LaFeO_3$

Rietveld refinements of $LaFeO_3$ samples are presented in Figure C 7.

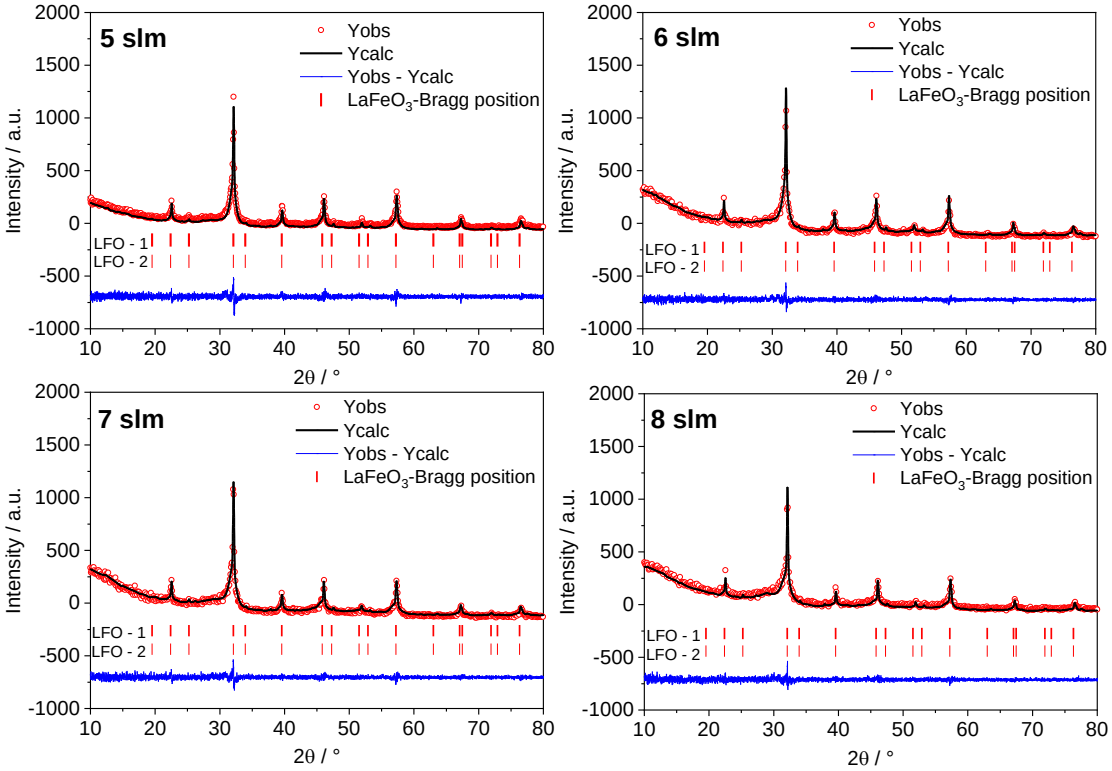

Figure C 7. Rietveld refinements of $LaFeO_3$ samples. The same orthorhombic (ICSD 28255) phase was loaded twice to Maud. The designated LFO-1 and LFO-2 phase have the same crystal structure and space group but present different concentration and crystallite size.

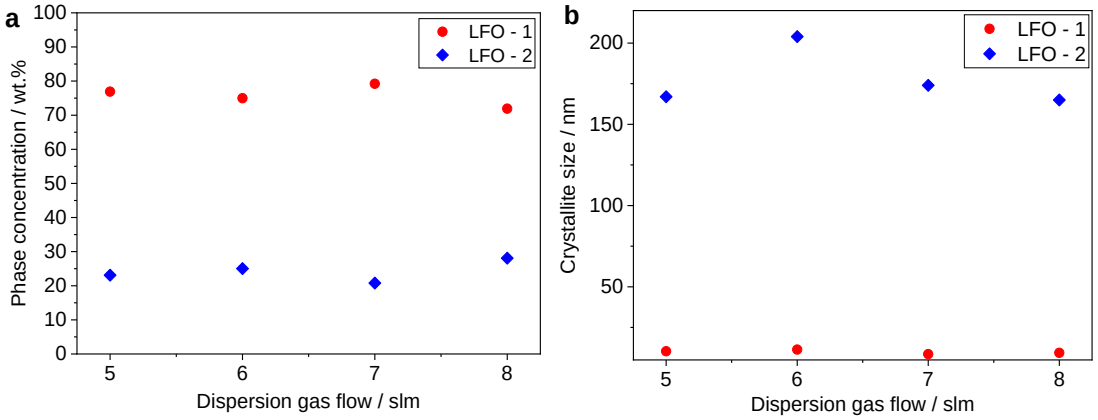

Figure C 8. (a) Concentration of LFO-1 & LFO-2 as a function of the dispersion gas flow. (b) Crystallite size of LFO-1 & LFO-2 as a function of the dispersion gas flow.

In case of $LaFeO_3$, the modification of the dispersion gas flow did not significantly affect the concentration of the LFO-1 and LFO-2 phases (Figure C 8a). The LFO-1 concentration presented an average of 75.7 Wt.% while the LFO-2 phase concentration counted with an average of 24.3 Wt.%. In parallel, the crystallite sizes (Figure C 8b) of the LFO-1 and LFO-2 phase were as well not importantly affected by the dispersion gas flow, with an average of 178 nm for the LFO-2 phase and an average of 10 nm for the LFO-1 phase. These results agree with the TEM (Figure 42) and BET SSA (Figure 45) results.

c. $LaCoO_3$

Rietveld refinements of $LaCoO_3$ samples are presented in Figure C 9.

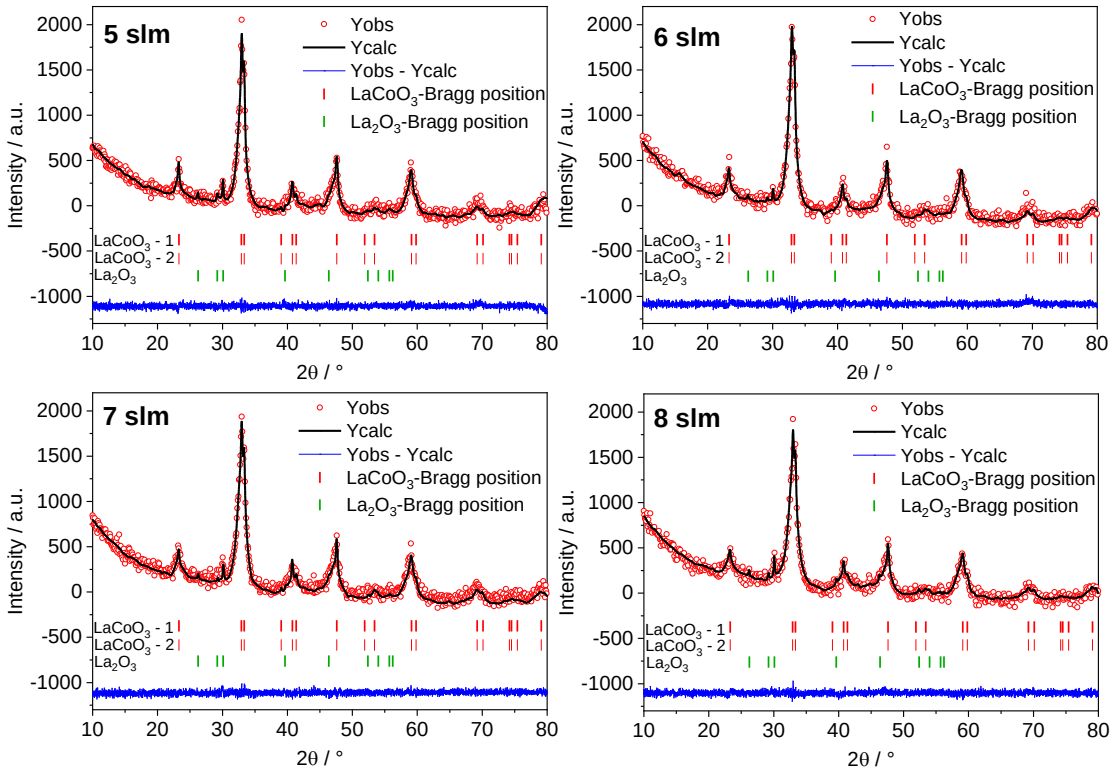

Figure C 9. Rietveld refinements of $LaCoO_3$ samples. The same rhombohedral (ICSD 201763) phase was loaded twice to Maud. The designated $LaCoO_3$-1 and $LaCoO_3$-2 phase have the same crystal structure and space group but present different concentration and crystallite size.

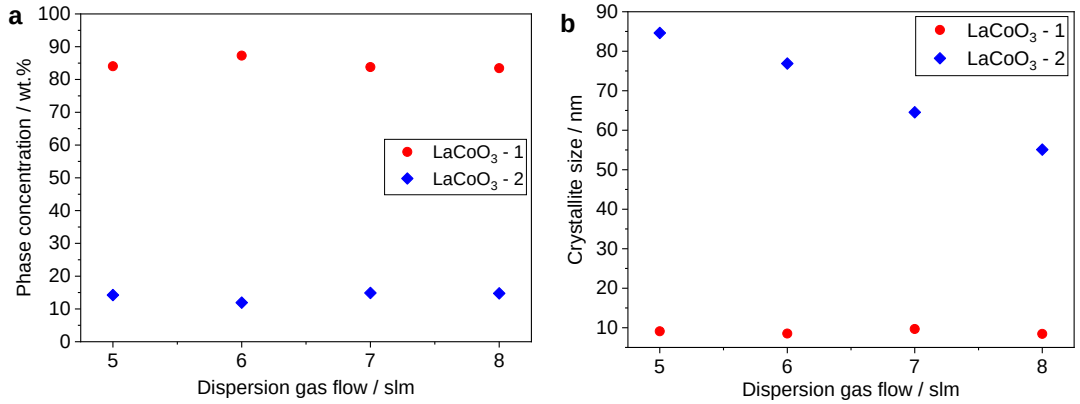

Figure C 10. (a) Concentration of $LaCoO_3$-1 and $LaCoO_3$-2 as a function of the dispersion gas flow. (b) Crystallite size of $LaCoO_3$-1 & $LaCoO_3$-2 as a function of the dispersion gas flow. The results concerning the La_2O_3 phase (concentration <3 % and crystallite size about 100 nm) of were not included in the figures.

The mass concentrations (Figure C 10a) of the $LaCoO_3$-1 (average of 84.6 Wt.%) and $LaCoO_3$-2 (average of 14 Wt.%) phases were not affected by the change of the dispersion gas flow. This was also the case for the crystallite size (average of 9 nm) of the high-concentration $LaCoO_3$-1 phase (Figure C 10b). On the contrary, the crystallite size of the low-concentration $LaCoO_3$-2 phase decreased linearly with the increase of the dispersion gas flow, from 85 nm (5 slm) to 55 nm (8 slm). These results are also in accordance with the TEM and BET SSA results (Figure 42 and Figure 45) from the chapter 6.3.1, in which the primary particle

size obtained from the analysis of TEM images was not modified by the change of the dispersion gas flow while the specific surface area increased from 66 m^2/g (5 slm) to 95 m^2/g (8 slm).

TEM images

a.) $LaMnO_3$

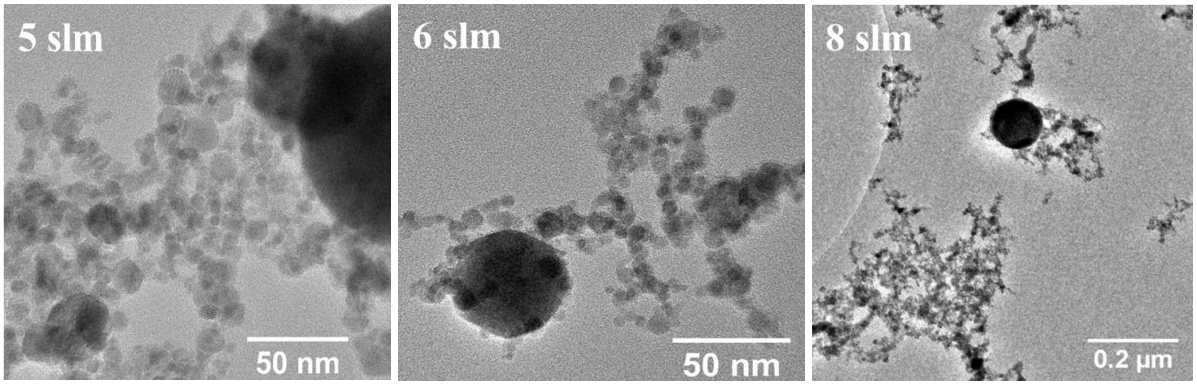

b.) $LaFeO_3$

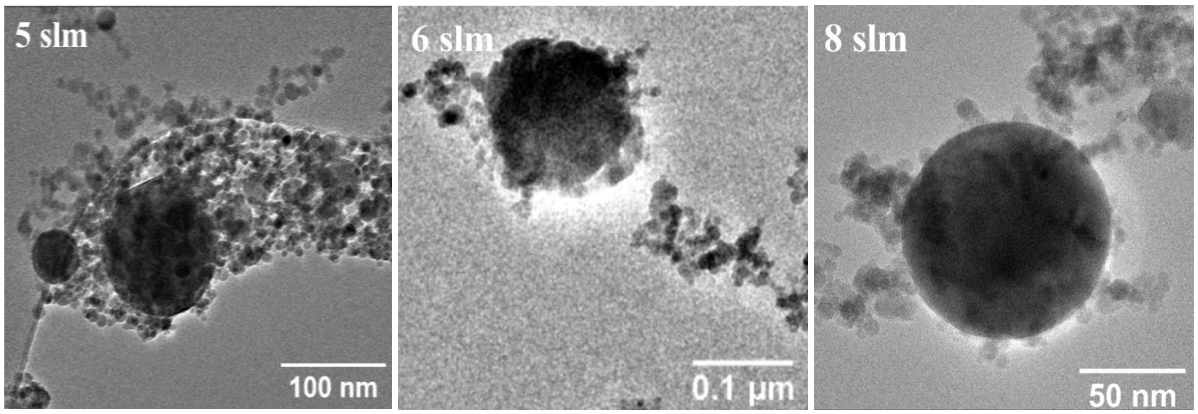

c.) $LaCoO_3$

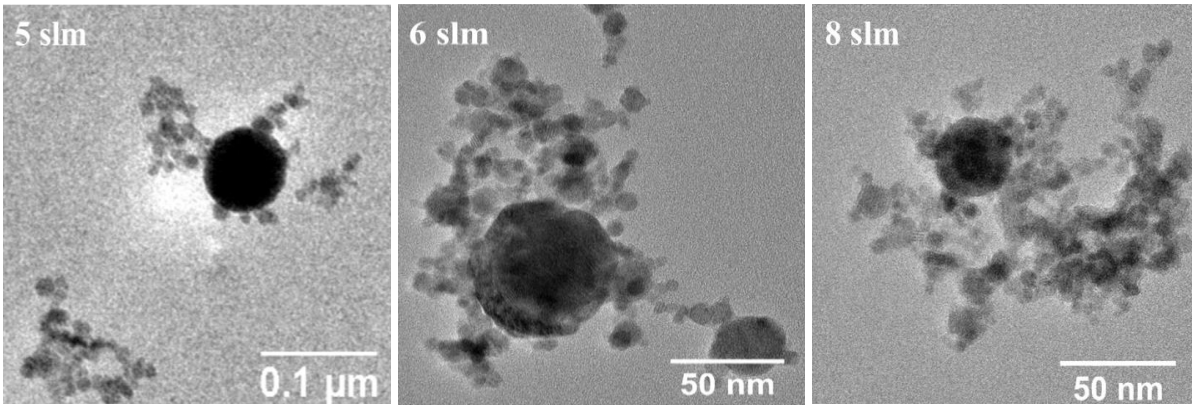

Figure C 11. TEM images depicting both high-size and low-size particles of the studied perovskite-like oxides synthesized using different dispersion gas flow rates (here: 5, 6 and 8 slm and in chapter 6.3.1: 7 slm – Figure 43): a.) $LaMnO_3$, b.) $LaFeO_3$, c.) $LaCoO_3$.

Phase-Doppler anemometry (PDA) measurements at HAB = 20 mm

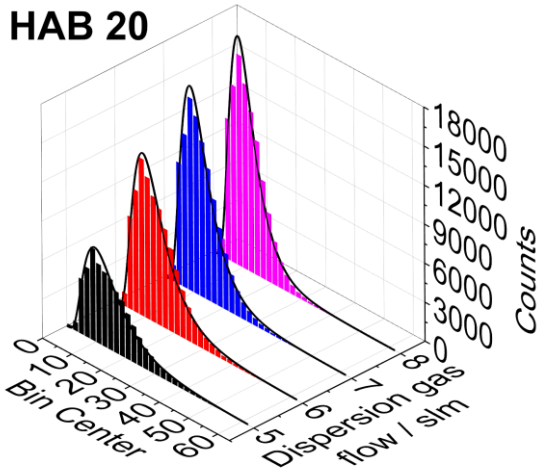

Figure C 12. Droplet-size distributions as a function of the dispersion gas flow at HAB = 20 mm.

12 Acknowledgments

Throughout my life I have met persons that were able to take chances on me and to give me the opportunity to contribute in some way to a common goal. I want to thank all of them for their trust, I hope they give me the opportunity to keep learning from them and I also hope to become as wise as they are. Two of these persons are Prof. Dr. Hartmut Wiggers and Prof. Dr. Christof Schulz, my two supervisors. I am so fortunate to have met them and to interact with them. They show me that it is possible to be kind, humble, hard-working and highly-achieving.

I am grateful for the financial support provided from the German Academic Exchange Service (DAAD). I was awarded a full doctoral scholarship that allowed me to conduct independent research for 4 years. Thank you very much to the Colombian DAAD office for the great advice and to the German DAAD section for the continuous and patient support.

I was also accepted to be part of the IMPRS RECHARGE of the Max-Planck-Institute for Chemical Energy Conversion. I would like to thank Prof. Dr. Frank Neese for this great opportunity which has allowed to meet great scientists and friends and to access world-class facilities to characterize materials. I also thank very much Mrs. Rita Groever for all the support and for making possible so many activities, meetings and conferences. Thank you very much for supporting my idea of organizing a conference in France. To all my fellow students from IMPRS RECHARGE, I'm grateful to have met you. You're inspiring people!

My research was possible thanks to a huge network of people working in administrative, technical, engineering or scientific parts of the University of Duisburg-Essen and the Institute for Combustion and Gas Dynamics (IVG) – Reactive Fluids (RF). I start thanking Barbara Nota and Barbara Graf for all the support in so many important parts related to documents, orders, logistics, and so on. You keep the institute smoothly running. I also thank all the technical/engineering staff of IVG: Ludger Jerig, Sebastian Rosendahl, Beate Endres, Erdal Akyildiz, Jörg Albrecht, Natascha Schlösser, and Birgit Nelius. Thank you for all the countless times you helped me devising/setting up/fixing instruments/reactors/experiments.

To all the previous and current colleagues of the Nanoparticle Synthesis Group of IVG-RF, I thank you very much for all the nice times, discussions and collaboration. Regarding the latter point, I thank Jasmina Kovacevic for introducing the spray-flame reactor to me and for being always so kind and patient, Malini Dasgupta for XRD and Raman measurements, Paolo Fortugno for Raman measurements, Yusuf Ali and Alexander Tarasov for XPS measurements, Baris Alkan for XRD measurements, Mohaned Hammad for functionalization/application experiments, Moritz Löwenich and Stefan Kilian for SEM measurements, Sascha Apazeller for TGA/DSC and PDA measurements, Hans Orthner for various equipment/devices, Beate Endres for BET measurements, Adrian Münzer, Stefan Kuns, Frederik Kunze, Ahmed Al-Kamal and Jonas Twellmann for the nice discussions. Thanks a lot to my ex-colleague Yee Hwa Sehlleier for being so nice and easy-going. I thank very much my ex-colleague and friend Lisong Xiao for all the time we shared our office and the nice Chinese restaurants he showed me. Thanks a lot to my ex-colleague and friend Sebastian Kluge for running with me and while doing so, for showing me Duisburg and discussing science and life. I'm grateful to my colleague and friend Samer Suleiman for the nice photos of the spray-flame, our talks, for coming to Colombia for my wedding, for being so kind to everyone. I would also like to thank the other colleagues from IVG, especially Paul Sela for the GC/MS measurements, Florian Schneider for the PDA measurements, Prof. Dr. Thomas Dreier for all the discussions, Sadrollah Karaminejad for the high-speed camera measurements and for devising/trying with me so many experiments. I'm grateful to my friend Stanislav Musikhin for all our conversations, lunches/dinners, for going to swim with me and for being so nice and funny. I thank all the Fluid Dynamics team, especially Patrick Wollny, Dr. Irenäus

Wlokas, and Prof. Dr. Andreas Kempf for the spray-flame synthesis related simulations. I also thank my former students Julian Neises, Patrick Wischnewski, and Jan Goldau for the hundreds of FTIR and UV-Vis measurements that they performed.

The main characterization of my samples was possible with the help and contribution of many persons and research institutions. I thank very much all the scientists from ICAN, especially Markus Heidelmann for TEM measurements and Ulrich Hagemann for XPS/Raman measurements. I thank Joachim Landers, Soma Salamon, and Prof. Dr. Heiko Wende for the Mößbauer measurements/analysis. I acknowledge all the great scientists from the group of Prof. Dr. Markus Winterer: Alexander Kompch and Stevan Ognjanovic for showing me how to operate the XRD device and the theory behind, Claudia Gorynski, Alexander Levish, and Viktor Mackert for helping with the XRD measurements. I would like also to thank Prof. Dr. Doru Lupascu and Merlin Schmuck for XRD measurements.

I want to thank all my other collaborators for all their work and their contributions. Thanks a lot to Maik Dreyer, Dr. Klaus Friedel-Ortega and Prof. Dr. Malte Behrens for the catalytic measurements/analyses and to Anna Rabe for the XRD measurements. Thanks a lot to Julia Büker, Daniel Waffel, Tobias Falk and Prof. Dr. Martin Muhler for all the catalysis measurements. Thanks a lot to Michael Braun and Prof. Dr. Corina Andronescu for the electrocatalytic measurements. I'm grateful to Wiebke Kaziur and Prof. Dr. Torsten Schmidt for the GC/MS measurements that were so relevant for my investigation. Thanks a lot to Prof. Hamid Reza Arandiyan from the University of Sidney and Dr. Yuan (Helena) Wang of UNSW for the catalytic measurements, which were also performed at the UdeA, for which I'm grateful to my former M. Sc. supervisor and friend Prof. Jaime Gallego and to Juan David Tapia.

I thank all the research groups and scientists from the Collaborative Research Centre / Transregio 247 "Heterogeneous Oxidation Catalysis in the Liquid Phase" for providing such a great scientific environment for the advancement of the synthesis, characterization and evaluation of catalysts. I thank Dr. Franziska Günther for the great support and organization within the CRC. Thanks a lot to the executive board – Prof. Dr. Malte Behrens, Prof. Dr. Martin Muhler and Prof. Dr. Christof Schulz – for letting me be part of such an important project. Thanks a lot to my fellow PhD students for allowing me be their deputy-representative and thanks to Anna Rabe for her great work as main representative.

I thank my former boss, mentor and friend Enrique Posada for all the lessons about creativity and engineering. I apply them every day! I thank all my friends which nurture my life with their opinions, advices and very different points of view.

I thank all my family for their support and love. I especially thank my parents (Martha & Ramiro) for raising me as a curious and kind person, my brother (Joan) for showing me other perspectives and my grandmother (Margarita) for teaching me by example that I can accomplish anything I set my mind to. I thank my parents-in-law (Blanca Nelly and Hector), my brother-in-law Felipe, my sister-in-law Corina and my niece/goddaughter Amelia for all the support, advice, kindness and great times all around the world.

Most importantly, I would like to thank my beautiful wife Catherine and my daughter Maia. You inspire me to be a better person and professional and you fill each day with love, compassion, and peace.

DOI: 10.17185/duepublico/74891
URN: urn:nbn:de:hbz:464-20211105-155711-2